BONNER METEOROLOGISCHE ABHANDLUNGEN

Heft 72 (2016) (ISSN 0006-7156)
Herausgeber: Andreas Hense

Markus Übel

SIMULATION OF MESOSCALE PATTERNS AND DIURNAL VARIATIONS OF ATMOSPHERIC CO_2 MIXING RATIOS WITH THE MODEL SYSTEM TERRSYSMP-CO_2

BONNER METEOROLOGISCHE ABHANDLUNGEN
Heft 72 (2016) (ISSN 0006-7156)
Herausgeber: Andreas Hense

Markus Übel

SIMULATION OF MESOSCALE PATTERNS AND DIURNAL VARIATIONS OF ATMOSPHERIC CO_2 MIXING RATIOS WITH THE MODEL SYSTEM TERRSYSMP-CO_2

Simulation of mesoscale patterns and diurnal variations of atmospheric CO_2 mixing ratios with the model system TerrSysMP-CO_2

DISSERTATION
ZUR
ERLANGUNG DES DOKTORGRADES (DR. RER. NAT.)
DER
MATHEMATISCH-NATURWISSENSCHAFTLICHEN FAKULTÄT
DER
RHEINISCHEN FRIEDRICH-WILHELMS-UNIVERSITÄT BONN

vorgelegt von
Dipl.-Meteorologe
Markus Übel
aus
Bamberg

Bonn, Dezember, 2015

Diese Arbeit ist die ungekürzte Fassung einer der Mathematisch-Naturwissenschaftlichen Fakultät der Rheinischen Friedrich-Wilhelms-Universität Bonn im Jahr 2015 vorgelegten Dissertation von Markus Übel aus Bamberg.

This paper is the unabridged version of a dissertation thesis submitted by Markus Übel born in Bamberg to the Faculty of Mathematical and Natural Sciences of the Rheinische Friedrich-Wilhelms-Universität Bonn in 2015.

Anschrift des Verfassers: Address of the author:

Markus Übel
Meteorologisches Institut der
Universität Bonn
Auf dem Hügel 20
D-53121 Bonn

1. Gutachter: Prof. Dr. Andreas Bott,
Rheinische Friedrich-Wilhelms-Universität Bonn
2. Gutachter: Prof. Dr. Clemens Simmer,
Rheinische Friedrich-Wilhelms-Universität Bonn

Tag der Promotion: 13. April 2016

Danksagung

Zuerst möchte ich mich herzlich bei meinem Betreuer Prof. Dr. *Andreas Bott* für die Unterstützung in den letzten Jahren und einer immer offenen Bürotür bedanken. Durch ihn wurde es überhaupt erst möglich, innerhalb eines interdisziplinären Projekts forschen zu dürfen.

Ich bedanke mich ferner für die finanzielle Unterstützung durch den DFG-Sonderforschungsbereich "Transregional Collaborative Research Centre 32 – Patterns in Soil-Vegetation-Atmosphere-Systems" (TR32/2 2011 3009725).

Mein besonderer Dank geht an *Volker Küll*, der wie ein zweiter "Doktorvater" für mich war und sich sehr viel Zeit für mich genommen hat. Die vielen wissenschaftlichen Diskussionen mit ihm, inklusive hilfreicher Ideen auf unterschiedlichsten Gebieten, trugen wesentlich zum Gelingen dieser Arbeit bei. Durch seine immensen Programmierkenntnisse und die vielen schnellen und praktischen Hilfen bei diversen technischen Problemen wurde mir die Arbeit in vielerlei Hinsicht erleichtert. Zudem half mir Volkers Unterstützung bei jeglichen sonstigen Schwierigkeiten während meiner Zeit als Doktorand und die vielen humorvollen Momente mit ihm sorgten für die nötige Auflockerung im akademischen Alltag.

Außerdem möchte ich mich bei *Michael Herbst* herzlich bedanken, der einem Meteorologen wie mir die Prozesse im Boden näher gebracht hat und mir mit seinen Ideen wesentlich beim Einbau der Bodenatmungsparametrisierungen in TerrSysMP-CO_2 geholfen hat. Michael nahm sich immer spontan und bereitwillig für meine Fragen die nötige Zeit.

Großer Dank gilt auch meinen beiden studentischen Hilfskräften *Melanie Kern* und *Anna-Marie Jörss*, die nicht nur regelmäßig die CO_2-Messgeräte am Jülicher Messturm kalibriert und betreut haben, sondern auch die gemessenen Daten aufbereitet und visualisiert haben.

Bedanken möchte ich mich auch bei *Martin Lennefer* und *Alexander Graf*, die es einem Modellierer wie mir erst möglich gemacht haben, die nötigen Messwerte zur Verifikation meiner Modellergebnisse zu beschaffen, angefangen bei der Auswahl des geeigneten Messgeräts über die Installation am Messturm bis hin zur Einweisung in Melanies und Annas Tätigkeiten. In diesem Zusammenhang danke ich auch *Marc von Hobe*, der mir einerseits zusätzliche CO_2-Messungen am Jülicher Messturm zur Verfügung gestellt hat und zudem in mehreren Diskussionen mit seinem Wissen über Messtechnik mögliche Fehlerquellen bei den Messmethoden verhinderte und dazu beitrug, einen wertvollen Datensatz für die Modellverifikation zu erzeugen.

Vielen Dank auch an *Anja Stadler* für die Bereitstellung von Messdaten zu LAI, CO_2-Assimilation und Respiration auf den Messfeldern in Selhausen und Merzenhausen zur Verifikation meiner Ergebnisse.

Weiterhin möchte ich mich bei *Hugo Denier van der Gon* bedanken, der mir die aktualisierten Daten der "TNO-MACC_II emission inventory" zur Verfügung gestellt hat, sowie bei *Johannes Klimpt*, der die Daten zu hochaufgelösten anthropogenen CO_2-Emissionen aufbereitete.

Ganz herzlich möchte ich zu meinem Zimmerkollegen und Freund *Werner* danke sagen, der mir nicht nur in der Anfangszeit mit viel Geduld meine ersten Programmierversuche leichter machte, sondern es auch ermöglichte, dass mein Steckenpferd – die tägliche Wettervorhersage – nie zu kurz kam. Die Arbeitszeit mit Werner im Büro war immer angenehm und nie langweilig.

Nicht zu vergessen sind all meine Korrekturleser, die für den letzten Schliff meiner Dissertation sorgten, im Einzelnen *Alex*, *Lilo*, *Sebi*, *Tanja* und *Volker* – euch allen vielen Dank.

Zu guter Letzt bedanke ich mich bei meiner Familie, meinem Bruder *Michael*, *Klaus* und insbesondere meiner Mutter *Gertrud*, die zwar immer noch nicht genau weiß, was ich alles erforscht habe, dafür aber zu jeder Zeit an mich geglaubt hat und immer ein offenes Ohr für all meine Zweifel und Gedanken während der letzten Jahre hatte. Sie hat mich immer wieder an meine Stärken erinnert und stand mir unermüdlich mit Rat und Tat zur Seite. Vielen, vielen Dank dafür!

Markus Übel
Bonn, Dezember 2015

Zusammenfassung

Mit dem gegenwärtigen Trend hin zu präzisen regionalen Klimasimulationen werden Informationen über die räumliche Verteilung mesoskaliger CO_2-Quellen/Senken immer wichtiger. Eine häufig verwendete Methode, um an diese Flüsse zu gelangen, ist inverse Modellierung. Dabei wird die Variabilität atmosphärischer Beobachtungen in atmosphärische Tracertransport-Modelle assimiliert, um mesoskalige und regionale CO_2-Flüsse abzuschätzen. Flugzeugmessungen zeigen deutliche mesoskalige Strukturen in der atmosphärischen CO_2-Verteilung, welche nur teilweise von Klimamodellen mit relativ groben Gitterauflösungen abgebildet werden können.

Die Hauptziele der vorliegenden Arbeit liegen darin, zu verstehen, welche Prozesse (z. B. synoptische Strömungen, heterogene Landnutzung, komplexes Terrain) diese Strukturen verursachen und wie die variablen CO_2-Gehalte die stomatäre Steuerung von Transpiration und Photosynthese beeinflussen. Dazu wird das mesoskalige terrestrische Modellsystem TerrSysMP verwendet, welches das atmosphärische Modell COSMO (Version 4.21) mit dem Community Land Model (CLM3.5) koppelt, das zudem mit dem hydrologischen Modell ParFlow gekoppelt werden kann. TerrSysMP wird mit einer vollständig prognostischen Behandlung atmosphärischer CO_2-Konzentration erweitert, was zur neuen Modellversion TerrSysMP-CO_2 führt. Dieses Modell umfasst eine gegenseitige Kopplung von CO_2 (Atmosphäre ↔ Biosphäre): Die aktuellen CO_2-Mischungsverhältnisse werden verwendet, um mit CLM die biogenen CO_2-Flüsse zu berechnen und im Gegenzug bestimmen diese Flüsse prognostisch die atmosphärische CO_2-Verteilung. CLM wird sowohl mit dem Kohlenstoffumsatz-Modell RothC erweitert, welches die heterotrophe Bodenatmung berechnet, als auch mit einfachen Parametrisierungen zur Dekomposition von organischem Material und zur autotrophen Bodenatmung. Außerdem vervollständigen hochaufgelöste anthropogene Emissionen den CO_2-Haushalt in TerrSysMP-CO_2.

Mit TerrSysMP-CO_2 werden hochaufgelöste Modellsimulationen für eine Region in Westdeutschland und Teilen der BeNeLux-Staaten durchgeführt. Das Gebiet schließt das Mittelgebirge Eifel sowie das dicht besiedelte Rheintal mit den Metropolen Köln, Düsseldorf und Bonn mit ein. Die Ergebnisse zeigen einen deutlich ausgeprägten CO_2-Tagesgang in der planetaren Grenzschicht. Die höchsten Konzentrationen treten am frühen Morgen auf, als Folge von bodennaher CO_2-Ansammlung durch Bodenatmung. Mit dem Einsetzen der Photosynthese wird in der Atmosphäre ein starker CO_2-Rückgang simuliert, gefolgt von turbulentem Durchmischen innerhalb der Grenzschicht am Tage. Dabei ist der Einfluss von komplexem Terrain und anthropogenen Emissionen auf die raum-zeitlichen Muster atmosphärischer CO_2-Mischungsverhältnisse von besonderem Interesse. Während der Nacht entstehen zwischen engen Tälern und Bergrücken starke horizontale CO_2-Gradienten, bedingt durch orographisch induzierte Turbulenzmuster und mesoskalige atmosphärische Strömungen. Zudem werden stromabwärts dicht besiedelter Regionen deutlich erhöhte CO_2-Konzentrationen simuliert. Außerdem führen die variablen CO_2-Mischungsverhältnisse zu leichten Veränderungen der simulierten Photosynthese- und Transpirationsraten aufgrund der Beeinflussung der Öffnung von Blattstomata auf die zur Verfügung stehenden atmosphärischen CO_2-Konzentrationen.

Das Modellverhalten von TerrSysMP-CO_2 wird mit Eddy-Kovarianz Messungen von CO_2 und Energieflüssen verifiziert. Außerdem wird die simulierte vertikale Verteilung atmosphärischer CO_2-Konzentrationen mit Beobachtungen verglichen, welche an einem 124 m hohen Turm in der Nähe von Jülich durchgeführt wurden.

Die neuen Einblicke in die Prozesse, welche die mesoskaligen Strukturen in den atmosphärischen CO_2-Mischungsverhältnissen beeinflussen, können dabei helfen, CO_2-Beobachtungen an Land und an Küsten besser in inverse Modellierungsstudien zu integrieren.

Summary

With the recent trend towards precise regional climate simulations information of the spatial distribution of CO_2 sources and sinks at the mesoscale scale becomes more important. A common method to obtain these fluxes is inverse modeling, i. e. the variability of atmospheric CO_2 observations is assimilated into atmospheric tracer transport models to estimate mesoscale and regional scale CO_2 fluxes. Aircraft measurements indicate distinct mesoscale patterns in the atmospheric CO_2 distribution which can only partly be resolved by climate models using a rather coarse grid resolution.

The main objectives of the present study are to understand which processes (e. g. synoptic flow, land use heterogeneity, complex terrain) generate these patterns and how the variable atmospheric CO_2 contents influence the stomatal control of transpiration and photosynthesis. For that, the mesoscale terrestrial model system TerrSysMP is used that couples the atmospheric model COSMO (version 4.21) to the Community Land Model (CLM, version 3.5) which can again be coupled to the hydrological model ParFlow. TerrSysMP is extended by a fully prognostic treatment of atmospheric CO_2 concentrations forming the new model version TerrSysMP-CO_2. This model includes a two-way coupling of CO_2 (atmosphere $\leftrightarrow$ biosphere): the actual CO_2 mixing ratios are used to calculate the biogenic CO_2 fluxes with CLM and, in turn, these fluxes prognostically cause the atmospheric CO_2 distribution. CLM is extended by the carbon turnover model RothC calculating heterotrophic soil respiration as well as by simple parameterizations for decomposition of organic matter and autotrophic respiration. Moreover, high-resolution anthropogenic emissions complete the CO_2 budget in TerrSysMP-CO_2.

High-resolution model simulations are performed using TerrSysMP-CO_2 for a region in western Germany and parts of BeNeLux. The domain includes the low mountain range Eifel as well as the densely populated Rhine valley with the metropolises Cologne, Dusseldorf and Bonn. The results show a pronounced diurnal cycle of CO_2 in the planetary boundary layer (PBL). The highest concentrations occur in the early morning being the result of near surface CO_2 accumulation due to soil respiration. With the onset of photosynthesis a strong decrease of atmospheric CO_2 concentrations is simulated followed by turbulent vertical transport within the PBL at daytime. The influence of complex terrain and anthropogenic CO_2 emissions on the spatio-temporal patterns of atmospheric CO_2 mixing ratios is of particular interest. During night strong horizontal CO_2 gradients arise between narrow valleys and mountain ridges caused by orographically induced turbulent patterns and mesoscale atmospheric flows. Moreover, downstream of densely populated regions significant higher CO_2 concentrations are simulated. Additionally, the variable atmospheric CO_2 mixing ratios slightly modify simulated photosynthesis and transpiration rates due to the response of the stomatal opening of leaves on available atmospheric CO_2 concentrations.

The model performance of TerrSysMP-CO_2 is verified with eddy-covariance measurements of CO_2 and energy fluxes. Moreover, the simulated vertical distribution of atmospheric CO_2 concentrations is compared with observations of CO_2 made at a 124 m tall tower near Jülich.

The new insights into the processes influencing mesoscale patterns of atmospheric CO_2 mixing ratios can help to better integrate terrestrial and coastal CO_2 observations into inverse modeling studies.

Contents

1. Introduction

1.1. CO_2 cycle of a terrestrial biosphere

Carbon dioxide (CO_2) makes the greatest anthropogenic contribution to the greenhouse effect, in addition to the most important natural greenhouse gas H_2O. Before the industrial era (≈ 1750) atmospheric CO_2 concentrations were almost constant, 280 ± 10 ppmv (Prentice *et al.*, 2001), but since then CO_2 contents have risen with the fastest increase between the 1950s and today. In March 2015, the global mean CO_2 content has exceeded 400 ppmv.

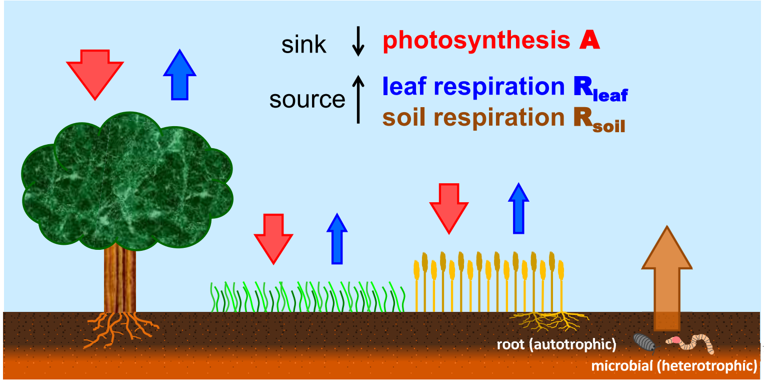

Figure 1.1.: Biogenic CO_2 fluxes of a terrestrial ecosystem.

The major components of the atmospheric CO_2 budget are the exchange between the ocean and the atmosphere, between the terrestrial biosphere and the atmosphere as well as anthropogenic disturbances, e. g. fossil fuel burning and land use change (e. g. McGuire *et al.*, 2001). On interannual time scales the ocean is the largest CO_2 sink of the earth whereas the CO_2 uptake by the terrestrial biosphere is small. However, on diurnal time scales an efficient CO_2 exchange happens between the atmosphere and terrestrial ecosystems (Fig. 1.1). It is responsible the diurnal and seasonal variations of atmospheric CO_2 contents. Plants take up CO_2 from the atmosphere needed for *photosynthesis* (A). The amount of CO_2 being fixed during photosynthesis is known as *gross primary production* (GPP). About half of GPP is incorporated into new plant tissue (leaves, roots, wood), i. e. *net primary production* (NPP), whereas the other half is respired back to the atmosphere by *autotrophic respiration* (R_a) (Ryan, 1991). Plants respire both aboveground by leaves (*leaf respiration* R_{leaf}) and belowground by roots (*root respiration* R_{root}). In addition to the plants, the soil also releases CO_2 into the atmosphere (*soil respiration* R_{soil}). R_{soil} itself consists of R_{root} and *heterotrophic* (or *microbial*) *respiration* (R_h). R_h describes the CO_2 exchange between the soil and the atmosphere by decomposition of soil organic matter (SOM) through microbes (bacteria, fungi) and soil fauna, i. e. small animals living in the soil and in the forest floor (e. g. earthworms, woodlouses). The decomposition of dead plant material (litter) also contributes to R_h. Total respiration ($R_{soil} + R_{leaf}$) almost balances GPP and the small remaining amount of CO_2 is known as *net ecosystem production*

(NEP). The biogenic CO_2 budget of a terrestrial ecosystem then can be written as

$$\text{NEP} = \text{GPP} - (R_{leaf} + R_{root}) - R_h = (\text{GPP} - R_a) - R_h = \text{NPP} - R_h = \text{GPP} - R_{leaf} - R_{soil}. \quad (1.1)$$

While photosynthetic CO_2 uptake only occurs at daytime, R_{leaf} and R_{soil} is active the entire day. In other words, an ecosystem can be regarded as a sink of atmospheric CO_2 at daytime and a source at night causing a pronounced diurnal variation in the lower atmosphere.

In addition to the biogenic CO_2 fluxes, since the begin of the industrial era the humans disturb the biogenic CO_2 budget by a new atmospheric CO_2 source, referred to as anthropogenic CO_2 emissions. These are primarily the result of consumption of energy from fossil fuels needed for, e. g., public electricity, industry or road and sea traffic. A part of the anthropogenic emissions is taken up by the ocean and to a smaller amount by the land. The remaining part is responsible for the recent global increase of CO_2 in the atmosphere (Prentice *et al.*, 2001).

1.2. Why is mesoscale modeling of CO_2 variability important?

The importance of increasing atmospheric CO_2 contents for the estimation of future global warming in different climate scenarios is well known. At the global and continental scale, an accurate quantifaction of the CO_2 budget and the distribution of CO_2 sources/sinks is crucial for precise climate simulations. The terrestrial CO_2 fluxes are studied with a combination of atmospheric CO_2 measurements and numerical models (e. g. Peters *et al.*, 2010) as well as recently by the application of satellite-based observations of atmospheric CO_2 concentrations (e. g. Boesch *et al.*, 2011). On the other hand, at the local scale the CO_2 exchange of ecosystems is investigated with eddy covariance (EC) measurements. However, a large mismatch exists between both scales as stated, e. g., in Dolman *et al.* (2006) and Ter Maat *et al.* (2010) motivating the research community to explore CO_2 fluxes at intermediate scales (regional and mesoscale). To bridge the gap between local and global scale this study deals with the diurnal variability of CO_2 fluxes as well as with atmospheric CO_2 patterns on the mesoscale.

Dolman *et al.* (2006) and Sarrat *et al.* (2007b) found high mesoscale gradients in the spatial CO_2 distribution in the planetary boundary layer (PBL). They stated that the variability of the atmospheric flow requires mesoscale modeling to properly resolve these gradients. Moreover, with these models "our process understanding of the major controls of the emission and uptake of CO_2 at the regional scale" (Dolman *et al.*, 2006, p. 1368) can be improved. The question arises what are the main controlling factors (e. g. land use heterogeneity, synoptic flow, mesoscale flow, anthropogenic emissions) to explain CO_2 gradients at the regional and mesoscale for which there are limited observations (Nicholls *et al.*, 2004; Ter Maat *et al.*, 2010). This knowledge is necessary to upscale local flux measurements to the mesoscale distribution of CO_2 fluxes (Dolman *et al.*, 2006) and provides valuable information for many research fields (e. g. crop modeling, land management strategies, plant physiology, micrometeorology and others).

A common method to obtain the magnitude and distribution of regional CO_2 fluxes is inverse modeling. The variability of atmospheric CO_2 observations is assimilated into global atmospheric tracer transport models to estimate regional CO_2 fluxes needed for global studies (Prentice *et al.*, 2001). However, this method includes several uncertainties caused on the one hand by the limited number of tall tower CO_2 measurements (i. e. mathematically the inversion problem is highly underdetermined) and on the other hand by the quality of the atmospheric transport in the models (van der Molen and Dolman, 2007; Tolk *et al.*, 2009; Pillai *et al.*, 2011). The latter cannot account for mesoscale flow patterns being important for the atmospheric CO_2 distribution, as mentioned above, as well as for the heterogeneity of surface CO_2 fluxes (e. g. stated in Pérez-Landa *et al.*, 2007; Ahmadov *et al.*, 2007). All these limitations are even more evident for the recent trend towards regional scale climate simulations. Therefore, there is a consensus among researchers that inversions need to focus on smaller scales (e. g. Ahmadov *et al.*, 2007; Pérez-Landa *et al.*, 2007; Pillai *et al.*, 2011). First steps towards regional scale inversions for limited domains have already been done in the last decade (e. g. Geels *et al.*, 2007; Lauvaux *et al.*, 2008; Gerbig *et al.*, 2009) but the spatial resolution of these models can only partially resolve complex mesoscale atmospheric flow patterns.

Another uncertainty of inverse modeling is the so called "representation error" (i. e. is the CO_2 mixing ratio measured on a tower representative for the grid box of the atmospheric model?). Especially for regional inversions more continental (i. e. non-background) observations are needed which, however, are influenced by local surface CO_2 fluxes and mesoscale transport phenomena (Pillai *et al.*, 2011). Van der Molen and Dolman (2007) demonstrated that even moderate orography causes horizontal CO_2 gradients of 35 ppmv in the PBL disturbing the link between surface fluxes and atmospheric CO_2 concentrations. They also stated that almost all continental and coastal tall towers are influenced by mesoscale flow patterns (e. g. land-see breezes, mountain-valley breezes) which cannot be neglected for inversions. High-resolution mesoscale modeling is an essential diagnostic tool for the quantification of the effects of both the atmospheric flow and surface CO_2 fluxes. Pillai *et al.* (2011) and van der Molen and Dolman (2007) proposed to nest high-resolution mesoscale models around each measurement tower into coarser transport models to minimize the representation error (see also Rödenbeck *et al.*, 2009). The model introduced in the present study can be applied for such purposes.

In order to sharpen the understanding of the processes causing mesoscale CO_2 heterogeneities the coupled terrestial and atmospheric model TerrSysMP (Shrestha *et al.*, 2014) has been extended by the implementation of a prognostic atmospheric CO_2 tracer which is coupled to the biogeophysical parameterizations of the net ecosystem exchange (NEE). This includes the extension of the terrestrial component by parameterizations of autotrophic and heterotrophic respiration. The performance of this new model system "TerrSysMP-CO_2" is verified with eddy covariance (EC) stations operated at different canopy types as well as with measured CO_2 mixing ratios at a tall tower. Both the distribution of CO_2 sources/sinks and the processes causing the observed spatio-temporal variations of atmospheric CO_2 mixing ratios are explored. A special focus is on the evolution of CO_2 heterogeneities induced by complex terrain as well as on the influence of anthropogenic emissions in a densely populated region in Central Europe.

1.3. Mesoscale modeling of CO_2 heterogeneity – state-of-the-art

In the last decade, the heterogene CO_2 fluxes and CO_2 distributions were investigated with mesoscale numerical models. One of the first study was the work of Nicholls *et al.* (2004). They analyzed atmospheric CO_2 variations in the Great Lakes region (USA) using a coupled biosphere–atmosphere model. With a multi-scale strategy having the finest grid resolution in a small domain around a 400 m tall tower they identified diurnal, local and regional scale variations in the atmospheric CO_2 content. Moreover, they showed that, in addition to biological processes at the surface, regional scale CO_2 variability is caused by meteorological processes induced by complex terrain (e. g. katabatic winds) as well as by different turbulent properties.

During the CarboEurope regional experiment strategy (CERES, Dolman *et al.*, 2006) in a rather flat region in southwestern France with weak anthropogenic emissions, several mesoscale numerical studies have been perfomed. Ahmadov *et al.* (2007), Sarrat *et al.* (2007a) and Sarrat *et al.* (2009) used two different model systems for the analysis of mesoscale atmospheric CO_2 variability. The model results were compared with surface observations (tower observations, EC stations) as well as with aircraft measurements in order to study the distribution of CO_2 in the well-mixed PBL. Both simulations were able to identify different horizontal patterns in the atmospheric CO_2 distribution which can be explained by the dominant land use in that regions and they found that land-sea breezes can have a significant influence on the three-dimensional (3D) patterns of CO_2 in this region. With an intercomparison study of Sarrat *et al.* (2007b) the performance of five different biosphere–atmosphere models with different levels of complexity were compared using the same horizontal resolution for all models in order to estimate the uncertainty of mesoscale simulations caused by different parameterizations.

Moreover, Tolk *et al.* (2009) analyzed surface CO_2 fluxes and atmospheric CO_2 concentrations over the Netherlands and investigated in detail the contribution of different CO_2 sources/sinks (nearby vs. distant fluxes, anthropogenic emissions) explaining the CO_2 content measured on the Cabauw tower. Ter Maat *et al.* (2010) and Smallman *et al.* (2013) studied CO_2 fluxes and atmospheric CO_2 patterns using different regional atmospheric models coupled to more advanced land surface models over the Netherlands and Scotland, respectively.

Another focus is on the influence of complex terrain on the atmospheric CO_2 distribution. During the Regional Assessment and Modelling of the Carbon Balance in Europe (RECAB) project Pérez-Landa *et al.* (2007) used a Lagrangian particle disperison model coupled to an idealized biospheric model to analyze the spatio-temporal variability of CO_2 in the Valencia coastal region (Spain). They demonstated the effect of orography on the nocturnal near surface CO_2 accumulation as well as a land-sea breeze influencing atmospheric CO_2 in this region. Van der Molen and Dolman (2007) identified large effects of relatively moderate topography on atmospheric CO_2 patterns in central Siberia and could relate these to the turbulent behavior of the atmosphere which is significantly influenced by orography. Moreover, Pillai *et al.* (2011) used both an Eulerian and a Lagrangian tracer transport model together with a diagnostic biosphere model to simulate orographically induced patterns in the atmospheric CO_2 concentration around a tower at the Ochsenkopf (Fichtelgebirge) in Germany. They showed that a high model resolution is necessary to capture these mesoscale circulations.

Some of above described studies use highly simplified *diagnostic* models describing the biosphere with satellite indices (Ahmadov *et al.*, 2007; Pillai *et al.*, 2011) or use idealized fluxes (Pérez-Landa *et al.*, 2007). In contrast, in the present study *process-based* parameterizations of canopy fluxes and soil respiration are used (Chap. 2). Especially a significantly advanced parameterization of soil respiration is applied compared to the simple temperature relationships used in all former simulations. The studies using process-based models have a relatively coarse grid resolution of 8 km (Sarrat *et al.*, 2009), 6 km (Smallman *et al.*, 2013) and 4 km (Tolk *et al.*, 2009; Ter Maat *et al.*, 2010) being appropriate for the flat terrain of their domains. Instead, here a grid size of 1.1 km for the atmospheric transport and 500 m for the land surface is used which is necessary for a region characterized by complex terrain and densely populated areas (Chap. 3). Another limitation in most studies is a course resolution of anthropogenic emissions ranging from 1° (Pérez-Landa *et al.*, 2007; Ter Maat *et al.*, 2010) to 10 km (e. g. Ahmadov *et al.*, 2007; Tolk *et al.*, 2009; Sarrat *et al.*, 2009). In the study presented here, high-resolution dataset describes anthropogenic emissions. With this model the spatio-temporal variations of CO_2 fluxes are investigated and horizontal and vertical gradients of atmospheric CO_2 concentrations within the PBL are analyzed (Chap. 4–7).

2. CO_2 fluxes and two-way coupling of CO_2 in TerrSysMP-CO_2

2.1. The coupled model system TerrSysMP

In this section, the Terrestrial Systems Modeling Platform "TerrSysMP" (Shrestha *et al.*, 2014) is introduced (Fig. 2.1). It consists of the regional weather prediction model COSMO ("Consortium for Small-scale Modeling"), the Community Land Model (CLM) and the hydrological model ParFlow, externally coupled with the OASIS3 coupler. Since in this study only the atmospheric (COSMO) and terrestrial model component (CLM) of TerrSysMP is used, the hydrological component ParFlow is not further considered. In the following subsections basic information of the participating model components of TerrSysMP is presented.

Figure 2.1.: TerrSysMP, a model platform consisting of the COSMO model (version 4.21), CLM (version 3.5) and ParFlow, externally coupled with OASIS3.

2.1.1. The regional weather prediction model COSMO

The COSMO model is a non-hydrostatic limited-area numerical weather prediction (NWP) model and was developed in its basic version (formerly known as "Lokal Modell" (LM)) at the German Meteorological Service (Deutscher Wetterdienst, DWD). The aim was to design a regional NWP model to be applied for operational weather prediction and various scientific applications on the meso-γ and meso-β scale. At DWD the COSMO model is run operationally since end of 1999 and it is still being advanced. In TerrSysMP, the COSMO model version 4.21 is used. The following model descriptions are based on Baldauf *et al.* (2011) and on Part I and II of the COSMO model documentation (Doms and Baldauf, 2015; Doms *et al.*, 2011).

The core of the COSMO model is the numerical solution of the primitive thermo-hydrodynamic equations describing fully compressible flow in a moist atmosphere. Based on the budget equations representing the basic conservation laws of momentum, mass and internal energy and on the ideal gas law, prognostic equations can be derived for relative velocity $\mathbf{v}$, temperature T, pressure p and specific water in gaseous q^v, liquid q^l and frozen q^f form. Due to the limited spatial and temporal resolution of NWP models, an averaging of these equations is necessary resulting in prognostic equations of the corresponding mean values containing subgrid-scale transport processes. With the use of some simplified thermodynamics (see Doms and Baldauf, 2015, Chap. 3.2 for more details), the final set of equations describing the evolution of non-hydrostatic compressible mean flow can be written as[1]

$$\frac{d\mathbf{v}}{dt} = -\frac{1}{\rho}\nabla p + \mathbf{g} - 2\mathbf{\Omega}\times\mathbf{v} - \frac{1}{\rho}\nabla\cdot\mathbb{T} \tag{2.1a}$$

$$c_p\frac{dT}{dt} = \frac{1}{\rho}\frac{dp}{dt} + \frac{1}{\rho}Q_h \tag{2.1b}$$

$$\frac{dp}{dt} = -\frac{c_p}{c_v}p\nabla\cdot\mathbf{v} + \left(\frac{c_p}{c_v} - 1\right)Q_h \tag{2.1c}$$

$$\frac{dq^v}{dt} = -\frac{1}{\rho}\nabla\cdot\mathbf{F}^v - \frac{1}{\rho}(I^l + I^f) \tag{2.1d}$$

$$\frac{dq^{l,f}}{dt} = -\frac{1}{\rho}\nabla\cdot(\mathbf{P}^{l,f} + \mathbf{F}^{l,f}) + \frac{1}{\rho}I^{l,f} \tag{2.1e}$$

$$\rho = \frac{p}{R_L T_{virt}}. \tag{2.1f}$$

In these equations ρ, $\mathbf{g}$, $\mathbf{\Omega}$, c_p, c_v, R_L and T_{virt} denote air density, acceleration of gravity, angular velocity of the earth, specific heat at constant pressure and volume, the gas constant of dry air and virtual temperature. The continuity equation is replaced by the prognostic equation of pressure (Eq. 2.1c). Q_h contains all diabatic effects and is defined as

$$Q_h = l_V I^l + l_S I^f - \nabla\cdot(\mathbf{H} + \mathbf{R}) \tag{2.2}$$

where l_V and l_S denote latent heat of vaporization and sublimation, respectively, and I^l and I^f describe the phase transition rates of liquid and frozen water.

The subgrid-scale transport processes containing in Eqs. 2.1a–2.1e are the turbulent transport of momentum (described with the general stress tensor $\mathbb{T}$), the turbulent transport of sensible heat (described with the heat flux vector $\mathbf{H}$), the radiative net flux $\mathbf{R}$, the turbulent fluxes of water in gaseous ($\mathbf{F}^v$), liquid ($\mathbf{F}^l$) and ice phase ($\mathbf{F}^f$) and the diffusion fluxes of liquid water and ice ($\mathbf{P}^{l,f}$). These subgrid-scale processes are expressed by means of physical parameterizations. Grid-scale cloud microphysics and precipitation are calculated with a Lin-type one-moment cloud scheme that predicts cloud water, rainwater, cloud ice, snow and graupel (Lin *et al.*, 1983; Reinhardt and Seifert, 2006). Subgrid-scale cloudiness is described by an empirical function depending on relative humidity and height. Shallow convection is parameterized with a simplified version of the mass-flux convection scheme of Tiedtke (1989) extracting the part for shallow convection from the complete convection scheme. The turbulence parameterization is similar to the level-2.5 scheme of Mellor and Yamada (1982) and adapted to the use for the COSMO model (Raschendorfer, 2011). For radiative processes a δ-two-stream parameterization (Ritter and Geleyn, 1992) is included in COSMO. More information on the physical parameterizations can be found in "Part II" of the COSMO documentation (Doms *et al.*, 2011).

The model equations are numerically solved using the finite differences method on a rotated spherical grid arising from the usual geographical coordinate system by a displacement of the model north pole. This displacement is performed in such a way that the model equator is located in the model domain of interest to minimize the convergence of the meridians. In the vertical, a time-independent generalized terrain-following stretched grid of 50 model layers is used with a vertical grid spacing increasing with height. Thus, especially in the lower atmosphere the model has a relatively fine vertical grid resolution. Caused by the compressibility of

---

[1] the bar and hat symbols indicating mean values are omitted for convenience

the non-hydrostatic COSMO model, sound waves and high frequency gravity waves are parts of the solution of the system of equations. To avoid numeric instabilities or, alternatively, a very short integration time step, a time-splitting method is applied in the Runge-Kutta integration scheme. The prognostic equations (Eq. 2.1) are split into a slow and a fast part. Advection, Coriolis forces and tendencies from the physical parameterizations are slow processes. The fast parts are the pressure gradient term in Eq. 2.1a and the working terms in Eqs. 2.1b and 2.1c leading to sound waves and the buoyancy terms leading to excitation of gravity waves. With this time-splitting approach, in numerical simulations with the COSMO-DE grid size of about 2.8 km a integration time step of 25 s is sufficient. In high-resolution runs with a grid size of about 1.1 km a 10 s time step is used. More information on the dynamics and numerics of COSMO can be found in "Part I" of the COSMO documentation (Doms and Baldauf, 2015).

Different from the operational configuration of the COSMO model as described in Baldauf *et al.* (2011), in this study a one-dimensional flux-form advection scheme with a new correction of time-splitting errors (Schneider and Bott, 2014) is used. This is an advanced version of the positive definite advection scheme of Bott (1989). The new advection scheme is numerically more stable than the original scheme of the COSMO model and behaves better in strong deformational flow fields (e. g. in complex terrain, at meteorological fronts). Additionally, for model runs with a 2.8 km grid spacing the hybrid mass flux convection scheme HYMACS (Kuell and Bott, 2008) is used for shallow, midlevel and deep convection including a gust front parameterization and non-local effects of cell aging (Kuell and Bott, 2011). HYMACS is applied to avoid an underestimation of moist convection in weakly forced synoptic situations at this intermediate grid spacing where deep convection is only partially resolved. In the model runs with a grid size of 1.1 km deep convection is assumed to be resolved on the model grid and, thus, the convection scheme of Tiedtke (1989) is used for shallow convection as described above. Finally, some model tuning parameters are adopted from the setup of high-resolution model runs described in Schomburg *et al.* (2010).

2.1.2. The Community Land Model (CLM)

CLM is the soil and vegetation component of TerrSysMP. CLM (former "Common Land Model") is a single-column soil-snow-vegetation biophysical model and was designed by combining the best features of three land surface models: the NCAR Land Surface Model (LSM) of Bonan (1996), the Biosphere-Atmosphere Transfer Scheme (BATS) of Dickinson *et al.* (1993) and the Institute of Atmospheric Physics, Chinese Academy of Sciences land model (IAP94) of Dai and Zeng (1997). CLM was first introduced to the modeling community in Dai *et al.* (2003) and is still being advanced. In TerrSysMP the model version CLM3.5 is used which has been released in May 2007 including several model improvements regarding canopy processes, surface and subsurface soil hydrology (see Oleson *et al.*, 2010, for more details). It is a very modular land surface model that can be applied from regional to global scale and from daily to decadal timescales. CLM can easily be extended with additional sub-models such as a dynamic global vegetation model (DGVM) or a biogeochemical model simulating the carbon-nitrogen cycle (CN-model, see Section 2.4.2). The following descriptions are based on Dai *et al.* (2003) and on the technical model documentation of CLM4.0 (Oleson *et al.*, 2010).

CLM consists of one vegetation layer, 5 snow layers (if a snow pack exists) and 10 unevenly spaced vertical soil layers characterizing the shallow soil in the upper 3.43 m. Spatial land surface heterogeneity is represented as a nested subgrid hierarchy. Each model grid cell can incorporate multiple *landunits*, each landunit can consist of different *columns* and each column can have multiple *plant functional types* (PFTs). The current landunits are glacier, lake, wetland, urban and vegetated. The column level handles the variability in the soil and snow state variables within a single landunit. The soil thermal and hydraulic parameters are derived from depth-varying sand and clay percentages using the relations of Clapp and Hornberger (1978). The 16 PFTs of CLM differ in plant physiology and structure and capture the biogeophysical and biogeochemical properties of different plant species in terms of their functional characteristics. For the calculation of the biogeophysical processes CLM needs an atmospheric forcing to be read from a file (stand-alone configuration of CLM) or being performed by a NWP or climate model coupled to CLM. Moreover, CLM requires information of land surface characteristics, i. e. land cover type, soil texture and soil color (needed for soil albedo). Additional model input data are time invariant morphological (e. g. canopy roughness, leaf dimension, rooting depths), optical (e. g. albedos of thick canopy) and physiological vegetation properties (e. g. leaf C:N ratio, maximum rate of carboxylation at 25 °C). Finally, time varying model input data (e. g. leaf area index (LAI)) can either be read in or calculated with the DGVM or CN-model.

The physical and biophysical soil and vegetation processes are parameterized as follows. Surface and canopy albedo is calculated using a two-stream radiative transfer model. The fluxes of momentum, sensible heat and water vapor between the canopy top and the atmosphere are derived from the Monin-Obukhov similarity theory. Turbulent eddy fluxes within the canopy and between the canopy and the ground are represented as a pathway from the ground to the atmosphere using characteristic conductances (considered to be in series) that are multiplied with the quantity differences. The parameterization of canopy transpiration and canopy evaporation is adopted from BATS and a simple parameterization of ground evaporation is included in CLM. The coupled stomatal resistance and photosynthesis model is described in Section 2.3.3. The canopy or vegetation temperature T_v is derived from the equation of canopy energy conservation:

$$-S_v + L_v(T_v) + H_v(T_v) + l_V E_v(T_v) = 0 \tag{2.3}$$

where S_v is the solar radiation absorbed by the vegetation, L_v is the net long-wave radiation absorbed by the vegetation and H_v and $l_V E_v$ describe sensible and latent heat fluxes from the vegetation with the latent heat of vaporization l_V. This equation is solved for T_v by the Newton-Raphson iteration method and the heat and water vapor fluxes from the vegetation and from the ground must be balanced by heat and water vapor fluxes to the atmosphere. The soil heat transfer is calculated from the heat diffusion equation:

$$c_h \frac{\partial T}{\partial t} = -\frac{\partial F}{\partial z} + l_{V,S} \tag{2.4}$$

Here, c_h, T, z and $l_{V,S}$ denote volumetric heat capacity, soil/snow/ground temperature, soil depth and latent heat of phase change, respectively. The heat flow F is described by the Fourier law for heat conduction in the subsurface (F_z) and by the energy conservation equation at the ground surface (F_g):

$$F_z = -\lambda \frac{\partial T}{\partial z} \qquad \text{at soil depth } z \tag{2.5a}$$

$$F_g = -S_g + L_g(T_g) + H_g(T_g) + l_V E_g(T_g) \qquad \text{at the ground} \tag{2.5b}$$

Eq. 2.5a specifies the heat flux in the subsurface at soil depth z and λ is the thermal conductivity. The heat flux into the soil or from the soil to the canopy at the ground depends on the solar (S_g) and net longwave radiation (L_g) absorbed by the ground and on the sensible (H_g) and latent heat fluxes ($l_V E_g$) at the ground surface. The ground temperature T_g and the temperatures of each soil/snow layer are predicted from Eqs. 2.5 using the Crank-Nicholson numerical scheme.

The temporal change of liquid canopy water (i. e. dew) w_{dew} can be described with a simple mass balance equation[2]:

$$\frac{\partial w_{dew}}{\partial t} = P - D_d - D_r - E_w \tag{2.6}$$

Precipitation P arriving at the top of the vegetation is either intercepted by foliage and stems or directly falls through the gaps between the leaves to the ground. The amount of direct throughfall D_d depends exponentially on the leaf and stem area indices (LAI, SAI). D_r describes the canopy drip, i. e. the outflow of water stored on foliage and stems when water storage exceeds the maximum holding capacity. A further loss of canopy water results of evaporation from the wet canopy (E_w). The vertical soil moisture transport is governed by infiltration, surface and sub-surface runoff, gradient diffusion, gravity, canopy transpiration by root extraction, and interactions with groundwater. It is predicted with a multi-layer model (see Zeng and Decker, 2009). For one-dimensional vertical flow of liquid water in soils, the conservation of mass is stated as

$$\frac{\partial \theta_{liq}}{\partial t} = -\frac{\partial q}{\partial z} - f_{root} TP^{can} \tag{2.7}$$

where θ_{liq} is the volumetric content of liquid water in the soil and q is the soil water flux. The latter term specifies the loss of soil water through root water uptake depending on canopy transpiration TP^{can} and on the root fraction f_{root}. The upper boundary condition of Eq. 2.7 is the infiltration flux into the top soil layer. The water flow below the ground (q_z) can be characterized by Darcy's law and the net water flow at the soil surface (q_g) is described with a balance equation:

$$q_z = -k\left(\frac{\partial h}{\partial z} + 1\right) \qquad \text{at soil depth } z \tag{2.8a}$$

$$q_g = D_d + D_r - E_g - R_{surf} \qquad \text{at the ground} \tag{2.8b}$$

In Eq. 2.8a k is the hydraulic conductivity and h is the soil matric potential (also referred to as pressure head). Both k and h vary with soil water content and soil texture based on Clapp and Hornberger (1978) and Cosby *et al.* (1984). q_g depends on the direct throughfall of precipitation D_d, the throughfall of canopy dew D_r, ground evaporation E_g and surface runoff R_{surf}. The latter consists of overland flow due to saturation and infiltration excess and is parameterized by the runoff model of Niu *et al.* (2005). Additionally, belowground runoff (i. e. base flow) has to be considered consisting of bottom drainage, saturation excess and lateral subsurface runoff due to local slopes. More detailed information on the physical and biophysical parameterizations and the numerical schemes can be found in the corresponding chapters of Oleson *et al.* (2010).

2.1.3. Coupling of COSMO and CLM via the external coupler OASIS3

The model components of TerrSysMP are coupled with the coupler OASIS3 (Valcke, 2013). The description of the coupling follows Shrestha *et al.* (2014). OASIS3 uses the multiple-executable approach which means that each model has its own executable coupled externally with coupling interfaces between the models. These interfaces organize the model initialization

---

[2] Due to the focus of this study on the summer period the processes of soil ice and snow are left out in the following equations to avoid non-necessary complexity.

and definition (e. g. model grid, model partition, coupling variables), the sending and receiving of coupling fields and the finalization of the simulation. Via an OASIS3 configuration file the user defines the coupling frequency, the spatial grid specification of all coupled 2D fields as well as the temporal and spatial transformations of the coupled fields. In the standard configuration of TerrSysMP a time averaging is applied for most variables when the coupling interval is greater than the integration time step of one or more model components. Only precipitation sent from the COSMO model to CLM is integrated over the coupling interval. Moreover, OASIS3 performs a spatial interpolation of the coupled fields. Between COSMO and CLM this is required because COSMO is discretisized on a rotated geographical grid whereas the CLM variables are defined on a regular geographical coordinate system having a finer horizontal grid resolution. TerrSysMP uses a bilinear interpolation for the COSMO fields and a distance weighted averaging for the CLM fields. TerrSysMP allows for the participating models to be driven both stand-alone or in a coupled mode (COSMO–CLM, CLM–ParFlow, COSMO–CLM–ParFlow). In this study, only the coupling of COSMO with CLM is used and described in some detail.

CLM requires information of the state of the atmosphere (lowermost COSMO level) at the current time step for the calculation of the biogeophysical processes. Via the OASIS3 interface CLM receives from COSMO air temperature (T), zonal and meridional wind speed (u, v), specific humidity (q^v), convective and grid-scale precipitation sums (rain/snow/graupel), atmospheric pressure (p), incident direct and diffuse shortwave radiation ($\downarrow S_{dir}$, $\downarrow S_{dif}$), incident longwave radiation ($\downarrow L$) and the atmospheric reference height. Using these forcing variables CLM computes the surface energy fluxes (latent and sensible heat, LH and SH), zonal (τ_x) and meridional (τ_y) momentum fluxes, direct and diffuse albedo (a_{dir}, a_{dif}) and emitted longwave radiation ($\uparrow L$). These fluxes are sent to COSMO via the coupling interface of OASIS3. This means that in TerrSysMP the multi-layer soil and vegetation model TERRA_ML of the operational COSMO model is completely replaced by CLM if a coupled COSMO–CLM simulation is performed. Thus, the CLM surface fluxes are used to determine the updated dimensionless surface transfer coefficients of heat, moisture and momentum. The vertical gradients between the surface level and the lowest COSMO grid level are calculated with the surface temperature (T_{surf}) and surface specific humidity (q^v_{surf}) from the previous COSMO time step. The new T_{surf} and q^v_{surf} are determined with $\uparrow L$ and LH, respectively, received from CLM. An alternative coupling method of TerrSysMP (not used in this study) is to update the COSMO surface transfer coefficients as well as T_{surf} and q^v_{surf} directly by sending the aerodynamic resistances of momentum, heat and water as well as the surface temperature and surface humidity, calculated with CLM, to COSMO instead of sending the corresponding surface fluxes.

With the external coupler grid resolutions different for COSMO and CLM can easily be applied. Thus, the original grid cell hierarchy of CLM is no longer necessary. Instead, a finer CLM grid spacing than the COSMO grid can be used to account for land surface heterogeneity. Every CLM grid cell then consists of only one landunit, one column and one PFT and the OASIS3 coupler provides the scaling between the COSMO grid and the CLM grid with a mosaic-like approach. The coupling frequency and the CLM time step of 15 minutes (900 s) is equal to the calling frequency of the radiation scheme of the COSMO model. However, COSMO needs a considerably shorter dynamical integration time step of 10 s (Section 2.1.1). More information on the model coupling of TerrSysMP can be found in Shrestha *et al.* (2014).

2.2. Two-way coupling cycle of CO_2 in TerrSysMP-CO_2

The main "technical" objective of this study is the development of a fully prognostic treatment of atmospheric CO_2 in TerrSysMP. In order to realize this, the CO_2 concentration has to be implemented in COSMO as a new prognostic variable (see Section 2.6.1). Additionally, the two-way coupling between COSMO and CLM via the OASIS3 coupler has to be extended by CO_2 and some modifications and model extensions are necessary in CLM3.5 (see Sections 2.3–2.5) to completely simulate the net CO_2 exchange between the soil, the vegetation and the atmosphere. The resulting advanced version of TerrSysMP is the basis of the "scientific" objective – the numerical investigation of spatio-temporal variability of mesoscale CO_2 patterns in the atmosphere. This new model version is referred to as *TerrSysMP-CO_2*.

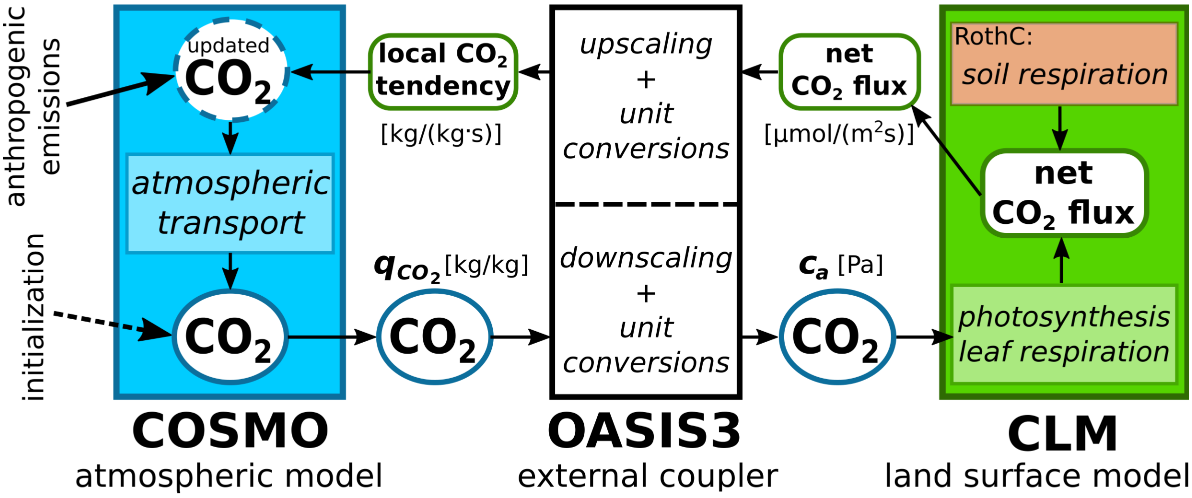

Figure 2.2.: Two-way coupling cycle of CO_2 in TerrSysMP-CO_2 including the CO_2 input fields of COSMO (initialization, anthropogenic emissions) and the involved canopy and soil processes (respiration ($R_{leaf}+R_{soil}$), photosynthesis) of the biogenic net CO_2 flux in CLM.

Fig. 2.2 shows the two-way coupling cycle of CO_2 in TerrSysMP-CO_2. In this context, two-way coupling means that both CLM uses the prognostic atmospheric CO_2 distribution to calculate the canopy fluxes and COSMO receives the net CO_2 flux from CLM as the lower boundary condition of the atmospheric CO_2 field. At the beginning of the numerical simulation, the atmosphere has to be initialized with a 3D distribution of CO_2 (dashed arrow). In addition to the standard atmospheric forcing variables (see previous section) at every coupling time step the atmospheric CO_2 distribution of the lowermost COSMO level has to be sent to CLM. OASIS3 converts the mass specific CO_2 mixing ratio $q_{CO_2,surf}$ [kg kg^{-1}] to atmospheric CO_2 partial pressure c_a [Pa] as used in CLM3.5 (see Eq. 2.11 and Section 2.3.3):

$$c_a = q_{CO_2,surf} \cdot M_{ma}/M_{CO_2} \cdot p_{surf} \tag{2.9}$$

where M_{CO_2} and M_{ma} are the molar masses of CO_2 and moist air at the surface, respectively, and p_{surf} is the atmospheric pressure at the surface level. OASIS3 also performs the downscaling of CO_2 to the finer grid size of about 500 m of CLM. CLM then receives c_a as additional prognostic forcing variable for the calculation of the actual photosynthesis rate in the canopy fluxes module (Section 2.3.3). Moreover, the canopy fluxes module is extended by a simple representation of leaf respiration (Section 2.3.4). Soil respiration is calculated with the additionally implemented carbon turnover model RothC-26.3 (Jenkinson, 1990) and with a newly developed parameterization of autotrophic respiration (Sections 2.4–2.5). The resulting net CO_2 flux – consisting of photosynthesis, leaf and soil respiration – has to be sent as an additional coupling variable to COSMO at every coupling time step. The OASIS coupler now performs the upscaling of the CLM flux to the coarser grid spacing of about 1.1 km of COSMO. Moreover, the net CO_2 flux [μmol(CO_2)$m^{-2}s^{-1}$] is converted to a local tendency of the CO_2 mixing ratio [kg $kg^{-1}s^{-1}$] in the lowest COSMO grid box. The atmospheric CO_2 field is updated by the local tendencies received from CLM and by anthropogenic emissions. The latter are read hourly into COSMO and the actual emissions between two full hours are obtained by linear interpolation between two consecutive hourly emissions. Finally, the calculated atmospheric transport (i. e. advection, turbulence, convection) of the updated CO_2 mixing ratios in COSMO provides the CO_2 distribution for the next integration time step. One coupling time step later, the same CO_2 coupling cycle can start with the new CO_2 mixing ratio.

2.3. Photosynthesis and leaf respiration

2.3.1. Photosynthesis, transpiration and leaf respiration – an overview

This section gives an overview on the chemical and physical processes and on the relationships between photosynthesis, transpiration and leaf respiration, orientated on the descriptions in Bonan (2008). In vegetated canopies the leaves of plants take up CO_2, needed for *photosynthesis*, through small pores (i. e. stomata) in the leaf surface. Photosynthesis occurs in chloroplasts within the leaf cells and is the process by which carbohydrates are produced from CO_2 and water (H_2O) using light energy that is absorbed by the green leaves. This chemical reaction can be written as

$$n\mathrm{CO_2} + 2n\mathrm{H_2O} \xrightarrow{PAR} (\mathrm{CH_2O})_n + n\mathrm{O_2} + n\mathrm{H_2O} \tag{2.10}$$

where n is the number of molecules of CO_2 that combine with H_2O to form carbohydrates. PAR denotes the absorbed photosynthetically active radiation (wavelength: 0.4–0.7μm). The compound $(CH_2O)_n$ represents the general structure of a carbohydrate (e. g. sugar, starch). Oxygen (O_2) is released to the atmosphere. The biochemistry of photosynthesis consists of three processes: the chemical processes of *light reaction* converting light energy into chemical energy and *dark reaction* using CO_2 and the energy of the light reaction to form carbohydrates and, third, the physical process of *diffusion* of CO_2 into the leaf controlled by the stomata.

In the first step of the Calvin cycle (dark reaction) the enzyme Ribulose-1,5-biphosphate-carboxylase/-oxygenase (*RuBisCO*) is involved in the carbon fixation, i. e. the conversion of CO_2 to energy-rich carbohydrates. In this biochemical process CO_2 is bond on Ribulose-1,5-biphosphate (RuBP) (*carboxylation*). Instead of CO_2 also O_2 can be added to RuBP in the RuBisCO reaction (oxygenation) which is detrimental for the photosynthesis productivity because this product cannot be used within the Calvin cycle. The oxidation of RuBP is referred to as photorespiration. Most plant species can be classified into C_3- and C_4 plants. *C_3 plants* (e. g. trees, crops, temperate and arctic grasses) use RuBisCO for the carbon fixation as described above and are most efficient at temperate temperatures (15–25 °C) and moderate irradiation whereas hot and dry weather, especially in combination with high irradiation and water deficiency is detrimental due to the closing of the stomata at these conditions. Contrary to this, C_4 plants (e. g. tropical grasses, sugar cane, maize) can manage these climate conditions because these species are less dependent on the actual stomatal diffusivity. The reason for this is that C_4 plants actively assimilate CO_2 in advance to the conversion to carbohydrates and the Calvin cycle is spatially separated from the CO_2 assimilation. Thus, C_4 plants occur predominantly in tropical climate whereas most plants in the temperate zone are of the C_3 type. In all model domains of TerrSysMP used in this study mainly C_3 plants occur and, thus, in the following sections only the equations and relationships of C_3 plants are considered[3].

The diffusion of CO_2 from the surrounding air into the leaf is controlled by variation of the opening of the stomata. Numerically this physical control is parameterized by means of a *stomatal resistance* r_{st} $[\mathrm{s\,m^{-1}}]$ (the reciprocal of stomatal conductance g_{st}), see Fig. 2.3. Typical values of r_{st} range from $100\,\mathrm{s\,m^{-1}}$ (stoma open) to $>5000\,\mathrm{s\,m^{-1}}$ (stoma closed)[4]. The stomata open (i. e. low r_{st}, high g_{st} values) to allow CO_2 uptake needed for photosynthesis. Concurrently with the CO_2 diffusion into the leaf, water vapor diffuse from the saturated leaf interior through the stomata to the atmosphere, referred to as *leaf transpiration*. Thus, stomata close on situations where the leaf is threatened with desiccation due to the loss of intercellular water during transpiration. In other words, plants regulate the stomatal opening in such a way that on the one hand the (gross) photosynthesis rate A (i. e. the rate of CO_2 assimilation) $[\mu\mathrm{mol(CO_2)m^{-2}s^{-1}}]$ is maximized and on the other hand the leaf transpiration rate TP $[\mathrm{mm\,s^{-1}}$ or $\mathrm{W\,m^{-2}}]$ (i. e. loss of intercellular H_2O) is minimized, also known as the photosynthesis–transpiration compromise (see Fig. 2.3). Therefore, photosynthesis and transpiration are directly related via r_{st}. Due to the response of r_{st} on spatio-temporal variability of atmospheric CO_2 the water exchange between the vegetated canopy and the atmosphere is not only influenced by atmospheric humidity but also by variable atmospheric CO_2 concentrations. Additional environmental conditions control the opening of the stomata (see also Section 2.3.3). Solar radiation has a strong influence on the stomatal opening and r_{st} decreases until light saturation (limited by the RuBisCO activity) is reached. Furthermore, stomata partly close at temperatures higher or lower than the optimum temperature range (see above). To avoid desiccation the stomata close either when the atmospheric humidity is very low (i. e. increased transpiration caused by the increase of the water vapor pressure deficit between the leaf and the atmosphere) or when the loss of water by transpiration exceeds the root water uptake in situations with low soil moisture (soil water stress). Finally, r_{st} is controlled by nitrogen availability needed for the photosynthesis process.

Additionally to the physiological control of r_{st}, a thin (1–10 mm) laminar layer surrounding the leaf surface, commonly referred to as *leaf boundary layer* regulates the CO_2 and H_2O flux. This environmental regulation can be parameterized with the boundary layer resistance r_b that acts in series with r_{st}. r_b decreases with increasing atmospheric wind speed and decreasing leaf diameter. Contrary to r_{st}, r_b also controls the sensible heat flux, i. e. the heat transfer between the leaf and the atmosphere. The physiological and environmental regulation of CO_2 and H_2O fluxes between the ambient air and the leaf interior by r_{st} and r_b (Fig. 2.3) can be written as

$$\boxed{A = \frac{c_a - c_i}{(1.37 \cdot r_b + 1.65 \cdot r_{st}) p_{atm}} = \frac{c_a - c_s}{1.37 \cdot r_b \, p_{atm}}, \qquad TP = \frac{e_a - e_i^*}{r_b + r_{st}} = \frac{e_a - e_s}{r_b}} \tag{2.11}$$

In these equations, c_a and c_i denote the CO_2 partial pressure [Pa] of the ambient air and the intercellular CO_2 partial pressure, respectively, and p_{atm} is the atmospheric pressure at the surface. The factors 1.37 and 1.65 are the ratios of diffusivity of CO_2 to H_2O for r_b and

---

[3] More detailed explanations on the chemical processes of light and dark respiration (Calvin cycle) as well as on characteristics of C_3 and C_4 plants can be found in Bonan (2008) or other textbooks.

[4] CLM3.5 uses $20000\,\mathrm{s\,m^{-1}}$ for maximum stomatal resistance

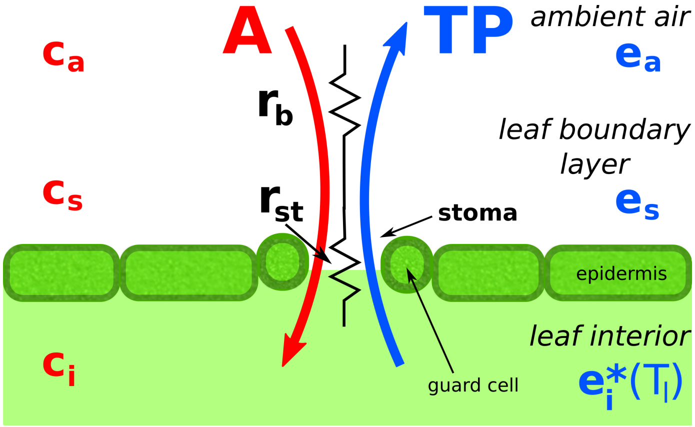

Figure 2.3.: Physiological and environmental regulation of the CO_2 (leaf photosynthesis rate A) and H_2O flux (leaf transpiration rate TP) between the ambient air and the leaf interior by the stomatal resistance r_{st} and the leaf boundary layer resistance r_b.

r_{st}. Similarly, e_a denotes the water vapor pressure of the ambient air and $e_i^* = e_i^*(T_l)$ is the saturated water vapor pressure inside the leaf at the leaf temperature T_l. Eq. 2.11 can also be expressed with the water vapor pressure at the leaf surface e_s and the CO_2 partial pressure at the leaf surface c_s, with $c_s = c_a - 1.37 \cdot r_b \, p_{atm} \, A$ (see Fig. 2.3), showing that due to the CO_2 uptake at daytime the CO_2 concentration at the leaf surface can be considerably lower than the CO_2 concentration in the ambient air.

The complement of photosynthesis is *respiration* which produces energy needed to maintain plant functions (maintenance respiration) and to grow new plant tissues (growth respiration). For this energy production the organic compounds (e. g. glucose $C_6H_{12}O_6$) are oxidized and the chemical reaction of respiration can be formulated as

$$C_6H_{12}O_6 + 6O_2 \rightarrow 6CO_2 + 6H_2O \tag{2.12}$$

About 50% of CO_2 absorbed in the photosynthesis process is released again by plant respiration (Ryan, 1991). Thus, respiration of plants is an atmospheric CO_2 source. Whereas CO_2 uptake only occurs through the stomata of leaves, the plants respire through the whole plant tissue, i. e. foliage, roots and woods. The aboveground CO_2 release to the atmosphere consists of respiration of leaves, i. e. *leaf respiration* R_{leaf}, and to a small extent of woody material (stems, branches). Belowground CO_2 release from roots to the soil (root respiration R_{root}) is a major part of autotrophic respiration (see Section 2.5 and Fig. 1.1). (Leaf) respiration increases exponentially with temperature and takes place simultaneously with photosynthesis. Similar to photosynthesis, leaf respiration ceases at low temperatures because the biochemical activity of the enzymes is inhibited at temperatures below the freezing point. In the following subsections the representation of photosynthesis and leaf respiration in CLM3.5 is described.

2.3.2. Canopy integration approaches – from leaf to canopy level

In climate as well as in land surface models, the resistances r_b and r_{st} – representing H_2O and CO_2 diffusion at an individual leaf as a direct response of stomata to environmental conditions (e. g. light, water, temperature) – have to be upscaled to a *canopy resistance* r_{can} describing the water and CO_2 fluxes of a canopy of leaves. For that, canopy approaches with different levels of complexity can be used to estimate the exchange of moisture, heat and CO_2 between the land surface (ground, vegetation) and the lower part of the PBL (see Bonan, 2008).

The simplest approach is a single bulk surface combining the vegetation and the ground and is based on an effective surface temperature (T_{es}) and vapor pressure (e_{es}). Evapotranspiration and sensible heat fluxes are parameterized with a single surface resistance (r_{es}) acting in series with an *aerodynamic resistance* (r_a). The most complex approach is a multi-layer vegetation parameterization simulating explicitly moisture, energy and CO_2 fluxes between the ground and the lower canopy, between different layers in the canopy and between the upper canopy and the lower PBL. Each vegetation layer has different H_2O and CO_2 partial pressures and temperatures and the fluxes are simulated with several representative canopy resistances.

Canopy integration schemes with an intermediate level of complexity – currently applied in most land surface models – are parameterizations which represent canopy processes with one vegetation or canopy layer. A partitioning of the canopy exchange into vegetation and ground fluxes is made, based on vegetation (T_v, e_v) and ground (T_g, e_g) temperatures and vapor pressures. An aerodynamic resistance ($r_{a,can}$) describes ground sensible heat fluxes and ground evaporation within the canopy. Additionally, a canopy resistance (r_{can}) accounts for the water and CO_2 exchange between the foliage and the canopy air. As in all other approaches the turbulent fluxes between the canopy and the lower PBL (T_{atm}, e_{atm}) are governed by an aerodynamic resistance (r_a). One example of a *one vegetation layer* approach is the land surface parameterization TERRA_ML (Doms *et al.*, 2011) of the operational COSMO model using highly simplified relationships (e. g. $T_v = T_g$, water vapor flux between the plant foliage and the canopy air is equal to the flux between the air inside and the air above the canopy). A common assumption of one vegetation layer schemes is to represent the canopy as a "big-leaf" having the same plant physiological properties and environmental controls as all leaves of the canopy. Therefore, all relationships that are valid at leaf scale (e. g. Eqs. 2.11, 2.17, ...) also hold for this virtual big leaf. To obtain a resistance which is representative for the canopy of leaves (r_{can}), the leaf resistances r_{st} and r_b (cf. Fig. 2.3) have to be scaled with the leaf area index[5] L. This means that canopy transpiration TP^{can} is parameterized with $r_{can} = (r_{st} + r_b)/L$ and canopy photosynthesis A^{can} is governed by $r_{can} = (1.65 \cdot r_{st} + 1.37 \cdot r_b)/L$ (cf. Eq. 2.11).

A major disadvantage of the "one-big-leaf" assumption is that the difference of the physiological properties between leaves in the overstory, influenced by high irradiance, and leaves in the understory at low light conditions cannot be considered. This leads to biases in the estimation of TP^{can} and A^{can} (e. g. Wang and Leuning, 1998; Dai *et al.*, 2004). The mesoscale model of Ter Maat *et al.* (2010), e. g., using the Collatz model (see Section 2.3.3) upscaled with the one-big-leaf approach overestimates the reduction of A when clouds attenuate solar radiation. The one vegetation layer scheme of CLM3.5 (Thornton and Zimmermann, 2007) uses a "two-big-leaf" assumption. In this extended form of the "big-leaf" approach the canopy is partitioned into *sunlit* and *shaded leaves* (Fig. 2.4). Sunlit leaves receive (and absorb) unattenuated direct beam solar radiation ($\downarrow S_{dir}$) and diffuse solar radiation (originating from scattered direct beam radiation or from atmospheric diffuse solar radiation ($\downarrow S_{dif}$)). Shaded leaves receive (and absorb) scattered diffuse solar radiation only. A simple model of radiative transfer proposes an exponential decrease of solar radiation S with increasing *overlying leaf area index* (x_L), i. e. $S(x_L) = S_0 \exp(-K x_L)$ where S_0 is the solar radiation at the top of the canopy ($\downarrow S_{dir} + \downarrow S_{dif}$) and K is the direct beam light extinction coefficient which varies with the solar

---

[5] Leaf area index L: m^2 (one-sided) leaf area per m^2 ground area

zenith angle (Dai *et al.*, 2004). The fraction of sunlit and shaded leaves (f_{sun}, f_{sha}) is given by

$$f_{sun}(x_L) = e^{-Kx_L}, \qquad f_{sha}(x_L) = 1 - f_{sun}(x_L) \tag{2.13}$$

Due to the dependency of K on the solar zenith angle, f_{sun} and f_{sha} vary over the course of a day and through the year. From these expressions the sunlit and shaded canopy LAI (L^{sun}, L^{sha}) can be easily derived:

$$L^{sun} = \int_0^L f_{sun}(x_L)dx = \frac{1 - e^{-KL}}{K}, \qquad L^{sha} = L - L^{sun} \tag{2.14}$$

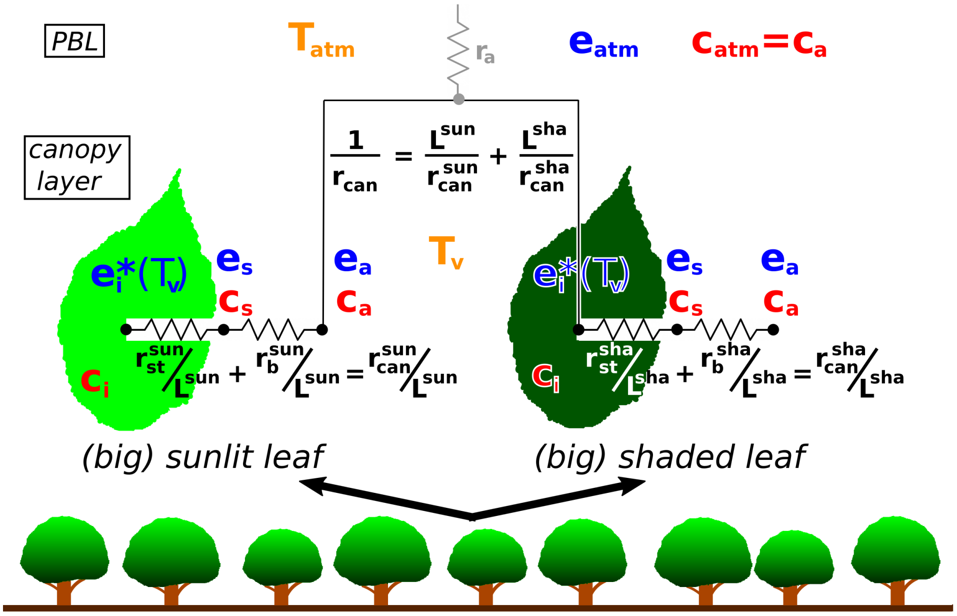

Figure 2.4.: Canopy resistances for photosynthesis and transpiration at the canopy scale described with a "two-big-leaf" canopy integration scheme.

Using L^{sun} and L^{sha}, the canopy resistances for the (big) sunlit and (big) shaded leaf (r_{can}^{sun}, r_{can}^{sha}) can be derived similarly as for the "one-big-leaf" assumption (see Fig. 2.4):

$$\frac{r_{can}^{sun}}{L^{sun}} = \frac{r_{st}^{sun}}{L^{sun}} + \frac{r_b^{sun}}{L^{sun}}, \qquad \frac{r_{can}^{sha}}{L^{sha}} = \frac{r_{st}^{sha}}{L^{sha}} + \frac{r_b^{sha}}{L^{sha}} \tag{2.15}$$

The resistances $r_{st}^{sun/sha}$ and $r_b^{sun/sha}$ are used to determine the transpiration and photosynthesis fluxes between the foliage and the canopy air for sunlit and shaded fractions in analogy to TR and A of an individual leaf (Eqs. 2.11). For photosynthesis, the resistances have to be multiplied with the same ratios of diffusivity of CO_2 to H_2O as in the left equation of Eq. 2.11. In this context, $e_i^*(T_v)$ is the saturation vapor pressure at the vegetation temperature T_v (instead of the leaf temperature T_l) and c_i is the intercellular CO_2 partial pressure. e_s and c_s are the corresponding partial pressures at the virtual leaf surfaces of the (big) sunlit and (big) shaded leaves. The CO_2 partial pressure and the vapor pressure within the canopy can be seen as partial pressures of the ambient air of the big leaves (i. e. $e_v = e_a$). The whole canopy resistance r_{can} (or canopy conductance g_{can}) which governs the water and CO_2 exchange between the foliage and the canopy air can be interpreted as both resistances r_{can}^{sun} and r_{can}^{sha} acting in parallel and are scaled by L^{sun} and L^{sha}, i. e.

$$g_{can} = \frac{1}{r_{can}} = \frac{L^{sun}}{r_{can}^{sun}} + \frac{L^{sha}}{r_{can}^{sha}} \tag{2.16}$$

The turbulent moisture transfer from within the canopy (e_a) to above the canopy (e_{atm}) as well as the sensible heat transfer is regulated with the aerodynamic resistance r_a. Thus, one can conclude that water vapor must first diffuse through the stomata to the leaf surface ($r_{st}^{sun/sha}/L^{sun/sha}$), then from the leaf surface to the ambient canopy air ($r_b^{sun/sha}/L^{sun/sha}$) and finally to the air above the canopy (r_a).

2.3.3. The coupled stomata–photosynthesis model in CLM

Both in atmospheric models (NWP and climate) and in land surface models two different types of modeling approaches are applied to estimate the canopy resistance r_{can}. One way to parameterize r_{can}, used in most current atmospheric models, is the common Jarvis-Stewart approach (Jarvis, 1976; Stewart, 1988). This is a *phenomenological* approach based on empirical relations between r_{can} and environmental variables using statistical relationships to determine the model parameters from measurements for different plant types. Thus, with the Jarvis-Stewart approach r_{can} is predicted *diagnostically* depending on functions of solar radiation, atmospheric specific humidity and temperature at a reference height, and soil water availability. Each of these functions are assumed to be independent of each other. These missing correlations of the environmental parameters are a major constraint of this approach as stated in Collatz *et al.* (1991). Moreover, the influence of atmospheric CO_2 concentration on r_{can} is not considered. This method is applied, e. g., in the vegetation model TERRA_ML, based on the BATS model parameterizations (Dickinson *et al.*, 1993). However, the Jarvis-Stewart approach is not the best option for atmospheric models because the prognostic environmental variables are, among others, themselves functions of r_{can} (Ronda *et al.*, 2001). The second and more appropriate way to calculate the water and CO_2 exchange is to use a *semi-mechanistic* model (e. g. Wang and Leuning, 1998; Ronda *et al.*, 2001). These models consider plant physiological controls of stomatal resistance r_{st}, biochemical processes of gross photosynthesis A and biophysical regulations of transpiration TR. Usually the physiological processes are simulated by coupling A – being a function of environmental and leaf parameters and r_{st} – with r_{st} – being a function of environmental and intercellular CO_2 and H_2O concentration and A (Fig. 2.5). Finally, r_{st} (and r_b) have to be upscaled from leaf to the canopy level (r_{can}) (see previous section). In this approach r_{can} is calculated *physically* based with the attempt to address the fundamental underlying mechanisms and thus r_{can} is only an indirect function of environmental parameters.

In CLM3.5 the plant physiological approach is applied. The core of the canopy fluxes module is based on the model of Collatz *et al.* (1991), referred to as the "Collatz model". The model is modified with a significantly improved parameterization of the maximum rate of carboxylation $V_{c,\max}$ (see below) which was the most critical problem in their model. The general concept of the Collatz model is that at leaf level the responses of r_{st} to changes in the environmental conditions can be partitioned into components depending on photosynthesis A and others that are independent of A. Therefore, independent sub-models can be adopted to calculate r_{st} and A. The photosynthesis model requires (among others) the intercellular CO_2 partial pressure c_i as input being a function of c_s and r_{st} whereas the stomatal model calculates r_{st} requiring (among others) A as input (see Fig. 2.5). Both models are coupled numerically with an iterative solution of r_{st} according to Bonan (1996). In CLM3.5 the basic equations are solved for sunlit and shaded leaves to give sunlit and shaded stomatal resistance (r_{st}^{sun}, r_{st}^{sha}) according to Eq. 2.15. Canopy photosynthesis A^{can} is also scaled for the sunlit and shaded fraction of the LAI, i. e. $A^{can} = A^{sun}\,L^{sun} + A^{sha}\,L^{sha}$.

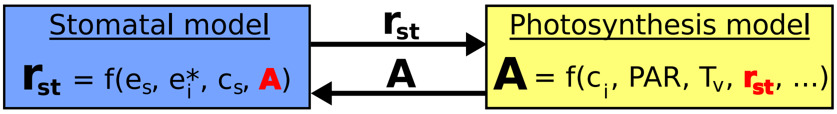

Figure 2.5.: Coupling of a stomatal model with a photosynthesis model.

Stomatal model. In the canopy fluxes model of CLM3.5 the leaf stomatal resistance r_{st} (or leaf stomatal conductance g_{st}) is calculated similar to the Ball-Berry conductance model (Ball, 1988) which is part of the Collatz model. The primary difference between the CLM implementation and that used in the Collatz model is that in CLM3.5 the *gross* photosynthesis rate A is used instead of *net* photosynthesis (i. e. gross photosynthesis A minus leaf respiration R_{leaf}). The response of r_{st} to A and environmental conditions can be parameterized by

$$\boxed{g_{st} = \frac{1}{r_{st}} = m\frac{A}{c_s}\frac{e_s}{e_i^*}p_{atm} + g_{st,\min}} \tag{2.17}$$

In this equation, m is an empirical scaling factor of the linear dependency of the stomatal conductance ($g_{st} = 1/r_{st}$) on A and environmental variables. In CLM, $m = 9$ is used for most C$_3$ plants and $m = 6$ for needleleaf trees. e_i^* is the saturation vapor pressure inside the leaf at the vegetation temperature T_v (cf. Eq. 2.3) and $g_{st,\min}$ is the minimum stomatal conductance when A is zero to give a maximum stomatal resistance of 20000 s m^{-1}.

If CLM is coupled to an atmospheric model, the environmental conditions occurring in Eq. 2.17 are prognostic variables calculated in the atmospheric model, i. e. the environmental variables are 2D-fields varying in longitude (lon), latitude (lat) and in time (t).

$$\begin{array}{ll}
\textbf{TerrSysMP} & \textbf{TerrSysMP-CO}_\mathbf{2} \\
\left.\begin{aligned} e_s &= e_s(lat, lon, t) \\ p_{atm} &= p_{surf}(lat, lon, t) \end{aligned}\right\} \text{prognostic,} &
\left.\begin{aligned} e_s &= e_s(lat, lon, t) \\ p_{atm} &= p_{surf}(lat, lon, t) \\ c_s &= c_s(lat, lon, t) \end{aligned}\right\} \text{prognostic} \\
c_s \qquad \text{diagnostic} &
\end{array} \tag{2.18}$$

In the coupled COSMO–CLM configuration of TerrSysMP the water vapor pressure at the leaf surface e_s is determined from the atmospheric specific humidity at surface level (q_{surf}^v) as simulated with COSMO and converted to the partial pressure e_{atm} in OASIS3. The aerodynamic resistance r_a is used to determine the ambient water vapor pressure e_a in the canopy layer (see Section 2.3.2) and applying Eq. 2.11 (right equation) finally yields e_s. In addition, the atmospheric pressure of COSMO at surface level (p_{surf}) is an atmospheric forcing variable of CLM. However, the CO$_2$ partial pressure at the leaf surface (c_s) is diagnostically calculated from a constant number mixing ratio (default in CLM3.5: 355 ppmv) for the ambient CO$_2$ concentration (c_a). In contrast, the two-way coupling of CO$_2$ in TerrSysMP-CO$_2$ additionally includes c_s as a prognostic variable, i. e. spatio-temporal varying atmospheric forcing variable, influencing r_{st}. The CO_2 concentration at the leaf surface (c_s) is determined by converting the CO_2 mixing ratio of the lowermost COSMO level with Eq. 2.9 to the ambient CO_2 partial pressure c_a and then by applying Eq. 2.11 (left equation) c_s can be obtained. The atmospheric CO_2 mixing ratio in COSMO itself is influenced by biogenic CO_2 fluxes (see Section 2.2). Thus, in TerrSysMP-CO_2 the calculation of r_{st} (Eq. 2.17) is not only influenced by the spatio-temporal variability of atmospheric humidity but also by the natural variability of atmospheric CO_2. This leads to a more consistent representation of the stomatal control of the H_2O and CO_2 exchange between the canopy and the atmosphere. Hence, with this additional degree of freedom also the humidity in the PBL can be indirectly influenced by spatio-temporal variable CO_2.

Photosynthesis model. The leaf photosynthesis A of C_3 plants is determined with a modified version of the biochemical model of Farquhar *et al.* (1980) as integrated in the Collatz model. This model calculates the activity of photosynthesis on the basis of enzyme kinetics of RuBisCO in the dark reaction and the regeneration of RuBP in the light reaction (see Section 2.3.1). There are different limitations to the rate of CO_2 assimilation (by photosynthesis A). The model strategy is that the minimum rate resulting of one of the limitation relations controls CO_2 assimilation at the leaf level, i. e. $A = \min(w_c, w_j, w_e)$. The RuBisCO limitation w_c describes the rate of CO_2 fixation in the carboxylation of RuBP in the Calvin cycle. This limitation is formally written as

$$w_c = \frac{V_{c,\max}(c_i - \Gamma_*)}{c_i + K_c(1 + o_i/K_o)}. \tag{2.19}$$

In this equation $V_{c,\max}$ is the maximum rate of carboxylation [μmol(CO_2)$m^{-2}s^{-1}$] and Γ_* is the CO_2 compensation point [Pa] (i. e. the CO_2 concentration where A equals R_{leaf}). $o_i = 0.0209 \cdot p_{atm}$ is the O_2 partial pressure and K_c and K_o are the Michaelis-Menten constants [Pa] for CO_2 and O_2 depending exponentially on T_v. The light limitation rate w_j describes the maximum rate of carboxylation allowed by the capacity to regenerate RuBP in the light reaction and can be written as

$$w_j = \frac{(c_i - \Gamma_*) \cdot 4.6 \cdot PAR \cdot \alpha}{c_i + 2\Gamma_*}. \tag{2.20}$$

Thus, w_j is mainly controlled by the absorbed photosynthetically active radiation PAR [$\mathrm{W\,m^{-2}}$] which is converted to photosynthetic photon flux assuming 4.6 μmol photons per Joule and α is the quantum efficiency [μmol(CO_2) μmol(photons)$^{-1}$]. Finally, CO_2 assimilation can be limited by the capacity for the export or utilization of the carbohydrates produced in the photosynthesis process which is about 50% of $V_{c,\max}$, i. e.

$$w_e = 0.5 \cdot V_{c,\max}. \tag{2.21}$$

At low light intensity the light limitation (w_j) controls gross photosynthesis A that is then independent of $V_{c,\max}$. Above some level of solar radiation, the RuBisCO limitation (w_c) controls A until the upper limit of the capacity utilization (w_e) is reached. Both w_c and w_e depend strongly on $V_{c,\max}$ which is a function of several environmental variables (see next paragraph). As mentioned above, photosynthesis is calculated for sunlit and shaded leaves using PAR^{sun} and PAR^{sha} and $V_{c,\max}^{sun}$ and $V_{c,\max}^{sha}$.

Maximum rate of carboxylation. In CLM3.5 an advanced representation of the maximum rate of carboxylation $V_{c,\max}$ is implemented which explicitly considers structural and functional characteristics of the canopy used for the vertical canopy integration (Thornton and Zimmermann, 2007). At 25 °C, $V_{c,\max}$ is calculated as

$$V_{c,\max 25} = N_a \, F_{LNR} \, F_{NR} \, a_{R25} \tag{2.22}$$

where N_a is the area-based leaf nitrogen (N) concentration and F_{LNR} is the PFT dependent fraction of leaf N in RuBisCO. N_a and F_{LNR} show that the amount of N in the leaf strongly influences the productivity of photosynthesis of different plant species (see also Section 6.5). Therefore, N fertilization of crops can lead to considerably higher net primary production (NPP). In Eq. 2.22 $F_{NR} = 7.16$ is the mass ratio of total RuBisCO molecular mass to N in RuBisCO and $a_{R25} = 60$ is the specific activity of RuBisCO. The new approach of the canopy integration scheme of Thornton and Zimmermann (2007) is based on the hypothesis that the specific leaf area SLA (i. e. the ratio of leaf area to leaf mass) varies linearly with overlying LAI (x_L) within the canopy, i. e.

$$SLA(x_L) = SLA_0 + n_v x_L \tag{2.23}$$

where SLA_0 is the specific leaf area at the top of the canopy and n_v is a linear slope coefficient varying among different PFTs. In other words, this means that the ratio of leaf area to leaf mass increases from the top of the canopy to the ground (i. e. small thick leaves at the top and big thin leaves at the bottom of the canopy) counteracting the exponentially decrease of solar radiation. This hypothesis is supported by measurements within broadleaf and needleleaf forests in the temperate zone. Moreover, a vertically constant but PFT dependent leaf C:N ratio (CN_L) is assumed. The area-based leaf N concentration is then defined as

$$N_a = \frac{1}{CN_L \cdot SLA}. \tag{2.24}$$

Eq. 2.22 is calculated separately for sunlit and shaded leaves with the SLA for sunlit and shaded leaves (SLA^{sun}, SLA^{sha}). With the use of the sunlit and shaded canopy fraction f_{sun} and f_{sha} (Eq. 2.13) and the sunlit and shaded leaf area index LAI^{sun} and LAI^{sha} (Eq. 2.14) the mean values of SLA for the (big) sunlit and (big) shaded leaf are calculated as

$$SLA^{sun} = \frac{\int_0^L SLA(x_L) f_{sun}(x_L) dx}{L^{sun}} = \frac{-(cn_v K \, L + cn_v + cSLA_0 \, K - n_v - SLA_0 \, K)}{K^2 \, L^{sun}} \tag{2.25a}$$

$$SLA^{sha} = \frac{\int_0^L SLA(x_L) f_{sha}(x_L) dx}{L^{sha}} = \frac{L\Big(SLA_0 + \frac{n_v L}{2}\Big) - SLA^{sun} \, L^{sun}}{L^{sha}} \tag{2.25b}$$

where $c = \exp(-KL)$. In CLM the slope coefficient is $n_v = 0$ for all shrub, grass and crop PFTs which considerably simplifies Eqs. 2.25a and 2.25b. Eq. 2.24 is calculated for sunlit and shaded leaf fractions using Eqs. 2.25a and 2.25b. Thus, the canopy integration scheme of Thornton and Zimmermann (2007) explicitly connects the canopy photosynthesis A^{can} with structural (n_v, $L^{sun/sha}$) and functional (SLA, Eq. 2.22) characteristics of the canopy.

In addition to the variation on available N and the distinction between $V_{c,\max}^{sun}$ and $V_{c,\max}^{sha}$ for sunlit and shaded leaves, $V_{c,\max}$ (and thus A^{can}) varies with canopy temperature T_v, soil water and the season of the year:

$$V_{c,\max} = V_{c,\max 25} \cdot (Q_{10})^{\frac{T_v - 25}{10}} \cdot f(T_v) \cdot f(DL) \cdot \beta_{tran} \cdot a(N) \tag{2.26}$$

$V_{c,\max}$ varies with T_v [°C] according to a Q_{10} value of 2.4, i. e. a temperature increase of 10 °C yields an increase of $V_{c,\max}$ by a factor of 2.4. This exponential relationship describes the temperature dependency of the activity of the RuBisCO enzyme. A similar behavior can be observed in the enzymatic process of heterotrophic respiration (Section 2.4.5). Additionally, $f(T_v)$ is a function that mimics a thermal inhibition of RuBisCO activity at temperatures exceeding 35 °C. $f(DL)$ introduces a seasonal variation of $V_{c,\max}$ scaled for the daylength (DL) with the maximum of $V_{c,\max}$ at the maximum daylength in summer. Moreover, the beta transpiration factor β_{tran} is a further scaling factor describing the influence of soil water on $V_{c,\max}$ depending on the soil water potential of each soil layer, the root distribution and a PFT dependent response to soil water stress. β_{tran} is 1 when the soil is wet, and thus transpiration is not limited due to soil water stress, and reaches zero when the soil is very dry, i. e. transpiration is restricted by closing the stomata. Finally, the nitrogen availability factor $a(N)$ considers N limitation of $V_{c,\max}$ and varies among PFTs. The PFT dependent values F_{LNR}, CN_L, SLA_0, n_v and $a(N)$ as well as the functions $f(T_v)$, $f(DL)$ and β_{tran} can be found in Chap. 8 of Oleson *et al.* (2010). The most important fact is that Eq. 2.26 explains the dependency of the photosynthesis rate A on environmental conditions and – coupled to the stomatal model (Eq. 2.17) – also the reaction of stomatal opening on these environmental parameters.

2.3.4. Inclusion of leaf respiration in the canopy parameterization of CLM

Additionally to CO_2 assimilation plants also release CO_2 primary from their roots to the soil (R_{root}) and from leaves to the atmosphere (R_{leaf}, see Sections 2.3.1 and 1.1). The leaf respiration R_{leaf} is also known as dark respiration because light is not directly necessary for the respiration processes. In CLM respiration is only calculated in the optional DGVM and the CN-model (see Sections 2.1.2 and 2.4.2). In the canopy fluxes routine of CLM R_{leaf} is not simulated and thus only CO_2 assimilation is considered in the default configuration of CLM which is chosen in this study. Therefore, the canopy fluxes scheme has to be extended with respect to CO_2 respiratory diffusion through leaves. Due to the strong connection of R_{leaf} with the photosynthesis process, Farquhar *et al.* (1980) proposed a rather simple relationship between R_{leaf} and $V_{c,\max}$ which was also adopted with a slightly modified scaling in the Collatz model. At the leaf level, Collatz *et al.* (1991) calculated leaf respiration R_{leaf} as

$$R_{leaf} = 0.015 \cdot V_{c,\max}. \tag{2.27}$$

The same relationship is used in this study but upscaled to the canopy level and with the improved representation of $V_{c,\max}$ as described in the previous section. Via $V_{c,\max}$ the exponential increase of enzyme activity with temperature is considered in this simple parameterization. The upscaling of Eq. 2.27 from leaf to canopy scale is performed in analogy to the canopy photosynthesis A^{can}:

$$R^{can}_{leaf} = 0.015 \cdot \left(V^{sun}_{c,\max}\, L^{sun} + V^{sha}_{c,\max}\, L^{sha}\right). \tag{2.28}$$

In contrast to photosynthesis, plants release CO_2 also during night. When no solar radiation is available (i. e. $PAR = 0$) the distinction between sunlit and shaded fractions is not necessary and $V^{sun}_{c,\max} = 0$. Thus, during night R^{can}_{leaf} is determined with

$$R^{can}_{leaf} = 0.015 \cdot V^{sha}_{c,\max}\, L \tag{2.29}$$

with $f_{sha} = 1$. With the extension of the canopy integration scheme by R^{can}_{leaf} the aboveground CO_2 fluxes ($A^{can} - R^{can}_{leaf}$) of a plant canopy are completed.

2.4. Heterotrophic soil respiration

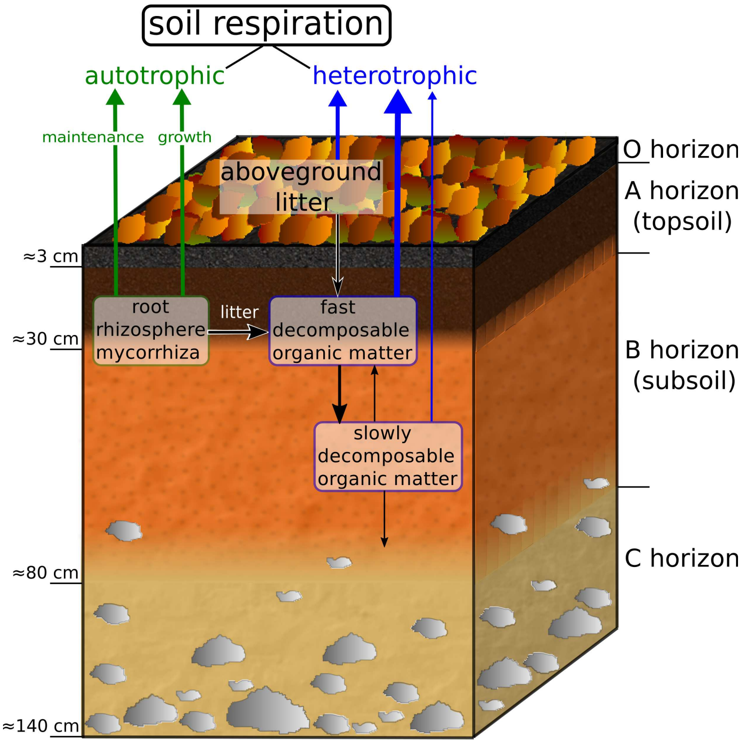

Figure 2.6.: Soil horizon classification and flow chart of organic carbon exchange (black arrows) and transformation including the auto- (green arrows) and heterotrophic (blue arrows) CO_2 production in the topsoil, subsoil and aboveground litter layer. The thickness of the arrows demonstrates the relative contribution of different processes to total soil respiration.

2.4.1. Soil respiration and soil horizons – an overview

Soil respiration is the dominant biogenic source of atmospheric CO_2 resulting from CO_2 production below the ground and its release to the atmosphere. It is a combination of *biotic*, *chemical* and *physical* processes. The *biotic* process describes the CO_2 production by autotrophic (Section 2.5) and heterotrophic respiration. Three processes contribute to *autotrophic respiration*: the CO_2 release through plant roots to the soil (root respiration) as well as CO_2 production of microorganisms and bacteria in the root zone (rhizosphere respiration) and of symbiotic mycorrhizal fungi (mycorrhizal respiration), see Fig. 2.6. Autotrophic respiration is strongly linked to plant and root metabolism by allocation of photosynthetic carbon to root growth and maintenance (e. g. Ryan and Law, 2005). *Heterotrophic respiration* describes the decomposition of fast and slowly decomposable organic carbon in the organic and mineral soil by microbes and soil fauna as well as litter decomposition (e. g. Hanson *et al.*, 2000). *Chemical* oxidation of soil minerals is relatively small compared to the biotic processes and can be neglected at temperate soil and atmospheric temperatures (Ryan and Law, 2005). The *physical* processes are CO_2 degassing to the atmosphere and diffusive and convective transport of CO_2 through the soil. The intensity of total soil respiration is mainly controlled by soil temperature, soil moisture and plant metabolism. Among these, soil temperature is the most sensitive factor (Lloyd and

Taylor, 1994). The relative contribution of auto- and heterotrophic respiration depends on the season of the year, the vegetation type and the soil texture with the highest autotrophic contribution in the early growing season when photosynthetic carbon is mainly allocated to active root growth (Hanson *et al.*, 2000).

CO_2 production occurs in different soil layers with different characteristics, commonly referred to as *soil horizons*, with different soil organic matter (SOM) contents (see Fig. 2.6). In most soils the A horizon is the uppermost *mineral* soil layer containing a relatively high amount of (partly) decomposed SOM. Thus, this layer holds the biggest part of total organic carbon (TOC) of the soil. TOC is the organic carbon content of SOM which is typically estimated to be 58% of SOM (e.g. Nelson and Sommers, 1996). Due to the high importance of TOC on heterotrophic respiration, most of the biological activity and CO_2 production and most of the soil organisms are concentrated, there. The A horizon is also referred to as *topsoil* and is represented by the uppermost 5 soil layers (0–29 cm depth) in CLM. The B horizon (or *subsoil*) contains a high variety of mineral substances washed in from the topsoil. This zone occupies much less and higher decomposed SOM and produces less CO_2 than the topsoil. The C horizon is characterized by low biological activity and negligible SOM and is of minor relevance to soil respiration. Especially in forest soils, a thin *organic* matter layer (O horizon), also referred to as forest floor, overlays the mineral soil horizons. This zone contains primary of SOM which is to some portion slightly decomposed (O_i), intermediate decomposed (O_e) and highly decomposed or humified (O_a). Although it is only a few centimeters thick this horizon produce much of CO_2 by decomposition of fresh organic matter. The O horizon is covered by aboveground litter (e. g. dead leaves, dead organisms) which is not or only slightly decomposed (O_i).

2.4.2. The CN-model of CLM3.5 – is it applicable for diurnal flux variability?

CLM3.5 includes a terrestrial biogeochemistry model with a fully prognostic treatment of the carbon (C) and nitrogen (N) cycles that can be optionally coupled to the standard configuration of CLM3.5 (see Oleson *et al.*, 2010, Chap. 14). This Carbon-Nitrogen Model (CN-model) has been developed by merging the biophysical framework of CLM3.0 with the C and N dynamics of the process-based ecosystem simulation model Biome-BGC (Thornton *et al.*, 2002; Thornton and Rosenbloom, 2005). The CN-model calculates fully prognostically C and N state variables, commonly referred to as C- and N-pools, in the vegetation, litter and SOM. These pools describe the C and N content of the leaf, stem (live, dead), coarse root (live, dead) and fine root matter as well as long-term and short-term storage pools for each vegetation tissue and pools characterizing the growth respiration storage, the maintenance respiration reserve and retranslocated nitrogen. In summary, there are 20 vegetation C- and 19 N-pools.

In the CN-model, autotrophic respiration is divided into maintenance respiration, which is a function of live biomass, tissue N concentration and temperature, and growth respiration being a simple proportion of 0.3 of total new carbon allocated to vegetation growth. There are complex relationships prognostically calculating the allocation of assimilated C during photosynthesis to actual plant growth, long-term growth storage and maintenance respiration reservoirs. The litter and SOM pools are structured as a converging cascade decomposing with their representative decomposition rates to stronger decomposed SOM pools. Similar to the assumptions of the RothC model (see the following sections), the resulting heterotrophic respiration depends on soil temperature and moisture availability. Both photosynthesis and decomposition rates are limited by nitrogen availability. This N limitation is also fully prognostic depending on the relative demand of plant mineral N uptake and N immobilization by the litter and soil decomposition process. For more details on the CN-model the reader is referred to Chap. 14 of Oleson *et al.* (2010) and studies applying the Biome-BGC (e. g. Thornton *et al.*, 2002; Thornton and Rosenbloom, 2005).

The applicability of the CN-model on the calculation of hourly variations of carbon, energy and water fluxes is questionable. The Biome-BGC is originally designed for simulating interannual variability of NEE, NPP and carbon stocks (e. g. White *et al.*, 2000; Thornton *et al.*, 2002, and others). A daily time step is used for the calculation of water, carbon and nitrogen fluxes. This procedure include a prognostic treatment of the seasonal timing of new vegetation growth and litterfall resulting in a prognostic LAI as well as parameterizations of fire and mortality. In simulations of the presented study (1 day up to 1 week), all of these processes can be neglected and most of the *prognostic* C- and N-pool of the CN-model can be considered to be *constant* over time. Moreover, the utilization of the CN-model with a sub-hourly time step to characterize diurnal variations of auto- and heterotrophic respiration is not tested.

A further disadvantage of the CN-model is the need for a long spin-up run to reach a steady-state solution of all C- and N-pools. Steady-state means that all state variables and long-term mean fluxes are stationary on the longest time scale of variability in the atmospheric forcing and model processes, i. e. the C- and N-pools as well as the mean fluxes are stable on the climate scale whereas decadal or interannual variability can occur caused by climate variations. The main purpose of this preprocessing is to reach a dynamic equilibrium of SOM with respect to the climate conditions, vegetation ecophysiology and soil properties. Especially for high-resolution model simulations this spin-up procedure is very expensive in terms of CPU time because a model run of several thousands of years is necessary running the model under its native dynamics. Thornton and Rosenbloom (2005) proposed several methods to accelerate the spin-up. However, there are still long model simulations of ∼1000 years required without any guarantee that the simulated equilibrium SOM conditions meet the real SOM distribution.

Due to these tedious and possibly unsuitable model behaviors for diurnal variations, only the biophysical part of CLM3.5 is used, as described in Section 2.3, and the CN-model is switched off. Instead, additional parameterizations simulating autotrophic and heterotrophic respiration have been implemented in CLM and are described in the following sections.

2.4.3. Simulation of carbon decomposition with RothC

The RothC-26.3 model (RothC) is based on the Rothamsted carbon turnover model (Jenkinson, 1990) and is a relatively simple model which simulates the decomposition of organic plant material in the mineral soil (A, B horizons). This model has recently been used, e. g., in studies of Herbst *et al.* (2008) and Bauer *et al.* (2012). Similar to the carbon turnover parameterization in the CN-model, RothC uses a carbon pool concept to calculate carbon decomposition by soil microorganisms. In RothC, SOM is divided into five carbon pools (C-pools):

- decomposable plant material (DPM), optimum decomposition rate λ_{DPM}: 10 years^{-1}
- resistant plant material (RPM), λ_{RPM}: 0.3 years^{-1}
- microbial biomass (BIO), λ_{BIO}: 0.66 years^{-1}
- humified organic matter (HUM), λ_{HUM}: 0.02 years^{-1}
- inert organic matter pool (IOM), no decomposition

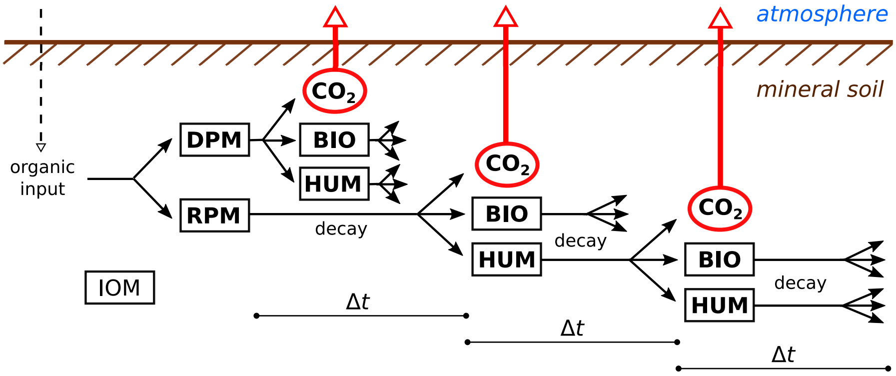

Figure 2.7.: Schematic description of the C-pool concept of RothC (modified and extended from Jenkinson, 1990).

Each of these C-pools can be deemed to be carbon state variables biologically decompose by first-order reaction kinetics, i. e. by an exponential decay with a characteristic rate constant λ. Fig. 2.7 explains the C-pool concept of RothC: Fresh plant material consists of DPM and RPM which both decay to BIO and HUM with their representative optimum decomposition rates λ_{DPM} and λ_{RPM}. In this process CO_2 is generated which is released to the atmosphere. BIO and HUM further decompose with their rate constants λ_{BIO} and λ_{HUM}, respectively, and form more BIO, fresh HUM and CO_2. To account for the sensitivity of microbial activity on soil temperature and soil moisture as well as on plant growth, the *optimum* decomposition rates λ_{C_i} have to be multiplied with rate modifying factors. Thus, the decomposition equations can be written as

$$\boxed{C_{i,new} = C_i \cdot \exp\big(-f(T_{soil}) \cdot f(h) \cdot c_r \cdot \lambda_{C_i} \cdot \Delta t\big)} \tag{2.30}$$

where C_i represent the C-pools DPM, RPM, BIO and HUM and $C_{i,new}$ the resulting C-pools after decomposition during the time interval Δt. $f(T_{soil})$ is a function representing the sensitivity of soil respiration on soil temperature (T_{soil}) and $f(h)$ describes the moisture reduction of carbon decomposition which depends on the soil water pressure head (h). The plant retainment factor c_r describes the deceleration of decomposition when plants grow and is set to 0.6 if the soil is vegetated and 1.0 if the soil is bare according to Jenkinson (1990). Multiplying λ_{C_i} with the rate modifying factors $f(T_{soil})$, $f(h)$ and c_r lead to the resulting decomposition rates under these soil conditions. A detailed description of the rate modifying functions $f(T_{soil})$ and $f(h)$ used in this study can be found in Section 2.4.5.

Whereas the decomposition rate is assumed to be independent of the soil texture, the partitioning of decomposed material (i.e. $\Delta C_i = C_i - C_{i,new}$) between CO_2, HUM and BIO depends on the percentage clay content of the soil:

$$b = \frac{CO_2}{BIO + HUM} = 1.67 \cdot \big(1.85 + 1.6\exp(-0.0786 \cdot clay)\big) \tag{2.31}$$

Thus, the fraction of CO_2 production of the total decomposed material is $b/(b+1)$.

2.4.4. Determination of the initial C-pools of RothC

As all carbon turnover models, RothC needs an initial partitioning of SOM into C-pools that are in equilibrium. To avoid a long spin-up simulation, Weihermüller *et al.* (2013) developed simple pedotransfer functions (PTFs) to initialize the C-pools of the RothC model. These PTFs only depend on the clay content and the TOC content.

For the determination of the TOC content of each grid column of the NRW domain (see Section 3.1), TOC data of the Landesamt für Natur, Umwelt und Verbraucherschutz Nordrhein-Westfalen (LANUV) are used. This dataset contains measured TOC contents [%] at more than 500 locations in the Rur catchment resolved for different soil depth intervals as well as the associated land use. With averaging of all available TOC profiles having the same land use, representative TOC depth profiles were determined for each land cover. These TOC depth profiles were linearly interpolated to the soil levels of CLM and the different land use classes were allocated to the appropriate plant functional type (PFT). To convert the percentage TOC content to [$\mathrm{t\,ha^{-1}}$], needed for the PTFs, the bulk density or compactness ρ_B of the soil has to be known. For agriculture, grassland and shrub $\rho_B = 1.35\,\mathrm{g\,cm^{-3}}$ was assumed for the topsoil (i. e. 0–30 cm depth) and $\rho_B = 1.45\,\mathrm{g\,cm^{-3}}$ for the subsoil (i. e. 30–100 cm depth) (M. Herbst, personal communication, May 2013). For forest soils the proposed formula in a report of the Hessisches Landesamt für Umwelt und Geologie (HLUG; Wegener, 2008) was used: $\rho_B = 0.2038\ln(h_{soil}) + 0.7516$ where h_{soil} is the soil depth.

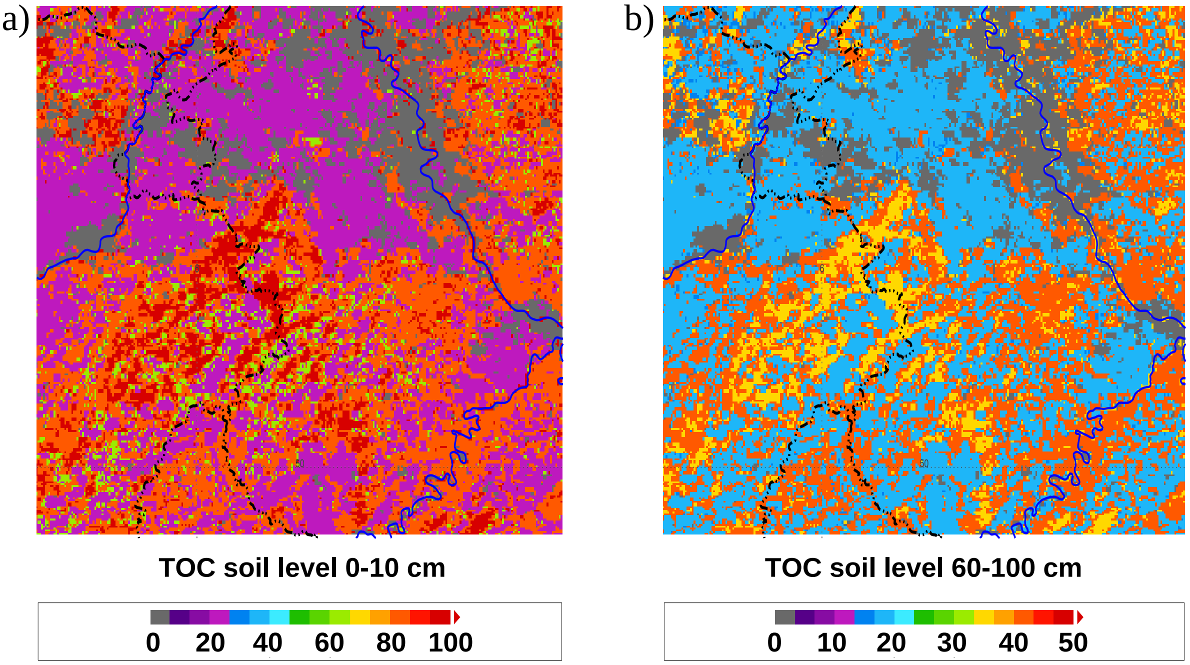

Figure 2.8.: Measured PFT-dependent TOC [$\mathrm{t\,ha^{-1}}$] in the NRW domain: a) 0–10 cm depth, b) 60–100 cm depth.

Fig. 2.8 depicts the averaged TOC content of the measured PFT-dependent depth profiles in the upper topsoil (0–10 cm) and in the lower subsoil (60–100 cm). In the upper 10 centimeters of the soil (Fig. 2.8a) considerably more TOC was found in needleleaf (94 $\mathrm{t\,ha^{-1}}$) and broadleaf (81 $\mathrm{t\,ha^{-1}}$) forests than in agricultural areas (25 $\mathrm{t\,ha^{-1}}$). This is a result of tillage which leads to a vertical mixing of TOC in the topsoil whereas in unmanaged soils more logarithmically shaped TOC profiles occur. Thus, in the lower subsoil (Fig. 2.8b) the TOC content is low with only 34 $\mathrm{t\,ha^{-1}}$ in needleleaf and 43 $\mathrm{t\,ha^{-1}}$ in broadleaf forests in this 40 cm deep soil interval. The relative difference to agricultural fields (17 $\mathrm{t\,ha^{-1}}$) is less than in the topsoil. The total

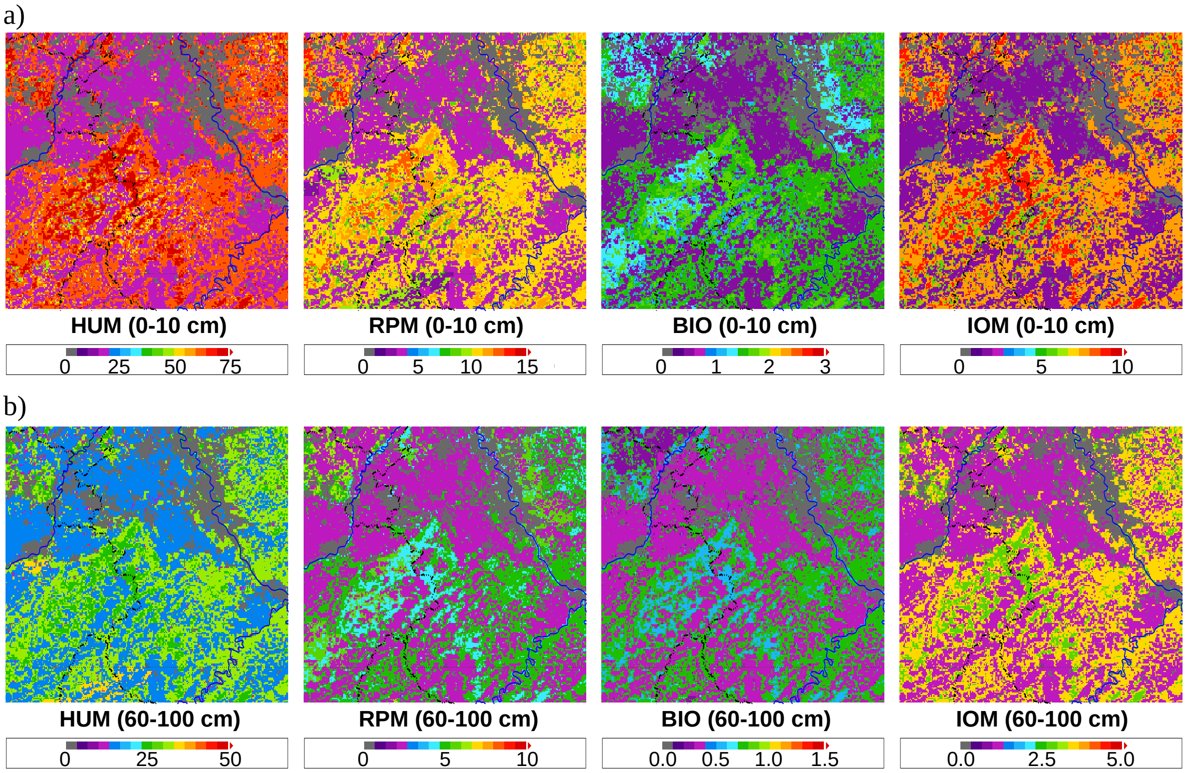

Figure 2.9.: C-pools [$\mathrm{t\,ha^{-1}}$] in the NRW domain derived with the PTFs of Weihermüller *et al.* (2013).

TOC content was determined to be $224\,\mathrm{t\,ha^{-1}}$ for needleleaf and $254\,\mathrm{t\,ha^{-1}}$ for broadleaf forest, $196\,\mathrm{t\,ha^{-1}}$ for shrub, $220\,\mathrm{t\,ha^{-1}}$ for grassland and $123\,\mathrm{t\,ha^{-1}}$ for agricultural areas.

With the knowledge of the PFT and the clay content of each CLM grid cell, the partitioning of TOC into C-pools can be derived applying the PTFs of Weihermüller *et al.* (2013) for all CLM soil levels l:

$$IOM(l) = 0.049 \cdot TOC(l)^{1.139} \tag{2.32a}$$

$$RPM(l) = \big(0.1847 \cdot TOC(l) + 0.1555\big)\big(clay(l) + 1.2750\big)^{-0.1158} \tag{2.32b}$$

$$HUM(l) = \big(0.7148 \cdot TOC(l) + 0.5069\big)\big(clay(l) + 0.3421\big)^{0.0184} \tag{2.32c}$$

$$BIO(l) = \big(0.0140 \cdot TOC(l) + 0.0075\big)\big(clay(l) + 8.8473\big)^{0.0567} \tag{2.32d}$$

Fig. 2.9 depicts the partitioning of TOC into the C-pools used in RothC. In the mineral soil, the biggest portion of TOC ($\approx 75\%$) is already humified (HUM), i. e. slowly decomposable, whereas only small amounts are allocated to the RPM (≈ 10–15%) and BIO pool ($\approx 2\%$). The remaining TOC (≈ 8–10%) forms the IOM pool. In the subsoil very sparse fast decomposable organic matter (BIO) is found (Fig. 2.9b).

The main advantages of this method are the avoidance of a long spin-up run and the application of *measured* TOC depth profiles located in NRW for the determination of the initial RothC carbon pools in CLM.

2.4.5. Parameterization of heterotrophic respiration in TerrSysMP-CO_2

For the calculation of heterotrophic respiration in TerrSysMP-CO_2, the above described TOC profiles and PTFs have been included into the module which initializes the CLM. Moreover, the RothC model equations (see Section 2.4.3) have been implemented into the CLM module which calculates soil hydrology. Whereas the original RothC model is a one-layer model considering vertically averaged moisture and TOC contents of the topsoil and atmospheric temperature, in this study Eqs. 2.30 and 2.31 were solved for each CLM soil layer separately with the C-pools, soil temperatures and pressure heads occurring in these soil levels. Heterotrophic respiration is considered occurring in the soil levels 1–7 (0–83 cm depth, i. e. A, B horizons) only. Finally, the sum of generated CO_2 in these CLM soil layers gives the total heterotrophic CO_2 production in the mineral soil. These CO_2 production rates could be coupled to a CO_2 transport model, e. g., SOILCO2 (see Šimůnek and Suarez, 1993; Herbst *et al.*, 2008). However, the results already show a good representation of the diurnal variation of heterotrophic respiration *without* simulated CO_2 transport below the ground. Thus, the generated CO_2 in each soil layer is released to the atmosphere instantaneously.

To account for the temperature sensitivity of microbial decomposition (see Eq. 2.30), several temperature functions $f(T_{soil})$ have been implemented. One possibility is the temperature dependency of RothC:

$$f(T_{soil}) = \frac{47.9}{1 + \exp\left(\frac{106}{T_{soil}+18.3}\right)}. \tag{2.33}$$

T_{soil} [°C] of each soil layer[6] is used instead of the atmospheric temperature as assumed in Coleman and Jenkinson (2008).

CO_2 production by soil microorganisms is an enzymatic and temperature dependent reaction. Already at the end of the 19th century van't Hoff and Arrhenius found exponential relationships between enzyme activity and temperature (van't Hoff, 1884; Arrhenius, 1898). Van't Hoff proposed an empirical exponential relation whereas Arrhenius developed a more physically based relationship using an activation energy, i. e. the minimum energy needed for a chemical reaction. Even this activation energy is not a constant value and decreases with increasing temperature (see Lloyd and Taylor, 1994). However, the deviation of the exponential relationship due to varying activation energy is relatively small in a wide range of soil temperatures. Since this activation energy depends on the composition of the soil that is not sufficiently known in CLM, the relationship suggested by van't Hoff is included in CLM as a second option of $f(T_{soil})$. This empirical formula can be expressed as a Q_{10} relationship:

$$f(T_{soil}) = \exp\left(\frac{\ln Q_{10}}{10}(T_{soil} - T_{ref})\right). \tag{2.34}$$

T_{ref} is the reference temperature of RothC (9.25 °C) where $f(T_{soil}) = 1.0$. Measured Q_{10} values vary over a wide range (see Lloyd and Taylor, 1994; Suarez and Šimůnek, 1993) but climate models mostly use $Q_{10} = 2.0$ (see e. g. Davidson and Janssens, 2006) which means that soil respiration doubles with a temperature increase of 10 °C. However, Graf *et al.* (2008) found that Q_{10}=2.5 was well within the uncertainty range identified in their study.

Fig. 2.10a depicts all temperature functions $f(T_{soil})$ being tested in this study. At T_{soil} below the RothC reference temperature ($T_{ref} = 9.25$ °C) all temperature functions are less than 1 and

---

[6] For a better readability, in Eq. 2.33–2.35 the index l representing the dependency of the soil temperature $T_{soil}(l)$ and pressure head $h(l)$ from the soil level l is omitted.

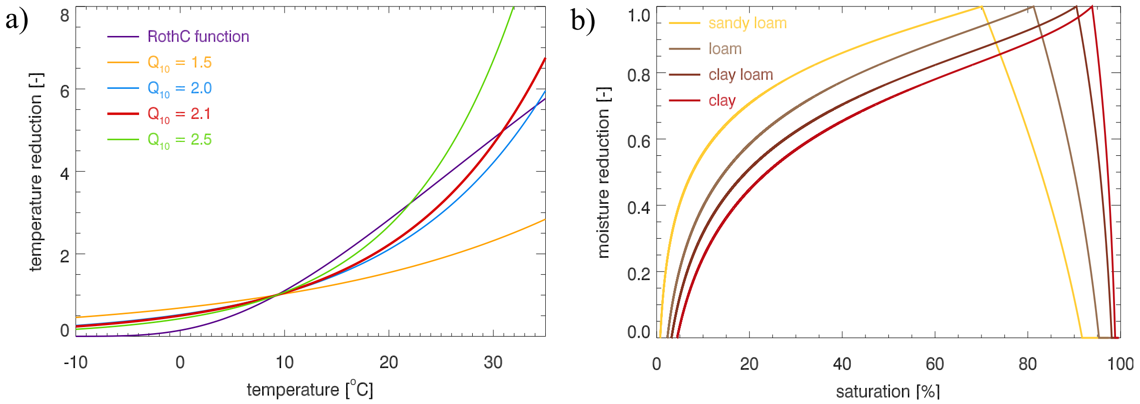

Figure 2.10.: Modifying factors of microbial decomposition used in this study: a) different temperature dependencies $f(T_{soil})$; b) moisture reduction $f(h)$ depending on saturation and soil type.

vice versa. Below T_{ref} the RothC function (Eq. 2.33) has lower values than all Q_{10}-functions and is set to 0 for $T < -4\,°\mathrm{C}$ considering the cessation of microbial activity if the soil freezes. After a relatively strong increase (0–10 °C) the RothC function has approximately a linear behavior and has higher values than the Q_{10}-functions at moderate temperatures and lower values at high T_{soil}. The function $Q_{10} = 1.5$ shows a too weak temperature dependency. With values of 2.0, 2.1 and 2.5 the Q_{10}-functions are comparable at temperatures up to 15 °C but significantly differ at high soil temperatures (e. g. $T_{soil} > 25\,°\mathrm{C}$). As a result of the pure exponential behavior of the Q_{10}-functions, microbial activity is overestimated at very low T_{soil} (freezing soil) and at very high T_{soil} (decreasing Arrhenius activation energy). However, at soil temperatures that usually occur in the temperate zone the Q_{10}-behavior of heterotrophic respiration is an appropriate assumption. In this work, $Q_{10} = 2.1$ is chosen which is also used in the CANDY model (Franko *et al.*, 1995) and corresponds to an activation energy of 55.5 $kJmol^{-1}$ as used in SOILCO2 (Suarez and Šimŭnek, 1993).

To consider the effect of moisture reduction ($f(h)$), the assumption of SOILCO2 is used (see Eq. 44 in Šimŭnek and Suarez, 1993):

$$f(h) = \frac{\log|h| - \log|h_1|}{\log|h_2| - \log|h_1|} \qquad h \in [h_2, h_1] \tag{2.35a}$$

$$f(h) = \frac{\log|h| - \log|h_3|}{\log|h_2| - \log|h_3|} \qquad h \in [h_3, h_2] \tag{2.35b}$$

$$f(h) = 0 \qquad h \in [-\infty, h_3] \cup [h_1, +\infty] \tag{2.35c}$$

In Eq. 2.35, h represents the pressure head [m], $h_2 = -1\,\mathrm{m}$ is the pressure head for optimal soil respiration, $h_3 = -10^5\,\mathrm{m}$ is the pressure head when production ceases and h_1 is equal to the air entry pressure (also referred to as saturation suction). h_1 depends on the soil texture and hydraulic conductivity and is diagnostically predefined in CLM for the given soil type. The values of h_2 and h_3 are adopted from Suarez and Šimŭnek (1993).

Fig. 2.10b depicts the dependency of $f(h)$ on soil water saturation of different soil types using the Mualem–van Genuchten approach (van Genuchten, 1980) to convert pressure head to volumetric water content. A strong increase of $f(h)$ is seen from very low saturation ($h \ll 0$) to higher soil water contents (Eq. 2.35b) with the strongest increase for coarse-grained soils (e. g. sandy loam) and a more moderate increase for fine-grained soils (e. g. clay). Above the optimum saturation ($h_2 = -1\,\mathrm{m}$) $f(h)$ strongly decreases to 0 when the soils are nearly saturated (h_1) due to missing oxygen and, therefore, low CO_2 diffusion rates (Eq. 2.35a). The optimum saturation depends on the soil texture and is about 90% for "clay-loam", the most common soil type in the NRW domain (see Section 3.1). Even after long and dry weather events in the summer season the saturation rarely falls below 50% (i. e. $f(T_{soil}) \in [0.75, 1.0]$), except for the uppermost centimeters of the soil, and thus, $f(h)$ is of minor importance compared to $f(T_{soil})$. In the summer season, detrimental high soil saturation occurs only for several hours after very strong localized rain events (see Section 4.3.1).

Compared to previous mesoscale models analyzing CO_2 fluxes and atmospheric CO_2 concentrations (cf. Section 1.3) the parameterization of heterotrophic respiration in TerrSysMP-CO_2 is significantly advanced. The representation of soil respiration ranged from constant fluxes for different land use classes (Pérez-Landa *et al.*, 2007) to simple functions of R_{soil} on temperature, e. g. a linear relation on temperature (Ahmadov *et al.*, 2007; Pillai *et al.*, 2011), a Q_{10}-function similar to this work (Sarrat *et al.*, 2009) or the approach of Lloyd and Taylor (1994) (Tolk *et al.*, 2009; Ter Maat *et al.*, 2010). None of these studies used measured TOC profiles for the calculation of soil respiration and except for Nicholls *et al.* (2004) TerrSysMP-CO_2 is the only model which prognostically considers the effect of soil moisture on R_{soil}.

2.4.6. Respiration of aboveground litter and in the O horizon

Additionally to respiration in the mineral soil, especially in forests, the decomposition of aboveground litter and in the forest floor (O horizon) are important sources of CO_2 to the atmosphere. In grassland and agricultural soils the O horizon is negligible and significant litter respiration occurs only several days after grass cutting or after harvest. Hence, in CLM respiration of litter ($\mathrm{O_i}$) and in the O horizon ($\mathrm{O_e}$, $\mathrm{O_a}$) is only considered for forest PFTs.

The forest soils of the above described dataset of the LANUV contain an on average 2.6 cm thick O horizon, both for broadleaf and needleleaf forests, containing an average TOC content of 30–35% (i. e. SOM ≈ 50–60%). In the analyses of the HLUG (Wegener, 2008) a TOC of $9.0\,\mathrm{t\,ha^{-1}}$ for aboveground litter and $19.8\,\mathrm{t\,ha^{-1}}$ for the O horizon have been determinend for forests in Hessen. These values are used as basis for the calculation of litter and O horizon decomposition in CLM. Aboveground litter and the O horizon can be considered to be additional carbon pools having their representative decomposition rates. Zhang *et al.* (2008) describe several relationships between litter decomposition rates and meteorological, chemical and geographical variables. Applying a relationship between mean annual precipitation, mean temperature and geographical latitude, a litter decomposition rate of λ_{litter}=0.4 years^{-1} seems to be appropriate for the NRW domain. The TOC of the already partly decomposed O horizon ($\mathrm{O_e}$, $\mathrm{O_a}$) is assumed to be composed of 20% litter, 5% BIO and 75% HUM resulting in a decompositition rate of λ_O=0.13 years^{-1}. The RothC equations (2.30) and (2.31) are adopted to litter and the O horizon using a clay content of 0%. Again, a Q_{10}=2.1 describes the dependency of microbial activity on the CLM ground temperature T_g. The pressure head of the uppermost soil level is used to consider moisture reduction (Eq. 2.35). Borken *et al.* (2003) found a strong dependency of litter and O horizon decomposition on water availability resulting in spontaneous respiration increases after rain events followed by a fast decrease to the rates prior to the rain event already just after a few days. They relate this effect to relatively fast drying of the forest floor (especially aboveground litter) in summertime. This fast drying of aboveground litter cannot be considered using the moisture of the uppermost soil layer which may lead to slightly overestimated respiration rates after a long period with missing precipitation.

2.5. Autotrophic respiration

2.5.1. Autotrophic respiration and carbon allocation in plants

Autotrophic soil respiration is a combination of respiration of living root tissue (root respiration) and activity of microorganisms and fungi in the rhizosphere (mycorrhizal and rhizosphere respiration), as defined in Section 2.4.1, with the major contribution coming from root respiration (Moyano *et al.*, 2008). The contribution to total soil respiration ranges from 10 to 90% (Hanson *et al.*, 2000) and depends on numerous parameters (e. g. plant matter, temperature, season, ...). However, in most ecosystems about one to two thirds of soil respiration are produced in living roots and the rhizosphere.

Autotrophic respiration is strongly connected to photosynthetic activity and is often divided into *maintenance respiration*, i. e. maintenance of living plant cells (e. g. protein replacement, membrane repair), and *growth respiration*, i. e. the synthesis of new tissue from glucose and minerals (e. g. cell expansion, cell wall synthesis) (see Bonan, 2008; Ryan, 1991). At seasonal time scales, maintenance respiration increases exponentially with temperature but water stress can reduce photosynthesis and, thus, maintenance respiration or indirectly by changing priorities of carbon allocation to leaves, storage, wood and fine roots (Ryan, 1991). The contribution of growth respiration, i. e. total carbon cost minus carbon incorporated into plant matter, shows a seasonal variability and has its maximum in the early growing season when a high amount of photosynthetic carbon is allocated to excessive root growth. On average, ≈ 75–80% of plant CO_2 release is generated by maintenance respiration.

On short time scales, the controlling processes of autotrophic respiration are more complex and are in the focus of current research. In the past 10 years, numerous studies show a direct link of diurnal cycles of photosynthesis and autotrophic respiration with some time delay in the respiration signals in most ecosystems. In forest canopies, the time-lag between peaks in photosynthesis and soil respiration ranges from 7–12 h (Tang *et al.*, 2005) to 1–10 days (e. g. Ekblad and Högberg, 2001; Moyano *et al.*, 2008; Bahn *et al.*, 2008). This time-shift supposes a delay being proportional to plant height with a factor of 0.2–2 $\mathrm{m\,h^{-1}}$. This is consistent with more abrupt reactions of soil-respired CO_2 (less than 2 h) found in a pulse-labeling experiment under sunny conditions on a grassland site (Bahn *et al.*, 2009) and in a study of Graf *et al.* (2011) who identified a time-lag of only 15 min on a sugar beet field having a vegetation height of 40 cm. However, Högberg and Read (2006) showed a reduction of soil respiration of 40% on a grassland site within 2 days after shading. The time-lag between photosynthesis and autotrophic respiration is often explained by the time needed for the downward transport of assimilated carbohydrates during photosynthesis from leaves to fine roots. Tang *et al.* (2005), however, assumed that the short time-lag is likely the result of a carbon concentration wave propagation which is faster than the real translocation of carbohydrates. The slower reaction found in Högberg and Read (2006) could be an effect of the daily sum of photosynthesis which leads to inter-diurnal variability. Furthermore, Moyano *et al.* (2008) mentioned that there is no simple connection between photosynthesis and autotrophic respiration because roots, mycorrhiza and rhizoshere microorganisms react with different time-lags (1 day for mycorrhizal respiration and 4 days for root respiration in their study).

2.5.2. A simple parameterization of autotrophic respiration

The time-lag of some days between photosynthesis and autotrophic respiration in forest canopies itself makes it difficult to built an appropriate parameterization which directly simulates the dependence of autotrophic respiration on *previous* photosynthetic activity on a diurnal scale. Additionally, the complex processes described above causing the still unclear correlation between plant height and delay (one order of magnitude) of the respiration signal further strengthens the uncertainty of such a parameterization. Thus, in this study a rather simple relationship between autotrophic respiration and the mean canopy photosynthesis rate ($\overline{A^{can}}$) has been developed following the assumption of Ryan (1991) who pointed out that total plant respiration is about 50% of gross photosynthesis for many plant species:

$$\overline{R_{plant}} = (\overline{R^{can}_{leaf}} + \overline{R_{auto}}) = 0.5 \cdot \overline{A^{can}} \quad \Longrightarrow \quad \boxed{\overline{R_{auto}} = 0.5 \cdot \overline{A^{can}} - \overline{R^{can}_{leaf}}} \tag{2.36}$$

In this formula, $\overline{R_{plant}}$ represents the mean total plant respiration consisting of the mean respiration rates of leaves ($\overline{R^{can}_{leaf}}$), wood and belowground autotrophic respiration[7] ($\overline{R_{auto}}$). Different time scales can be used for these mean fluxes. In this work, monthly mean values are used and a linear interpolation between two monthly respiration rates leads to the mean autotrophic respiration for the considered day of the simulation. However, also daily means would be possible to simulate autotrophic respiration with Eq. 2.36. Whereas sub-diurnal variability of autotrophic respiration, caused by changes in the photosynthetic activity, cannot be considered with this expression, the parameterization can be easily extended with a soil moisture dependency similar to that of heterotrophic respiration. For this, a moisture reduction factor $\widehat{f_{hauto}}$ is determined as a vertical average of $f(h)$ (Eq. 2.35) weighted with the effective root fraction $f_{e,root}(l)$ of each CLM soil level l which describes the root distribution in the soil:

$$\widehat{f_{hauto}} = \frac{\sum_{l=1}^{10}\big(f(h,l) \cdot f_{e,root}(l)\big)}{\sum_{l=1}^{10} f_{e,root}(l)} = \sum_{l=1}^{10}\big(f(h,l) \cdot f_{e,root}(l)\big) \tag{2.37}$$

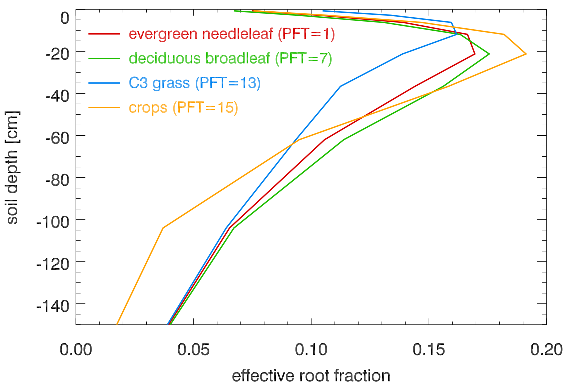

Figure 2.11.: Effective root fraction of the most important PFTs of CLM occurring in the NRW domain.

The effective root fraction $f_{e,root}$, i. e. the root fraction of soil layer l from the whole plant root in the soil, depends on the PFT (see Fig. 2.11). For crops the root fraction in the topsoil is higher than for forest PFTs because the roots of trees penetrate deeper into the subsoil than those of crops. Broadleaf trees have a higher $f_{e,root}$ below 17 cm depth and in the subsoil than needleleaf trees which are shallow root trees. C_3 grass has a higher $f_{e,root}$ in the upper 10 cm of the soil compared with other PFTs. For most plant species (except grassland) the highest amount of roots (33–37%) is concentrated in the CLM soil layers 4 and 5 (i. e. 9.05–28.9 cm) and, thus, these levels are most important for the moisture dependency (Eq. 2.37) of root respiration.

Finally, to obtain the actual autotrophic respiration rate adjusted with the actual moisture conditions in the root zone, the mean respiration rate of Eq. 2.36 is normalized with the monthly mean of the vertically averaged moisture reduction factor $\overline{\widehat{f_{hauto}}}$ and then multiplied with the actual moisture reduction factor $\widehat{f_{hauto}}$:

$$R_{auto} = \widehat{f_{hauto}} \cdot \overline{R_{auto,n}} = \widehat{f_{hauto}}\big(\overline{R_{auto}}/\overline{\widehat{f_{hauto}}}\big) \tag{2.38}$$

---

[7] This parameterization only distinguishes between "leaf" (R^{can}_{leaf}) and "non-leaf" plant respiration (R_{auto}). Whereas in non-forest PFTs R_{auto} represents belowground autotrophic respiration, on forest PFTs R_{auto} also contains aboveground respiration of woody material which, however, plays only a minor role.

where $\overline{R_{auto,n}}$ is the normalized monthly mean of autotrophic respiration. Thus, a decrease of R_{auto} at high soil saturation can be simulated with this parameterization.

For the determination of monthly autotrophic respiration rates, 1-year CLM simulations were performed driven with hourly COSMO-DE analyses for the corresponding year of interest. Thus, the influence of deviations in the mean monthly weather conditions (e. g. temperature, solar radiation, precipitation) on autotrophic respiration can be simulated. One example of these effects can be identified by comparing the considerably higher autotrophic respiration rates in April 2014 with those in April 2012. In April 2014 unusually high temperatures and above-average hours of sunshine caused high photosynthetic activity. In contrast, in April 2012 both the temperature and the hours of sunshine were considerably below the mean climatic conditions leading to lower photosynthesis rates and, thus, lower autotrophic respiration than in 2014. Similar correlations between weather conditions and photosynthesis/respiration can be seen for most of the simulated months.

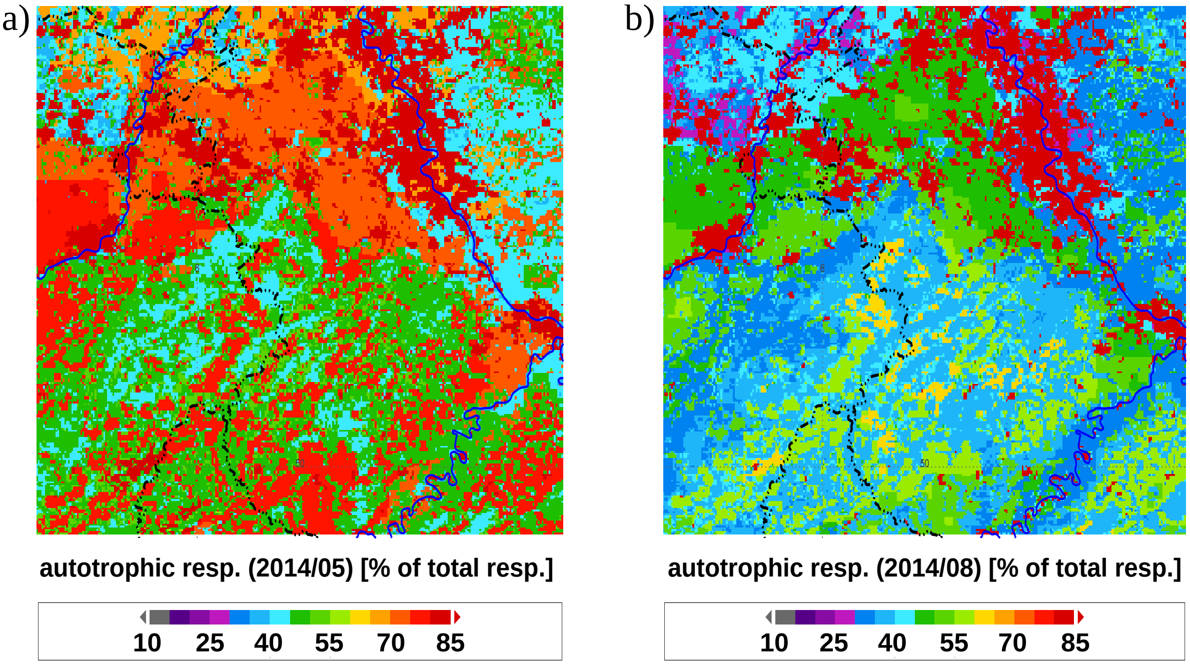

Figure 2.12.: Percentage of autotrophic respiration to total soil respiration using the winter wheat plant-physiological parameters of Sulis *et al.* (2015) for crops (PFT=15) in a) May 2014 and b) August 2014. The dark red areas are urban, i. e. no heterotrophic respiration is calculated.

Furthermore, seasonal variations in the relative contribution of autotrophic respiration to total soil respiration are well simulated with this parameterization. Fig. 2.12 depicts the percentage of autotrophic respiration to total soil respiration. Especially at agricultural areas (i. e. PFT 15, "crops") in May 68–78% of total soil respiration is produced by the autotrophic component (3.7–3.9 μmol(CO$_2$)m^{-2}s^{-1}) because excessive root growth occurs in this growing stage leading to high growth respiration amounts. In mid- and late sommer (i. e. July–September), the autotrophic contribution is considerably lower with only 35–62% because most of the autotrophic respiration can be attributed to maintenance respiration. Moreover, the observed LAI, being an input parameter of CLM, is reduced due to partly harvested agricultural fields and explains the decrease of autotrophic respiration (1.8–1.9 μmol(CO$_2$)m^{-2}s^{-1}). Both in May and August the autotrophic percentage is higher in mountainous regions than in flat terrain and along the Rhine because considerably higher temperatures in the topsoil of agricultural areas lead to higher heterotophic respiration rates in the flat regions. In forest canopies, the difference of autotrophic percentage between the early growing season and late summer is weaker but clearly identifiable with about 40–50% in May and about 30–40% in August 2014.

To conclude, all simulated relative contributions of autotrophic respiration to total soil respiration lie within the range of most of the reported percentages in Hanson *et al.* (2000), but agricultural fields tend to higher percentages than the mean of the non-forest sites in their described studies. The dependency of autotrophic respiration on the LAI (Bahn *et al.*, 2008) and on temperature (Ryan, 1991) is included in the mean photosynthesis rates. The error made with neglecting diurnal variability of photosynthetic activity on autotrophic respiration is small compared to the uncertainty of photosynthesis and heterotrophic respiration.

2.6. Atmospheric CO_2 transport and anthropogenic emissions

2.6.1. CO_2 – an atmospheric tracer in COSMO

Additionally to the prediction of all prognostic meteorological variables, the COSMO model is also used to calculate the transport of CO_2 in the atmosphere. Since this is not part of the standard applications of the COSMO model, CO_2 had to be included as a new prognostic variable into the atmospheric component of TerrSysMP-CO_2. This has been realized by introducing a passive fluid tracer in the COSMO model which is influenced by all atmospheric transport processes that are either calculated explicitly (horizontal and vertical advection) or are parameterized (vertical turbulence, convection). In this context, "passive" means that the properties of the tracer cannot be changed by chemical reactions/transformations or transitions of the state of aggregation. Thus, the newly implemented tracer can be applied for air mass transport studies (e. g. Uebel and Bott, 2015) or for analyzing the spread of every extensive quantity for which this passive behavior holds without interacting with other prognostic variables of the model. The prognostic equation of the tracer (i. e. in the context of this work the mass-specific CO_2 content q_{CO_2}) budget may formally be written as

$$\boxed{\frac{\partial q_{CO_2}}{\partial t} = -\mathbf{v} \cdot \nabla q_{CO_2} + \left(\frac{\partial q_{CO_2}}{\partial t}\right)_{\text{turb}} + \left(\frac{\partial q_{CO_2}}{\partial t}\right)_{\text{conv}} + \left(\frac{\partial q_{CO_2}}{\partial t}\right)_{\text{source}}} \tag{2.39}$$

The first term on the right hand side of this equation describes the advection of CO_2 with the atmospheric wind field while the second and third terms denote CO_2 concentration changes due to subgrid-scale turbulent mixing and convectively induced mass transport. The last term includes all sources/sinks of CO_2, i. e. photosynthesis, respiration and anthropogenic CO_2 emissions. Thus, via this term the atmospheric CO_2 is directly influenced by biogenic CO_2 fluxes, calculated with CLM and transferred to the atmosphere at the lowermost COSMO level (see Section 2.2 for more details). Due to the direct link between the atmospheric CO_2 distribution, photosynthesis and transpiration via the stomatal resistance (Section 2.3.3), the atmospheric CO_2 now becomes *active* because with this coupling the water and heat transfer at the land surface is directly influenced by the prognostic atmospheric CO_2 content. Nevertheless, the *passive* behavior of the tracer in the atmospheric part of TerrSysMP-CO_2 allows to include several tracers into the COSMO model[8]. With the use of additional CO_2 tracers the influence of different CO_2 sources/sinks and transport processes can be separated. For example, by comparing the concentrations of the "active" CO_2 with an additional CO_2 tracer which is only influenced by biogenic CO_2 fluxes the effect of anthropogenic emissions on the simulated CO_2 distribution can be quantified or even the individual canopy fluxes of CO_2 can be separated.

2.6.2. High-resolution data of anthropogenic CO_2 sources

In addition to the biogenic fluxes of CO_2, as described in Sections 2.3–2.5, since the begin of the industrialization the humans contribute significantly to the atmospheric CO_2 budget. Despite of a reduction of 20% since 1990, in Germany about 841 millions of tonnes (mio. t) CO_2 were emitted in 2013 (Umweltbundesamt, 2015, online) with about 1/3 produced in North Rhine-Westphalia (NRW). These *anthropogenic CO_2 emissions* are further CO_2 sources which are included in the last term of Eq. 2.39.

In this study, the most recent high-resolution gridded dataset of European anthropogenic CO_2 emissions is used, made by the "Netherlands Organisation for Applied Scientific Research", TNO (H. Denier van der Gon, personal communication, Oct. 2013), following the methodology outlined in Kuenen *et al.* (2014) and Pouliot *et al.* (2012) for air pollutants. This *emission inventory* (i. e. a complete, consistent and spatially distributed collection of emission data for past and present times) is an update of the TNO-MACC_II emission inventory (Kuenen *et al.*, 2014). It is based on yearly official reports of emitted air pollutants submitted from 51 countries in Europe and North America, including the EU as a whole. The source of emissions is classified into 10 Source Nomenclature for Air Pollution (SNAP) sectors. Among these, the following SNAP sectors produce CO_2:

- *SNAP 1*: Power generation (e. g. public electricity, district heating plants, coal mining)
- *SNAP 2*: Non-industrial combustion plants (commercial and institutional plants, residential plants and others)
- *SNAP 3*: Industrial combustion plants
- *SNAP 7*: Road transport (e. g. passenger cars, light duty and heavy duty trucks, busses, motorcycles)
- *SNAP 8*: Other mobile sources and machinery (e. g. railways, waterways, sea traffic)
- *SNAP 9*: Waste treatment and disposal (e. g. waste incineration)

From these sectors, SNAP 1 is the strongest source, followed by SNAP 3, SNAP 2 and SNAP 7 (McInnes, 1996). Before the official national reports were included into the emission inventory, they underwent various consistency checks and gaps or unreliable data were replaced by model data or by TNO's default emission inventory, if necessary (Kuenen *et al.*, 2014; Visschedijk *et al.*, 2007). However, for EU Member States reported emissions are the primary data source. Finally, the national anthropogenic emissions were spatially distributed on a grid with 0.125°×0.250° (lat/lon) resolution, i. e. ≈ 15 km×15 km. For point sources (e. g. industrial

---

[8] Only *"one"* prognostic CO_2 concentration is used for the two-way coupling with CLM and then has an active behavior whereas all additional CO_2 tracers would be passive, i. e. their CO_2 concentrations cannot interact with any of the CLM and COSMO calculations.

plants, oil refineries, major airports, waste incinerators), simply the geographical coordinates were used to allocate the emissions to the appropriate grid box. Area sources (e. g. road traffic, residential plants, sea traffic) were distributed with the aid of spatial proxy data, such as road maps and traffic intensities, urban and rural population density or location and density of sea shipping routes.

This gridded TNO emission inventory was further disaggregated to a resolution of 1.0 km by the "Rheinisches Institut für Umweltforschung an der Universität zu Köln", RIU (P. Franke, E. Bem and J. Klimpt, personal communication, Oct. 2013). Similar to the strategy of TNO, the disaggregation at RIU was performed by applying high-resolution cadasters containing information on the source of emission for all SNAP sectors, their geographical locations and other proxy data needed for the downscaling from 15 km resolution to the desired 1 km resolution. Finally, these high-resolution anthropogenic CO_2 emissions were transferred from Lambert conformal conic coordinates of the RIU dataset to the rotated spherical grid of the COSMO model.

The dataset that is used for the simulations with TerrSysMP-CO_2 is depicted in Fig. 2.13. The upper map shows an example of a COSMO domain providing lateral boundary data for the simulations of the NRW domain (cf. Fig. 3.3). Over Germany and large parts of its bordering countries the high-resolution dataset of RIU is aggregated to the COSMO-DE grid boxes with a horizontal size of $\approx 2.8\,\text{km}\times 2.8\,\text{km}$. Farther outside the original TNO emission inventory with the coarser resolution of ≈ 15 km is used where the RIU cadaster information is not available. High anthropogenic CO_2 emissions are found in densely populated regions (e. g. Ruhr area, northern part of Belgium, the Netherlands, Paris). Moreover, the road network and the main sea shipping routes can be well identified. The lower map depicts the anthropogenic CO_2 sources emitted in the NRW domain with a resolution of ≈ 1.1 km. In the northern part of the domain and along the Rhine the anthropogenic emissions are very high, especially in the big cities Cologne (K), Bonn (BN), Aachen (AC), Maastricht (MA) and Liège (L). This is mainly caused by urban driving, residential and industrial combustion. In contrast, in the southwestern part of the domain (i. e. in the Eifel region) the CO_2 emissions are very low. By far the highest CO_2 emissions are produced by the three biggest lignite-fired power plants Neurath (Ne, 33.3 mio. t [2013]), Niederaußem (Ni, 29.5 mio. t [2013]) and Weisweiler (W, 18.8 mio. t [2013]) – being responsible for about 1/3 of the anthropogenic CO_2 emissions in NRW – as well as by several power plants along the river Maas in Belgium and the Netherlands. Thus, the NRW domain is an excellent modeling area to analyze the influence of anthropogenic emissions on the simulated atmospheric CO_2 concentrations. The "box" patterns in the lower map occur if a CO_2 emission in the TNO dataset cannot be allocated to a specific location with the aid of the RIU cadasters and, thus, the original TNO resolution is preserved.

2.6.3. Calculation of hourly anthropogenic CO_2 emissions

Since the COSMO model needs hourly anthropogenic emissions, the above described annual emissions have to be downscaled to hourly emissions for all grid points. Each of the SNAP sectors have different temporal variability. Seasonal variability, different emissions on working-days and at weekend-days as well as during daytime and nighttime have to be considered. To account for these temporal variations, *emission time factors* for each of the CO_2 emitting SNAPs are applied (see Table 2.1) which are used in the LOTOS-EUROS chemistry-transport model (Schaap *et al.*, 2005). Multiplication of the average monthly, daily and hourly emissions of each SNAP sector with the corresponding emission time factor results in hourly anthropogenic emissions obtained from the annual emission dataset (see example below).

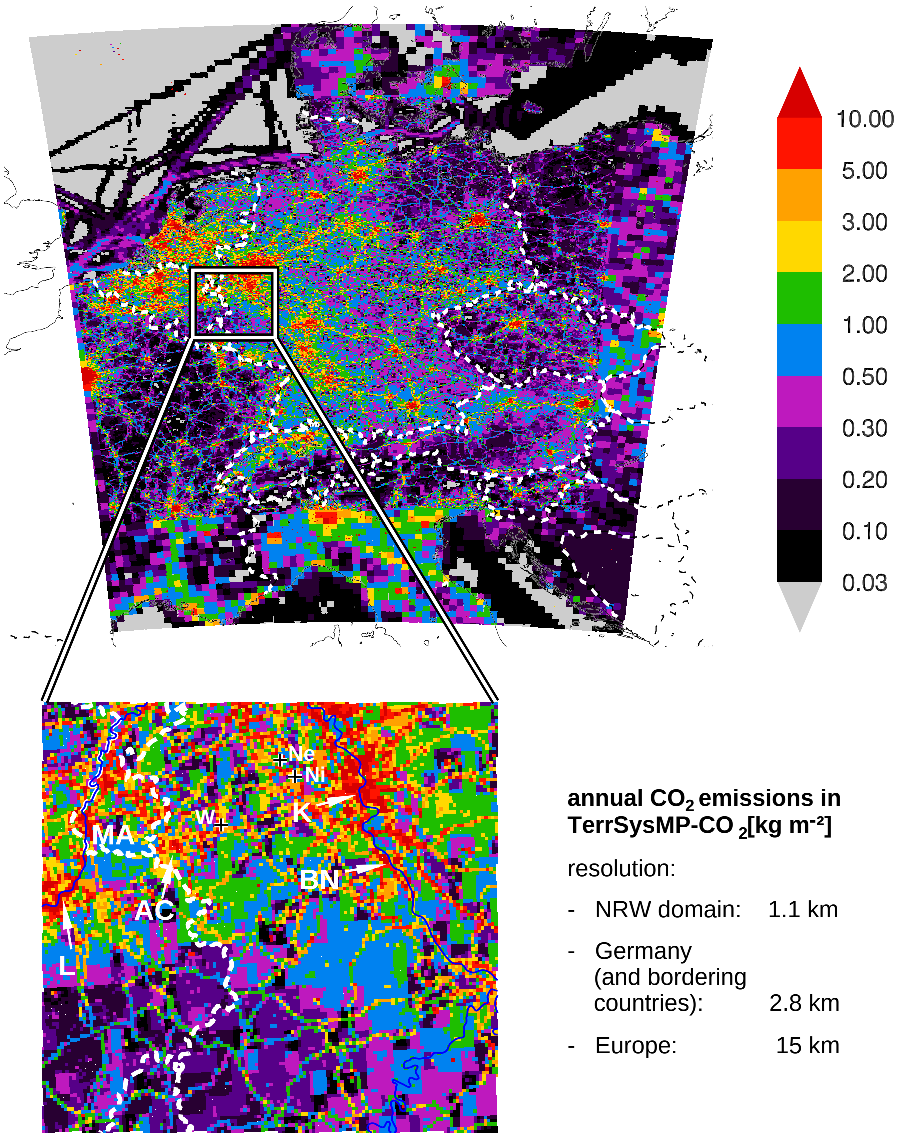

Figure 2.13.: Annual anthropogenic CO_2 emissions [kg m^{-2}] used in TerrSysMP-CO_2 for a nesting domain (upper map) and the NRW domain (lower map).

On a seasonal timescale, for example, considerably higher emissions can be found for SNAP 2 during winter with a factor of 1.7 for January compared with the summer months (0.2 for July), see Table 2.1a and Fig. 2.14a. This means that in January the monthly emission of SNAP 2 is 1.7 times higher than the mean monthly emission (factor 1.0) of this emission category. The main reason for this is domestic heating in the winter season which also leads to slightly more power generation (SNAP 1) than in the summer season. Even the effect of summer holidays can be seen with slightly less road transport (SNAP 7) in July and August than in June and September. During a week (Table 2.1b) especially road transport shows some variability with less traffic on weekend-days (factor 0.79 on Sunday) than on Friday (factor 1.14) when weekend and daily commuters as well as trucks are on the roads. In the strict sense even for different road types like motorways, rural and urban roads a different course of a)

SNAP	Jan	Feb	Mar	Apr	May	Jun	Jul	Aug	Sep	Oct	Nov	Dec
1	**1.2**	1.15	1.05	1.0	0.9	0.85	**0.8**	0.875	0.95	1.0	1.075	1.15
2	**1.7**	1.5	1.3	1.0	0.7	0.4	**0.2**	0.4	0.7	1.05	1.4	1.65
3	1.1	1.075	1.05	1.0	0.95	0.9	0.93	0.95	0.97	1.0	1.025	1.05
7	0.88	0.92	0.98	1.03	1.05	**1.06**	**1.01**	**1.02**	**1.06**	1.05	1.01	0.93
8	0.88	0.92	0.98	1.03	1.05	1.06	1.01	1.02	1.06	1.05	1.01	0.93
9	1.0	1.0	1.0	1.0	1.0	1.0	1.0	1.0	1.0	1.0	1.0	1.0

b)

SNAP	Mon	Tue	Wed	Thu	Fri	Sat	Sun
1	1.06	1.06	1.06	1.06	1.06	0.85	0.85
2	1.08	1.08	1.08	1.08	1.08	0.8	0.8
3	**1.08**	1.08	1.08	1.08	1.08	**0.8**	0.8
7	1.02	1.06	1.08	1.1	**1.14**	0.81	**0.79**
8	1.0	1.0	1.0	1.0	1.0	1.0	1.0
9	1.0	1.0	1.0	1.0	1.0	1.0	1.0

c)

SNAP	01	02	03	04	05	06	07	08	09	10	11	12	13	14	15	16	17	18	19	20	21	22	23	00
1	0.79	0.72	0.72	0.71	0.74	0.8	0.92	1.08	1.19	1.22	1.21	1.21	1.17	1.15	1.14	1.13	1.1	1.07	1.04	1.02	1.02	1.01	0.96	0.88
2	0.38	0.36	0.36	0.36	0.37	0.5	1.19	1.53	1.57	1.56	1.35	1.16	1.07	1.06	1.0	0.98	0.99	1.12	1.41	1.52	1.39	1.35	1.0	0.42
3	0.75	0.75	0.78	0.82	0.88	0.95	1.02	1.09	1.16	1.22	1.28	1.3	1.22	1.24	1.25	1.16	1.08	1.01	0.95	0.9	0.85	0.81	0.78	0.75
7	0.19	0.09	**0.06**	**0.05**	0.09	0.22	0.86	**1.84**	**1.86**	1.41	1.24	1.2	1.32	1.44	1.45	1.59	**2.03**	**2.08**	1.51	1.06	0.74	0.62	0.61	0.44
8	1.0	1.0	1.0	1.0	1.0	1.0	1.0	1.0	1.0	1.0	1.0	1.0	1.0	1.0	1.0	1.0	1.0	1.0	1.0	1.0	1.0	1.0	1.0	1.0
9	1.0	1.0	1.0	1.0	1.0	1.0	1.0	1.0	1.0	1.0	1.0	1.0	1.0	1.0	1.0	1.0	1.0	1.0	1.0	1.0	1.0	1.0	1.0	1.0

Table 2.1.: LOTOS-EUROS emission time factors for the CO_2 producing SNAP sectors: a) monthly factors, b) factors for the day of the weak, c) factors for the hour of the day [local time]. The bold and underlined numbers are referred to in the text.

road traffic densities is observed (McInnes, 1996), e. g. less urban traffic and more motorway and rural traffic on weekend-days than on working-days. However, this distinction is not made in the LOTOS-EUROS emission time factors. A similar effect with higher emission rates on working-days than on weekend-days can be found for industrial combustion (SNAP 3). During the day (Table 2.1c) road traffic (SNAP 7) shows the strongest variations. After midnight considerably less vehicles are on the roads than at daytime. Especially in the morning and in the early afternoon rush-hour traffic effects can be clearly identified (see Fig. 2.14b).

The application of the emission time factors is explained in an example. Assuming an annual emission of 7.5 kg(CO_2) m^{-2} of road transport (SNAP 7), e. g., a rural grid point including a motorway, the emission rate $E_{\text{SNAP}7,Aug,Sun,14}$ on Sunday, 25 August 2013 at 14 CEST (i. e. 12 UTC) is calculated as follows (see underlined numbers in Table 2.1):

$$\begin{aligned}
E_{\text{SNAP}7,Aug} &= (7.5kg(CO_2)m^{-2}yr^{-1}/12)\cdot 1.02 = 0.6375kg(CO_2)m^{-2}month^{-1}\\
E_{\text{SNAP}7,Aug,Sun} &= (E_{\text{SNAP}7,Aug}/31)\cdot 0.79 = 16.25g(CO_2)m^{-2}d^{-1}\\
E_{\text{SNAP}7,Aug,Sun,14} &= (E_{\text{SNAP}7,Aug,Sun}/24)\cdot 1.44 = 0.9748g(CO_2)m^{-2}h^{-1}\\
&= \underline{0.2708mg(CO_2)m^{-2}s^{-1}}
\end{aligned} \tag{2.40}$$

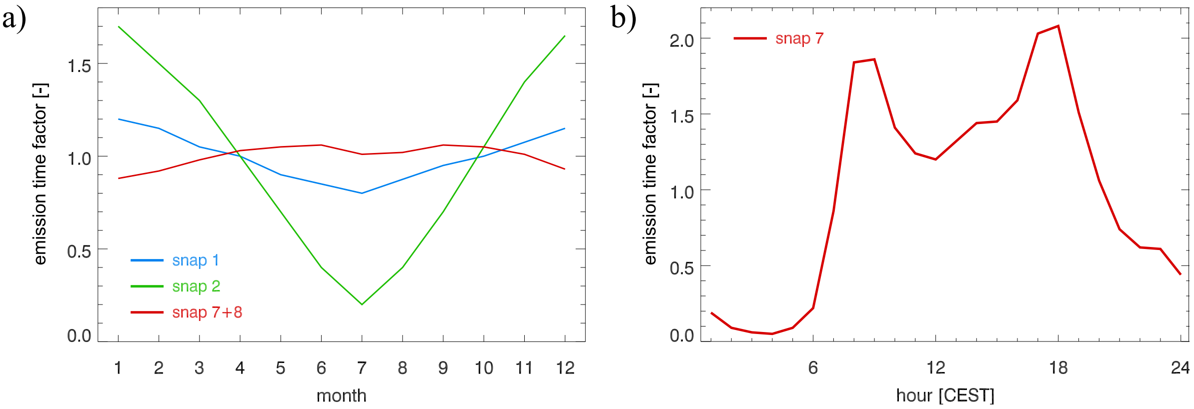

Figure 2.14.: LOTOS-EUROS emission time factors: a) monthly factors of SNAPs 1, 2, 7 and 8; b) hourly factors of SNAP 7.

This procedure has to be done for each of the SNAP sectors using their corresponding emission time factors. The resulting emission rates are read in hourly in COSMO and represent the anthropogenic CO_2 sources. Whereas the emissions of SNAPs 2, 7, 8 and 9 are included into the lowest COSMO model layer, the emissions of SNAP 1 and 3 are distributed to the levels 43–47 (95–500 m) with decreasing column densities with height. This is done to consider elevated sources (i. e. funnels) and the CO_2 release with some momentum and higher temperatures than in the environment resulting in thermodynamical ascent of the emitted CO_2.

Of course, these downscaled hourly emissions cannot be interpreted as exact descriptions of real regional emissions because extraordinary events (e. g. public holidays, rail strikes, ...) as well as regional effects (e. g. holiday traffic to the North Sea in Northern Germany and the Netherlands on motorways during summer, regional school vacations) cannot be considered with these emission time factors. Nevertheless, these hourly emission rates are a good approximation that can be used for modeling of mesoscale CO_2 variability.

2.7. Oceanic CO_2 exchange

The global oceans are an important atmospheric sink in the climatological CO_2 budget and a large CO_2 reservoir. However, for short-term atmospheric CO_2 variability the CO_2 exchange between the sea water and the atmosphere plays only a minor role. In some studies of mesoscale CO_2 variability in coastal regions using process-based numerical forecast models (e. g. Tolk *et al.*, 2009; Sarrat *et al.*, 2009; Ter Maat *et al.*, 2010) the simple relationship of Takahashi *et al.* (2002) was applied to estimate sea-air CO_2 fluxes. Takahashi *et al.* (2002) presented global maps of the monthly climatological distribution of the CO_2 partial pressure [Pa] in surface waters (c_{sw}) on the basis of numerous measurements since the 1960s. The net CO_2 flux across the sea surface then can be described with the difference between the atmospheric and the surface water partial pressure ($\Delta c|_{sea-air} = c_{sw} - c_a$) and a gas transfer coefficient depending on the wind velocity at the water surface. c_{sw} mainly depends on sea surface temperature and the biological productivity in the oceans. They identified the temperate oceans (i. e. 40–60° N and S) to be the major atmospheric CO_2 sink caused by a juxtaposition of cooling of poleward-flowing warm waters mixing with cold subpolar waters. The latter are rich in nutrients and thus lead to a strong biological drawdown. Additionally, the CO_2 flux is intensified by relatively high wind speeds in these regions. Takahashi *et al.* (2002) further found that, except for subtropical waters, the oceanic c_{sw} is nearly not influenced by the atmospheric CO_2 increase which means that the high-latitude oceans play an increasingly important role for the uptake of atmospheric CO_2 in the future climate.

In order to estimate the relevance of sea-air fluxes for CO_2 variability in the domain of interest in this study, the valuable dataset of the "CarbonTracker Europe" (2014) initiative was investigated (see also Peters *et al.*, 2010). This dataset provides oceanic CO_2 fluxes in $1^o \times 1^o$ resolution for the years 2001–2011. In these years, the average oceanic CO_2 flux at the North Sea for the months May–September was less than $-0.05\ \mu$mol $m^{-2}s^{-1}$ and slightly higher ($\approx -0.08\,\mu mol(CO_2)m^{-2}s^{-1}$) in the Atlantic near the coasts of Western Europe and it was always negative. During the winter season the flux as well as its variability was slightly higher at the North Sea mainly caused by higher wind speeds. These values show that the oceanic CO_2 flux is about two orders of magnitude smaller than the major natural terrestrial fluxes (i. e. photosynthesis, respiration) and anthropogenic emissions. Even the diurnal and monthly averaged terrestrial NEE (e. g. net CO_2 loss during summer) is more than one order of magnitude larger than the CO_2 exchange between the sea water and the atmosphere (see e. g. Section 7.3.6). Similarly to these findings, Tolk *et al.* (2009) calculated an average sea-air CO_2 flux of $\sim 0.02\,\mu mol(CO_2)m^{-2}s^{-1}$ at the North Sea and showed that the signal of this flux on the atmospheric CO_2 concentration at the Cabauw measurement tower is nearly undetectable although this tower is located at a distance of only 45 km to the coast. Therefore, for the NRW domain which is considerably farther inland, sea-air CO_2 fluxes can be neglected. Hence, in the current version of TerrSysMP-CO_2 the flux of CO_2 over sea is set to zero (in the nesting domains) which is also assumed in several studies analyzing mesoscale CO_2 variability with coupled biosphere–atmosphere models (e. g. Ahmadov *et al.*, 2007; Pérez-Landa *et al.*, 2007, and others).

3. Model domain and model input data

This chapter introduces the characteristics of the model domain and the model input data used for the numerical investigations of the spatio-temporal CO_2 variability in the atmosphere with TerrSysMP-CO_2. This includes a description of the CLM spin-up runs needed for the initialization of CLM with realistic soil moisture and temperature profiles. Moreover, the TerrSysMP-CO_2 model nesting procedure is explained providing initial and hourly lateral boundary conditions of all meteorological parameters *and* CO_2 for the COSMO model.

3.1. The NRW domain – numerical setup and characteristics

For the mesoscale analysis of atmospheric CO_2 concentrations the model domain and setup based on Shrestha *et al.* (2014) is used. In the atmospheric part of TerrSysMP-CO_2 (COSMO), the model north pole of the rotated geographical model grid (Section 2.1.1) is set to 40° N, 170° W. A horizontal grid spacing of 0.01° (lat/lon, rotated coordinates) is used which is about 1.1 km. The COSMO model domain covers a region of 167×167 km (150×150 grid points). In the vertical a stretched grid of 50 model layers is used having a layer thickness of 20 m at the surface, about 400 m in 5 km a.s.l. and 1000 m at the model top in 22 km a.s.l. Thus, especially in the lower atmosphere TerrSysMP-CO_2 has a relatively high vertical grid resolution with 8 and 16 layers below 500 and 2000 m, respectively. To account for the high spatial heterogeneity of the land surface, the vegetation and soil model component (CLM) has a smaller horizontal grid size of 0.005°×0.00775° (regular geographical coordinates), i. e. a grid spacing of about 500 m. Different from the model simulations in Shrestha *et al.* (2014), here the soil hydrological processes are calculated with CLM using a stretched vertical grid of 10 levels down to 287 cm, i. e. the hydrological model ParFlow is switched off.

Fig. 3.1 shows a map of the CLM topography with several additional information. The model domain encompasses the western part of Germany (**DE**, Deutschland) including the southwestern part of North Rhine-Westphalia (NRW) and parts of Rhineland-Palatinate (RLP). In the west, parts of Luxemburg (**LUX**), Belgium (**BE**) and the Netherlands (**NL**) are included in the domain. Due to the main part being in NRW, in this work the domain is referred to as the "NRW domain". The orography is very diverse with the mountainous region Eifel in the central and southern part characterized by hilly terrain (≈ 300–700 m a.s.l.) with the mountain ridges "Hohes Venn" and "Hohe Eifel" and narrow valleys (e. g. Ahr, Rur, Urft). Further hilly terrain is located in the southeastern (Hunsrück) and eastern part of the domain (Bergisches Land). In contrast, in the northern and northwestern part of the NRW domain the terrain is flat consisting of the "Kölner Bucht" and the "Jülicher Börde" in Germany as well as of parts of NL and BE. The Eifel and the Hunsrück are separated by the river Mosel and also the large rivers Maas and Rhine (Rhein) with several tributaries (e. g. Wied, Sieg, Agger) flow through this region. Especially along the Rhine one of the highest population densities of Central Europe is part of the model domain with the metropolises Cologne (K, Köln), Dusseldorf (D) and Bonn (BN). This allows a detailed investigation of anthropogenic emissions influencing the atmospheric CO_2 distribution. Further regions with high population densities are the cities

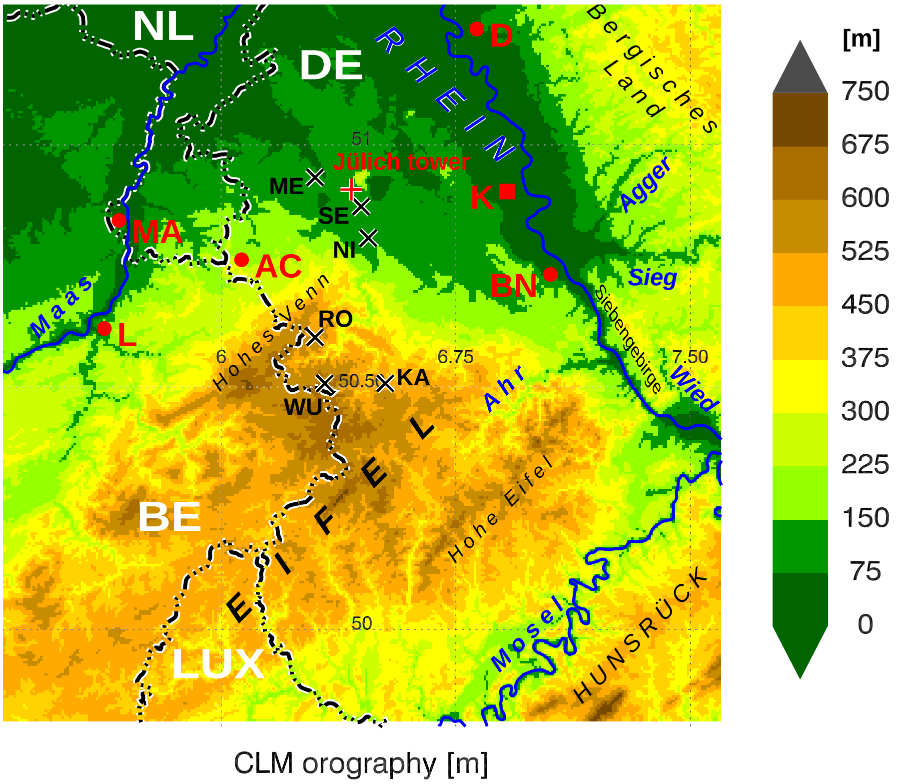

Figure 3.1.: Map of orographic height of the "NRW domain" with German place names. The domain includes the mountainous region Eifel and the flat terrain of the Kölner Bucht and Jülicher Börde. The biggest cities (■,●) are Aachen (AC), Bonn (BN), Cologne (K), Dusseldorf (D), Liège (L) and Maastricht (MA). The locations of the EC stations (×) used for model verification are Merzenhausen (ME), Selhausen (SE), Niederzier (NI), Rollesbroich (RO), Wüstebach (WU) and Kall-Sistig (KA). Moreover, the 124 m tall tower in Jülich (✚) is also marked in the figure. Additional descriptions are in the text.

Maastricht (MA), Aachen (AC) and Liège (L) whereas in the Eifel the population density is very low.

In Fig. 3.1, all eddy covariance (EC) stations are mapped which are used for verification of energy and CO_2 fluxes. The stations are installed near Merzenhausen (ME, 93 m a.s.l., agriculture[1]), Selhausen (SE, 105 m, agriculture), Niederzier (NI, 102 m, grassland), Rollesbroich (RO, 515 m, grassland), Wüstebach (WU, 610 m, spruce forest) and Kall-Sistig (KA, 499 m, grassland). Finally, the location of the 124 m tall tower of the "Forschungszentrum Jülich GmbH", in the following referred to as the "Jülich tower", is shown which is equipped with meteorological and CO_2 concentration instruments at several heights (see Section 7.1).

Fig. 3.2a) depicts the land cover in the NRW domain in terms of CLM plant functional types (PFT) based on MODIS land cover data (Shrestha *et al.*, 2014). It is characterized by deciduous broadleaf (30.8%) and evergreen needleleaf forest (9.7%), cropland (36.6%) and grassland (C_3 grass) (5.4%). A rather large fraction of the domain (13.5%) is urban. Broadleaf shrub (2.3%), evergreen broadleaf (1.3%) and deciduous needleleaf trees (0.3%) play a minor role and are artefacts of the MODIS land cover. Unfortunately, this PFT dataset does not distinguish

---

[1] details on the crop rotation at the Merzenhausen and Selhausen sites can be found in Section 5

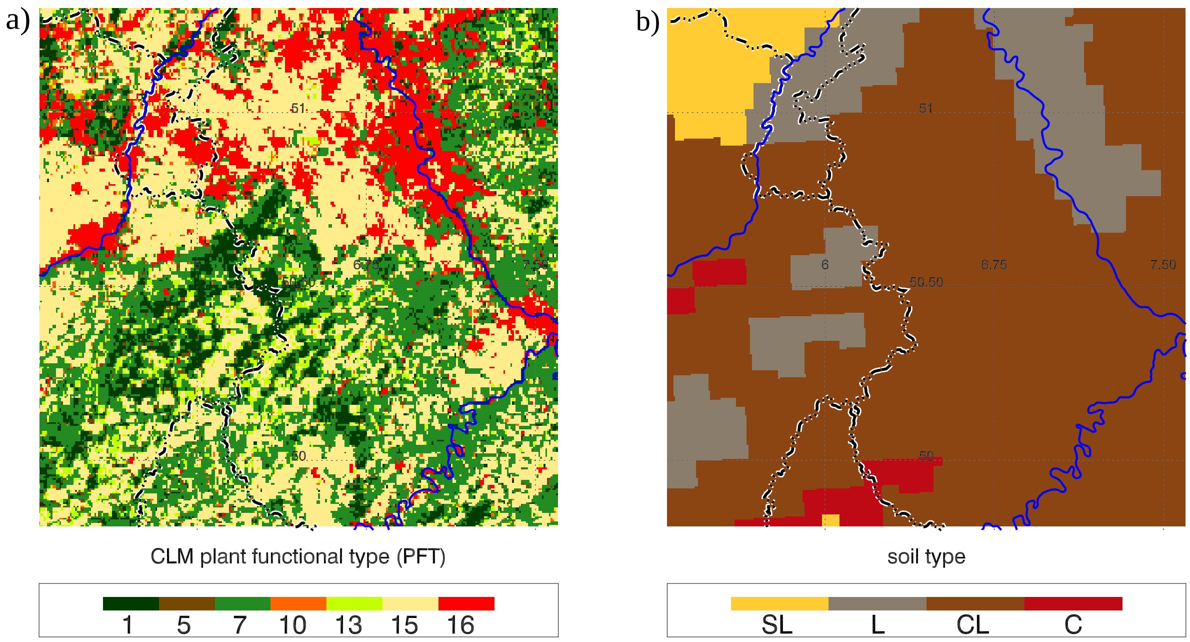

Figure 3.2.: Maps of a) CLM plant functional types and b) soil type classification in the NRW domain. The occurring PFTs are **1**: temperate evergreen needleleaf, **5**: temperate evergreen broadleaf, **7**: temperate deciduous broadleaf, **10**: temperate deciduous broadleaf shrub, **13**: C_3 grass, **15**: agriculture (crops), **16**: urban area. The soil is separated into sandy loam (SL), loam (L), clay-loam (CL) and clay (C).

between different cultivation forms (e. g. different crops, maize, sugar beet, vegetables, ...). In CLM, all of them are represented with PFT 15 (crops) having the same LAI and, in this work, either the standard crop plant physiological parameters of CLM or the "winter wheat" parameters of Sulis *et al.* (2015). The mountainous regions and the Mosel valley are dominated by broadleaf forest and especially above 500 m a.s.l. by needleleaf forest. The flat terrain is dominated by agriculture and urban areas. Grassland mainly occurs in hilly terrain. For all PFTs the predefined monthly values of LAI and SAI of Shrestha *et al.* (2014) are used.

The classification of the 10 CLM soil layers and the soil colors of the given soil types are adopted from Shrestha *et al.* (2014), based on the FAO/UNESCO Soil Map of the World (1974) as used in the external parameter set of the operational COSMO model (Fig. 3.2b). The predominant soil is clay-loam (35% clay, 35% sand). In the north-western part, sandy loam (10% clay, 65% sand) and loam (20% clay, 40% sand) are found. Moreover, loam occurs in the eastern part of the Rhine valley and in the belgian Eifel. Small areas are represented by clay (45% clay, 15% sand). The resolution of this map (5 arcmin) is rather coarse. A more detailed soil map as well as different clay contents in the topsoil and subsoil would be desirable in future studies.

3.2. TerrSysMP-CO$_2$ model nesting procedure

As every limited-area regional NWP model, TerrSysMP-CO$_2$ needs initial conditions (ICs) and lateral boundary conditions (LBCs) to enable realistic numerical simulations. Additional to the standard atmospheric state variables needed for COSMO, ICs and LBCs of CO$_2$ concentrations have to be provided for the NRW domain. The simplest assumption is the initialization with a horizontally homogeneous vertical CO_2 profile and a zero horizontal gradient of concentration at the model boundaries as performed in Sarrat *et al.* (2009). However, the NRW domain is much smaller than the the domain in their studies and, thus, the spatio-temporal distribution of CO_2 in the NRW domain is strongly influenced by advection of CO_2 into the domain at the lateral boundaries. Therefore, the zero horizontal gradient assumption would lead to a high loss of information.

In most numerical analyses of CO_2 variability using regional models, the limited domain was nested into a larger domain with a coarser resolution providing the fields of meteorological variables and CO_2 at the lateral boundaries. In the simulations of Smallman *et al.* (2013) the ICs and LBCs of the outer nesting domain were provided by 3-hourly CO_2 fields of "CarbonTracker Europe" (2014) with a resolution of $1^o \times 1^o$, similar to Tolk *et al.* (2009) who additionally nudged the nesting simulation to the CarbonTracker Europe CO_2 mixing ratios. Ahmadov *et al.* (2007) used the CO_2 contents of a global model with a similar horizontal resolution. In situations with moderate wind the outer domain of these studies was still too small (< 1000 km) so that in a 1-day simulation the inner domain was influenced by boundary effects of the outer domain. Thus, information of a background CO_2 (e. g. CarbonTracker Europe) was necessary.

Contrary to this procedure, Ter Maat *et al.* (2010) performed a model nesting with two steps. The outermost domain was about 4000×4000 km large and had a rather large grid size of 48 km. This domain was initialized with a horizontally homogeneous vertical CO_2 profile and the smaller domains are nested into this domain obtaining the prognostic CO_2 fields of the larger domains at the boundaries. The advantage of this procedure is that without nudging to a background CO_2 a free dynamical development of CO_2 mixing ratios is possible.

The nesting strategy used in the present study is somehow intermediate between these two approaches. Contrary to Ter Maat *et al.* (2010), only one nesting step is performed. However, compared to the inner domain, the used nesting domains (Fig. 3.3) are considerably larger than those of above described studies (Smallman *et al.*, 2013, and others). Depending on the predominant direction of the atmospheric flow, three different nesting domains provide the LBCs for the NRW domain (Fig. 3.3). This strategy ensures that at a moderate atmospheric mean flow ($\approx 10\,\mathrm{m\,s^{-1}}$ in the lower atmosphere), in a 24 h forecast the NRW domain is not influenced by lateral boundary effects of the outer domain. Thus, the knowledge of a background CO_2 for the LBCs of the outer domain is not necessary. With a horizontal grid size of 0.025^o (≈ 2.8 km), both for the atmospheric and the terrestrial components, the model resolution is considerably higher than those of above described nesting domains (6–48 km). For the simulation of the biogenic CO_2 sources/sinks the fully coupled COSMO–CLM setup of TerrSysMP-CO_2 is needed. For the outer domain, ICs and LBCs of all atmospheric variables are obtained by COSMO-EU model analysis data (grid size: 0.0625^o) provided by the DWD. Similar to Ter Maat *et al.* (2010), atmospheric CO_2 is initialized with a horizontally (and vertically) homogeneous concentration adjusted to the actual mean CO_2 mixing ratio at the time of the simulation. Hourly high-resolution anthropogenic CO_2 emissions are included according to Sections 2.6.2 and 2.6.3 (cf. Fig. 2.13).

For the case studies analyzed in Chap. 4–6, the nesting run is started 24 h before the starting time of the simulation with the NRW domain. This is done to provide a dynamically reasonable heterogeneous 3D-distribution of CO_2 as IC of the NRW domain. Fig. 3.4 gives an example of the near surface CO_2 distribution of a nesting simulation showing the heterogeneous distribution in the morning over land and distinctly lower CO_2 contents in the evening. The influence of important CO_2 sources within the domain (e. g. Rhine cities, power plants) and

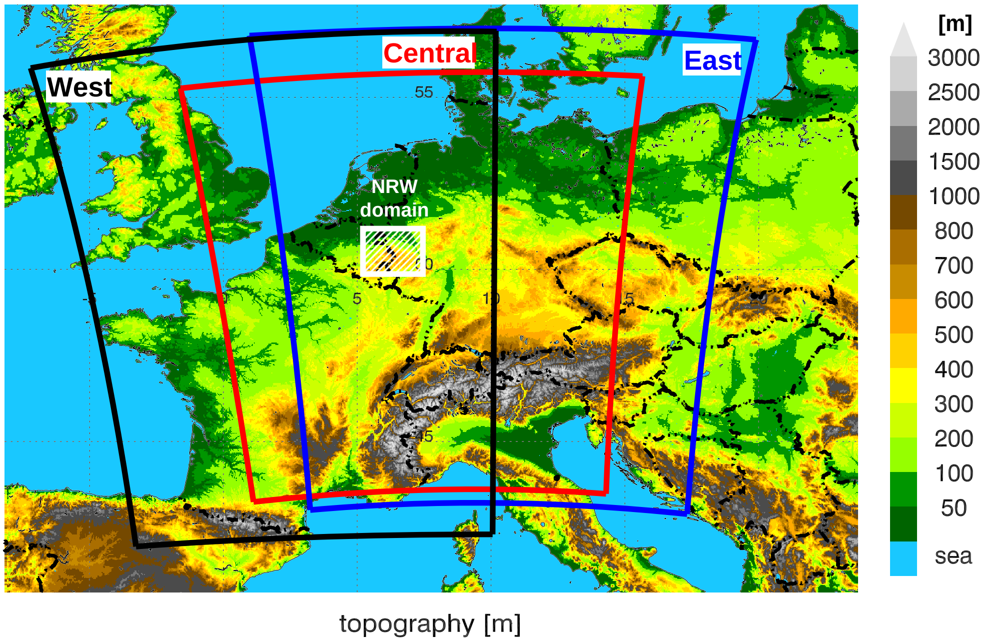

Figure 3.3.: Model nesting domains of TerrSysMP-CO_2 depending on the predominant direction of the atmospheric flow. The grid size of the nesting domains is 0.025° occupying 400×600 ("West"), 400×500 ("Central") and 425×560 ("East") grid points (lat/lon). The rotated north poles are the same as in the NRW domain.

outside the domain (e. g. Ruhr area, the Netherlands, Paris) are already included in the initial CO_2 distribution of the NRW domain. Moreover, the influence of land surface heterogeneity (e. g. orography, vegetation) and the effects of the atmospheric state (e. g. PBL height, mesoscale flow patterns) contribute to the initial 3D-field of CO_2. As for the meteorological fields, the CO_2 mixing ratios are linearly interpolated to the grid of the NRW domain. Within the NRW

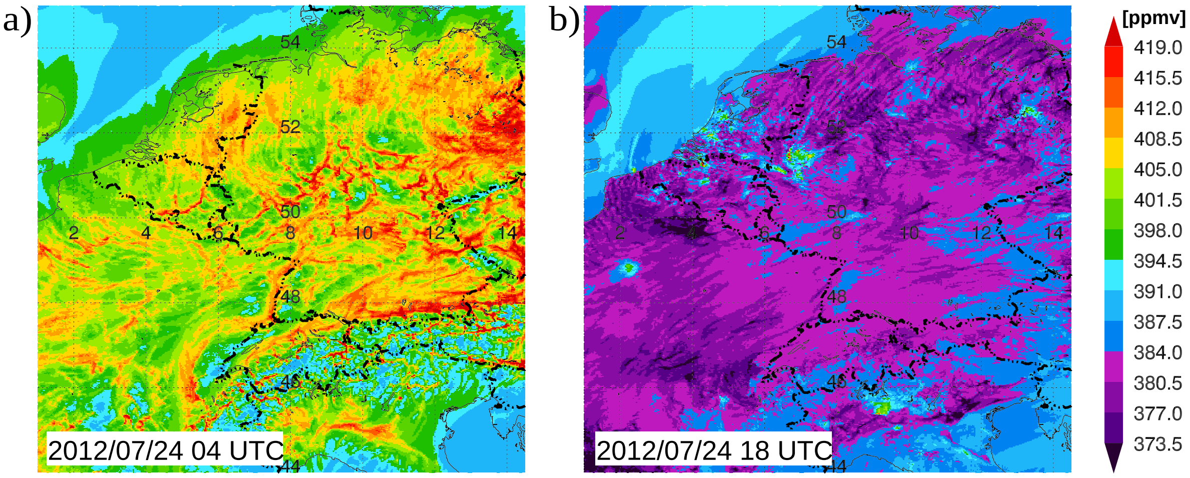

Figure 3.4.: Regional scale heterogeneity of the near surface CO_2 mixing ratio [ppmv], simulated with TerrSysMP-CO_2 (domain "Central") on 24 July 2012, a) 4 UTC and b) 18 UTC.

domain a relaxation zone of 15 km is applied in which the variables of the high-resolution model are gradually modified to blend them with the driving model variables. The nesting runs as well as the NRW simulations are always started at 18 UTC because at this time of the day the assumption of a horizontally and vertically homogeneous CO_2 distribution fits best the real atmospheric CO_2 field as a result of a deep and well-mixed PBL (Tolk *et al.*, 2009). After the initialization the nesting run provides hourly LBCs for the NRW domain.

The nesting strategy of the simulation of several consecutive days analyzed in Chap. 7 is slightly different. At the first day of the simulation, the same procedure as for the single case studies is performed. For the following days, the nesting runs are initialized with the 3D-field of CO_2 of the previous nesting simulation (see Section 7.3.1 for more details). The nesting runs are restarted every 24 hours to ensure that the *predicted* initial CO_2 field does not deviate too strong from the meteorological fields of COSMO-EU *analyses* used as ICs and LBCs of the new nesting run. Otherwise the initial CO_2 patterns of the previous run may not sufficiently correspond to the dynamical flow patterns of the COSMO-EU analyses leading to inconsistencies in the initialization of CO_2. This strategy allows a more accurate analysis of the CO_2 budget of TerrSysMP-CO_2 than forcing each nesting run to a constant initial CO_2 content. In other words, the net CO_2 source or sink of the entire NRW domain being the sum of all biogenic and anthropogenic CO_2 fluxes can be studied more precisely and possible inconsistencies in the interaction of the fluxes can be identified.

3.3. CLM spin-up for initial soil moisture and soil temperature

A realistic representation of soil water dynamics and heat transfer in the soil as well as the simulation of soil respiration and energy fluxes with CLM require a realistic initialization of the model state variables, in particular consistent vertical soil moisture and temperature profiles. In order to realize these profiles, a multi-year spin-up run of CLM, stand-alone with an appropriate atmospheric forcing, is necessary. In this study, CLM3.5 has been driven by hourly COSMO-DE model analyses. Starting with the default vertical soil temperature and soil moisture profiles of CLM3.5, the model has been run with a time step of one hour (the same as the atmospheric driving frequency) using the COSMO-DE analyses of 2012. This one-year simulation has been re-initialized 7 times until a dynamic equilibrium condition was reached. Of course, the CLM input parameters (e. g. LAI, soil map, PFT distribution) are the same as in the fully coupled TerrSysMP-CO_2 simulations. CLM restart files were produced in a daily interval (at 18 UTC) containing all fields needed for the initialization of CLM3.5. In addition to the soil temperature and moisture profiles, these restart files include amongst others canopy temperature and canopy interception water storage needed for the calculation of transpiration and photosynthesis. To obtain initial soil moisture and soil temperature profiles for the TerrSysMP-CO_2 simulations in 2014, CLM3.5 again has been run stand-alone, one-time initialized with the CLM fields at the end of 2012 using COSMO-DE analyses of 2013, continued by a further one-year simulation using COSMO-DE analyses of 2014. Whereas in the spin-up of the year 2012 the default plant physiological parameters of CLM have been used to represent PFT=15 (crops), in the spin-up runs of the years 2013 and 2014 the plant physiological parameters have been changed to the "winter wheat" parameters of Sulis *et al.* (2015). This change is necessary because, other than in the case studies of 2012, in the model simulations of 2014 these new plant physiological parameters have been used.

4. Spatio-temporal variability of CO_2 in the atmosphere and CO_2 fluxes

In this chapter, the spatio-temporal variability of CO_2 is analyzed for case studies with different weather situations in the summer seasons 2012/2013. Mesoscale simulations with TerrSysMP-CO_2 (COSMO–CLM) have been performed to investigate both the CO_2 patterns in the lower atmosphere and CO_2 and energy fluxes depending on different environmental conditions. The connection of atmospheric CO_2 patterns with atmospheric conditions and the resulting surface CO_2 fluxes as well as with mesoscale circulations induced by orographic effects is demonstrated.

4.1. Clear sky conditions

For the investigation of the general model behavior with respect to the biosphere–atmosphere exchange of heat, water and CO_2 as well as for the verification with measurements, days with cloudless conditions (i. e. "clear sky days") are most appropriate. This ensures a direct comparison of the simulated partitioning of latent and sensible heat fluxes and CO_2 uptake by different plant species with observations. On cloudy days the different cloud distribution of the simulation and in reality would complicate the verification. Hence, CO_2 fluxes and the resulting spatio-temporal variability of CO_2 are analyzed for three clear sky case studies:

- **CS2605**: initialization: 2012/05/25 18 UTC, 30 h simulation (background CO_2: 396 ppmv[1])
- **CS2407**: initialization: 2012/07/23 18 UTC, 30 h simulation (background CO_2: 388 ppmv)
- **CS1808**: initialization: 2012/08/17 18 UTC, 48 h simulation (background CO_2: 390 ppmv)

4.1.1. Meteorological situation of model case studies

The synoptic situation of 26 May 2012 (CS2605) is characterized by a high pressure system over the North Sea and southern Scandinavia leading to an easterly flow over Central Europe. In the night the temperatures drop to 7–10 °C in the Eifel and in the Mosel valley and to 10–12 °C in the Kölner Bucht and parts of Belgium[2]. At daytime, the temperatures increase to 19–21 °C in the Eifel and 23–25 °C in the Rhine valley and in the northern part of the NRW-domain. The day is completely cloudless both in the simulation and in reality. During night and in the early morning a light to gentle breeze (1–3 Beaufort, Bft) blows. In the narrow valleys of the Eifel and the Siebengebirge it is almost calm. Later in the morning in the flat terrain the easterly wind increases to a moderate to fresh breeze of 5–9 $\mathrm{m\,s^{-1}}$ (4–5 Bft, see Fig. 4.1c). The most striking feature of this day is the development of the atmospheric humidity in the PBL. In the morning, the 2 m dew point temperatures (T_{dew}) range from 4–7 °C in the Eifel and the Bergisches Land whereas west of the Rhine 8–11 °C are simulated (Fig. 4.1a). However, between 11 and 14 UTC several stripes with very low T_{dew} (0–4 °C) are calculated (cf. red areas in Fig. 4.1b, c) correlated

---

[1] CO_2 mixing ratio used for the initialization of the parent model domain

[2] Additional figures showing the weather situation of CS2605, CS2407 and CS1808 can be found in the appendix.

with rather high wind speeds. Minimum values of T_{dew} are reached around 14 UTC. In the ambient regions, a T_{dew} of 6–11 °C is simulated. These patterns are consistent with dew point temperatures at synoptic stations of DWD strongly fluctuating between 3 and 11 °C on this day. Hence, with this case study the response of different vegetated canopies on very dry atmospheric conditions can be analyzed.

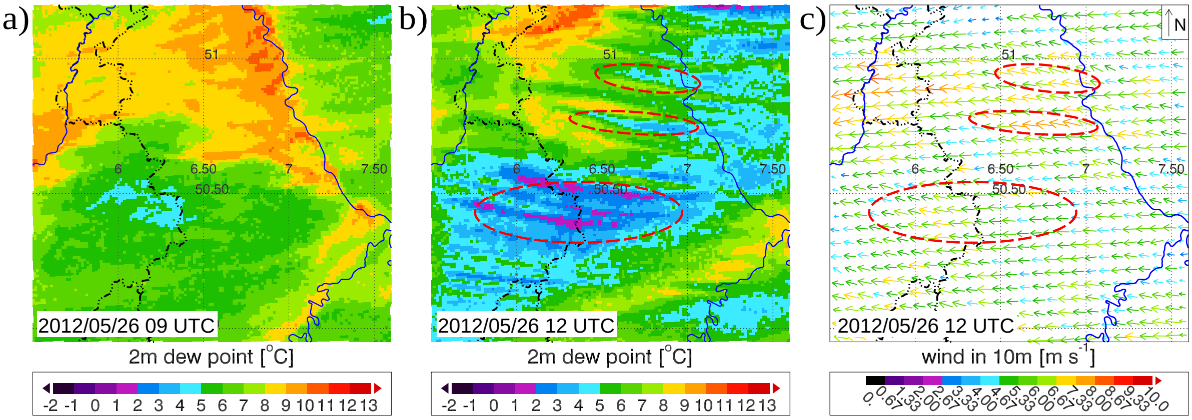

Figure 4.1.: 2 m dew point temperature [°C] on 2012/05/26 a) at 09 UTC and b) at 12 UTC and c) wind vectors [m s^{-1}] 10 m a.g.l. at 12 UTC, all simulated with TerrSysMP-CO_2 (CS2605).

On 24 July 2012 (CS2407), a high pressure system is located over Eastern Europe with weak pressure gradients over Central Europe. During night the temperatures drop to 9–12 °C at higher altitudes of the Eifel and to 12–15 °C in the other regions. Except for the mountain ridges of the Eifel and the Hunsrück, only a light to gentle breeze blows from E–SE. In narrow valleys, e. g. the valleys of the small rivers Rur and Erft (region R in Fig. 4.2a), Ahr (A) and Wied (W) as well as in some areas in the Mosel valley (M) almost calm conditions are simulated leading to a very stable stratification with cold near surface temperatures. In the early morning (5–7 UTC) the wind further decreases to 1–3 m s^{-1} (1–2 Bft) with calm regions in the Rhine valley and along the river Maas in NL and BE. At daytime, the temperatures increase to 21–23 °C at the mountain ridges in the Eifel and 26–28 °C along the Mosel and the Rhine and in valleys east of the Rhine. With the evolution of the convective boundary layer (CBL) the wind slightly increases and turns to more northern directions. At noon, the 2 m dew point temperatures range from 9–12 °C in the Eifel and the Bergisches Land to 11–16 °C in the flat terrain of the model domain (Fig. 4.2b). In the morning, T_{dew} is about 3–4 °C and in the afternoon on average 6–8 °C higher than in CS2605. Thus, the environmental conditions for the plants are better resulting in higher plant productivity. Except for a band with thin cirrus ranging from SW to NE (reduction in solar radiation of about 10%) this day is cloudless.

On 18 and 19 August 2012 (CS1808), the western part of Germany is located east of a long-wave trough over the North Atlantic. A southwesterly flow advects very hot air masses towards NRW. On 18 August the simulated maximum temperatures range from 26–29 °C in the Eifel to 29–32 °C in the northwestern part of the NRW-domain. On 19 August even higher temperatures of 27–29 °C in the Eifel and 31–33 °C in the flat terrain and in the Mosel valley are simulated. Unfortunately, on both days the afternoon temperatures are strongly underestimated compared to measured temperatures of 31–38 °C in that region. At daytime, similar wind speeds as in CS2407 occur (3–4 Bft) blowing from SE in the flat terrain and from S (SSW) over the Eifel on 18 (19) August. Channel effects can be seen in the Rhine valley on 18 August. The most

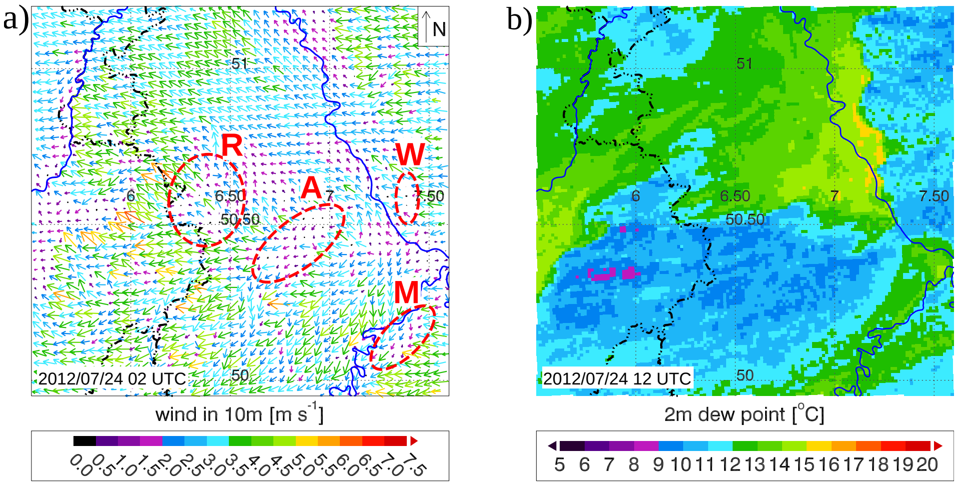

Figure 4.2.: a) Wind vectors [m s^{-1}] 10 m a.g.l. on 2012/07/24 02 UTC and b) 2 m dew point temperature [°C] at 12 UTC, simulated with TerrSysMP-CO_2 (CS2407).

striking feature of these days are the warm nighttime temperatures. Especially on 19 August, both in reality and in the simulations, the temperatures do not sink below 16–21 °C (Fig. 4.3a). North of the Eifel and the Hohes Venn very high minimum temperatures of 22–25 °C are simulated which are caused by the thermodynamically induced local wind system "Eifelföhn" (red areas in Figs. 4.3a, b). The same effect is observed on 18 August. On both days the dew point temperatures range from 13–17 °C in the Eifel to 17–21 °C in the flat terrain (Fig. 4.3c). The 18 August is a perfect clear sky day and on 19 August only in the northwestern part of the domain some clouds form in the afternoon.

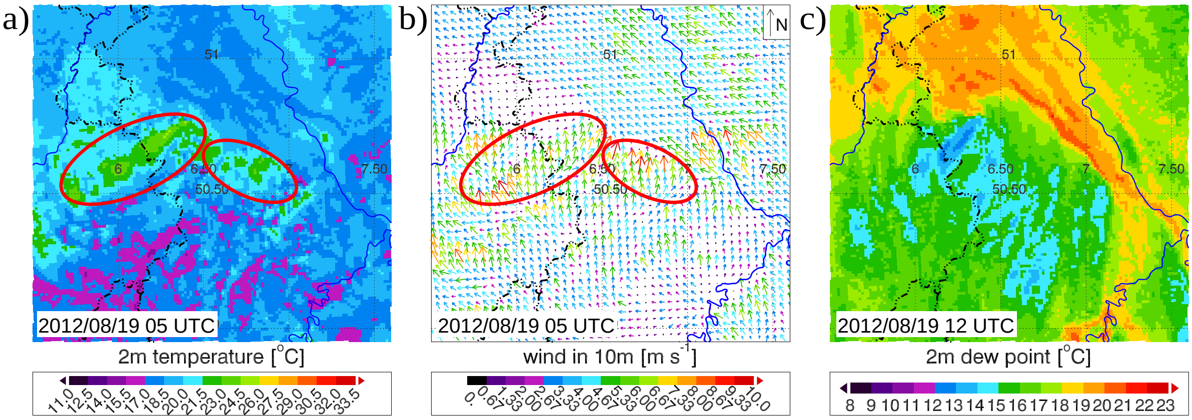

Figure 4.3.: a) 2 m temperature [°C] and b) wind vectors [m s^{-1}] 10 m a.g.l., both at 05 UTC and c) 2 m dew point temperature [°C] at 12 UTC, all simulated with TerrSysMP-CO_2 (CS1808).

In general, TerrSysMP-CO_2 captures the atmospheric conditions fairly well. Compared to observations, the nighttime temperatures as well as the spatial and diurnal variability in the PBL humidity and the wind evolution are well predicted. The high grid resolution allows the simulation of local wind systems (e. g. Eifelföhn or the calm conditions and stable stratifications in narrow valleys at night). In the evening the observed increase of the near surface atmospheric humidity caused by canopy transpiration combined with a beginning stabilization is slightly overestimated by TerrSysMP-CO_2. Solely the afternoon temperatures are underestimated on clear sky days, especially for CS1808 when temperatures greatly exceed 30 °C.

4.1.2. Canopy fluxes: photosynthesis, NEE and transpiration

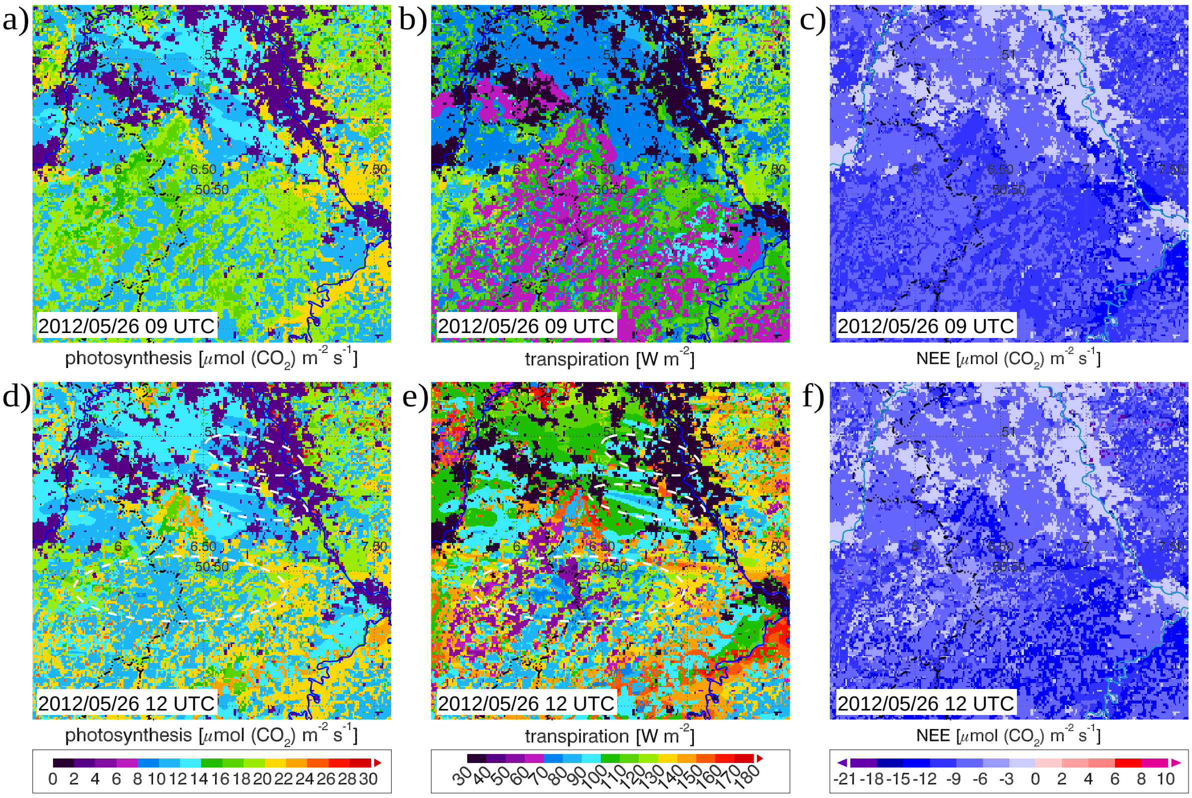

Figure 4.4.: Simulated canopy fluxes of CS2605: photosynthesis [μmol(CO_2)$m^{-2}s^{-1}$], transpiration [W m^{-2}] and NEE [μmol(CO_2)$m^{-2}s^{-1}$] at 09 UTC (a–c) and 12 UTC (d–f).

The atmospheric CO_2 mixing ratio in the CBL and the development of the CBL itself strongly depend on the canopy fluxes of CO_2, water and energy (e. g. Dolman *et al.*, 2006; Sarrat *et al.*, 2007a; Tolk *et al.*, 2009). Thus, in this section, the spatio-temporal variability of these fluxes is analyzed. Fig. 4.4a, b depict the photosynthesis and transpiration rate at canopy level of CS2605 at 9 UTC[3]. The strongest CO_2 assimilation is simulated for broadleaf (18–21 μmol(CO_2)$m^{-2}s^{-1}$) and needleleaf forests (15–18 μmol(CO_2)$m^{-2}s^{-1}$) whereas the corresponding rates for grassland and crops are lower (10–14 μmol(CO_2)$m^{-2}s^{-1}$). For crops these low photosynthesis rates are surprising because several studies in European regions (e. g. Sarrat *et al.*, 2007a; Sarrat *et al.*, 2009; Ahmadov *et al.*, 2007; Tolk *et al.*, 2009) as well as flux measurements in the NRW domain (Chap. 5) indicate very high assimilation rates of winter crops and vegetables. Hence, the plant physiological parameters of the crop PFT have to be adapted (see Section 6.5). Transpiration is low for crops and needleleaf forests (60–80 W m^{-2}) and higher for broadleaf forests (100–130 W m^{-2}).

---

[3] The default output of most CLM variables is the mean value averaged over the output time step. The CLM variables shown in this work represent a 30-min mean with the output time denoted in the figure descriptions.

Between 9 and 12 UTC the photosynthesis rates of crops and broadleaf forests slightly increase whereas in the central Eifel region (see lowest white oval in Fig. 4.4d) in needleleaf forests a reduction to 10–12 μmol(CO_2)$m^{-2}s^{-1}$ can be seen. Similarly, transpiration increases for all PFTs except for needleleaf forest where a reduction to only 40–80 W m^{-2} is simulated. In general, both photosynthesis and transpiration are rather low on this day resulting in high sensible heat fluxes (see e. g. Chap. 5). The reason for this is a partly closure of leaf stomata as a response to low atmospheric humidity. Already at 9 UTC, especially the stomatal resistance of shaded leaves (r_{st}^{sha}, Fig. 4.5a) is strongly correlated with the humidity distribution near the surface (cf. Fig. 4.1a) but also for sunlit leaves (r_{st}^{sun}, Fig. 4.5b) distinctly increased values ($\approx$500–900 s m^{-1}) are simulated ($r_{st} \approx 150$ s m^{-1} for optimal conditions). Consistent with a decrease of atmospheric humidity between 9 and 14 UTC (in combination with a temperature increase), r_{st}^{sha} and r_{st}^{sun} further increase (Fig. 4.5c, d). At noon, especially over crops and broadleaf forests the moisture dependency can be identified showing stripes with slightly increased r_{st} in regions with very dry atmospheric conditions (cf. marked areas of Figs. 4.1b and 4.5c, d). The reductions of photosynthesis and transpiration of needleleaf forests are caused by high stomatal resistances of 1800–2100 s m^{-1}. Hence, needleleaf trees are most sensitive to low atmospheric humidity, also found in Sarrat *et al.* (2009). A possible reason for that could be a low leaf boundary layer resistance (r_b). The dry regions are correlated with enhanced near surface winds. As mentioned in Section 2.3.1, r_b is directly proportional to the reciprocal of the wind speed and to the leaf diameter being lowest for the thin needles of this forest type. As response to the low r_b, needleleaf trees need the strongest stomatal closure (i. e. high r_{st}) under low atmospheric humidity to avoid desiccation. The combined r_{st}^{sha} and r_{st}^{sun} control photosynthesis and transpiration with a shaded fraction of $\approx$40% for crops, $\approx$50% for grassland and needleleaf forest and $\approx$65% for broadleaf forest at noon.

Finally, Figs. 4.4c, f depict the net ecosystem exchange[4] (NEE) of CS2605 at 9 and 12 UTC, i. e. the biogenic CO_2 sink/source resulting from CO_2 assimilation/respiration. At both times, the canopy is a moderate CO_2 sink. The net CO_2 uptake is 6–8 μmol(CO_2)$m^{-2}s^{-1}$ for crops and enhances from 10–12 μmol(CO_2)$m^{-2}s^{-1}$ to 11–14 μmol(CO_2)$m^{-2}s^{-1}$ for broadleaf forests between 9 and 12 UTC. For needleleaf forests a reduction to only 3–6 μmol(CO_2)$m^{-2}s^{-1}$ occurs. In the afternoon, the net CO_2 decreases for all PFTs caused by decreasing photosynthesis and increasing soil respiration (not shown).

Fig. 4.6 depicts the simulated canopy fluxes on 24 July 2012 (CS2407). Both photosynthesis and transpiration of needleleaf and broadleaf forests are considerably higher than in CS2605 although the temperatures are only slightly higher. At 9 UTC, the photosynthesis rates of broadleaf forests range from 20–23 μmol(CO_2)$m^{-2}s^{-1}$ in the southern part of the domain to 26 μmol(CO_2)$m^{-2}s^{-1}$ east of Cologne (Fig. 4.6a). A further increase to 24–28 μmol(CO_2)$m^{-2}s^{-1}$ between 9 and 12 UTC can be seen in a broad zone ranging from SW to NE of the NRW domain (Fig. 4.6c) with the maximum north of the Eifel where the surface dew point temperatures are highest (cf. Fig. 4.2b). Needleleaf forests also show a stronger CO_2 assimilation with about twice as high rates in the central Eifel region than in CS2605 at 12 UTC. However, comparable rates are simulated for crops because the better atmospheric conditions are compensated by a lower LAI (cereal crop fields are already harvested).

Similarly, canopy transpiration is stronger than in CS2605 increasing from 110–170 W m^{-2} to 190–260 W m^{-2} in broadleaf forest between 9 and 12 UTC (Fig. 4.6b, d). Distinctly higher

---

[4] NEE is negative for net CO_2 uptake and positive for net CO_2 release. For the single components (photosynthesis, leaf and soil respiration) absolute values are presented in this work.

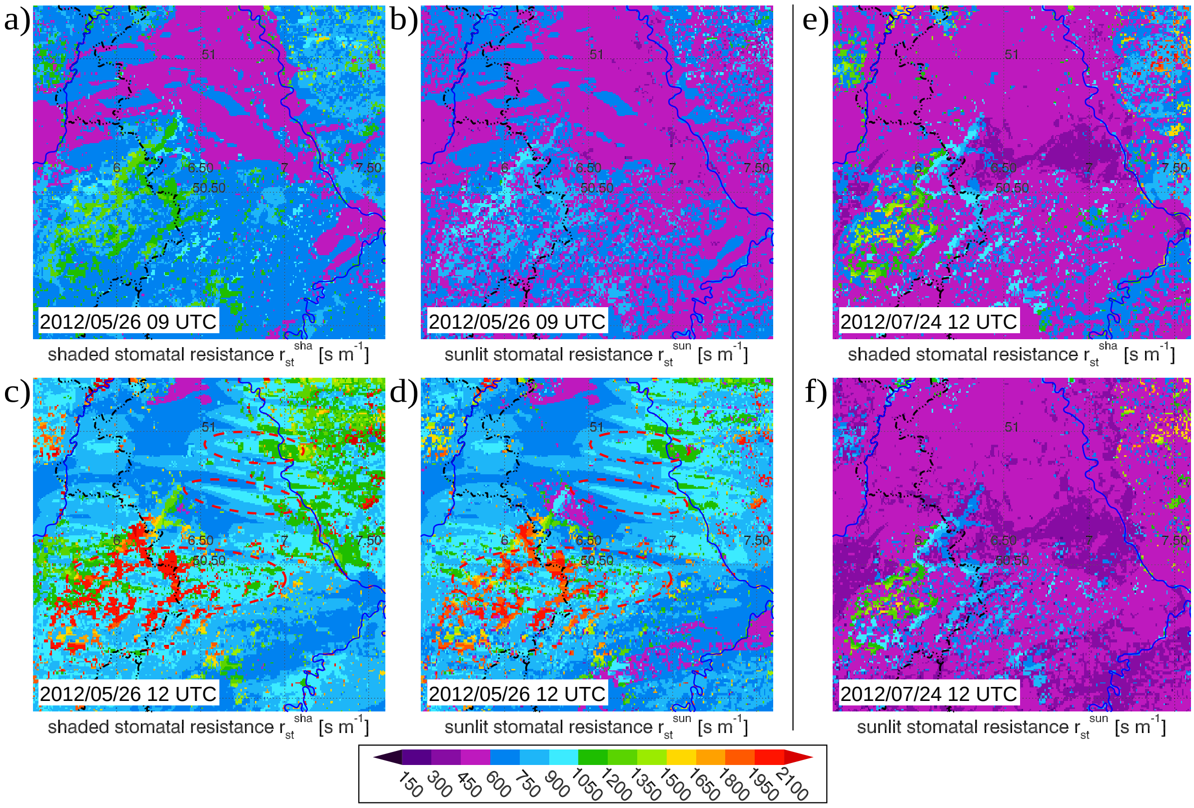

Figure 4.5.: Simulated stomatal resistances (shaded, sunlit) [s m^{-1}] of CS2605 at 09 UTC (a, b) and 12 UTC (c, d) and of CS2407 at 12 UTC (e, f), respectively.

transpiration rates than in CS2605 are simulated for needleleaf forests but comparable rates for crops. The differences between CS2605 and CS2407 again can be explained with the corresponding r_{st}. At 12 UTC, both r_{st}^{sha} and r_{st}^{sun} are about half as high than in CS2605 (cf. Fig. 4.5c, d with 4.5e, f), i. e. in CS2407 the atmospheric conditions are more favorable with respect to stomatal opening. Again, needleleaf forests occupy the highest r_{st} with maxima of 1300–1600 s m^{-1} in the driest region of Belgium, but in the central Eifel the corresponding values are distinctly lower than in CS2605 ($\approx$600–1000 s m^{-1}).

Fig. 4.6e, f depict the diurnal variability of leaf respiration (R_{leaf}^{can}, cf. Eq. 2.28). R_{leaf}^{can} is lowest in the early morning and highest in the afternoon, correlated with the temperature minimum and maximum at 4 UTC and 14 UTC, respectively. Contrary to photosynthesis, R_{leaf}^{can} is highest for needleleaf forests (1.7–2.2 μmol(CO_2)m^{-2}s^{-1} at 14 UTC). For broadleaf forests lower R_{leaf}^{can} are simulated (1.2–1.8 μmol(CO_2)m^{-2}s^{-1}) and for crops the rates are too low because of the inappropriate plant physiological parameters. In general, in most regions R_{leaf}^{can} compensates less than 10% of assimilated CO_2.

The diurnal variability of NEE is shown in Fig. 4.7. At night, the canopy is a source of atmospheric CO_2. The fluxes at 0 UTC (Fig. 4.7a) are stronger for forests than for crops and grassland because, additionally to autotrophic and heterotrophic respiration, the decomposition of aboveground litter and within the forest floor (O horizon) contributes to the CO_2 flux. The highest respiration rates are simulated for broadleaf forests with up to 9.5 μmol(CO_2)m^{-2}s^{-1} in the Bergisches Land and along the Hohes Venn. The respiration rates of needleleaf forests are

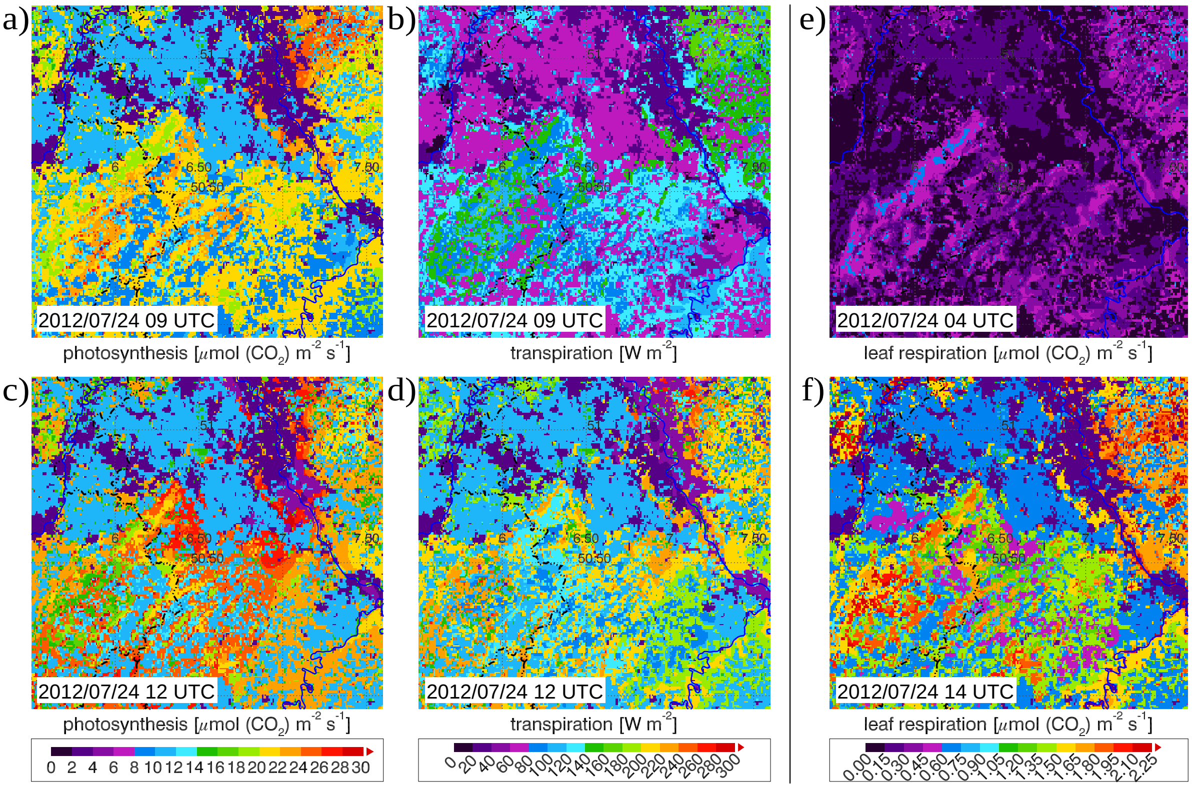

Figure 4.6.: Simulated canopy fluxes of CS2407: photosynthesis [μmol(CO_2)$m^{-2}s^{-1}$] and transpiration [W m^{-2}] at 09 UTC (a, b) and 12 UTC (c, d) and leaf respiration [μmol(CO_2)$m^{-2}s^{-1}$] at 04 UTC and 14 UTC (e, f).

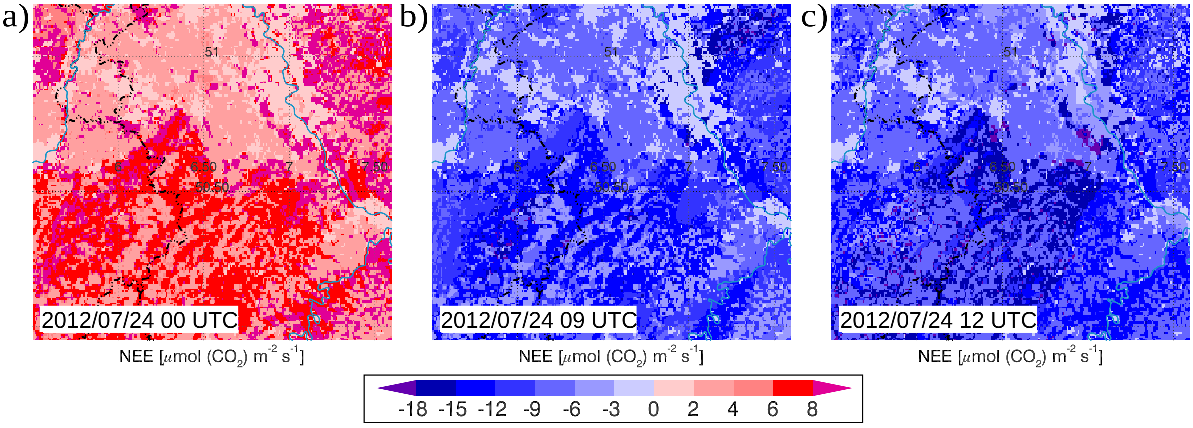

Figure 4.7.: Simulated NEE [μmol(CO_2)$m^{-2}s^{-1}$] of CS2407 at a) 00 UTC, b) 09 UTC and c) 12 UTC.

slightly lower (7–8 μmol(CO_2)$m^{-2}s^{-1}$), grassland and crops respire about 5 μmol(CO_2)$m^{-2}s^{-1}$ and 4 μmol(CO_2)$m^{-2}s^{-1}$, respectively. In the following hours total respiration slightly decreases due to decreasing atmospheric and soil temperatures which influence all respiration components. With increasing photosynthesis in the early morning, at about 6 UTC the canopy becomes a net sink of atmospheric CO_2 (not shown). Between 6 and 9 UTC, the net CO_2

uptake strongly increases and ranges from 5–8 μmol(CO_2)$m^{-2}s^{-1}$ for crops and grassland to 11–15 μmol(CO_2)$m^{-2}s^{-1}$ in forests (Fig. 4.7b). At noon, in most regions the net CO_2 uptake reaches its maximum with 13–19 μmol(CO_2)$m^{-2}s^{-1}$ in broadleaf forests. The highest uptake occur in regions where photosynthesis is strongest (Fig. 4.7b). However, especially in the eastern part of Belgium the net CO_2 uptake of needleleaf forests and in the Bergisches Land also the net CO_2 uptake of broadleaf forests decreases, both caused by moisture limitation of photosynthesis. Compared with the daytime NEE of CS2605 (cf. Fig. 4.4c, f), the net CO_2 uptake of CS2407 is considerably more effective due to higher photosynthesis rates.

The study of canopy fluxes of CS1808 gives no new insights into the relationship between the PBL conditions and the surface fluxes and is, thus, not further described in this section.

4.1.3. Spatio-temporal variability of atmospheric CO_2 mixing ratios

With the knowledge of the canopy fluxes the spatial patterns of CO_2 in the PBL as well as its diurnal variation can be analyzed. Several modeling studies have shown that both spatial heterogeneities of surface fluxes (NEE, LH, SH) and synoptic and mesoscale transport generate significant spatial heterogeneities of atmospheric CO_2 mixing ratios (e. g. Nicholls *et al.*, 2004; Ahmadov *et al.*, 2007; Sarrat *et al.*, 2007a, and others). One of the main objectives of the present study is to analyze which of these are the most important controlling processes in a terrestrial region characterized by very diverse land cover, complex orography (cf. Figs. 3.1 and 3.2a) and densely populated areas. Sarrat *et al.* (2009) and Pillai *et al.* (2011) found that a fine grid resolution of the atmospheric model is necessary to resolve mesoscale circulation systems (e. g. land-see breeze, mountain-valley breeze). The fine grid resolution as well as the physically based and plant physiologically consistent parameterizations of TerrSysMP-CO_2 calculating biogenic CO_2 fluxes offer new insights in spatio-temporal patterns of atmospheric CO_2. So far, no modeling study of atmospheric CO_2 heterogeneity has been performed using a comparable grid resolution for a region with similar diversity in land use and orography as in this work.

The spatio-temporal variations of CO_2 mixing ratios near the surface on 24 July 2015 (CS2407) is depicted in Fig. 4.8. During nighttime, mainly due to respiration ($R_{soil} + R_{leaf}$), a continuous increase of atmospheric CO_2 is simulated near the surface. In the early morning (4 UTC), the CO_2 concentrations are distributed very heterogeneously (Fig. 4.8a). In the flat terrain of Kölner Bucht and Jülicher Börde relatively homogeneous distributed mixing ratios of 410–420 ppmv are simulated. Distinctly more heterogeneity of the near surface CO_2 distribution can be seen in regions with complex terrain. On the mountain ridges of the Eifel (e. g. Hohes Venn, Hohe Eifel, central Eifel region) the CO_2 concentrations increase only slightly up to 390–405 ppmv (background CO_2: 388 ppmv) although these areas are mainly covered by forests with intense respiration. In contrast, in narrow valleys (e. g. Ahr, Mosel, Wied, Rur) a strong accumulation of CO_2 up to mixing ratios of 425–440 ppmv can be observed. A similar CO_2 accumulation can be found in valleys west of the Rhine (e. g. Sieg, Agger). The maxima of CO_2 mixing ratios in the narrow valleys are highly correlated with almost calm conditions (cf. Fig. 4.2a). A very stable stratified airmass develops (strong radiative cooling) which is decoupled from the synoptic flow. In nights with weak synoptic pressure gradients, a buoyancy-driven downslope flow along mountain slopes (i. e. valley breeze) can further increase the CO_2 mixing ratios in the valleys (Pillai *et al.*, 2011). The most important transport processes explaining the CO_2 patterns in complex terrain are discussed in the next section.

Fig. 4.9 depicts a representative vertical cross section (dashed line in Fig. 4.8a) reaching from [50.0 °N, 7.5 °E] to [51.2 °N, 5.9 °E]. The high atmospheric CO_2 mixing ratios in the northern

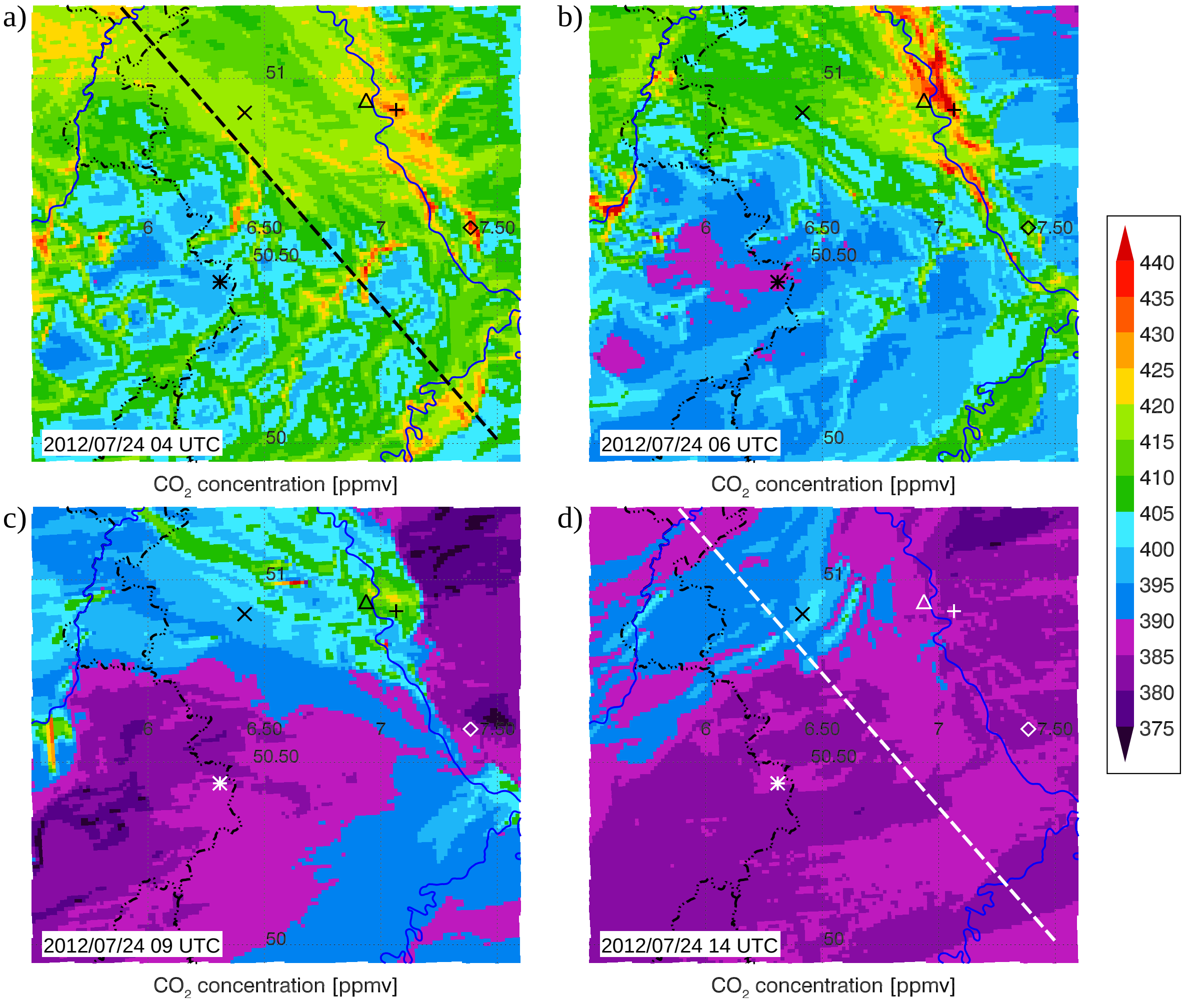

Figure 4.8.: Simulated CO_2 mixing ratios [ppmv] of CS2407 in the lowermost COSMO level ($\approx 10\,m$) at a) 04 UTC, b) 06 UTC, c) 09 UTC and d) 14 UTC. The marked locations are Jülich (×), Wied valley (◊), Central Eifel (✱), downtown of Cologne (△) and Köln-Gremberghoven (+). The cross sections shown in Fig. 4.9 are indicated as dashed lines.

flat terrain as well as along the southern mountain slope towards the Mosel valley (50.1–50.2 °N) and in the Ahr valley (50.45 °N) can be clearly identified. This CO_2 accumulation is restricted to the lowermost 200–300 m a.g.l. Depressed vertical turbulence in the shallow stable stratified nocturnal boundary layer, which develops in cloudless nights with low winds, causes a strong vertical CO_2 gradient and a strong near surface accumulation. Additionally, a deep residual layer with low CO_2 concentrations below 1000 m a.g.l. can be seen resulting from photosynthesis on the previous day occurring in the initial CO_2 field which has been simulated with the larger parent domain. In CS2605, a similar near surface CO_2 accumulation is simulated with a slightly deeper vertical extent (not shown).

With the onset of photosynthesis just after sunrise (≈ 4 UTC), in rural areas the CO_2 concentrations rapidly decrease although the net CO_2 uptake is rather low in the early morning. The transition from the shallow nocturnal PBL to a convective PBL occurs later in the morning than the change from a positive to a negative NEE explaining the strong CO_2 decrease. At the

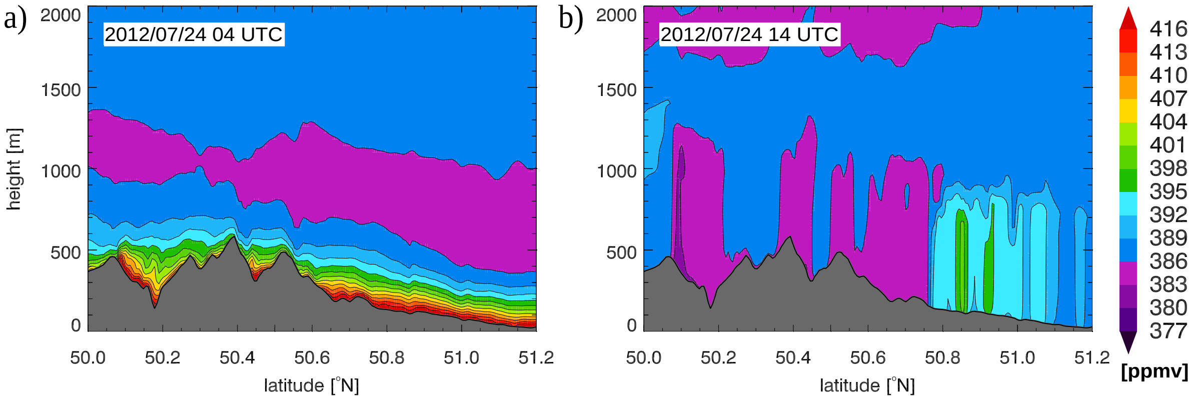

Figure 4.9.: Vertical cross sections of CO_2 mixing ratios [ppmv] of CS2407 (dashed lines in Fig. 4.8) at a) 04 UTC and b) 14 UTC.

same time, road traffic rapidly increases (morning rush hour at 6–7 UTC on Tuesday) causing a strong increase of CO_2 mixing ratios in and downstream of urban areas (Fig. 4.8b). Due to the contrasting behavior of rural and urban areas, at 6 UTC the greatest heterogeneity is simulated with less than 390 ppmv in eastern Belgium and more than 440 ppmv along the Rhine valley and in Liège. The local effects of fossil fuel emissions in cities have been indicated also, e. g., in Pérez-Landa *et al.* (2007) but with a very simplified representation of anthropogenic emissions in their study. In CS2605 (Saturday) the effect of anthropogenic emissions of each Rhine metropolis (Bonn, Cologne, Dusseldorf) is even more pronounced caused by calm conditions in the Rhine valley on this day (Fig. 4.10a). Due to stronger winds, in CS1808 the urban effect is less evident.

Between 7 and 12 UTC, in rural areas the reduction of CO_2 contents in the PBL continues reaching 370–385 ppmv (i. e. distinctly below the background CO_2 concentration) east of the Rhine and in Belgium (Fig. 4.8c). In the flat terrain as well as in urban areas the atmospheric CO_2 also decrease but the mixing ratios are still higher than in the mountainous regions ($\approx$ 395–410 ppmv). This is the result of anthropogenic emissions and lower simulated CO_2 assimilation rates of crops being dominant in that region (cf. Fig. 4.6). The sharp gradient west of Cologne is caused by a strong convergent wind field. In other regions, the horizontal CO_2 gradients begin to diminish with the development of a well-mixed CBL.

Compared with the CO_2 patterns at night and in the morning, at 14 UTC (Fig. 4.8d) the CO_2 mixing ratios are less heterogeneous (380–390 ppmv in most regions). Higher mixing ratios (390–400 ppmv) are simulated in the Jülicher Börde and southern part of the Netherlands partly caused by the inflow of higher concentrations at the lateral boundaries due to an intensified wind turning from E to NNE in that region. The trails of even higher CO_2 concentrations come from enormous CO_2 emissions of coal-fired power plants in Germany and along the Maas (in NL) being advected to the SW and vertically mixed within the CBL. At night, the emissions from chimneys are above the nocturnal PBL and, thus, do not effect the near surface CO_2 content. Fig. 4.9b depicts the same vertical cross section as described above. Contrary to the early morning, at 14 UTC NEE and fossil fuel emissions influence the entire CBL. The strong vertical CO_2 gradient at about 700–900 m a.g.l. indicates the CBL top. Below, vertically almost constant concentrations occur and above the CBL top the background CO_2 content remains. In the Eifel region, a loss of CO_2 is simulated due to the strong negative NEE of forests whereas in the northern flat terrain a net gain occurs as a combination of less negative NEE of crops, anthropogenic emissions and the inflow at the northern lateral model boundary. Although no flight measurements of CO_2 mixing ratios are available on this day, the results seem to be realistic when comparing with similar horizontal heterogeneities and vertical gradients observed at a comprehensive flight campaign performed for the CERES project in southwestern France in 2005 (see e. g. Dolman *et al.*, 2006; Ahmadov *et al.*, 2007; Sarrat *et al.*, 2007a).

Finally, between 17 and 19 UTC in combination with a strong increase of humidity (Section 4.1.1) in several regions the near surface CO_2 mixing ratio drops to 370–380 ppmv (Fig. 4.10b). At synoptic stations, the 2 m dew point temperatures increase but less clearly than in the simulation. A similar drop of near surface CO_2 is measured on the Jülich tower in some evenings during the summer season of 2014. However, this CO_2 decrease and humidity increase seem to be overestimated by TerrSysMP-CO_2. In the simulations of Nicholls *et al.* (2004) the same effect occurred. They explained this by an overestimation of photosynthesis and transpiration in the late afternoon when the near surface atmosphere has already started to stabilize.

In general, the spatio-temporal variability of CO_2 concentrations in the PBL is similar in CS2605 and CS1808[5]. In CS2605, additionally to the CO_2 accumulation in small valleys during nighttime, CO_2 accumulates north of the Eifel (luv) due to stronger advective transport (easterly winds) than in CS2407. In the afternoon, higher wind speeds as well as a deeper CBL lead to less heterogeneity. In CS1808, at night the CO_2 increase is even more pronounced than in CS2407 with mixing ratios locally exceeding 460 ppmv in the Mosel valley (Fig. 4.10c) because respiration is more intense in these nights due to very warm nighttime temperatures.

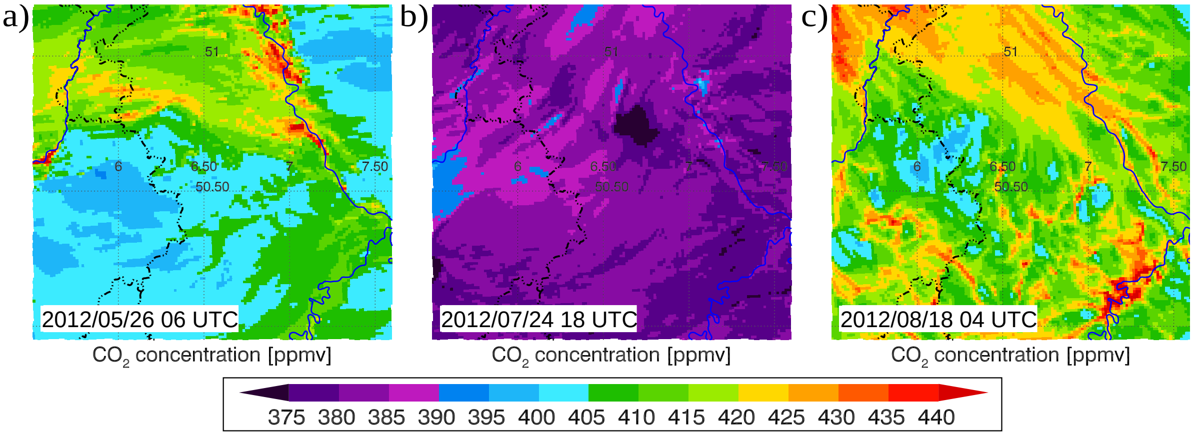

Figure 4.10.: Maps of CO_2 mixing ratios (lowermost COSMO level) [ppmv]: a) 2012/05/26, 06 UTC (CS2605), b) 2012/07/24, 18 UTC (CS2407), c) 2012/08/18, 04 UTC (CS1808).

The vertical distribution of CO_2 is analyzed with CS2605 at selected locations in the NRW domain. Similar to CS2407, in the narrow Wied valley a strong near surface CO_2 accumulation is simulated at night as well as a strong decrease with height (Fig. 4.11a). However, at a mountain ridge in the Eifel (615 m a.s.l.) only a slight increase of surface CO_2 (≈ 10 ppmv) is simulated (Fig. 4.11c) which is consistent with CO_2 observations at the top of the Ochsenkopf in Germany showing rather low diurnal variation (Pillai *et al.*, 2011). At 6 UTC, all profiles show decreasing CO_2 contents near the surface caused by already slightly negative NEE in the corresponding canopy (broadleaf forest at "Wied valley" and "Jülich", needleleaf forest

---

[5] Additional maps of near-surface CO_2 mixing ratios of CS2605 and CS1808 can be found in the appendix.

at "Central Eifel"). The break-up of the nocturnal boundary layer occurs just after that time leading to a 250 m deep CBL at 8 UTC. At the "Jülich" profile, located in flat terrain (Fig. 4.11b), the CO_2 mixing ratio in the CBL is still about 13 ppmv higher than in the free troposphere (weak crop activity + anthropogenic emissions). Between 14 and 18 UTC, a well-mixed PBL is simulated with vertically rather constant CO_2 contents. At the "Jülich" profile, the near surface drop of CO_2 can also be observed in CS2605. Compared with CS2407, the CBL is distinctly deeper (cf. Fig. 4.11 with Figs. 6.4 and 4.9b). The main reasons for this are higher sensible heat fluxes (and lower latent heat fluxes) in CS2605 than in CS2407 due to the weaker canopy transpiration and lower atmospheric humidity. In CS2605, the CO_2 content in the PBL is only slightly lower than in the free troposphere (≈ 3–4 ppmv at "Wied valley" and "Jülich" and ≈ 5 ppmv at "Central Eifel"). Stronger differences can be found in CS2407 (cf. Fig. 6.4). Thus, additionally to the net CO_2 flux at the surface, the height of the CBL top is an important controlling factor for determining the CO_2 concentration in the CBL. This has also been mentioned in former studies (e. g. Sarrat *et al.*, 2007b; Ter Maat *et al.*, 2010).

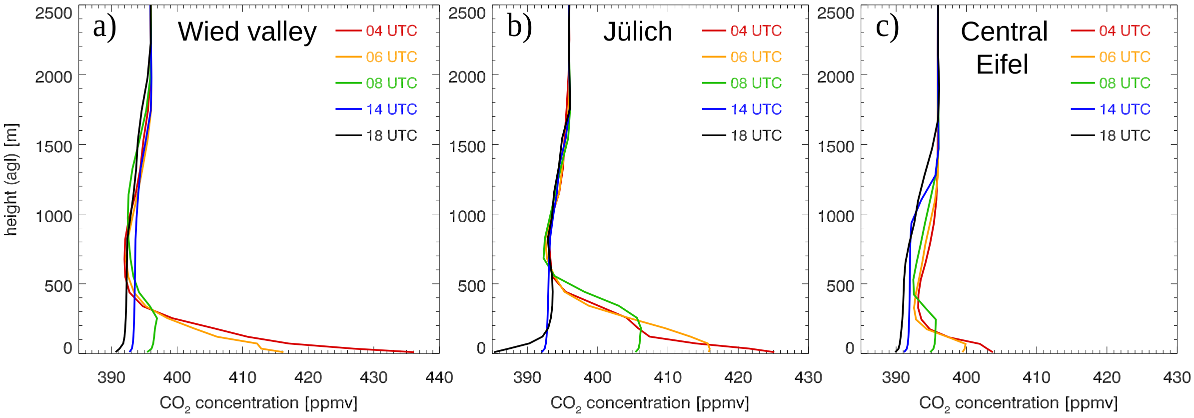

Figure 4.11.: Vertical CO_2 profiles [ppmv] at different times of the day for CS2605: a) in the Wied valley (◊), b) near Jülich (×) and c) at a mountain ridge in the Central Eifel (✻).

The temporal variation of atmospheric CO_2 mixing ratios is analyzed by means of time series at different locations (Fig. 4.12a). Again, the little diurnal variation at mountain ridges is apparent. One of the most interesting feature is the considerably slower decrease near Jülich than in the Wied valley although at both locations the landscape is covered by broadleaf trees having similar NEE. This can be explained by the low advective transport in the Wied valley, i. e. the highly negative NEE of broadleaf trees influences the local CO_2 mixing ratio directly. In contrast, with stronger winds higher CO_2 contents are advected to the Jülich grid point which result from the lower NEE of large arable areas east of Jülich. Moreover, the influence of anthropogenic emissions can be observed at the grid point located in the downtown of Cologne (△ in Fig. 4.8) with the highest CO_2 concentrations between 5 and 7 UTC. The strong decrease occurs two hours later than in rural areas. At noon and in the afternoon on all locations similar CO_2 contents are simulated. Fig. 4.12b depicts the diurnal variation near Jülich in different heights. As expected, the simulated amplitude decreases with increasing height. The height levels 73 m, 122 m and 561 m a.g.l. are included in the rising CBL at 6:00, 6:30 and 9:30 UTC. The similar mixing ratios afterwards show the well-mixed PBL except for the near surface drop in the evening. Observed CO_2 mixing ratios, operationally measured in 102.5 m a.g.l. at the

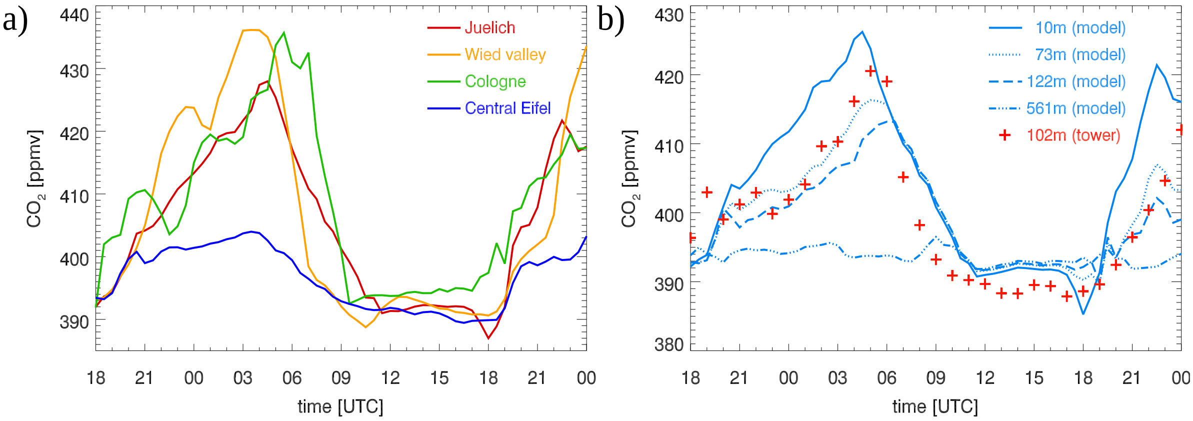

Figure 4.12.: Simulated time series of CO_2 mixing ratios [ppmv] of CS2605 at a) different locations (see Fig. 4.8, lowermost COSMO level) and b) at Jülich in different heights (blue lines) compared with observations in 102.5 m a.g.l. at the Jülich tower (red crosses).

Jülich tower[6] (see Section 7.1) match rather well with CS2605 showing only slightly lower CO_2 contents at daytime and a slightly higher diurnal amplitude.

In conclusion, the results indicate that in situations with a weak synoptic flow, in mountainous regions the CO_2 patterns are mainly generated by terrain induced local circulations, especially at night and in the morning. The CO_2 contents in narrow valleys strongly differ from those at elevated mountain ridges. A high grid resolution of the atmospheric model component is needed to capture these CO_2 patterns. Global models or regional models using grid sizes of several kilometers would fail to produce similar heterogeneities. This illustrates the still existing problem of estimating regional CO_2 fluxes from observed mixing ratios, e. g. at a tall tower, by means of regional-scale inverse modeling. Moreover, fossil fuel emissions, mainly caused by urban traffic and power plants, are an important source of atmospheric CO_2 in the NRW domain (see also Section 6.2). Especially in the morning rush-hour, significant higher CO_2 contents are simulated in and downstream of densely populated regions. After the development of a well-mixed CBL, the horizontal heterogeneities of atmospheric CO_2 are significantly reduced. Nonetheless, on days with low winds (e. g. CS2407) different CO_2 contents in the CBL are simulated in flat terrain (NEE of crops + anthropogenic emissions) and in mountainous regions (NEE of needleleaf/broadleaf forests). However, no clear correlation can be found between simulated CO_2 mixing ratios and landscapes covered by the same land use class (e. g. needleleaf forest at the Hohes Venn and in the western Eifel, cropland in the flat terrain, broadleaf forest in the eastern Eifel and in the Mosel valley). This demonstrates that the so called "CBL budget method" (Lloyd *et al.*, 2001), which determines surface fluxes at the scale of landscapes (≈ 1–10 km) by means of CO_2 profiles in the well-mixed CBL, cannot be applied for estimating NEE heterogeneities in the NRW domain. Qualitatively, this method has been used, e. g., in Dolman *et al.* (2006) or Sarrat *et al.* (2007b) attributing different CO_2 contents measured on a flight campaign in France to different land use classes. The simulations confirm the findings of van der Molen and Dolman (2007) showing that the CBL method can only be used in flat terrain and on days with very low wind speeds. Even with a light breeze (e. g. CS2407) the advective transport of fossil fuel emissions originating in the Rhine metropolises can distort flux estimates in the Jülicher Börde.

---

[6] data provided by Marc von Hobe, Forschungszentrum Jülich GmbH, IEK-7: Stratosphere (May 2014)

4.1.4. Influence of complex terrain on nocturnal CO_2 mixing ratios

The influence of topography on simulated near surface CO_2 mixing ratios was already stated, e. g., in Pérez-Landa *et al.* (2007) and Pillai *et al.* (2011). The different CO_2 contents above mountain ridges compared with those in valleys were explained by thermally induced mountain-valley circulations under weak synoptic pressure gradient conditions. Furthermore, intensified wind speeds induced by a buoyancy-driven katabatic downslope flow on the lee side of a mountain ridge, also referred to as "drainage flow", can have an effect on the observed and simulated nocturnal CO_2 concentrations (Pillai *et al.*, 2011). However, the locally convergent wind field of a nocturnal valley breeze solely cannot create horizontal CO_2 gradients originating from a rather homogeneous CO_2 distribution (i. e. $\nabla_h q_{CO_2} \approx 0$) remaining from the afternoon. Therefore, spatially different turbulent mixing or heterogeneities in the surface CO_2 sources are necessary to initiate horizontal CO_2 gradients (see Eq. 2.39). The reasons of the simulated strong horizontal CO_2 gradients in complex terrain are investigated in this section.

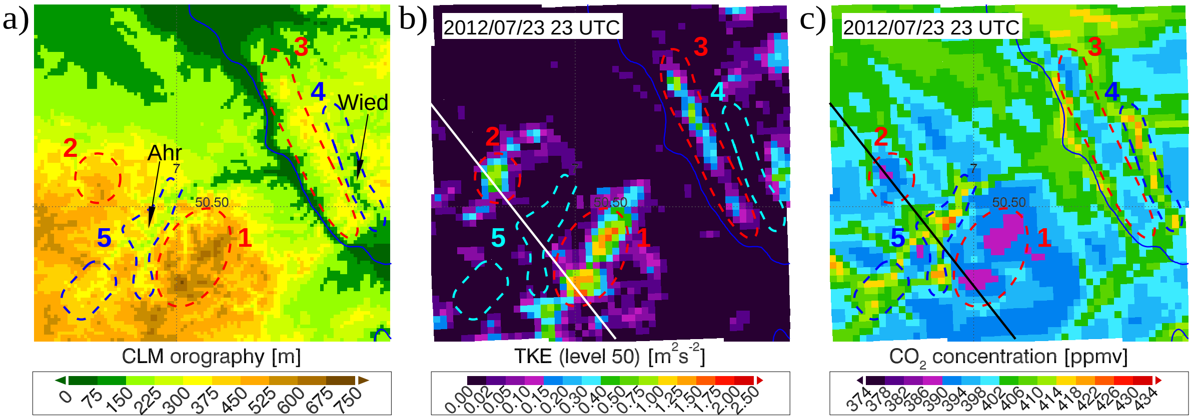

Figure 4.13.: a) Orographic height (Ahr-/Wied valley) [m], b) turbulent kinetic energy (TKE) [m^2s^{-2}] (COSMO half-level 50, $\approx$20 m), c) CO_2 mixing ratio [ppmv] (COSMO full-level 50, $\approx$10 m) on 2012/07/23, 23 UTC (CS2407). The dashed areas are referred to in the text.

Fig. 4.13 depicts the nocturnal conditions in the Ahr and Wied region standing out with high horizontal CO_2 gradients in CS2407 (see Fig. 4.8a). After sunset, in the valleys (blue regions) the formation of a stable nocturnal PBL due to thermal cooling at the surface leads to a consumption of turbulent kinetic energy (TKE). Contrary to this, between 20 and 23 UTC at the top of the mountains (red regions) TKE is produced. An analysis of the vertical structure of the wind field indicates an increase of 4–6 m s^{-1} of the wind speed in the lowermost 70 m where TKE is significant (not shown), i. e. wind shear is the source of TKE production. In flat terrain and in valleys the difference of the wind speeds in that heights is low ($\approx$1 m s^{-1}). At 23 UTC, along the Hohe Eifel (region 1) and the Siebengebirge (region 3) but also at a hill top north of the Ahr (region 2) significant TKE is simulated in the lower atmosphere (Fig. 4.13b) causing intensified vertical mixing of respired CO_2 at the surface. These areas are well correlated with local minima of the near surface CO_2 content (Fig. 4.13c). In contrast, in the Wied and Ahr valleys (i. e. TKE minimum in regions 4 and 5) local maxima of the CO_2 mixing ratios occur due to accumulation of locally respired CO_2 (calm conditions, see Fig. 4.2a).

The vertical cross section along the lines in Fig. 4.13 shows that the TKE maximum at the top of the mountain ridges is restricted to the lowest few decameters (Fig. 4.14a). The CO_2

maximum in the Ahr valley and at the lower part of the mountain slope to the north coincides with a lack of TKE (Fig. 4.14b). After 0 UTC, TKE reduces continuously due to decreasing wind speeds and is more concentrated to the mountain tops. However, TKE is still existing until the following morning. A valley breeze further intensifies the accumulation of CO_2 in the valleys which is shown in a second example below. Heterogeneities in the surface CO_2 flux cannot explain the strong horizontal CO_2 gradients because broadleaf forest with rather homogeneous respiration rates is the major source of CO_2 in both regions. A similar correlation between wind shear, TKE and near surface CO_2 contents can be seen in parts of the Mosel valley (not shown). These results confirm the findings of van der Molen and Dolman (2007) who have simulated local TKE maxima at the edge of the east Siberian plateau at night by means of a rather coarse atmospheric model (grid resolution: 27 km). With the fine grid resolution of TerrSysMP-CO_2 it has been demonstrated that the TKE production above hill tops is a typical feature in complex topography in nights with weak synoptic forcing.

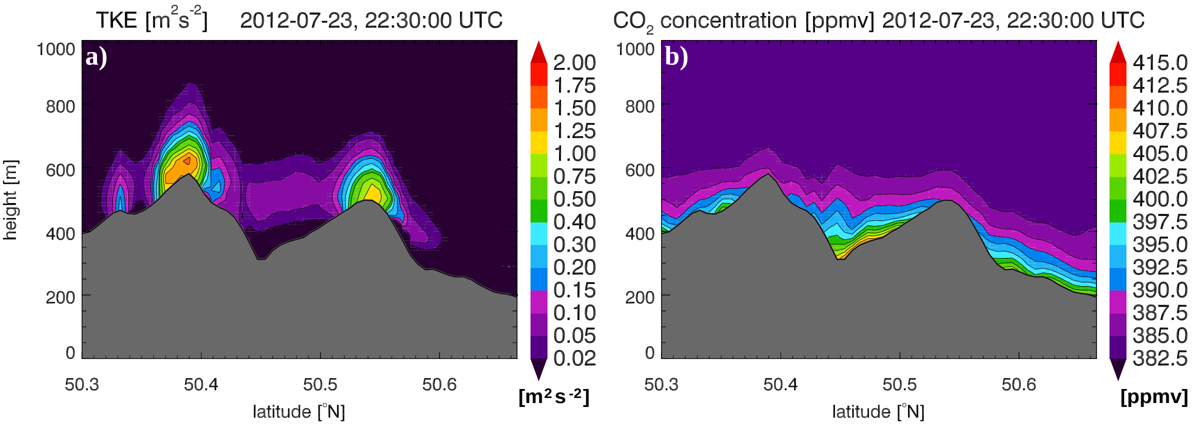

Figure 4.14.: Vertical cross sections (see black/white lines in Fig. 4.13) of a) TKE [m^2s^{-2}] and b) CO_2 mixing ratio [ppmv], both on 2012/07/23, 22:30 UTC (CS2407).

Fig. 4.15 depicts the most important processes explaining the near surface CO_2 patterns in the Rur and Urft region in the northern Eifel. Similar as in the Wied and Ahr region, after sunset significant TKE is produced (Fig. 4.15b) above the Hohes Venn (region 1) but also above other elevations (regions 2 and 3). Again, this leads to low CO_2 mixing ratios (Fig. 4.15c). In the Urft valley (regions 4), TKE has been consumed and the TKE minima coincide with local near surface CO_2 maxima. A second TKE minimum (region 5) is simulated in the Rur valley but it is shifted towards the northern mountain slope in its northern part. In the southern part, CO_2 accumulates at the bottom of the Rur valley due to negligible winds. However, in the northern part stronger south-easterly winds blow along the slope and at the top of the elevation. Thus, a stronger advective removal of locally respired CO_2 causes significantly reduced CO_2 contents. This wind pattern persists in the second half of the night (Fig. 4.15d, region A) and, thus, in this region the CO_2 concentrations remain low (Fig. 4.15f).

After 23 UTC, TKE decreases and at 2 UTC high TKE is only simulated at the Hohes Venn and at some hill tops whereas in widespread areas TKE is consumed (Fig. 4.15e). Hence, the increasing horizontal CO_2 gradients from 22:30 to 2 UTC can only partly be explained with the TKE distribution. The most striking features in the surface wind field at 2 UTC are strong convergences to the east/southeast of the Urft/Rur valley (regions B). A light to gentle southeasterly breeze (2–3 Bft) blows at the edge and along the lee side slope of the mountain

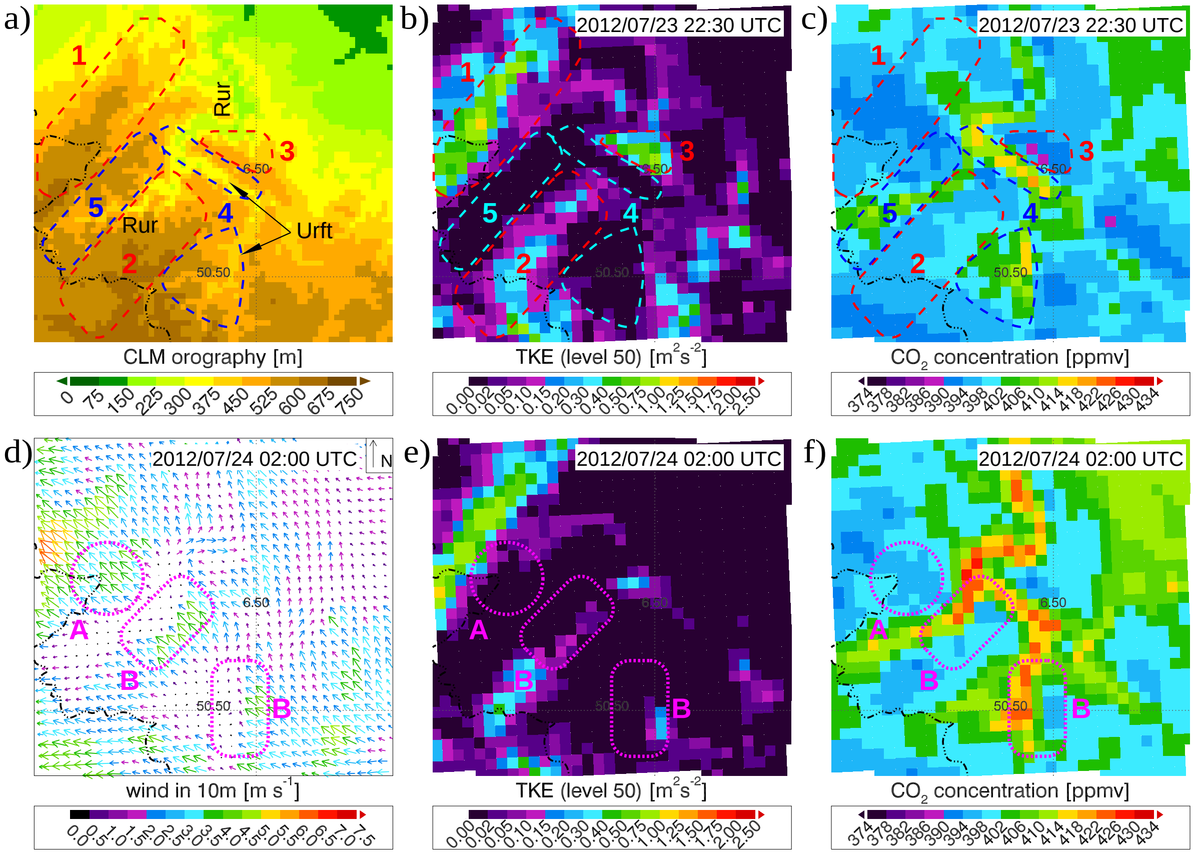

Figure 4.15.: a) Orographic height (Rur-/Urft valley) [m], TKE [$m^2 s^{-2}$] (COSMO half-level 50) (b, e) and CO_2 mixing ratio [ppmv] (COSMO full-level 50) (c, f) on 2012/07/23 22:30 UTC and 2012/07/24 02 UTC, d) wind vectors [$m\,s^{-1}$] 10 m a.g.l. on 2012/07/24 02 UTC (CS2407).

ridges whereas calm conditions characterize the lower parts of the valleys. This valley breeze advects the low CO_2 mixing ratios to be found at the mountain tops to the lee side and causing low CO_2 contents in the upper part of the mountain slopes (Fig. 4.15f). In contrast, further down and at the bottom of the Rur and Urft valley, locally respired CO_2 is not removed by advection and vertical mixing (TKE) in the stable PBL is suppressed, i. e. CO_2 can accumulate near the surface. In other words, the local tendency of CO_2 mixing ratios ($\partial q_{CO_2}/\partial t$, see Eq. 2.39) in the bottom of the valley is stronger than at the hill top and at the upper part of the lee side slope. Here, advective ($\mathbf{v} \cdot \nabla q_{CO_2}$) and turbulent transport ($(\partial q_{CO_2}/\partial t)_{turb}$) inhibits a strong local CO_2 tendency whereas both terms can be neglected at the bottom of the valley. Hence, the near surface CO_2 gradient continuously increases during night.

In summary, stronger vertical mixing at the hill tops, especially in the first half of the night, initially generates horizontal gradients of CO_2 mixing ratios and the orography induced convergences and divergences in the wind field can further intensify these gradients.

4.1.5. An analysis of soil respiration

Heterotrophic and autotrophic respiration as well as the moisture and temperature effects on respiration (Eqs. 2.34 and 2.35) have been analyzed in detail for CS2605 (moderate temperatures) and for CS1808 (high temperatures)[7]. Fig. 4.16 depicts the respiration rates of CS2605. The lowest heterotrophic respiration rates are simulated at 7 UTC with 1.5 μmol(CO_2)$m^{-2}s^{-1}$ for arable soils, 3.4–4.0 μmol(CO_2)$m^{-2}s^{-1}$ in forests in the Eifel and up to 4.5 μmol(CO_2)$m^{-2}s^{-1}$ in the Kölner Bucht (Fig. 4.16a). Respiration is slightly stronger in loam and sandy loam soils (northwestern NRW domain, Rhine valley) than in clay-loam. In the afternoon, heterotrophic respiration reaches its maximum (Fig. 4.16b) with 1.5–2.0 μmol(CO_2)$m^{-2}s^{-1}$ for arable soils and 4.0–5.5 μmol(CO_2)$m^{-2}s^{-1}$ in forests, depending on orographic height. Respiration of needleleaf and broadleaf forests is similar. Simulated autotrophic respiration is constant throughout the day and lowest for arable soils ($\approx$ 2.1 μmol(CO_2)$m^{-2}s^{-1}$) and highest for needleleaf and broadleaf forests (2.7 and 3.1 μmol(CO_2)$m^{-2}s^{-1}$, respectively), see Fig. 4.16c. Thus, the fraction of autotrophic respiration on total soil respiration is higher in agricultural soils than in forest soils. On 19 August 2012, high temperatures in the topsoil (see below) cause about 50% higher heterotrophic respiration rates than on 26 May. However, the absolute values of autotrophic respiration as well as the fraction on total soil respiration is less due to a decrease of autotrophic respiration in late summer (less growth respiration).

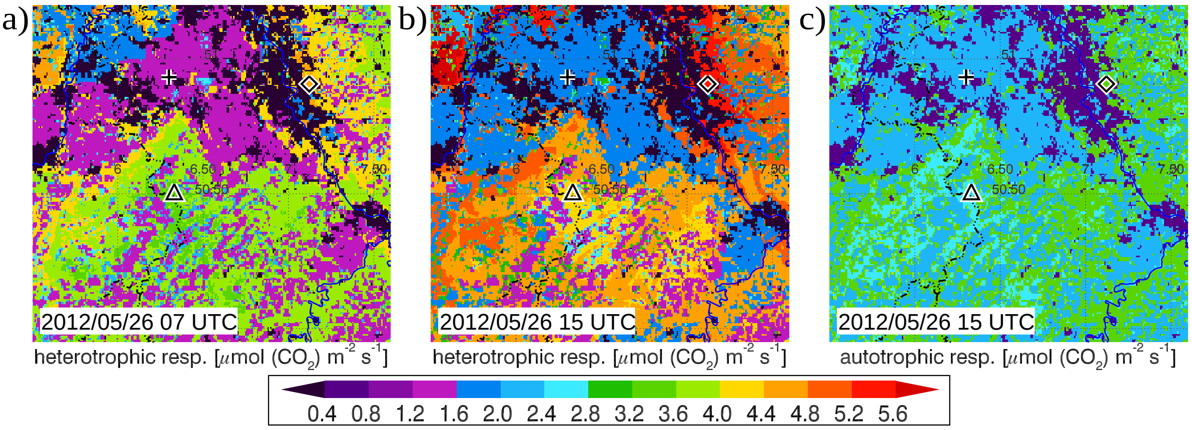

Figure 4.16.: Simulated heterotrophic respiration [μmol(CO_2)$m^{-2}s^{-1}$] on 2012/05/26 (CS2605) at a) 07 UTC and b) 15 UTC and c) autotrophic respiration at 15 UTC.

The effect of soil moisture on respiration is investigated with CS2605. In CLM soil layer 1 (0–1.75 cm) the soil water saturation of clay-loam increases from 72% in the flat terrain to 82% in the Eifel (Fig. 4.17a). Loam is less saturated (64% in NL, 67–73% in BE and Rhine valley) and sandy loam has the lowest water saturation due to lower water holding capacities. Hence, even after dry periods in summer, the loamy soils in the NRW domain do not dry out because capillary effects supply water from the deeper soil. This explains 2–4% more saturation in the morning than in the evening (not shown). These conditions lead to a moisture reduction factor $f(h)$ of 0.85–0.9 in the flat terrain and 0.92–0.96 in the mountainous regions (Fig. 4.17d), i. e. in the flat terrain (mountainous regions) CO_2 production in the uppermost 10 cm is 9–14% (3–7%) reduced from optimum respiration rates due to slightly too dry soils. The effect of different soil types on $f(h)$ is almost absent.

In soil layer 3 (4.5–9.1 cm) and 5 (16.6–28.9 cm, i. e. lower topsoil) the saturation is about 2% and 3–4% higher than in layer 1, respectively (Fig. 4.17b). This slight increase, however, increases $f(h)$ to 0.9–0.98, depending on orographic height (Fig. 4.17e). Thus, soil respiration

---

[7] Supplementary figures of this subsection can be found in the appendix.

is only slightly limited with respect to moisture in this soil layer. In the subsoil (layer 7, 49.3–83.0 cm), the soil water saturation is even higher ranging from 80% in the flat terrain to 88% in the Eifel and Bergisches Land (clay-loam). Again, the other soil types are less saturated (Fig. 4.17c). The effect of the higher moisture on CO_2 production is more complex than in the upper soil layers (Fig. 4.17f). Whereas in the flat terrain soil respiration is minimally limited due to too *dry* soils ($f(h) \approx 0.95$–0.98), in the western Eifel and parts of the Bergisches Land CO_2 production is stronger restricted due to too *moist* soils ($f(h) \approx 0.75$–0.9). These regions are surrounded by a zone with optimum conditions ($f(h) = 1$). Hence, only a few percent of water saturation determine moisture limitation effects of CO_2 production close to optimum conditions (see e. g. the conditions of loam along the Rhine). This fact makes it difficult to verify such effects on soil respiration with observations considering the strong heterogeneity in soil conditions and complex vertical structures of soils in reality. Moreover, in the deeper soil a slight influence of different soil types on $f(h)$ can be seen.

A comparison of the respiration rates of CS2605 with a simulation using $f(h) = 1$ (i. e. no moisture limitation) shows the strongest reduction in the lee of the Eifel ($0.6\,\mu\text{mol}(CO_2)\text{m}^{-2}\text{s}^{-1}$, i. e. $\approx 10\%$). The lower $f(h)$ in the subsoil has a smaller effect on total respiration because the CO_2 production in the subsoil is low (low temperatures, low TOC contents). Thus, in the humid conditions of the NRW domain the moisture reduction of soil respiration in the loamy soils is rather low. However, supersaturation in the subsoil or after periods with much precipitation can reduce respiration. In CS1809, $f(h)$ in the topsoil is similar but in the subsoil of the Eifel the water content is slightly lower causing almost optimum conditions (not shown).

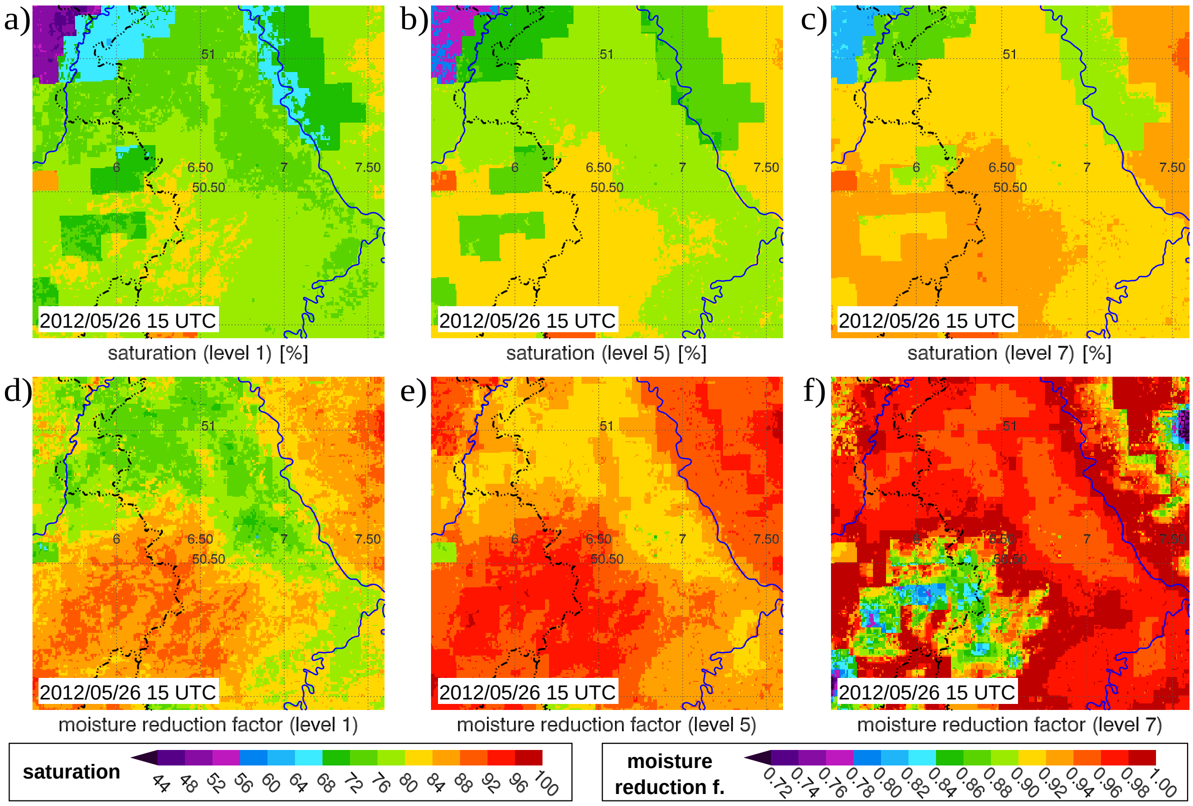

Figure 4.17.: Simulated soil water saturation [%] and moisture reduction factor $f(h)$ on 2012/05/26 15 UTC (CS2605) in CLM soil level 1 (a, d), level 5 (b, e) and level 7 (c, f).

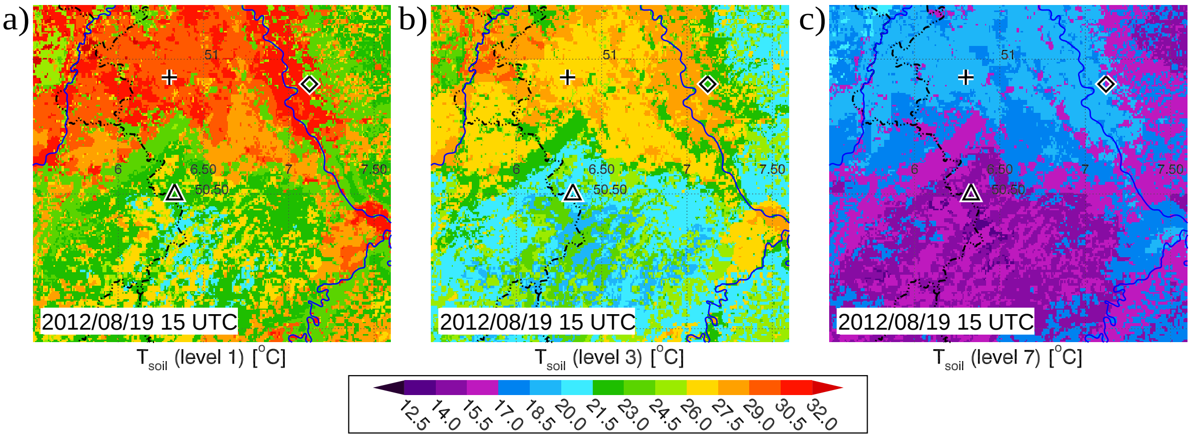

Figure 4.18.: T_{soil} [°C] on 2012/08/19 15 UTC (CS1808) in a) CLM soil level 1, b) level 3 and c) level 7.

Soil temperature (T_{soil}), the second and most important environmental control of heterotrophic respiration, is analyzed with CS1808. Both the diurnal variation and the maximum of T_{soil} in the topsoil are strongly PFT-dependent due to different LAIs and vegetation structures (crops: $\Delta T_{soil} \approx 13\,°\mathrm{C}$, forest: $\Delta T_{soil} \approx 6\,°\mathrm{C}$). The solar heating of the uppermost centimeters of the soil of crop fields (Fig. 4.18a) is stronger (26 °C in the Eifel, 28–31 °C in flat terrain on 19 August) than that of forest soils (21–24 °C). Using $Q_{10} = 2.1$ for the temperature dependency of soil respiration[8] ($f(T_{soil})$, Eq. 2.34) results in $f(T_{soil}) = 4.3$ ($T_{soil} = 29\,°\mathrm{C}$) and $f(T_{soil}) = 4.8$ ($T_{soil} = 30.5\,°\mathrm{C}$) in CLM soil layer 1 (0.7 cm) at the Merzenhausen field (+) on 18 and 19 August, respectively (Fig. 4.19b). This means that microbial activity is 4–5-fold higher than for $T_{ref} = 9.25\,°\mathrm{C}$. At the same time, in Eifel forests (e. g. Wüstebach, △) $f(T_{soil})$ is 2.4 (2.6) for $T_{soil} = 21\,°\mathrm{C}$ ($T_{soil} = 22\,°\mathrm{C}$), see Fig. 4.19a. Due to the exponential behavior of $f(T_{soil})$ the effect of PFT dependent T_{soil} on $f(T_{soil})$ is higher than for T_{soil} itself. At night, T_{soil} and $f(T_{soil})$ of different PFTs are less different and orography is the major controlling factor.

The diurnal variation of T_{soil} in soil level 3 (6.2 cm) is lower (crops: $\Delta T_{soil} \approx 9\,°\mathrm{C}$, forest: $\Delta T_{soil} \approx 3.5\,°\mathrm{C}$). T_{soil} increases to 26–28 °C in the flat terrain (arable land) and 19–23 °C in forest soils depending on orographic height (Fig. 4.18b). A phase shift of 2 h between level 1 and level 3 can be seen (Fig. 4.19). In the lower topsoil (level 5, 21.2 cm) the diurnal variation of T_{soil} is further dampened ($\Delta T_{soil} \approx 3\,°\mathrm{C}$) and a phase shift of 6 h is simulated. $f(T_{soil})$ shows only a low diurnal course with a slightly stronger variation in Merzenhausen due to higher T_{soil} of arable soils in flat terrain compared with forest soils in the Eifel. This indicates that most of the diurnal variation of heterotrophic respiration results in the upper 10 cm of the soil where T_{soil} is strongly influenced by atmospheric conditions and where the TOC is highest. CS1808 represents an extreme case with very high temperatures at daytime. At even higher temperatures ($T_{soil} > 30\,°\mathrm{C}$) soil respiration approaches a maximum because the upper limit of enzyme activity is reached.

Due to the stronger cooling of the uppermost topsoil and the phase shift between upper and lower topsoil, at night $f(T_{soil})$ is higher in level 5 than in the upper centimeters of the soil (Fig. 4.19). In the subsoil (level 7, 62 cm) T_{soil} is almost constant in time and slightly lower in forest soils than in arable soils and depends on orographic height (Fig. 4.18c). Whereas at night $f(T_{soil})$ is similar in all levels, at daytime $f(T_{soil})$ in the topsoil is distinctly higher.

---

[8] $Q_{10} = 2.1$ is the default in TerrSysMP-CO$_2$, used for most simulations. For CS2605 and CS2407 $Q_{10} = 2.0$ is used which results in almost the same respiration rates in the considered range of T_{soil} (see Fig. 2.10a).

In CS2605, T_{soil} is $\approx 6\,^{\circ}$C ($\approx 4\,^{\circ}$C) colder in arable (forest) topsoils and $\approx 2\,^{\circ}$C colder in the subsoil. These few degrees difference, however, cause significantly less diurnal variation of $f(T_{soil})$ in the topsoil with a maximum of 2.8 in Merzenhausen only (Fig. 4.19c). This is the main reason for the lower soil respiration in CS2605.

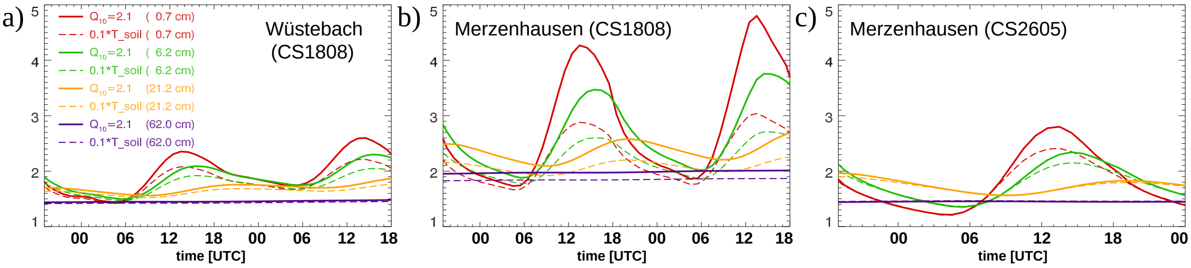

Figure 4.19.: Diurnal variation of T_{soil} [0.1°C] (dashed lines) and Q_{10}-factor of heterotrophic respiration (solid lines) in CLM soil level 1 (0.7 cm), level 3 (6.2 cm), level 5 (21.2 cm) and level 7 (62.0 cm) at Wüstebach (a: CS1808) and Merzenhausen (b: CS1808, c: CS2505).

Finally, the amount of CO_2 production in the forest floor (i. e. aboveground litter, O_e/O_a horizon, see Fig. 2.6), in the topsoil and in the subsoil is investigated (Figs. 4.20 and 4.21). In the morning of 19 August, in forests 38–45% of heterotrophic respiration originates from decomposition of litter and fresh organic matter in the only a few centimeter thick O horizon[9] (Fig. 4.20a). In the afternoon, the percentage in the forest floor is even higher (45–50%, see Fig. 4.20b) due to high temperatures. Fig. 4.21 indicates that both in broadleaf (Rhine valley, ◊) and needleleaf forests (Wüstebach) the diurnal variation of total heterotrophic respiration mostly results from the variation in this layer. Borken *et al.* (2003) found a strong reduction of respiration in the O horizon within a few days after the last rain event due to drying of leaf litter. In TerrSysMP-CO_2, $f(h)$ of soil level 1 is used for the moisture dependency of CO_2 production in the O horizon which possibly may lead to an overestimation in dry periods. However, this cannot be tested due to missing observations in the NRW domain. For arable and grassland soils the occurence of an O horizon is neglected.

In the mineral topsoil below the O horizon (0–29 cm), in the morning 38–42% (needleleaf) and 34–38% (broadleaf) of heterotrophic respiration is produced and a slightly less fraction in the afternoon (Fig. 4.20c, d). For arable soils the percentage in the topsoil is higher, 54–58% in the morning and 62–66% in the afternoon. The amount and percentage for grasslands is even higher (> 66–76%) due to a twice as high TOC content in the topsoil compared with arable soils but equal TOC contents in the subsoil. The diurnal variation of topsoil respiration is less than in the O horizon, but the dependence on T_{soil} is evident (Fig. 4.21b, c). In arable and grassland soils the entire diurnal variation comes from the topsoil (Fig. 4.21a).

The fraction of CO_2 production in the thicker subsoil (30–83 cm) is less with 14–18% (20–26%) in the morning and 10–14% (14–19%) in the afternoon for needleleaf (broadleaf) forests. Moreover, respiration is rather constant in time. The percentage of arable subsoils is higher (42–46% in the morning, 34–38% in the afternoon) than for grasslands (24–34%). Below 83 cm, CO_2 production is negligible (sparce TOC). Due to the assumption of only one soil type having the same clay content in all soil layers, the partitioning of TOC in C-pools is the same in each soil layer. However, usually the fraction of the already decomposed IOM pool is distinctly higher in the subsoil than in the topsoil. Otherwise, the percentage of fast (RPM) and slow

---

[9] in TerrSysMP-CO_2 this layer is considered as a 0-dimensional surface above the CLM soil layers

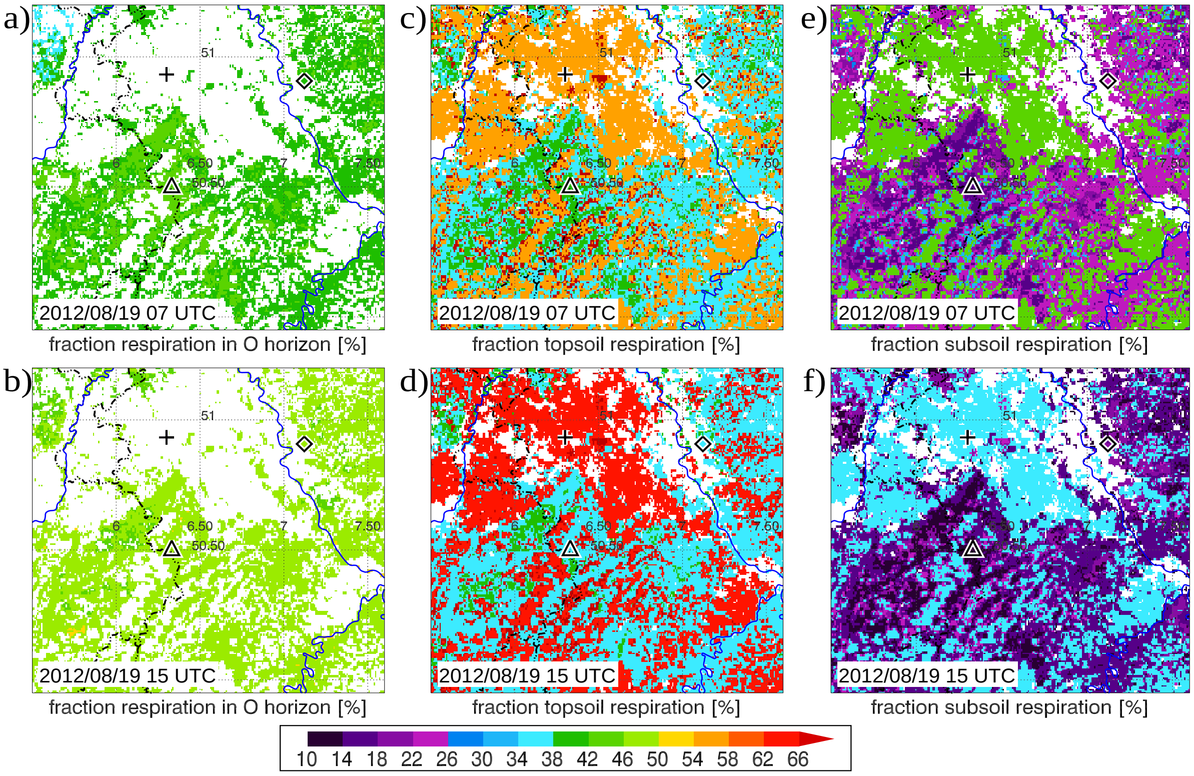

Figure 4.20.: Fraction [%] of respiration in the O horizon (a, b), topsoil [0–29 cm] (c, d) and subsoil [30–83 cm] (e, f) on total heterotrophic respiration on 2012/08/19 at 07 UTC (a, c, e) and at 15 UTC (b, d, f). In the white areas no litter/heterotrophic respiration is calculated.

(HUM) decomposing pools decrease with depth (Bauer *et al.*, 2012). Hence, respiration in the subsoil may be slightly overestimated in the simulations which would partly explain the too low diurnal variation of soil respiration (see Section 5.2). Increasing clay contents with depth would partially solve this problem. Autotrophic resiration is slightly lower than heterotrophic respiration in arable soils (Fig. 4.21a) and considerably lower in forest soils (Fig. 4.21b, c).

Soil respiration in CS2605 shows a similar behavior with slightly lower fractions in the O horizon and in the topsoil (lower T_{soil}) but with a higher amount of autotrophic respiration on total respiration due to higher growth respiration rates in spring (not shown).

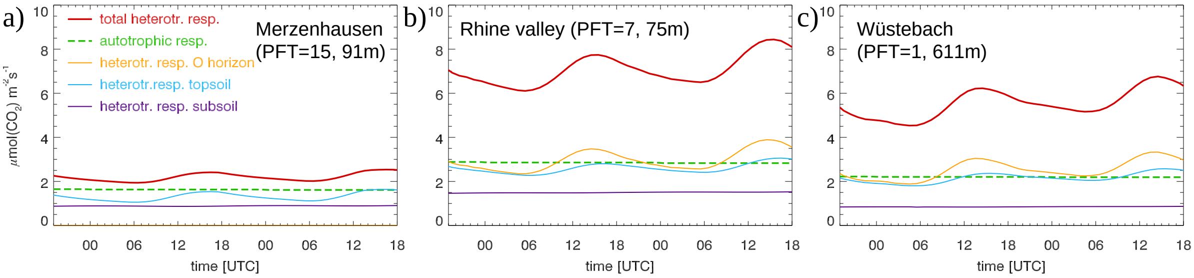

Figure 4.21.: Diurnal variation of heterotrophic respiration [μmol(CO$_2$)m^{-2}s^{-1}] (solid lines), its components (O horizon, topsoil, subsoil) and autotrophic respiration [μmol(CO$_2$)m^{-2}s^{-1}] (dashed line) of CS1808: a) Merzenhausen (+), b) Rhine valley (◊), c) Wüstebach (△).

4.1.6. CO_2 budget in the NRW domain

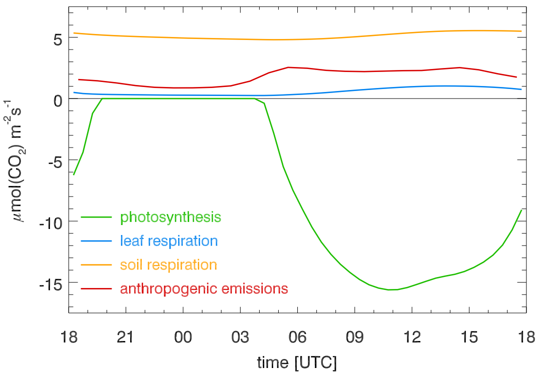

Figure 4.22.: Averaged CO_2 fluxes of CS2407 [μmol(CO_2)$m^{-2}s^{-1}$].

In order to examine if the different parameterizations of all biogenic CO_2 fluxes in CLM altogether lead to a realistic NEP as well as to estimate the contribution of anthropogenic emissions in the NRW domain, CO_2 budget calculations have been made by averaging all fluxes in space and time (Table 4.1). This reveals that, except on 19 August, on clear sky days the CO_2 uptake by plants (i. e. photosynthesis) cannot be compensated by total ecosystem respiration (i. e. leaf and soil respiration). Hence, in summer and spring on clear sky days the vegetated canopy acts as a natural CO_2 sink. Moreover, the averaged photosynthesis rates of CS1808 are lower than in CS2605 and in CS2407. This can be explained by heat stress of plants due to the very high temperatures on 18 and 19 August and by low LAIs, especially for crops. For leaf and soil respiration the temperature dependency is evident. The respiration rates of CS1808 are higher than in CS2605 and in CS2407 (moderate temperatures) leading to almost balanced biogenic fluxes on 18 and 19 August. Together with anthropogenic emissions, a weak net gain of atmospheric CO_2 is simulated for CS2605 and CS2407, and a significant gain for CS1808. The net CO_2 gain, even on clear sky days, seems to be unrealistic because CO_2 concentration measurements at the Jülich tower indicate a decrease of 20–25 ppmv for the averaged atmospheric CO_2 content between March/April and August/September (see Fig. 7.2). Horizontal advection from outside the domain or entrainment from the free troposphere cannot solely explain this CO_2 decrease. An explanation for the simulated net CO_2 gain are strongly underestimated photosynthesis rates of crops using the default plant physiological parameters of CLM (see Section 5.1 and Sulis *et al.*, 2015). Fig. 4.22 depicts the course of biogenic and anthropogenic CO_2 fluxes averaged over the NRW domain. As expected the anthropogenic emissions are higher at daytime (including rush hour effects) than at nighttime. Even in summer (i. e. without domestic heating) in the densely populated NRW domain about 20–25% of the total CO_2 source are human based (e. g. fossil fuel emissions of power plants, road traffic and industry).

date	**2012/05/26**	**2012/07/24**	**2012/08/18**	**2012/08/19**
photosynthesis	−7.088	−7.315	−6.253	−6.429
leaf respiration	*0.530*	*0.555*	*0.649*	*0.735*
soil respiration	*4.996*	*5.134*	*5.505*	*5.699*
total respiration	5.526	5.690	6.154	6.434
anthro. emissions	1.878 [Sat]	1.796 [Tue]	1.653 [Sat]	1.538 [Sun]
budget	**+0.316**	**+0.170**	**+1.553**	**+1.544**

Table 4.1.: CO_2 budget [μmol(CO_2)$m^{-2}s^{-1}$] of CS2605, CS2407 and CS1808 (− sink, + source).

4.2. Cloudy weather situation

After the detailed analysis of clear sky days, in the next sections the influence of clouds and precipitation on surface fluxes and on the atmospheric CO_2 distribution is investigated. Three additional case studies have been analyzed with TerrSysMP-CO_2 for days with clouds, convective precipitation and stratiform precipitation in the NRW domain:

- **CL0309**: initialization: 2012/09/02 18 UTC, 30 h simulation (background CO_2: 390 ppmv)
- **CP2005**: initialization: 2012/05/19 18 UTC, 48 h simulation (background CO_2: 396 ppmv)
- **SP1306**: initialization: 2013/06/12 18 UTC, 48 h simulation (background CO_2: 396 ppmv)

4.2.1. Meteorological situation of model case studies

The weather on 3 September 2012 (CL0309) is characterized by a high pressure system over the Atlantic Ocean and negligible pressure gradients in Central Europe. Hence, at night only a light breeze (1–2 Bft) is simulated and observed which further weakens in the morning leading to widespread almost calm conditions in the early morning (Fig. 4.23a). After 0 UTC, a band of low and midlevel clouds, resulting from a dissipating cold front, reaches the northwestern part of the model domain and in the morning it ranges from the southwestern to the northeastern part of the NRW domain where it remains rather stationary (Fig. 4.23b). The southeastern part of the NRW domain is cloudless. In the afternoon, the simulated clouds are concentrated in the mountainous regions (Fig. 4.23c). Satellite images show slightly thicker clouds which are located in the northern half of the NRW domain. The wind is light to gentle (2–3 Bft) at daytime and the temperatures are moderate (16–22°C). With this case study the effect of clouds and very low winds on canopy fluxes and on the atmospheric CO_2 contents is analyzed.

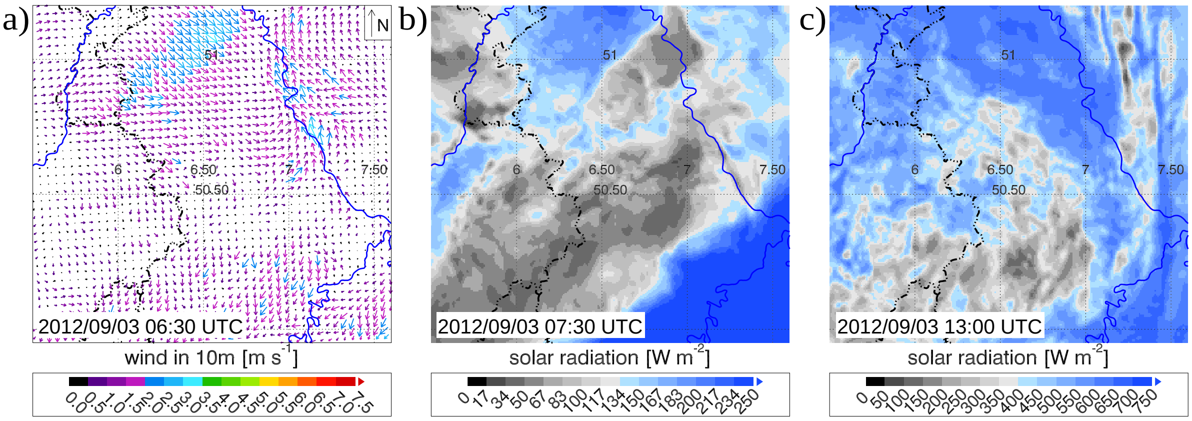

Figure 4.23.: a) Wind vectors [$m\,s^{-1}$] 10 m a.g.l. on 2012/09/03 06:30 UTC and solar radiation [$W\,m^{-2}$] at b) 07:30 UTC and c) 13:00 UTC, simulated with TerrSysMP-CO_2 (CL0309).

On 20 May 2012 (CP2005), in front of an upper-tropospheric low pressure system over Spain an elongated depression including a frontal zone is located over France and shifts northeastwards. In the simulations as well as in reality, prefrontal partial cloudiness occurs in the NRW domain. In the afternoon and evening several convective cells (showers and thunderstorms) develop traveling in northeastern direction over the western and northwestern part of the NRW domain. These widespread convective rain events are not captured by the model. Instead, in the late afternoon a single heavy convective cell develops in the Bergisches Land and a second even stronger thunderstorm is simulated in the eastern Belgium in the evening (see Fig. 4.31). Despite of this mismatch between the simulation and the observation, this case study can be used to analyze the effect of heavy precipitation on soil respiration (Section 4.3.1). In the morning of the subsequent day, at the northern side of a low pressure system over southern Germany residuals of frontal cloudiness with light rain shift retrograde towards the west and are located over the western model domain (Fig. 4.24a). Overlying cirrostratus and altostratus further attenuate solar radiation especially in the northern model domain. Additionally, in the afternoon low level clouds are advected from the east into the model domain (Fig. 4.24b). The temperatures are moderate on both days (17–25°C). For this day the effect of different solar radiation intensities on photosynthesis and transpiration is studied.

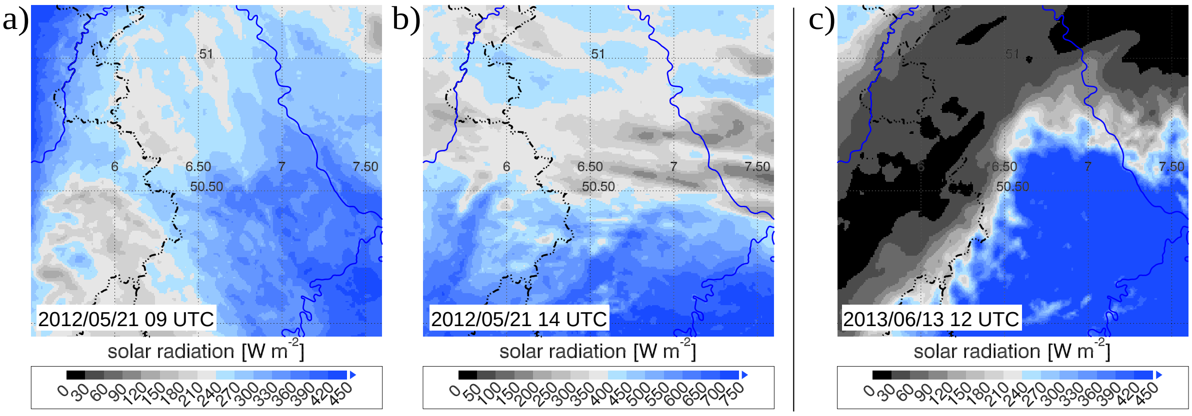

Figure 4.24.: Solar radiation [W m^{-2}] on 2012/05/21 a) 09 UTC and b) 14 UTC (CP2005) and c) on 2013/06/13 12 UTC (SP1306), simulated with TerrSysMP-CO_2.

On 13 June 2013 (SP1306), at first the weather is influenced by a moderate southwesterly flow (4 Bft) causing a rather warm night with 16–19 °C in the flat terrain and daytime temperatures of 23–26 °C in the southeast of the NRW domain. Until noon, the weather situation is more and more affected by a low pressure system over Great Britain. Ahead of its cold front thick stratiform clouds are simulated causing an attenuation of solar radiation below 50 W m^{-2} (Fig. 4.24c). The intense cold front passes the model domain between 14 and 20 UTC from northwest to southeast and induces stratiform precipitation with some convective cells embedded in this band of rain (see Section 4.3.2). With passing of the front the wind turns to west and intensifies. To the rear of the front, at night the considerably drier air mass cools down to 7–13 °C and the wind weakens. On 14 June, a high pressure system forms over Germany and fair weather conditions are simulated whereby the observed cloudiness is underestimated.

4.2.2. Influence of solar radiation on photosynthesis and transpiration

Both photosynthesis (A) and transpiration (TP) strongly depend on solar radiation: photosynthesis needs enough photosynthetically active (solar) radiation (PAR) to convert the light energy into chemical energy (light reaction, Section 2.3.1); transpiration depends on the available energy supplied by solar radiation. Due to the direct relationship between photosynthesis and transpiration via the stomatal resistance (r_{st}), the interrelation between solar radiation, photosynthesis, transpiration and r_{st} is analyzed in this section.

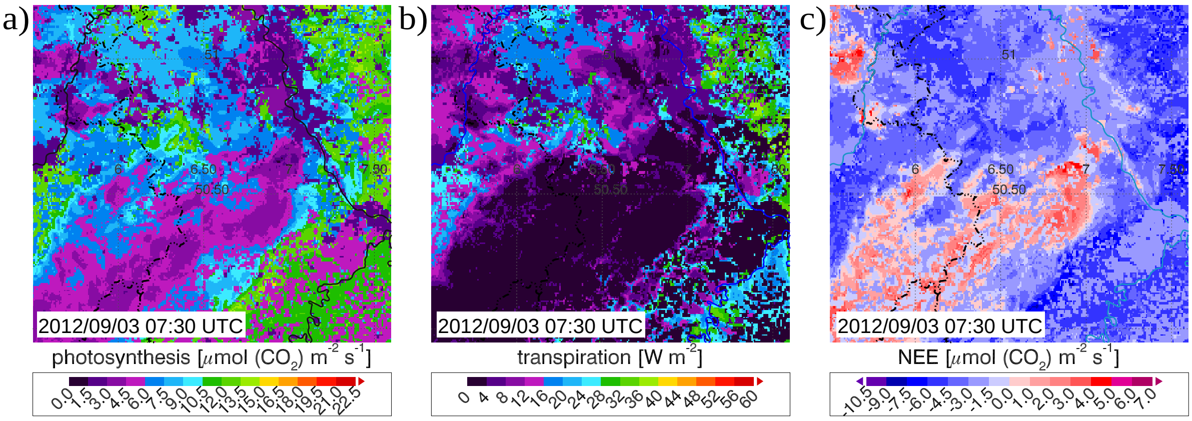

Figure 4.25.: Canopy fluxes on 2012/09/03 07:30 UTC: a) photosynthesis [μmol(CO$_2$)m^{-2}s^{-1}], b) transpiration [W m^{-2}], c) NEE [μmol(CO$_2$)m^{-2}s^{-1}], simul. with TerrSysMP-CO$_2$ (CL0309).

Fig. 4.25 depicts simulated CO$_2$ fluxes and transpiration in the morning of 3 September 2012. A comparison with the simulated cloud cover (Fig. 4.23b) indicates reduced photosynthesis where solar radiation is attenuated by clouds (Fig. 4.25a). In the southeastern part of the domain and in the Bergisches Land (solar radiation $\approx$ 200–250 W m^{-2}) for forests photosynthesis rates of 12–14 μmol(CO$_2$)m^{-2}s^{-1} are simulated. In cloudy regions ($\approx$ 35–100 W m^{-2}) the CO$_2$ uptake is distinctly lower (3–9 μmol(CO$_2$)m^{-2}s^{-1}), especially when solar radiation falls below 60 W m^{-2}. Here, the plants receive few PAR inhibiting photosynthesis by light limitation w_j (Eq. 2.20). Thus, the leaf stomata are only partly open ($r_{st}^{sun} \approx$ 1000–2000 s m^{-1}) to store water in the leaf interior whereas in the other regions the stomata are open ($r_{st}^{sun} \approx$ 350–600 s m^{-1}, see Fig. 4.26). In other words, in the cloudy regions the plants are in the transition from a "night mode" (r_{st} = max, A = 0, TP = 0) to a "daytime mode". The shaded stomatal resistance (r_{st}^{sha}) shows a similar behavior but the sunlit stomatal resistance (r_{st}^{sun}) is more sensitive to light limitation (not shown). The different response of r_{st}^{sun} and r_{st}^{sha} on limited solar radiation demonstrates the importance of a two-big-leaf canopy approach. Ter Maat *et al.* (2010), e. g., found a too strong reduction of photosynthesis at attenuated radiation using a one-big-leaf approach. The effect of clouds on transpiration is even stronger than for photosynthesis (TP < 5 W m^{-2}) due to limited solar radiation *and* high r_{st} (Fig. 4.25b). Leaf and soil respiration explain the plant canopy being still a CO$_2$ source in cloudy regions (NEE > 0) whereas in cloudless regions CO$_2$ assimilation exceeds respiration (NEE < 0), see Fig. 4.25c. In the afternoon, the radiative attenuation of convective cloudiness (Fig. 4.23c) has a negative effect on photosynthesis only below the most dense clouds (not shown).

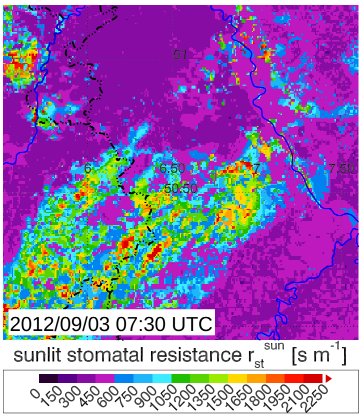

Figure 4.26.: Simulated r_{st}^{sun} [s m^{-1}], 2012/09/03 07:30 UTC.

On 21 May 2012 (CP2005), the relationship between A, TP and r_{st} is analyzed at 9 UTC, i. e. 1.5 h later than for CL0309. A broad band of stratiform clouds ranging from Luxemburg and Belgium to the region around Aachen (Fig. 4.24a) causes an attenuation of solar radiation to 150–250 W m^{-2} whereas in the other regions the solar radiation ranges from 300 W m^{-2} in

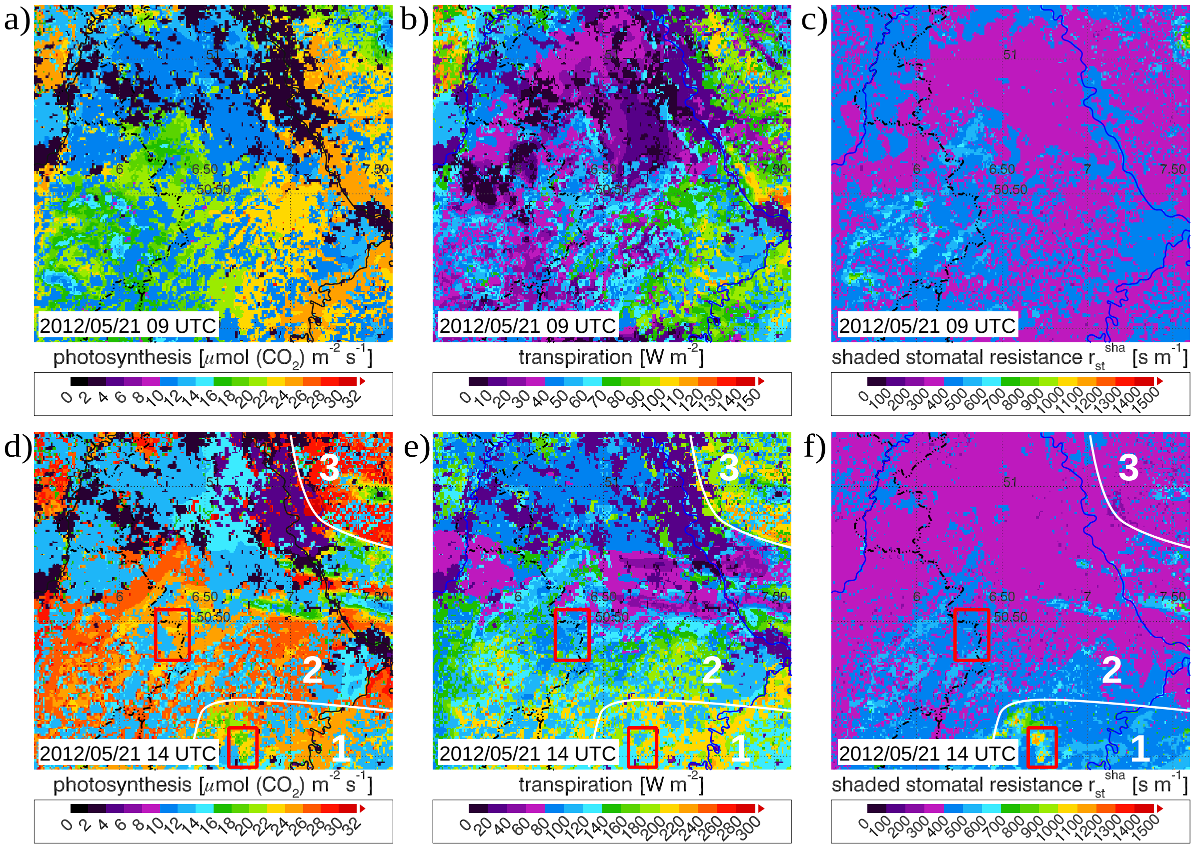

Figure 4.27.: Photosynthesis [μmol(CO$_2$)m^{-2}s^{-1}], transpiration [W m^{-2}] and r_{st}^{sha} [s m^{-1}] on 2012/05/21 09 UTC (a–c) and 14 UTC (d–f), simulated with TerrSysMP-CO$_2$ (CP2005).

the northeastern part to 430 W m^{-2} in the southeastern part of the NRW domain. Light limitation below the clouds leads to reduced photosynthesis rates of 15–21 μmol(CO$_2$)m^{-2}s^{-1} in broadleaf and needleleaf forests (Fig. 4.27a) compared to higher photosynthesis rates to the east (22–26 μmol(CO$_2$)m^{-2}s^{-1}). Transpiration is also reduced in the cloudy regions (Fig. 4.27b). Different from CL0309, below the clouds in the west, r_{st}^{sha} (and r_{st}^{sun}) is only slightly higher than in the east (Fig. 4.27c). The limited photosynthesis is partly compensated by limited transpiration due to the reduced solar radiation as well as by rather moist atmospheric conditions. Therefore, the stomata of leaves remain open allowing the uptake of CO$_2$ because the plants are not threatened by water loss (i. e. low transpiration rates).

In the afternoon (14 UTC), the situation is more complex. Again, in a region with thick clouds north of 50.5 °N photosynthesis and transpiration are reduced due to attenuation of solar radiation (cf. Figs. 4.24b and 4.27d, e). The more interesting feature is that in the southern model domain (region 1 in Fig. 4.27) photosynthesis of broadleaf forests is slightly lower (24–26 μmol(CO$_2$)m^{-2}s^{-1}) than in region 2 (26–28 μmol(CO$_2$)m^{-2}s^{-1}) although the solar radiation is higher in region 1 (600–750 W m^{-2}) than in region 2 (400–600 W m^{-2}). In the Bergisches Land (region 3) even higher photosynthesis rates are simulated (28–31 μmol(CO$_2$)m^{-2}s^{-1}) at similar solar radiation (400–500 W m^{-2}). In contrast, the transpiration rates of broadleaf forests in region 1 are higher (200–220 W m^{-2}) than in region 2 and 3 (160–200 W m^{-2}). Hence, on this particular day, the highest photosynthesis rates ("optimum conditions") are obtained at a solar radiation of about 400–600 W m^{-2}. At unattenuated solar radiation stronger transpiration and/or possible soil water stress ($\beta_{tran} < 1$, see Eq. 2.26) restrict photosynthesis. Hence, r_{st}^{sha} is slightly higher in region 1 ($\approx$ 400–550 s m^{-1}) than in region 2 ($\approx$ 350–450 s m^{-1}). The stronger CO$_2$ assimilation of broadleaf forests in region 3 than in region 2 is caused by higher atmospheric humidity ($T_{dew} \approx$ 15–18 °C in region 3, $T_{dew} \approx$ 11–15 °C in region 2), permitting even stronger stomatal opening ($r_{st}^{sha} \approx$ 300–400 s m^{-1}). r_{st}^{sun} shows a similar tendency but moisture restriction of photosynthesis is more evident for r_{st}^{sha}.

The influence of moisture stress in region 1 is even more pronounced in needleleaf forests (red boxes in Figs. 4.27d–f). In the southern box r_{st}^{sha} is distinctly higher than in the Central Eifel region. This allows higher photosynthesis rates (24–26 μmol(CO$_2$)m^{-2}s^{-1}) of needleleaf forests in the northern box than in the southern box (17–20 μmol(CO$_2$)m^{-2}s^{-1}). Furthermore, the photosynthesis rate of needleleaf forests in the cloud covered Eifel region is higher than on all clear sky days analyzed in Section 4.1.

Finally, below the very dense band of clouds on 13 June 2013 at 12 UTC (Fig. 4.24c) a similar strong inhibition of photosynthesis and transpiration is simulated than in the morning of 3 September 2012 in combination with stomatal closing in that region.

The results show that clouds can have very different effects on the behavior of plants simulated in the canopy fluxes module of TerrSysMP-CO$_2$. If solar radiation falls below 100 W m^{-2} the stomata of plants (partly) close (i. e. high r_{st}) because photosynthesis is not effective and leaf water can be saved. With more intense solar radiation ($\approx$ 100–300 W m^{-2}) both photosynthesis and transpiration is limited but r_{st} is only slightly increased. The light limitation of photosynthesis is partially compensated by low transpiration rates, i. e. leaves can leave their stomata open. Optimum conditions are simulated for solar radiation of about 400–600 W m^{-2} with effective CO$_2$ uptake and moderate transpiration whereas above 600 W m^{-2} the water loss by transpiration is high so that r_{st} again increases and photosynthesis is restricted. However, this upper threshold strongly depends on atmospheric humidity and temperature, soil water availability and on the PFT. Unfortunately, it is difficult to validate these effects against observed canopy fluxes because solar radiation is not measured at the EC stations. However, some comparisons of simulated and observed fluxes at cloudy conditions are shown in Chap. 5.

4.2.3. Spatio-temporal variability of atmospheric CO$_2$ mixing ratios

On 3 September 2012 (CL0309) the spatio-temporal variability of CO$_2$ mixing ratios is very pronounced. Whereas in the first half of the night in the flat terrain and in the mountainous regions a light southwesterly wind blows, east of the Rhine it is almost calm. This causes a distinctly stronger near surface CO$_2$ accumulation (435–460 ppmv) along the valleys of the Bergisches Land (e. g. Sieg, Agger) than in the other regions (Fig. 4.28a). After 0 UTC, east of the Rhine the CO$_2$ concentrations remain high but decreasing wind speeds allow also a strong CO$_2$ accumulation in the Ahr and Mosel valleys as well as in Belgium (Fig. 4.28b). Although soil respiration is already lower than in mid summer (weaker autotrophic respiration), in CL0309 the CO$_2$ contents near the surface are considerably higher than in CS2407 (cf. Fig. 4.8a) indicating again that the atmospheric flow is more important in determining the nocturnal CO$_2$ concentrations than the surface CO$_2$ flux itself.

At 6 UTC, very high CO$_2$ mixing ratios are simulated for CL0309 (Fig. 4.28c) reaching widespread 425–450 ppmv and up to 440–480 ppmv along and east of the Rhine. This can be explained with a combination of different processes. Firstly, very low wind speeds (0–2 m s^{-1} in most regions, see Fig. 4.23a) are simulated and, thus, anthropogenic emissions can cause a very prominent increase of near surface CO_2 mixing ratios in the flat terrain, especially in the urban area along the Rhine valley and in the Kölner Bucht (see Section 6.2 for more details). Moreover, clouds suppress or delay both the onset of CO_2 uptake by photosynthesis as well as the formation of a convective PBL in the early morning. Hence, clouds in combination with a weak atmospheric flow can result in very high CO_2 concentrations. The influence of clouds can be seen at 8 UTC as well, showing significantly lower CO_2 contents in the Hohe Eifel and the Hunsrück where a cloudless sky allows effective CO_2 assimilation (cf. Fig. 4.25a) whereas in the other Eifel regions the CO_2 concentrations remain elevated (Fig. 4.28d). Additionally, fossil fuel emissions in the Rhine metropolises and of the coal-fired power plants in the Jülicher Börde and along the Maas are apparent. In the following hours the influence of clouds on CO_2 contents in the PBL disappears and elevated CO_2 mixing ratios are only simulated downstream (northerly winds) of fossil fuel emissions (Fig. 4.28e). As in most situations, in the afternoon in the well-mixed PBL the CO_2 concentrations are rather homogeneous (Fig. 4.28f).

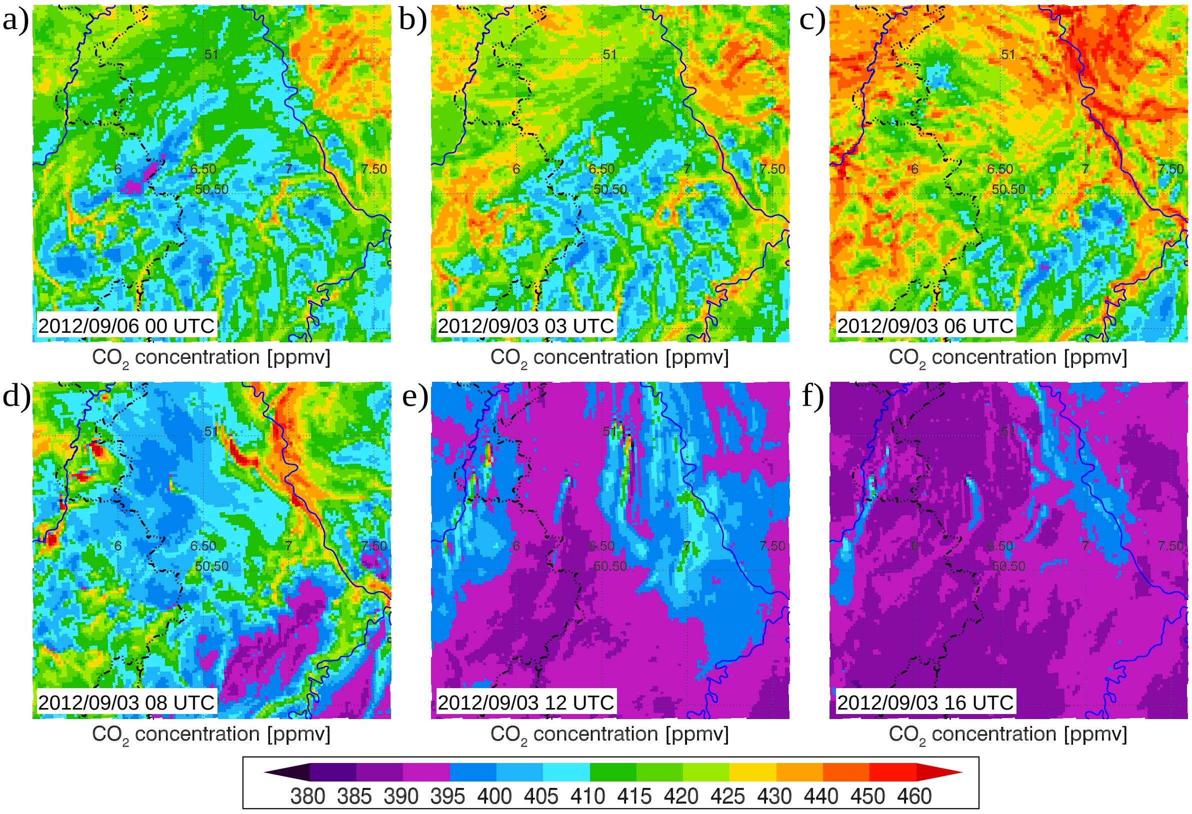

Figure 4.28.: Simulated CO_2 mixing ratios [ppmv] in the lowermost COSMO level on 2012/09/03 (CL0309) at a) 00 UTC, b) 03 UTC, c) 06 UTC, d) 08 UTC, e) 12 UTC and f) 16 UTC.

Similar to CL0309, in both nights of CP2005 (19/20 and 20/21 May) a weak synoptic flow (0–2 Bft) allows a strong nocturnal CO_2 accumulation yielding a diurnal CO_2 variation of on average 40 ppmv in the flat terrain. Locally, the CO_2 amplitudes are even higher, e. g. ≈ 50 ppmv in the Jülicher Börde (395–445 ppmv) on 20 May or 75 ppmv along the valleys in the Bergisches Land (370–345 ppmv) on 21 May (not shown). In contrast, except for the southeastern and eastern part of the NRW domain (wind: S–SW 2–3 Bft), in SP1306 (12/13 June 2013) the nocturnal CO_2 increase near the surface is weak (10–15 ppmv). In the Jülicher Börde and in the Netherlands, a moderate to fresh southwesterly wind (4–5 Bft) prevents the CO_2 increase almost completely. In the same region, the upcoming thick (pre-)frontal clouds in the morning hinder a CO_2 decrease due to lacking CO_2 uptake by plants. At 12 UTC, the relationship between clouds, biogenic CO_2 fluxes (i. e. NEE) and near surface CO_2 mixing ratios is apparent (see Figs. 4.29 and 4.24c). In the southeast high solar radiation (clear sky) makes a strong CO_2 uptake possible (i. e. NEE $\ll 0$). Below the band of clouds photosynthesis is suppressed and, thus, NEE is positive, especially in forests where soil and litter respiration is strong (Fig. 4.29b). Therefore, in these regions the CO_2 concentration in the PBL is 10–15 ppmv higher than in the southwest (Fig. 4.29a). Additionally, a moderate to fresh southwesterly wind (Fig. 4.29c) as well as entrainment of background CO_2 into the PBL due to vertical (pre-)frontal air mass transport further inhibit low CO_2 concentrations.

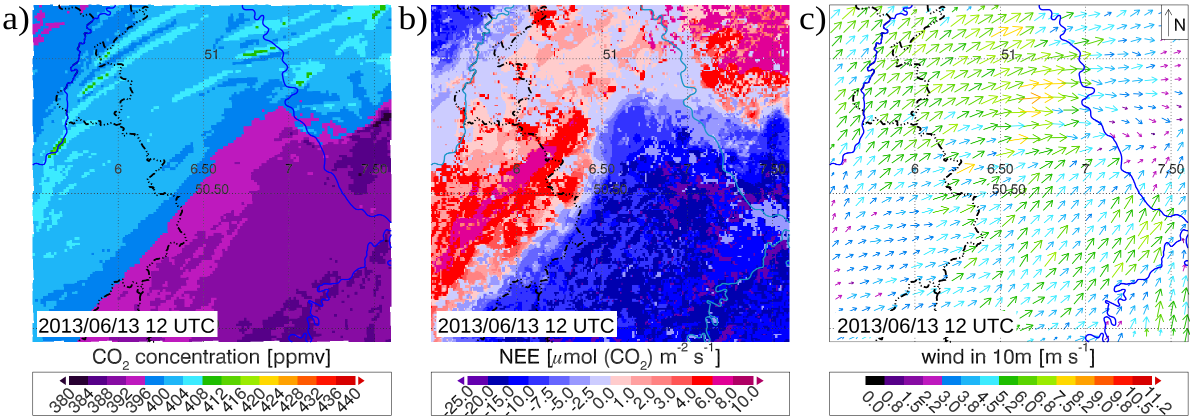

Figure 4.29.: a) Simulated CO_2 mixing ratio [ppmv] (lowermost COSMO level), b) NEE [$\mu mol(CO_2)m^{-2}s^{-1}$] and c) wind vectors [$m\,s^{-1}$] 10 m a.g.l., 2013/06/13 12 UTC (SP1306).

4.2.4. CO_2 budget in the NRW domain

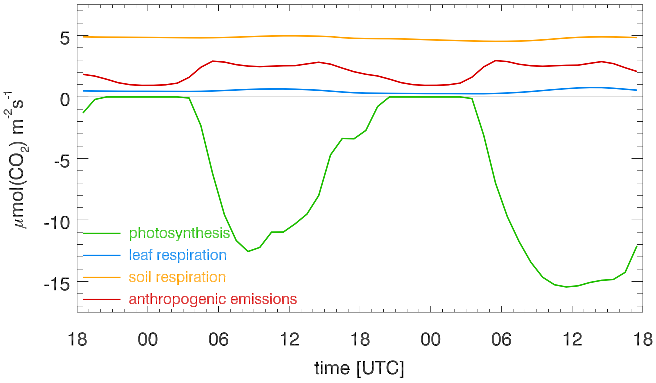

Figure 4.30.: CO_2 fluxes [$\mu mol(CO_2)m^{-2}s^{-1}$] of SP1306 averaged over the NRW domain.

In analogy to Section 4.1.6 the CO_2 budgets have been calculated for all case studies with clouds and precipitation (CP2005, CL0309, SP1306). In CL0309, caused by the widespread and thick stratiform cloudiness in the morning and cumulus cloudiness over mountainous regions in the afternoon, the average photosynthesis rate is considerably lower than in the clear sky cases (cf. Table 4.2 and 4.1). Contrary to this, ecosystem respiration is not affected by attenuation of solar radiation. Hence, together with anthropogenic emissions a net gain of atmospheric CO_2 is simulated for CL0309. On 13 June 2013 (SP1306), an overcast sky and stratiform rain in the afternoon yield even lower photosynthesis rates, although the LAIs are considerably higher than in CL0309. Fig. 4.30 shows a reduction of photosynthesis with upcoming thick clouds after 9 UTC. A second decrease occurs in the afternoon when rain is simulated. On this day, the biogenic net CO_2 flux is positive (i. e. net gain). In the following day, the photosynthesis curve is smoother because the sky is only partly covered by shallow cumulus clouds. In addition, the diurnal variation of anthropogenic emissions can be well seen in Fig. 4.30. An interesting outcome of these budget calculations is that, in contrast to all simulated clear sky days, on both days of CP2005 and on 14 June 2013 a net CO_2 loss is simulated although the sky is partly covered by shallow cumulus clouds (2012/05/20, 2013/06/14) or thin stratiform clouds (2012/05/21). If the attenuation of solar radiation is too weak to cause light limitation of photosynthesis or if the CO_2 uptake is not limited by atmospheric humidity or soil moisture, on cloudy days plants can assimilate more CO_2 than on clear sky days combined with a rather dry PBL or with high temperatures (heat stress). Another possible reason could be the additional source of diffuse radiation in occurrence of cumulus clouds that penetrates deeper into a forest canopy leading to a stronger CO_2 uptake (Freedman *et al.*, 2001).

date	**2012/05/20**	**2012/05/21**	**2012/09/03**	**2013/06/13**	**2013/06/14**
weather	*cloudy, shower*	*cloudy*	*cloudy*	*overcast, rain*	*partly cloudy*
photosyn.	−8.282	−8.092	−5.487	−4.897	−7.525
leaf resp.	*0.513*	*0.493*	*0.366*	*0.507*	*0.434*
soil resp.	*4.757*	*4.547*	*4.405*	*4.869*	*4.694*
total resp.	5.270	5.339	4.770	5.376	5.128
anthro.	1.773 [Sun]	2.221 [Mon]	2.200 [Mon]	2.025 [Tue]	2.047 [Fri]
budget	**−1.269**	**−0.532**	**+1.483**	**+2.504**	**−0.350**

Table 4.2.: CO_2 budget [μmol(CO_2)m^{-2}s^{-1}] of CP2005, CL0309 and SP1306 (− sink, + source).

4.3. Influence of rain on CO_2 fluxes

4.3.1. Local effects of strong convective precipitation on soil respiration

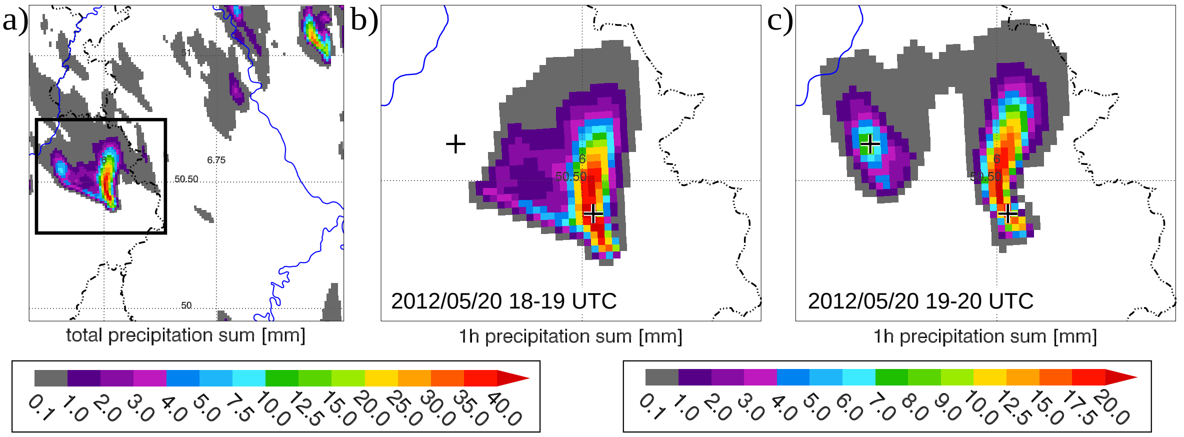

Figure 4.31.: a) Total simulated precipitation sum [mm] with CP2005 between 2012/05/19 18 UTC and 2012/05/21 00 UTC (left-hand legend) and 1h-precipitation sum [mm] in the boxed domain (right-hand legend) between b) 18–19 UTC and c) 19–20 UTC. The crosses mark the locations of time series shown in Figs. 4.33 and 4.35.

Convective rain events (e. g. thunderstorms) can change the soil hydrological conditions abruptly and often occur very locally. The effect of these local changes on soil respiration is analyzed in CP2005. As stated in Section 4.2.1, in the evening of 20 May 2012 a heavy thunderstorm develops in eastern Belgium in mountainous terrain. Between 18 and 19 UTC (Fig. 4.31b) the convective core drifts slowly northwards with 1h-precipitation sums up to 30 mm whereas a second branch with 4–7 mm is directed towards the northwest. Between 19 and 20 UTC (Fig. 4.31c) the thunderstorm splits into two convective cells with one moderate cell drifting northwestwards with maximum 1h-precipitation of about 8 mm and second a very intense and almost stationary cell with up to 25 mm precipitation per hour. Thus, in the central path of the northwards directed branch 30–40 mm precipitation is simulated within two hours (Fig. 4.31a). In the following hour both cells dissipate.

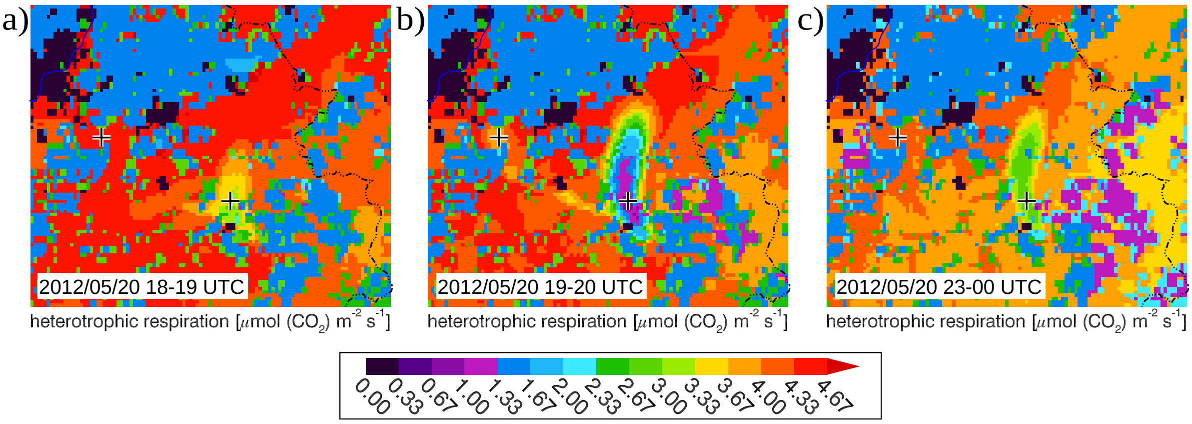

Figure 4.32.: Simulated heterotrophic respiration [μmol(CO_2)$m^{-2}s^{-1}$] (boxed domain of Fig. 4.31a) at 2012/05/20 between 18–19 UTC, 19–20 UTC and 23–00 UTC (2012/05/21).

Even between 18 and 19 UTC a significant reduction of heterotrophic respiration is simulated in the region with convective precipitation (Fig. 4.32a). Between 19 and 20 UTC in the core of the thunderstorm (15–40 mm) a further decrease can be seen with respiration rates of 0.9–1.3 μmol(CO_2)$m^{-2}s^{-1}$ compared to 4.0–4.5 μmol(CO_2)$m^{-2}s^{-1}$ in ambient forest PFTs. In the weaker convective branch (4–8 mm) heterotrophic respiration is only slightly reduced. In the following hours the heterotrophic respiration rates again increase but at 0 UTC (i. e. 3–4 h after the precipitation ceased) a reduction of about 30% is simulated in the strong convective part whereas no reduction can be identified in the region with weaker precipitation.

Fig. 4.33 depicts time series of total soil respiration and its compounds compared with a model simulation without moisture reduction. The time series of Fig. 4.33a is located at the grid point with the precipitation maximum (44.0 mm, clay-loam, needleleaf) whereas the right-hand time series is located in the center of the western convective cell (8.2 mm, clay-loam, broadleaf). Before and several hours after the rain event the water availability in the respiratory soil levels is nearly optimally (reduction of $R_h < 5\%$). The moisture reduction of autotrophic respiration is stronger due to a larger influence of the too wet subsoil. Caused by high amounts of rain in a short time period, total respiration is considerably reduced from 6.7 μmol(CO_2)$m^{-2}s^{-1}$ to 1.9 μmol(CO_2)$m^{-2}s^{-1}$ within two hours (Fig. 4.33a). The largest portion of this reduction ($\approx$ 3.5 μmol(CO_2)$m^{-2}s^{-1}$) results from heterotrophic respiration whereby more than 60% of this reduction comes from ceasing decomposition in the O horizon between 19 and 20 UTC.

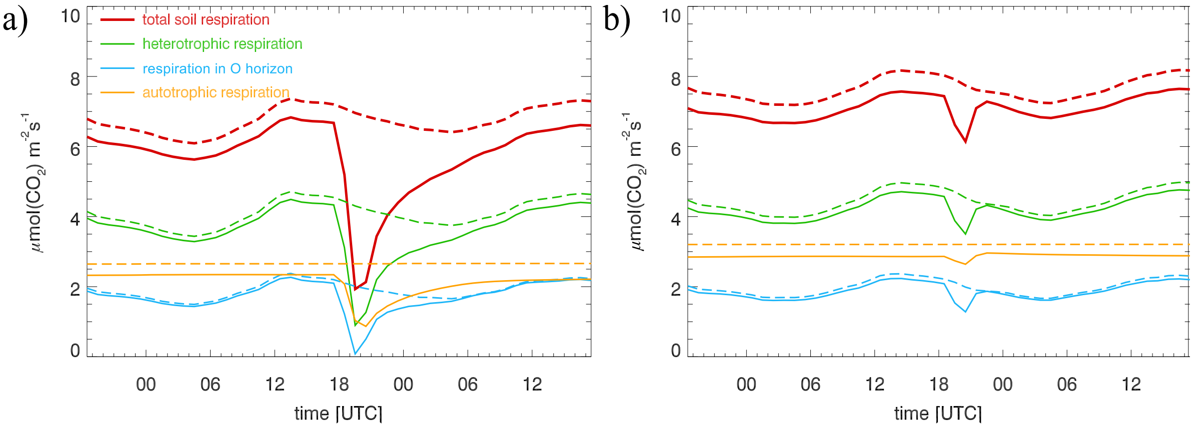

Figure 4.33.: Total respiration and its compounds [μmol(CO_2)$m^{-2}s^{-1}$] (solid lines) and the corresponding respiration rates without moisture reduction (dashed lines) of CP2005 for two selected grid points (see crosses in Fig. 4.32).

Thus one may conclude that the influence of heavy precipitation is stronger for forest PFTs with a O horizon than for grassland and arable soils. The initial respiration peaks shown in Borken *et al.* (2003) caused by wetting of dry litter cannot be simulated with the parameterization in TerrSysMP-CO_2 which may lead to an underestimation of respiration at the beginning of the rain event. Whereas respiration in the O horizon strongly increases after 20 UTC, total heterotrophic respiration shows some delay with the strongest increase after 21 UTC. Even in the morning hours of the 21 May (i. e. 10 h after the precipitation) a slight reduction is simulated. Autotrophic respiration shows a delay of 1–2 h between the minimum respiration rate and precipitation because the maximum effective root fraction is located between 17 and 29 cm depth, where the additional water arrives some hours after the rain event. The time series of respiration in the weaker cell shows only a reduction from 7.5 μmol(CO_2)$m^{-2}s^{-1}$ to 6.2 μmol(CO_2)$m^{-2}s^{-1}$ ($\approx$ 20%) within two hours. The reduction of autotrophic respiration is negligible (Fig. 4.33b). Contrary to Fig. 4.33a no long lasting reduction is simulated because the subsoil is not influenced. Again, about 75% of the reduction of heterotrophic respiration results from the O horizon.

Consistent with the decrease of heterotrophic respiration between 18 and 19 UTC, in the uppermost soil layer (0–1.75 cm) the moisture reduction factor $f(h)$ (Eq. 2.35) decreases from 0.96 to 0.55–0.8 (Fig. 4.34a) caused by an increase of soil water saturation from 80 to 85–95% for clay-loam and from 73% up to 86% in loamy soil (Fig. 4.34c). Between 19 and 20 UTC in the core of the eastern cell $f(h)$ decreases to 0.0–0.2 as the result of a soil water saturation of 97–100% for both soil types (see also Fig. 4.35a). In the weaker convective path the increase of saturation to 85–90% yields a $f(h)$ of 0.65–0.85. Just after the rain stops, the upper centimeters of the soil again dry out and $f(h)$ increases. At 0 UTC, the soil wetting can still be identified both in the weak and in the strong convective path (Fig. 4.34c) but heterotropic respiration in the upper soil layers is only reduced in the strong convective rain area (Fig. 4.34a). A slightly stronger reduction in loamy soil is caused by a slower seepage than in clay-loam. In soil layer 3 (4.5–9.1 cm, not shown in Fig. 4.34) a similar increase of soil water is simulated in regions with very strong precipitation ($>$ 30 mm) whereas in regions with less rain the saturation increase is weaker than in the uppermost soil layer (see also Fig. 4.35).

In the deeper topsoil (level 5, 16.6–28.9 cm), between 18 and 19 UTC no changes in soil

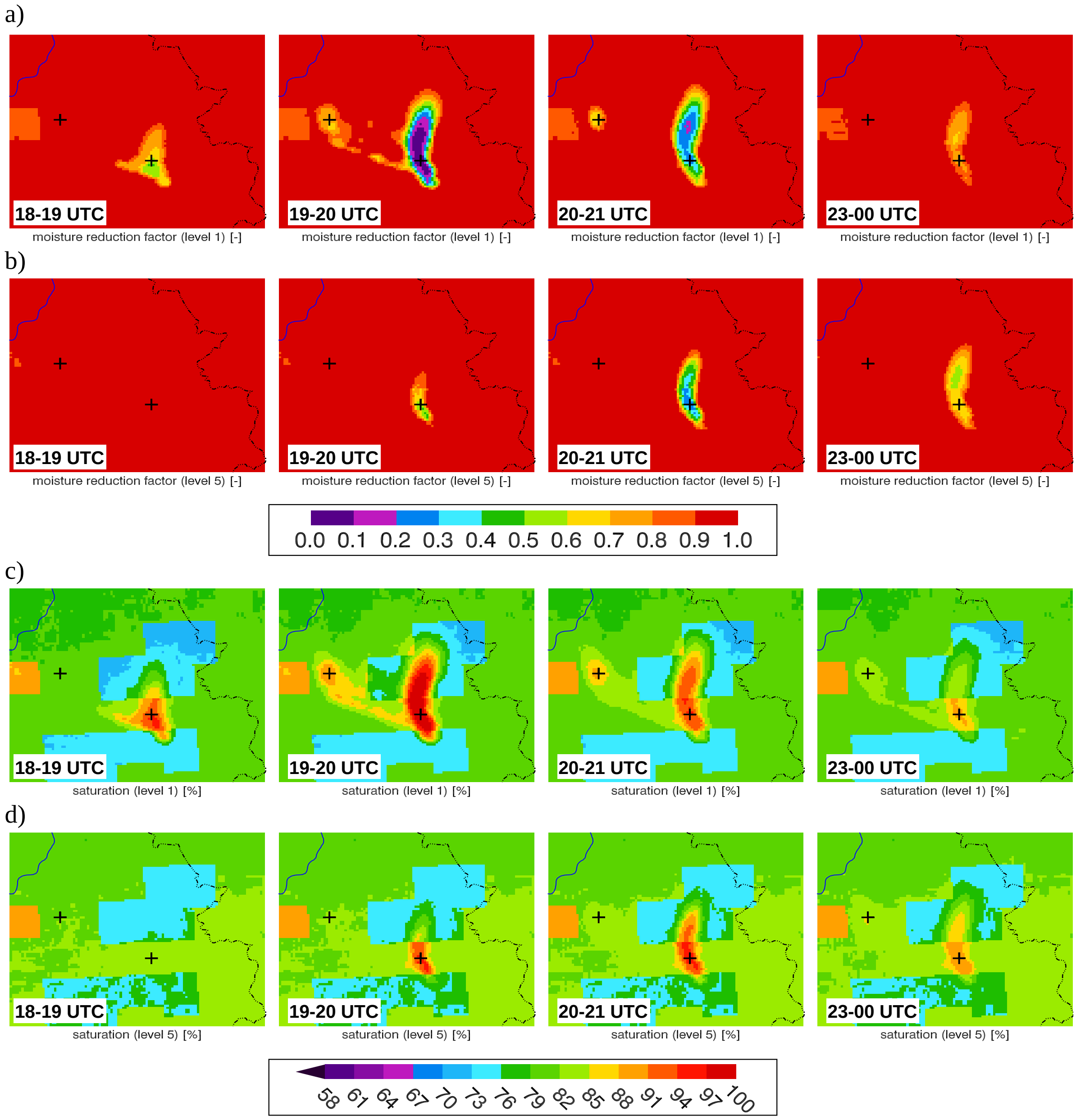

Figure 4.34.: Simulated moisture reduction ($f(h)$) of heterotrophic respiration and soil water saturation in 0.7 cm (level 1) (a, c) and in 21.2 cm (level 5) (b, d) at 2012/05/20, 18–19 UTC, 19–20 UTC, 20–21 UTC and 23–00 UTC (2012/05/21).

moisture can be identified and the maximum increase in soil moisture is simulated between 20 and 21 UTC yielding $f(h) = 0.25$–0.5 in the core of the thunderstorm (Fig. 4.34b, d). At about 0 UTC, the moisture reduction in this layer is stronger than near the surface, with again stronger reduction for loam than for clay-loam. In regions with weaker precipitation the soil water content increases only a few percent having a positive effect on $f(h)$ (Fig. 4.35b). The time delay of about one hour in level 5 as well as a considerably longer lasting effect of heavy rain on $f(h)$ can be clearly seen in Fig. 4.35a which is even significantly longer lasting in loam soils (not shown). The precipitation water of 44 mm reaches the subsoil (level 7, 49.3–83.0 cm) some hours after the thunderstorm dissipated yielding a soil water increase and $f(h)$ decreases to 0.55. After that increase no drying is simulated (Fig. 4.35a). Thus, in the subsoil even more than 20 hours after heavy rain heterotrophic CO_2 production is still attenuated. Moreover, the strong reduction and long lasting effect of autotrophic respiration is apparent. At the weak convective cell, heterotrophic respiration in the subsoil is not significantly modified (Fig. 4.35b).

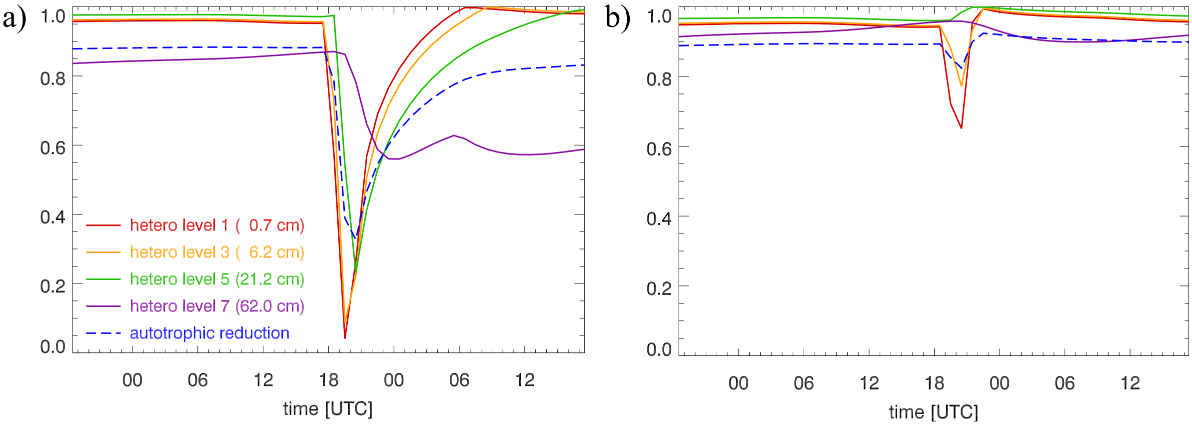

Figure 4.35.: Moisture reduction ($f(h)$) of heterotrophic respiration (solid lines) in different soil levels and of autotrophic respiration (dashed line) of CP2005 (same grid points is in Fig. 4.33).

These results show that heavy rain falling in a short period significantly reduces soil respiration both in the topsoil and in the subsoil. This reduction, caused by the increase of soil water up to 100% saturation (Eq. 2.35a), persists even several hours after the rainfall in the subsoil, at least when the soil water content is almost optimal ($f(h) \approx 1$) before the rain begins. Less amount of precipitation (< 10 mm) reduces soil respiration only slightly and for few hours. If the soil is detrimentally dry moderate rain can even have a positive feedback for microbial productivity (Eq. 2.35b, see also next section). The effect of soil moisture on the calculated respiration rates in different soil levels using Eq. 2.30 is simulated quite well, even without a coupling of RothC with a CO_2 transport model (e. g. SOILCO2). Nevertheless, the explicit calculation of CO_2 transport in the soil may further improve the model results (e. g. Herbst *et al.*, 2008), especially the exact timing of the response of soil respiration on heavy rain. Moreover, due to the 1D-behavior of CLM, moisture effects can only be analyzed for grid points that directly receive precipitation from COSMO because communication with neighboring grid cells is not possible in a COSMO–CLM configuration of TerrSysMP-CO_2. Thus, the influence of a strong surface runoff on neighboring grid cells (e. g. overland flow in brooks) – occurring especially in relation with very high rain rates – cannot be considered and an additional coupling with the hydrological model ParFlow could provide more precise results. However, except for such extreme rainfall, a coupling of COSMO with CLM (used in all simulations of this study) is an appropriate model setup for the simulation of canopy fluxes and atmospheric CO_2 dynamics.

4.3.2. Stratiform precipitation rain event

In SP1306 the effect of widespread stratiform precipitation on soil respiration is investigated. In the first 30 hours of the simulation 8–18 mm of rain are predicted in the western and north-western part of the domain and in the Siebengebirge and the Bergisches Land (Fig. 4.36a). In

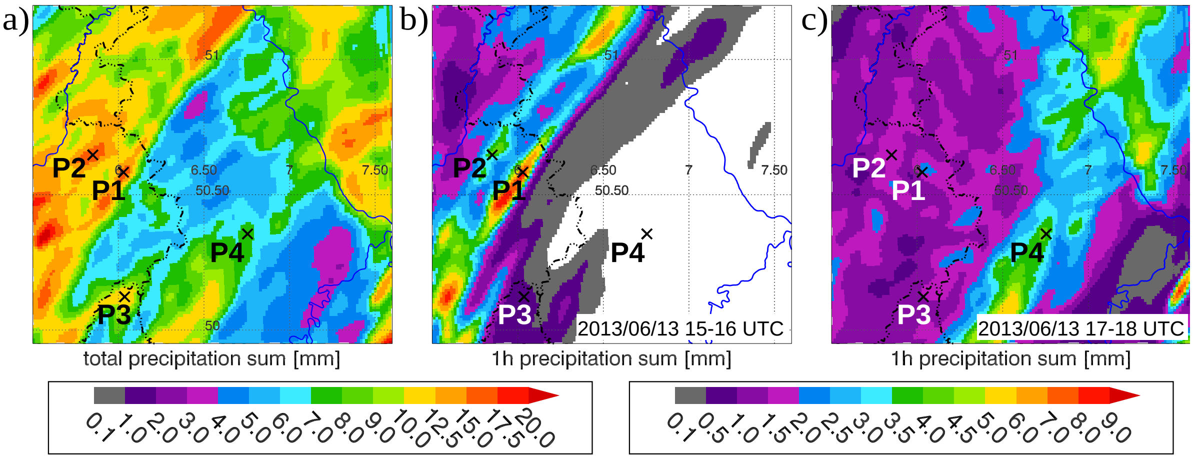

Figure 4.36.: a) Total simulated precipitation sum [mm] of SP1306 between 2013/06/12 18 UTC and 2013/06/14 00 UTC (left-hand legend) and 1h-precipitation sum [mm] (right-hand legend) between b) 15–16 UTC and c) 17–18 UTC (2013/06/13). P1–P4 mark the locations of time series analyzed in this section.

most regions of the Eifel and west of the Rhine less precipitation occurs (≈ 3–8 mm) with the minimum in the Mosel valley and in the lee of the Hohe Eifel. Except of some showery-like rain in the early hours of the model simulation, most of this rain is caused by an intense cold front in the afternoon and early evening of 13 June (Section 4.2.1). Along that front, moderate stratiform rain (2–4 mm h^{-1}) is simulated with some convectively induced intensifications (≈ 8 mm h^{-1}), see Fig. 4.36b. To the rear of this front light stratiform rain (1–2 mm h^{-1}) continues for 1–2 h which can be seen in the western part of Fig. 4.36c.

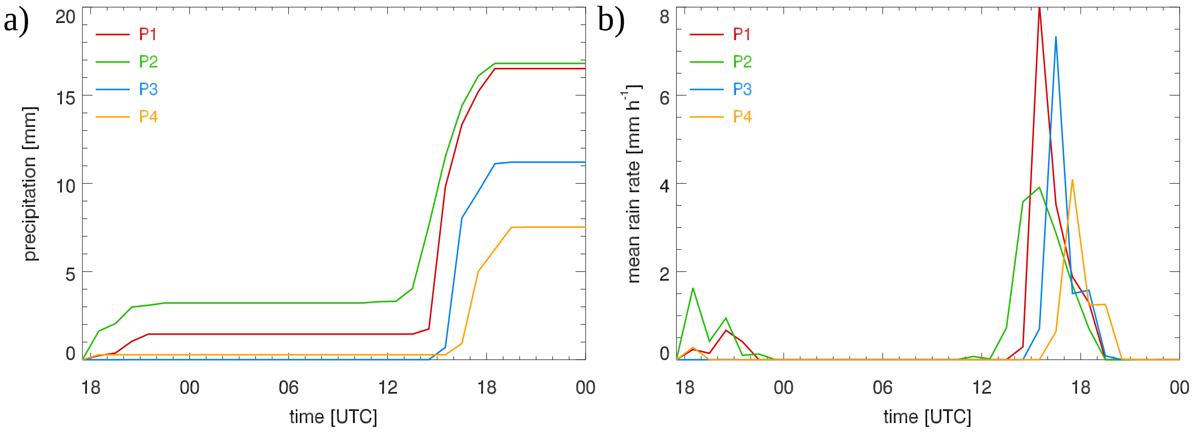

Figure 4.37.: a) Accumulated rain [mm] and b) mean hourly rain rate [mm h^{-1}] at P1–P4.

With the passage of the cold front, in SP1306 a significant reduction of auto- and heterotrophic respiration is only simulated in regions with convectively intensified rain with relatively high rain rates and high rain amounts. In contrast, in most areas with stratiform precipitation no reduction or even a slight increase of soil respiration can be identified (not shown). In order to investigate the influence of different total precipitation amounts and rain rates on soil respiration, 4 grid points (P1–P4) have been selected. At P1 and P2 similar amounts of rain (16.5 and 16.8 mm, see Fig. 4.37a) are simulated but P1 is influenced by convective rain between 15 and 16 UTC with a high mean hourly rain rate of 8.0 mm h^{-1}, whereas at P2 the rain is spread over several hours with a maximum rate of 3.9 mm h^{-1} only (Fig. 4.37b). With 11.2 mm at P3 less rain is simulated than at P1 and P2 but with a similar rain rate as for P1 between 16 and 17 UTC. At P4 7.5 mm of rain is accumulated in the model run.

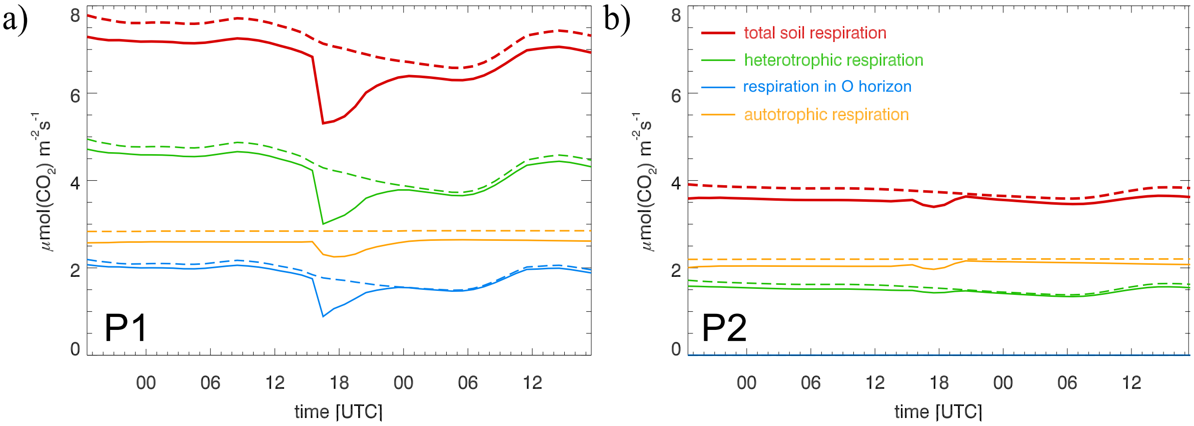

Figure 4.38.: Total soil respiration and its compounds [μmol(CO_2)$m^{-2}s^{-1}$] with moisture reduction (solid lines) and without moisture reduction (dashed lines) of SP1306 at P1 and P2.

Fig. 4.38 shows time series of soil respiration at P1 (needleleaf tree, loam) and P2 (crops, clay-loam). At P1, a significant decrease of soil respiration (≈ 20%) persisting for several hours is simulated as a result of relatively intense rain. Autotrophic respiration is only slightly reduced, but a considerable decrease of heterotrophic respiration in the mineral soil and in the O horizon can be seen. After this reduction, almost no difference occurs compared with the simulation without moisture reduction (dashed lines) due to optimal soil water conditions. Although at P2 the acummulated rain is similar to that of P1, here, soil respiration is only slightly reduced mainly due to a reduction of autotrophic respiration. Heterotrophic respiration is not significantly influenced because at crops no sensitive litter or organic matter layer is available and the weaker gradient in TOC depth profile at agricultural fields than at forest PFTs leads to a higher amount of heterotrophic respiration in the subsoil which is not influenced by the new rain water. Similar to P2, also at P3 (crops) only a moderate reduction is simulated and P4 (broadleaf tree) receives only a positive feedback as a result of moderate stratiform rain (not shown). Thus, instead of the amount of rain, the rain rate is the more important factor controlling soil respiration and the sensitivity of heterotrophic respiration on precipitation also depends on the PFT with the characterizing TOC depth profile.

In order to understand the different influences of rain on soil respiration, the moisture reduction $f(h)$ is analyzed. Fig. 4.39 depicts $f(h)$ in the uppermost soil layer. At 13 UTC (i. e. prior to the passage of the front) in the northwestern part of the domain as well as in the Kölner Bucht and Jülicher Börde the topsoil is quite dry leading to a $f(h)$ of 0.88–0.92 whereas in the rest of the domain the soil moisture is less detrimental for heterotrophic respiration (Fig. 4.39a). Some hours later, $f(h)$ decreases to 0.45–0.8 where convectively intensified rain was falling in the previous hour. These areas are surrounded by a widespread increase of $f(h)$ to 0.96–1.0 (Fig. 4.39b). After the passage of the front (Fig. 4.39c) some regions with reduced $f(h)$ of 0.7–0.85 can be identified (i. e. too high soil water content in these areas) whereas in most regions the stratiform precipitation of about 3–9 mm yields an increase of moisture in the topsoil

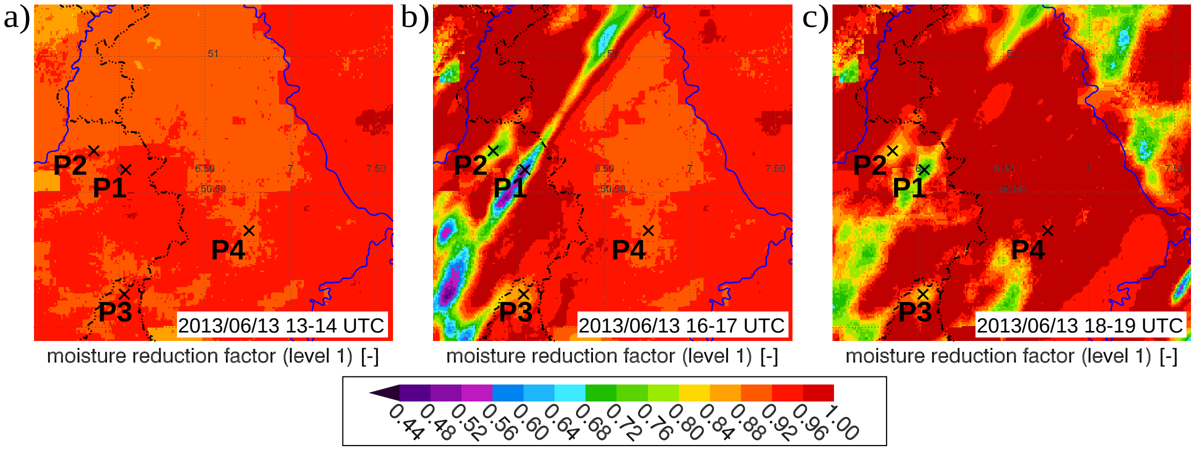

Figure 4.39.: Simulated moisture reduction ($f(h)$) of heterotrophic respiration in 0.7 cm (level 1) on 2013/06/13 (SP1306), a) 13–14 UTC, b) 16–17 UTC and c) 18–19 UTC.

resulting in almost optimal conditions for microbial activity ($f(h) \approx 1$). These improved soil water conditions (compared to Fig. 4.39a) continue for several hours and are achieved also in the regions with initially detrimental feedbacks of precipitation. Deeper in the soil (10–30 cm) the negative effects of precipitation diminish more and more in intensity and spatial extent, while the predominant feature is an increase of $f(h)$ with some delay to the rain (not shown). Similarly, the moisture reduction factor of autotrophic respiration increases slightly from 0.89–0.94 to 0.92–0.98 after precipitation except for the regions which are influenced by relatively strong convective rain.

Fig. 4.40 depicts the moisture reduction of P1–P4 in different soil layers. At P1 (high amount of rain, high rain rate) the strong decrease of $f(h)$ from 0.95 (72% saturation of loam) to 0.5 (89% saturation) in level 1 and to 0.67 one hour later in level 3 is evident (Fig. 4.40a). After a slight initial increase in level 5, about three hours after the strong rain event, $f(h)$ decreases. From 23 UTC to the end of the simulation the water conditions in the topsoil are better than prior to the rain. The decrease of autotrophic respiration is mainly caused by moisture reduction in the topsoil. In this grid cell even the subsoil (layer 7, 49–83 cm) is influenced leading to slightly too wet conditions compared to the optimum conditions prior to the rain. Although the accumulated rain at P2 (high amount, moderate rate) is comparable to P1, the feedback on respiration is fairly different (Fig. 4.40b). The moisture reduction is considerably less than at P1 with $f(h)$ decreasing from 0.93 (78% saturation of clay-loam) to 0.73 (89% saturation) in level 1 and to 0.82 in level 3. Prior to this decrease even a rain induced short-term increase of $f(h)$ can be identified. In contrast, in layer 5 (16.6–28.9 cm) the feedback on microbial activity is only positive. In spite of distinctly less rain at P3 (moderate amount, high rate), the higher rain rate than at P2 (Fig. 4.37b) yields similar time series of $f(h)$ with even slightly stronger reductions in level 1 and 3 just after the precipitation (Fig. 4.40c). Thus, not only the amount of rain but especially the rain rate controls the feedback of precipitation on soil respiration. At P4 (moderate amount, moderate rate) no negative effects of stratiform rain but an increase of $f(h)$ in all topsoil levels can be seen, showing that moderate rain improves the soil water conditions if the soil is too dry before the rain event. The same holds for the moisture reduction of autotrophic respiration.

These results show that precipitation can lead to very different responses on soil respiration.

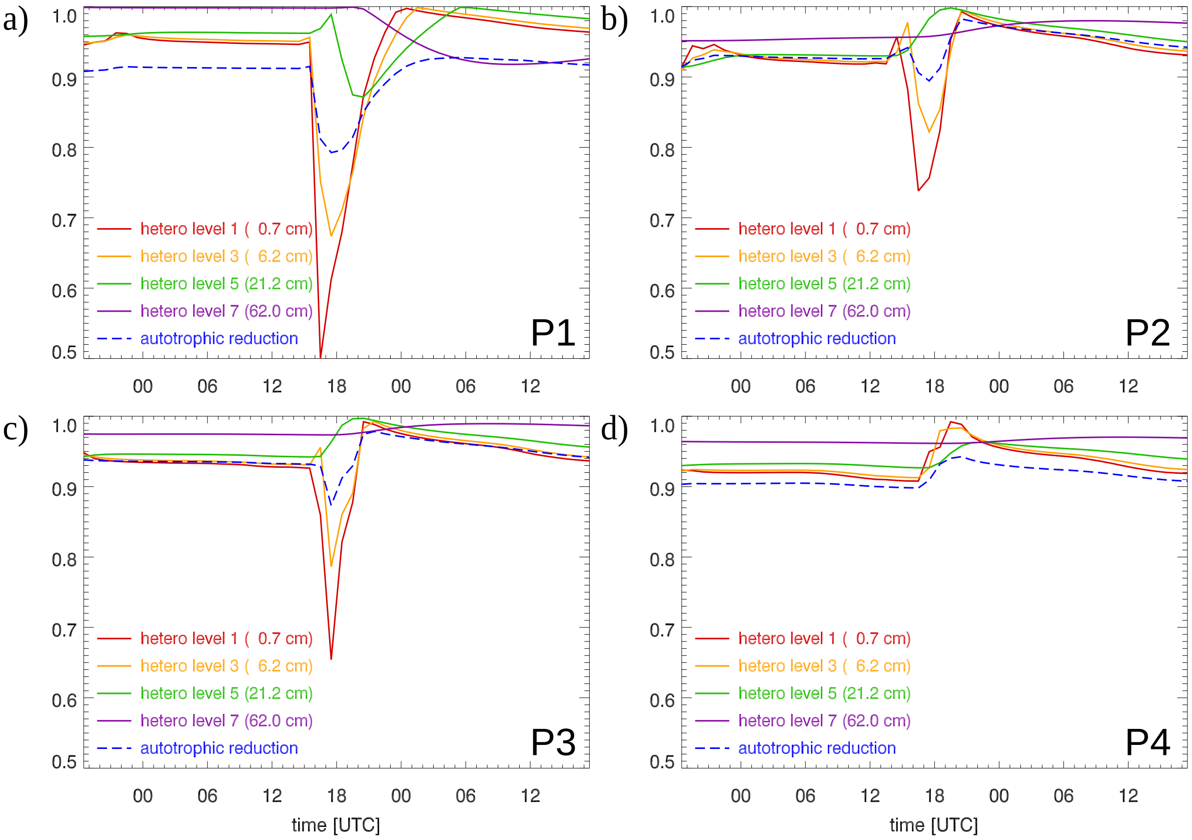

Figure 4.40.: Simulated moisture reduction ($f(h)$) of heterotrophic respiration (solid lines) in different soil levels and of autotrophic respiration (dashed line) of SP1306 at P1–P4.

Whereas intense rain (i. e. high rain rates) causes a strong reduction of soil respiration due to too wet conditions in the topsoil (see also Section 4.3.1), the same amount of rain, falling over a longer period (moderate rain rate), can also have a positive effect on soil respiration. Especially when the topsoil is rather dry (e. g. after a long summer period without precipitation) rain has predominantly positive effects on microbial activity because the topsoil becomes wetter leading to an increase of $f(h)$. However, if the soil moisture before the rain event is already in its optimum regarding microbial decomposition, additional precipitation can lead to a decrease of heterotrophic respiration. Hence, the initial soil moisture as well as the amount of rain and its intensity control the feedbacks on soil respiration. If the soil is only slightly too dry for optimal productivity rates, only a window of few percents in soil saturation decides if additional water is positive or (very) negative for soil respiration (see also Fig. 2.10b). This fact makes it difficult to compare these effects with measurements because the soil texture and heterogeneity as well as the actual moisture content itself may be very different to the simulations.

All effects of precipitation on soil respiration analyzed in Section 4.3 cannot be considered with the mesoscale biosphere–atmosphere models of past studies (Section 1.3) because the parameterizations in these models only depend on T_{soil}. The explicit consideration of soil moisture changes in TerrSysMP-CO_2 leads to a more consistent representation of soil respiration.

5. Verification of CO_2 and energy fluxes

In this chapter the simulated canopy fluxes (NEE, latent and sensible heat fluxes) and soil respiration are compared with measurements performed at several locations in the NRW domain.

5.1. Verification of NEE, latent and sensible heat fluxes

The net CO_2 flux between the canopy and the atmosphere (NEE) and the partitioning of absorbed solar radiation in latent and sensible heat fluxes are compared with EC measurements at six locations (see Fig. 3.1). The sites at Rollesbroich (RO), Niederzier (NI) and Kall-Sistig (KA) are grassland, whereby the observations at NI and KA were made with one mobile EC station and are not available at the same time. The EC station near Merzenhausen (ME) was placed at a winter wheat field (2012/13, 2013/14). A second field near Selhausen (SE) was tilled with potatoes (2012), winter wheat (2012/13) and oilseed raddish (2013/14). Both fields were managed according to standard agronomic practice (e. g. N fertilization, weed and diseases control). The EC station near Wüstebach (WU) was installed in 40 m a.g.l. above a spruce forest (i. e. evergreen needleleaf). Whereas ME, SE and NI are located in the flat terrain near Jülich, RO, WU and KA are in the Eifel region.

All EC stations are equipped with the LI-7500 gas analyzer[1] measuring high-frequent CO_2 and H_2O mixing ratios and with the CSAT3 3D sonic anemometer[1] measuring the velocity of the three wind components. The resulting EC fluxes used for verification of TerrSysMP-CO_2 are mean fluxes over an interval of 30 minutes. The fluxes are quality flagged (Mauder *et al.*, 2013) to filter out unrealistic CO_2, LH and SH fluxes. Moreover, the post-processing of the raw data includes the *random errors* of all fluxes, i. e. an uncertainty estimation determined with the individual uncertainty of each measurement variables. For the verification of simulated NEE two different CO_2 fluxes can be used. Cov$(CO_2'w')$ describes the covariance of the measured fluctuations of CO_2 mixing ratios (CO_2') and vertical velocity (w') and represents the CO_2 flux at the measurement height (2 m a.g.l., except for WU). For the measured "NEE" flux a *storage term* is added which is calculated by vertically integrating the difference of the actual CO_2 mixing ratio and that of the last 30 min interval assuming a vertically constant CO_2 content. Thus, this term represents a lower limit of respired CO_2 below the observation. Fig. 5.1 depicts the correlation of both CO_2 fluxes at ME (agriculture), RO (meadow) (years: 2011–2013) and WU (forest, 2013–2014). The scatter in the diagrams of ME and RO is rather weak and, thus, both CO_2 fluxes can be used for verification of simulated NEE. However, at the WU site the scatter is more pronounced indicating a non negligible "storage" of respired/absorbed CO_2 within the forest canopy (below 40 m a.g.l.). Unfortunately, for the year 2012 at WU only Cov$(CO_2'w')$ is available which has to be kept in mind for the following comparisons.

Additionally, on selected days in 2012 with fair weather conditions measurements of NEE, soil respiration and LAI were performed at the Merzenhausen winter wheat field and a winter wheat

---

[1] LI-7500 Open Path Gas Analyzer (LI-COR Biosciences, Lincoln, USA); CSAT3 (Campbell Scientific, Logan, USA); LI-6400XT Portable Photosynthesis System (LI-COR); LI-8100 Automated Soil Gas Flux System (LI-COR); LI-3100C Leaf Area Meter (LI-COR); SunScan Canopy Analysis System (Delta-T Devices, UK)

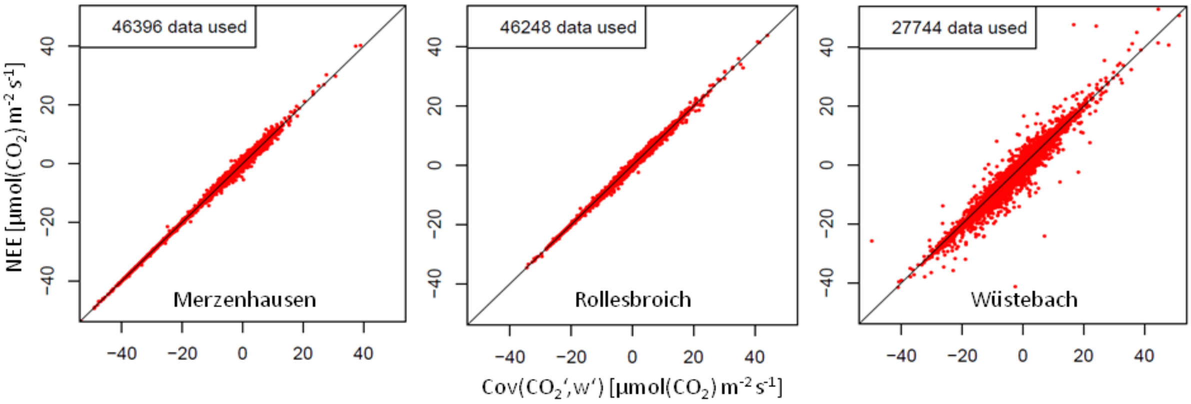

Figure 5.1.: Correlation of Cov($CO_2'w'$) and NEE measured with the EC stations at ME, RO and WU.

field near Selhausen (Stadler *et al.*, 2015; Kupisch *et al.*, 2015). At these fields several 1 m × 1 m plexiglass chambers are installed equipped with the LI-6400XT system[1] measuring CO_2 concentration changes within the chamber to estimate canopy level gas exchange (i. e. NEE) and with the LI-8100 system[1] measuring the rate of CO_2 increase within the chamber to estimate soil respiration (Kupisch *et al.*, 2015). The averaged fluxes of all chambers at each field are used for verification of simulated fluxes, there. The LAIs were determined destructively with the LI-3100C meter[1] and non-destructively with a SunScan analyzer[1] (Stadler *et al.*, 2015). Because these measurements were in each case made the day before the analysed periods of CS2605 and CS2407, two additional model runs have been performed for 25 May and 23 July 2012 using the background CO_2 of CS2605 and CS2407 as IC and LBCs, respectively.

Whereas photosynthesis is solely controlled by the stomatal resistance, the latent heat flux is composed of canopy transpiration, canopy evaporation and ground evaporation. On clear sky days canopy evaporation is negligible, except for some dew deposit at night and evaporation of dew in the morning. In Fig. 5.2 the simulated CO_2, latent and sensible heat fluxes are compared with EC and chamber measurements at different locations and for different land use. Obviously, at daytime the NEE of crops simulated with TerrSysMP-CO_2 cannot describe the strong CO_2 uptake of the winter wheat field in Merzenhausen (ME). One reason for this strong underestimation[2] of NEE may be a too low LAI (2.2 in TerrSysMP-CO_2). The non-destructively determined LAI at 17 May is very high, 5.81 (Stadler *et al.*, 2015), and the crop is rapidly growing (increase of canopy height from 65 cm to 84 cm between 16 and 31 May). In the maximum growing and flowering phase crops have a peak in seasonal NEE. A similar underestimation of NEE can be seen at the Selhausen (SE) winter wheat field on 25 May. Here, the green fraction of the destructive LAI is on average 2.78 and the non-destructive LAI is 3.36 (Kupisch *et al.*, 2015), i. e. lower than in Merzenhausen. Two days prior to the measurements the field had been fertilized and, thus, photosynthesis is not N limitated. In contrast, CLM uses a N limitation factor $a(N)$ of 0.61 for crops (Oleson *et al.*, 2010), i. e. 39% reduction of maximum photosynthesis. An additional and even more important reason for the NEE underestimation is the unappropriate plant physiological parameter set of the PFT "crop" in CLM (see Section 6.5). Noticeable in all simulated NEE curves of crops is a flattening between 9 and 17 UTC not occurring in the observations. Without any other restrictions

---

[2] Under-/overestimation of NEE refers to the absolute values, i. e. underestimation of NEE at night means too weak CO_2 release whereas at daytime underestimation of NEE means a too weak CO_2 uptake by the canopy.

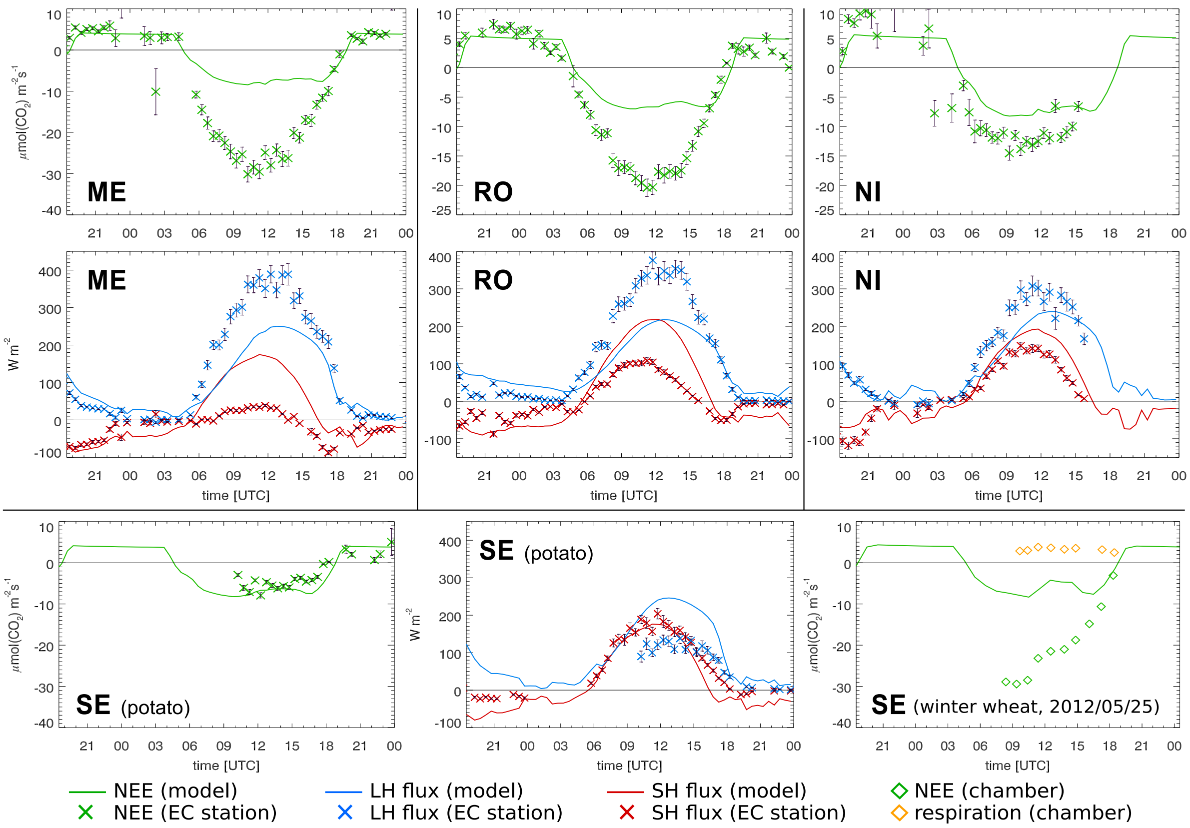

Figure 5.2.: Comparison of simulated NEE [μmol(CO$_2$)m^{-2}s^{-1}], LH and SH fluxes [W m^{-2}] with EC fluxes at Merzenhausen, Rollesbroich, Niederzier and Selhausen on 2012/05/26 and with chamber measurements (NEE, respiration) at Selhausen on 2012/05/25. The error bars denote the corresponding random errors.

the plant physiological parameters lead to a $V_{c,\max}$ of about 20–25 μmol(CO$_2$)m^{-2}s^{-1} for the simulated canopy temperatures (25–28 °C in the afternoon). Hence, the capacity utilization limitation of photosynthesis w_e (Eq. 2.21) is already reached for photosynthesis rates of 10–12.5 μmol(CO$_2$)m^{-2}s^{-1}, i. e. higher photosynthesis rates are not possible with this parameter set. In combination with respiration, this upper limit of photosynthesis explains the saturation of NEE at about -8 μmol(CO$_2$)m^{-2}s^{-1}. The strong underestimation of photosynthesis has also an influence on the LH/SH partitioning showing a significant underestimation of LH and an overestimation of SH fluxes simulated with TerrSysMP-CO$_2$. However, the simulated respiration rates are in accordance with the observations for both fields.

Similarly, the simulated grassland NEE underestimates the CO$_2$ uptake of the meadow in Rollesbroich (RO) between 7 and 16 UTC. The observed NEE continuously decreases to -20 μmol(CO$_2$)m^{-2}s^{-1} until 11 UTC followed by an increase (i. e. decrease of photosynthesis) afterwards (14–18 UTC). In contrast, the simulated NEE decreases to -7 μmol(CO$_2$)m^{-2}s^{-1} at 9 UTC, afterwards being rather constant until 17 UTC. The slight dent between 12 and 15 UTC results possibly from partly closure of the stomata to avoid desiccation in the afternoon caused by low dew point temperatures (see Fig. 4.1b). The flattening again indicates a capacity utilization limitation at lower photosynthesis rates than for midlatitudal grasslands. Soil respiration is predicted realistically, cf. the simulated and measured NEE at night. Consistent with the underestimation of photosynthesis too low transpiration rates cause an underestimation of the simulated LH fluxes and an overestimation of the SH fluxes. Footprint calculations for the EC station show that 55–75% of the measured fluxes come from the meadow with a grass height of 56 cm whereas 4–20% originate from the adjacent meadow (grass height: 20 cm). The measured NEE fluxes at the river meadow near Niederzier (NI) better coincide with the simulations. The observations show only a slightly stronger CO_2 uptake at daytime but rather constant NEE rates between 8 and 15 UTC. As a direct consequence, the partitioning of LH and SH is better than at Rollesbroich with only slightly lower (higher) LH (SH) fluxes in the simulation than those of the EC station. Different from Rollesbroich, the grass had been cut at 18 May (vegetation height ≈ 10 cm) explaining the lower photosynthesis rates.

The coincidence of the simulated NEE and SH flux with the measured fluxes at the potato field near Selhausen is well but for the wrong reasons. The potato plants began to sprout a few days before the considered day and have a vegetation height of only 10 cm on 25 May. Hence, the simulated LH flux is overestimated because at the potato field most of the LH flux results from ground evaporation and not from plant transpiration as in the simulation.

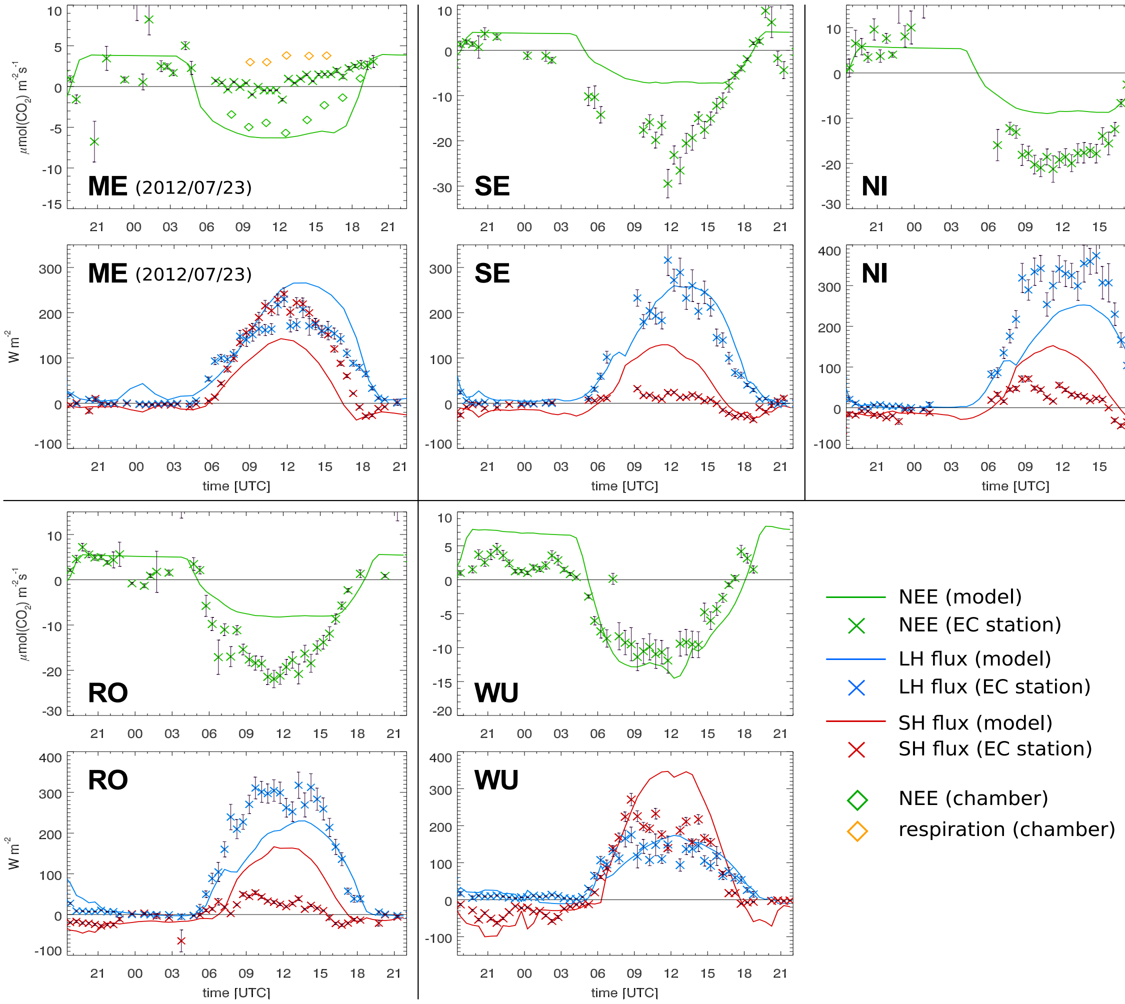

Figure 5.3.: As Fig. 5.2 but at Selhausen, Niederzier, Rollesbroich and Wüstebach on 2012/07/24 and EC and chamber measurements in Merzenhausen on 2012/07/23.

The comparison of the fluxes of CS2407 is depicted in Fig. 5.3. The winter wheat field in Merzenhausen is fully matured (Gelbreife, vegetation height: 92 cm, harvest: between 2 and 9 August). Hence, the NEE measured at the EC station on 23 July shows almost no photosynthesis. The simulated NEE is stronger negative, the LH flux is overestimated (overestimation of transpiration) and the SH flux is underestimated. The non-destructive LAI is still rather high (4.01), however it contains of green, senescent and dead leaves. Probably, the green fraction of the LAI is low[3]. The chamber measurements indicate still low photosynthesis with NEE rates between -4 and $-6\,\mu\text{mol}(\text{CO}_2)\text{m}^{-2}\text{s}^{-1}$ and respiration rates of 3–4 $\mu\text{mol}(\text{CO}_2)\text{m}^{-2}\text{s}^{-1}$. This illustrates the uncertainty of both measurement methods, e. g. the chamber can influence the microclimate and, thus, the CO_2 availability in the air modifying gas exchange (Langensiepen *et al.*, 2012). The daytime NEE of the potato field at Selhausen is strongly underestimated by TerrSysMP-CO_2. Thus, the plant physiological parameters are not suitable for broadleaf crops, too. The simulated LH flux seems to be realistically but the SH flux is strongly overestimated. Hence, in the model a higher fraction of solar radiation than at the potato field is absorbed by the canopy although the potato field is fully grown (plant height: 77 cm on 19 July).

For both grassland sites, Niederzier and Rollesbroich, at daytime the NEE is again underestimated, i. e. the capacity utilization limitation of photosynthesis is simulated at too low photosynthesis rates. However, the parameterization of canopy fluxes (NEE, SH and LH) seems to be consistent because the stronger the underestimation of NEE the stronger is the underestimation of simulated LH fluxes (and overestimation of SH fluxes) of all grassland and crop comparisons. Interestingly, similar to 26 May, the measured NEE curve at Niederzier is flatter at noon than the one in Rollesbroich although the grass of the meadow in Niederzier is very high (19 July: 59 cm, 2 August: 68 cm). The measured NEE in Rollesbroich is more negative than in Niederzier although 60–80% of the fluxes (footprint analysis) originate from the adjacent meadow having a grass height of 20 cm only. This probably indicates different plant physiological behaviors of the two grasses[4] demonstrating the limits of a model verification with 1–2 test sites for each vegetation class and with a limited number of case studies.

Different from agricultural and grassland fields the simulated fluxes of needleleaf forest describe the measured fluxes above the spruce forest near Wüstebach (WU) fairly well. Both the simulated absolute values and the course of NEE are in good agreement with the EC fluxes at daytime. The same holds for the LH fluxes. Between 10 and 14 UTC the SH fluxes are overestimated by TerrSysMP-CO_2, however the simulation of the previous day is in good accordance with measured LH *and* SH fluxes (not shown). Compared with the energy and CO_2 fluxes of grassland, winter wheat (CS2605) and potatoes (CS2407) in their mature stage, the needleleaf forest has the lowest NEE and LH fluxes and the highest SH fluxes. Thus, it is the only vegetated canopy having a Bowen ratio (i. e. SH/LH) greater than 1 at noon and in the afternoon. This agrees well, e. g., with measured and simulated fluxes of grassland, winter wheat and a pine forest in southwestern France (Sarrat *et al.*, 2009) which show the same behavior. At first glance, the simulated nighttime respiration is overestimated by TerrSysMP-CO_2. However, NEE is compared with $\text{Cov}(CO_2'w')$ in 40 m a.g.l. which does not necessarily represent the true CO_2 release of leaf and soil respiration (Fig. 5.1). Especially during clear sky nights, a strong temperature inversion inhibits a turbulent transport of respired CO_2 up to the measurement height, i. e. CO_2 is stored within the canopy (forest height $\approx$ 20–25 m) until the nocturnal PBL dissipates in the morning (see also Section 7.3.5).

---

[3] cf. green LAI at the winter wheat field in Selhausen < 0.5, harvest: 27 July

[4] the RO site is managed with liquid manure and possibly does not represent an unmanaged European C_3 grass

In CS1808 the potato field in Selhausen is well represented by TerrSysMP-CO_2 (Fig. 5.4). The nocturnal respiration seems to be simulated realistically (insofar as the EC fluxes are reliable) as well as the maxima of the rather weak daytime CO_2 uptake because the aboveground plant fraction is already declining (plant height: 43 cm). Noticeable on both days is an overestimation of NEE in the afternoon. The reason for this are hot temperatures (18 August: > 30 °C, 19 August: > 35 °C) in combination with moderate PBL humidity causing a closure of the stomata of potato plants. The dip in the simulated NEE also indicates moisture limitation, but the reduction is less pronounced than in the observations because broadleaf crops are more susceptible for moisture limitation than cereal crops. Additionally, the simulated afternoon temperatures are too low in CS1808 which further weakens the effect of stomatal closure.

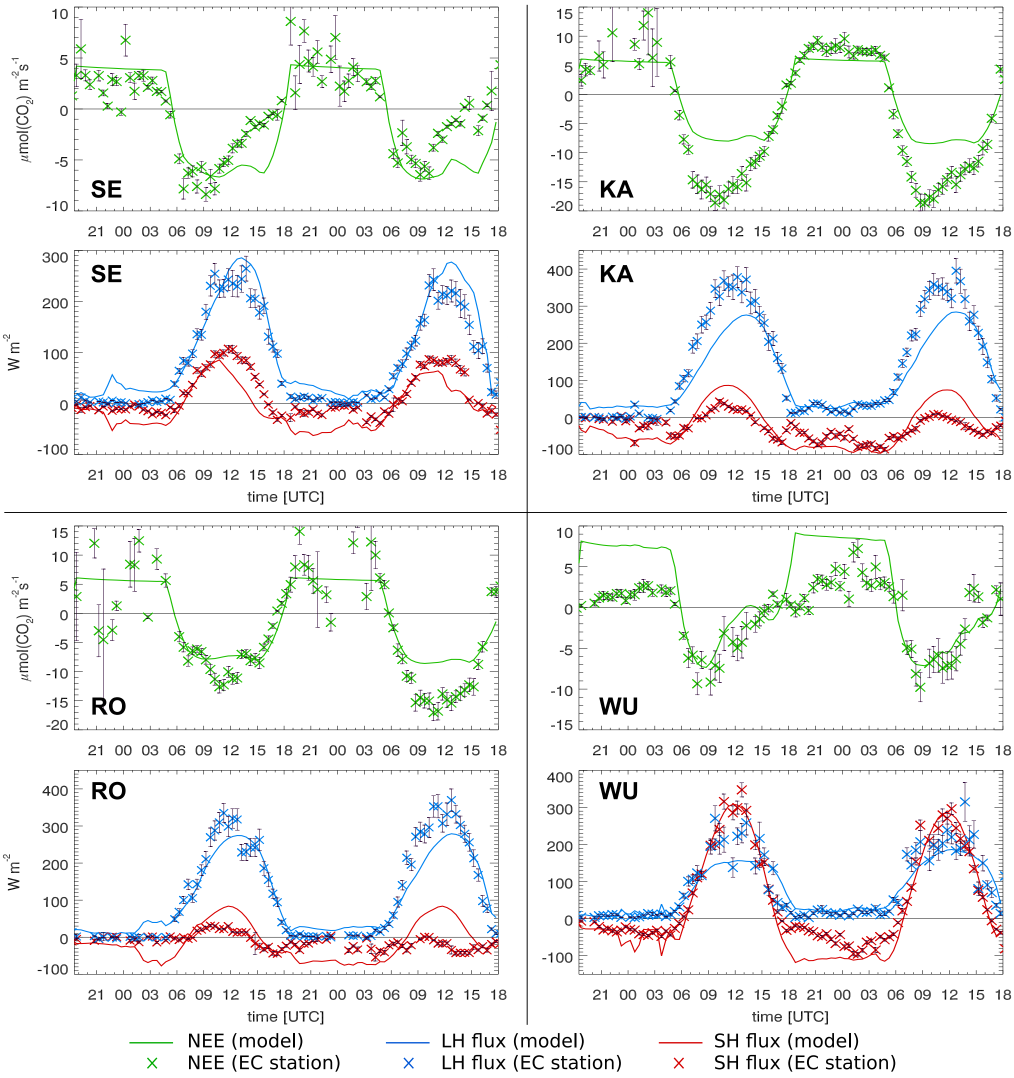

Figure 5.4.: As Fig. 5.2 but at Selhausen, Kall-Sistig, Rollesbroich and Wüstebach on 2012/08/18–19.

The simulated daytime NEE of grassland is again too low with a stronger deviation for the pasture near Kall-Sistig (KA) than for Rollesbroich. Between 14 and 24 August the grass of Kall-Sistig was rapidly growing from 15 cm to 39 cm and in Rollesbroich on 14 August a grass height of 17 cm was measured, i. e. similar grass heights at both meadows. Nighttime respiration cannot be analyzed except for the second night in Kall-Sistig indicating slightly higher rates in the observations. Due to lower simulated SH fluxes than in CS2605 and CS2407 (nighttime and daytime) the overestimation of daytime SH fluxes is less pronounced than in the other case studies. At both grasslands the LH fluxes are slightly understimated, especially between 7 and 13 UTC. In the early morning and in the afternoon, combined with a better agreement of photosynthesis, also the simulated LH fluxes are in accordance with the observations.

The daytime NEE of needleleaf forest agrees fairly well with the observations in Wüstebach showing the maximal CO_2 uptake at about 9 UTC and a decrease of photosynthesis afterwards coming along with increasing atmospheric temperatures. Moreover, the simulated energy fluxes are in accordance with the EC fluxes. Similar to CS2407 and contrary to the other PFTs the SH fluxes of needleleaf forests are higher than the LH fluxes because transpiration of needleleaf trees is lowest. Hence, the plant physiological behavior of this PFT is well represented by TerrSysMP-CO_2. On 18 August, the measured LH fluxes tend to be slightly higher than in the simulations but the fluxes are strongly fluctuating. The measured nighttime NEE clearly shows the decoupling of the EC flux from the actual respired CO_2 within the forest. Although in both nights the soil temperatures and soil moistures are similar, the EC fluxes are very low in the first night but higher and more fluctuating in the second night. These differences cannot be explained by different soil respiration so that lacking turbulence in the windless first night must cause the low NEE rates. Thus, nighttime respiration of a forest cannot be analyzed with EC fluxes, at least when a stable stratified nocturnal PBL is observed.

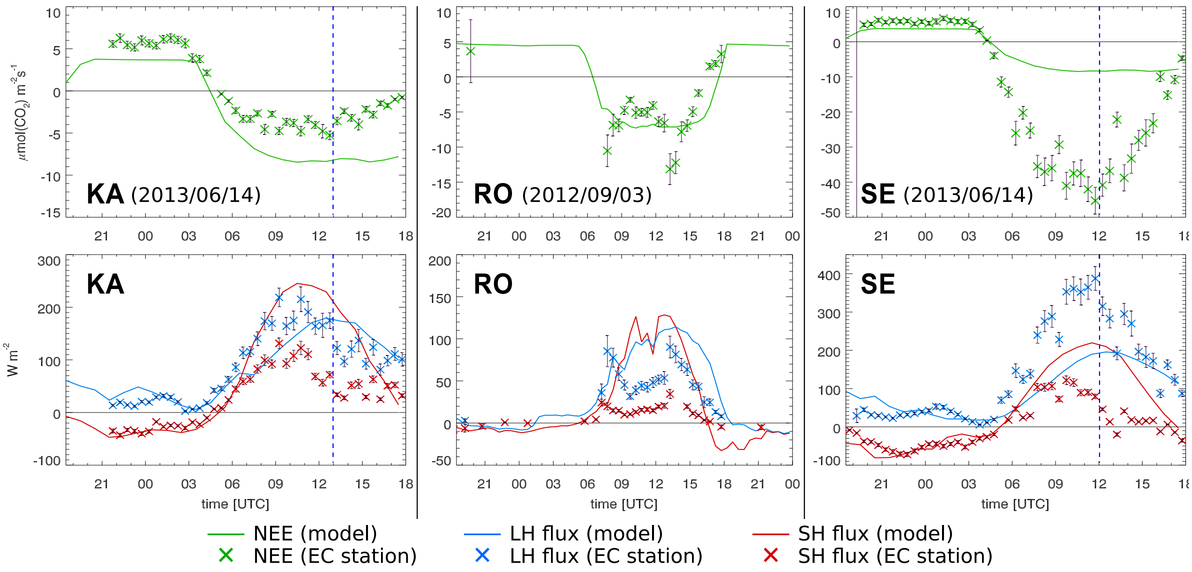

Figure 5.5.: As Fig. 5.2 but at Kall-Sistig and Selhausen on 2013/06/14 and Rollesbroich on 2012/09/03.

The verification of the effect of clouds on observed NEE and energy fluxes is difficult. Incident solar radiation is not available for the considered EC stations. Hence, only energy fluxes can be considered. Moreover, either the exact location and thickness of simulated clouds does not coincide with observed clouds or the occurrence of clouds is correlated with increased wind speeds and precipitation and, thus, EC fluxes are not available for these intervals. Nevertheless, with Fig. 5.5 an attempt is made to qualitatively analyze the effect of clouds on observed NEE and energy fluxes. On 14 June 2013, the simulated daytime NEE of grasslands is slightly stronger than in Kall-Sistig as a result of slightly underestimated soil respiration and a grass height of less than 20 cm. After 13 UTC (dashed line) the solar radiation at Kall is significantly attenuated, indicated by reduced LH and especially by reduced SH fluxes. In contrast, NEE shows no clear reduction after 13 UTC. This is consistent with the findings of Section 4.2.2 showing that moderate attenuation of solar radiation stronger reduces transpiration than photosynthesis because the stomatal resistance remains low.

On 3 September 2012, in Rollesbroich a strong attenuation of solar radiation can be observed between 9 and 13 UTC which significantly reduces LH ($< 50\,\mathrm{W\,m^{-2}}$) and SH fluxes ($< 20\,\mathrm{W\,m^{-2}}$). Different from the previous example this radiative attenuation is strong enough to efficiently reduce photosynthesis. The simulated incident solar radiation is overestimated for this period and, thus, also the energy fluxes and NEE are reduced. Finally, on 14 June 2013 the unappropriate parameterization of crops in CLM is apparent. However, the focus is on the attenuation of radiation after 12 UTC indicated by reduced LH and SH fluxes in the observations. Similar to the pasture near Kall-Sistig, the NEE of the winter wheat field in Merzenhausen is not significantly influenced demonstrating that moderate solar radiation is enough to take up CO_2 efficiently by photosynthesis of cereal crops being in the mature stage (vegetation height: 80 cm). Of course, these few examples are not enough to verify the influence of clouds on simulated NEE and energy fluxes against corresponding observations.

From the comparison of simulated and observed fluxes the following conclusions can be drawn. The simulated NEE and energy fluxes of needleleaf forest agree fairly well with the EC fluxes above a spruce forest in Wüstebach. The seasonal LAI and the plant physiological parameters of needleleaf forest seem to be appropriate. Unfortunately, for broadleaf forests (31% land cover) no observations are available for verification. Both cereal (e. g. winter wheat) and broadleaf crops (e. g. potatoes) in their growing and mature stage cannot be described with the plant physiological parameters of PFT=15 (crops) in CLM (see also Sulis *et al.*, 2015) and with *one* seasonal LAI for both plant types. The comparisons indicate a strong underestimation of NEE at daytime as well as an underestimation of LH fluxes and an overestimation of SH fluxes at Selhausen (potatoes) and Merzenhausen (winter wheat). The major reason for this are the used plant physiological parameters being inappropriate for intensively managed agricultural fields (e. g. N fertilization) in Central Europe. The capacity utilization limitation of photosynthesis is reached at too low photosynthesis rates and the N limitation factor of crops may be adapted for fertilized cultivation. Keeping in mind that agriculture (i. e. PFT=15) is the dominant PFT in the NRW domain (37%) these inaccurate fluxes may have a significant influence on the PBL evolution and the atmospheric CO_2 contents. Thus, the plant physiological parameters have to be adapted (see Section 6.5). Similarly, the simulated daytime CO_2 assimilation of grasslands is underestimated, however grassland plays a minor role in the NRW domain (5% land cover). The deviation of the fluxes from the observations depends also on the actual grass height.

In general, the canopy parameterization of CLM is consistent which means that an underestimation of NEE leads to an underestimation of LH fluxes via the link between photosynthesis and transpiration and the energy fluxes are simulated well if the simulated NEE is in agreement with the observations. Both the simulations and observations of needleleaf trees show the lowest NEE and highest SH fluxes. *Measured* NEE and LH fluxes of agricultural fields are highest. This is in accordance with the results of comparable model studies and measurement campaigns in Europe (e. g. Ahmadov *et al.*, 2007; Sarrat *et al.*, 2009; Tolk *et al.*, 2009). The present comparisons are a first step towards a comprehensive model validation. For more quantitative conclusions more model simulations as well as more measurement stations are necessary. However, this is beyond the scope of this study.

5.2. Verification of soil respiration

In this section, soil respiration, calculated with the newly implemented parameterizations of hetero- and autotrophic respiration in TerrSysMP-CO_2 (Sections 2.4 and 2.5), is compared with measurements at the Rollesbroich site as well as for the winter wheat fields in Merzenhausen and Selhausen. In Rollesbroich, soil respiration was measured automatically with the LI8100 system[1] in a polypropylene collar (20 cm diameter) inserted into the soil (Borchard *et al.*, 2015) and soil temperature (T_{soil}) and moisture was measured with the 5TM sensor (Degacon Devices, USA) 5 cm below the ground. The upper soil is classified as clay-silt (Cambisol, 61% silt, 20-22% sand, 17–19% clay) with a thickness of 0.5–2.0 m and an estimated TOC content of $\approx 207\,\mathrm{t\,ha^{-1}}$ in the upper 70 cm (Steffens, 2007; Qu *et al.*, 2015) (TerrSysMP-CO_2: $219\,\mathrm{t\,ha^{-1}}$ in 0–83 cm). Similarly, the soil at the Selhausen site is a glay-silt (Luvisol, 60–70% silt, 15–22% clay, 10–20% sand) with a high gravel content in the eastern part. At the field in Merzenhausen silt-loam (haplic Luvisol) is dominant (Stadler *et al.*, 2015) with an even higher silt content (80-85%, ≈ 15% clay, 3% sand). In TerrSysMP-CO_2 at all locations clay-loam is assumed (35% clay, 35% sand, 30% silt), i. e. the real soils have lower clay and sand contents and higher silt contents. Hence, the water holding capacities are probably higher than in the model.

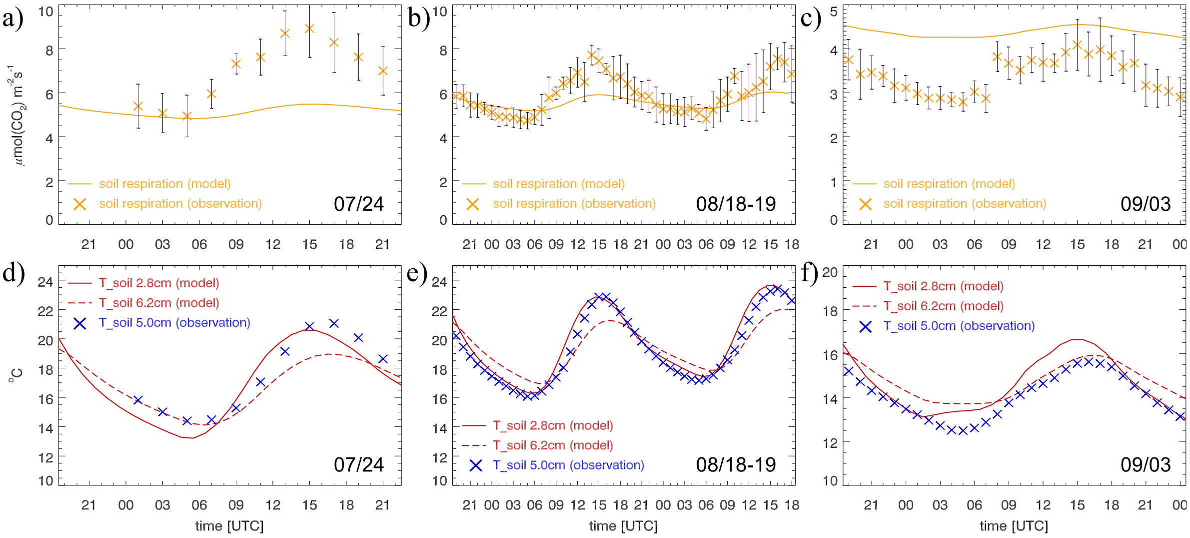

Figure 5.6.: Comparison of simulated and observed soil respiration $[\mu\mathrm{mol(CO_2)m^{-2}s^{-1}}]$ and soil temperature [°C] in Rollesbroich on 2012/07/24 (a, d), 2012/08/18–19 (b, e) and 2012/09/03 (c, f). The error bars in a–c denote the standard deviation of the measurements.

The measured soil respiration and T_{soil} of Rollesbroich are compared with the simulations of CS2407, CS1808 and CL0309. On 24 July the simulated soil respiration agrees well with the observations at night but it is underestimated at daytime (Fig. 5.6a), i. e. the diurnal variation is underestimated in the model. The measured T_{soil} in 5 cm depth is compared with the simulated T_{soil} in 2.8 cm (CLM soil level 2) and 6.2 cm (level 3). Whereas the timing of the maximum/minimum better conforms with the simulated variation of T_{soil} in 6.2 cm, the amplitude is similar to that in 2.8 cm (Fig. 5.6d). In general, CS2407 simulates T_{soil} well with only a slightly lower T_{soil} in 6.2 cm in the afternoon. Thus, the smaller amplitude of simulated soil respiration cannot be explained by T_{soil}. One reason of the underestimated soil respiration at daytime may be a dense tangle of roots in the upper soil in Rollesbroich which is highly sensitive on T_{soil} variations and causes higher respiration rates than for typical grassland sites (M. Herbst, personal communication, July 2014). Moreover, at a volumetric water content (θ) of 0.37–0.39 $m^3\,m^{-3}$ soil respiration is not moisture limited. However, the moisture limitation factor ($f(h)$) in CS2407 is also high ($\approx$0.95). Similar to CS2407, the diurnal variation of soil respiration in CS1808 is lower than in the observations, but the rates agree well at night and are less underestimated at daytime (Fig. 5.6b). The simulated and measured T_{soil} are 2–4 °C warmer than on 24 July and the measured variation is in accordance with the simulated T_{soil} in 2.8 cm whereas the phase is shifted one hour earlier than in 6.2 cm (Fig. 5.6e). The measured θ of 0.29–0.30 $m^3\,m^{-3}$ (porosity: 0.44 $m^3\,m^{-3}$ in 5 cm) suggests a stronger moisture limitation than in the model ($\theta = 0.34\,m^3\,m^{-3}$, $f(h) \approx 0.9$, porosity: 0.44 $m^3\,m^{-3}$). On 3 September, the simulated soil respiration is slightly higher than in the observations which can be explained by slightly higher T_{soil} in CL0309 (Fig. 5.6c, f) and a lower measured porosity in the subsoil which may lead to supersaturation. The observed diurnal variation is less than in the other cases due to lower T_{soil}. Moisture limitation in the topsoil is weak in the model and in reality ($\theta = 0.35\,m^3\,m^{-3}$ in TerrSysMP-CO_2, $\theta = 0.36\,m^3\,m^{-3}$ in the observations).

Fig. 5.7 compares simulated and observed soil respiration at winter wheat fields near Jülich. The simulated rates at Selhausen (25 May) are in the error range of most observations. Similarly, the simulated soil respiration agrees fairly well with the observations near Merzenhausen (23 July). Despite of the different soil types of the model and at the measurement sites with different water holding capacities and clay contents, the simulated respriation rates have a high degree of agreement with the observations. However, these soil types are loamy and do not dry out. Therefore, moisture limitation is not particularly important in the NRW domain.

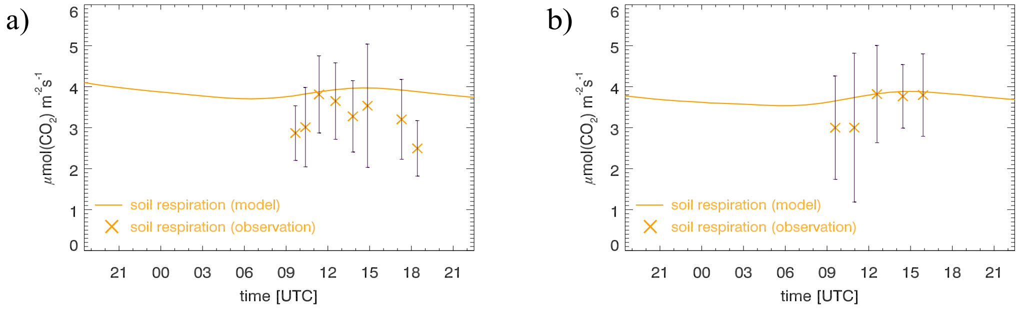

Figure 5.7.: As Fig. 5.6 a–c, but in a) Selhausen on 2012/05/25 and b) Merzenhausen on 2012/07/23.

In summary, at Rollesbroich T_{soil} is simulated faily well. The soil respiration is in the range of the obervations and the underestimation of the diurnal variation is not surprising, because the simulated autotrophic fraction of soil respiration is almost constant (see Section 2.5.2). Moreover, the Q_{10} of 2.1 for temperature sensitivity is possibly not appropriate for this special meadow because in nature the Q_{10} dependency of respiration is very variable (e. g. Lloyd and Taylor, 1994). The too high simulated fraction of CO_2 production in the subsoil at rather constant T_{soil} (see Section 4.1.5) as well as the disregarded CO_2 diffusion in the soil can further cause deviations from the observations. Nevertheless, compared with the absolute deviations and with the uncertainties of simulated photosynthesis rates the deviations of soil respiration are low, especially for typical conditions at night ($T_{soil} \approx$ 5–15 °C). Thus, the newly implemented parameterizations are well suited for an estimation of nighttime CO_2 accumulation in the atmosphere whereas at daytime NEE is primarily controlled by photosynthesis. Unfortunately, no measurements are available for the verification of soil and litter respiration in forests.

6. Sensitivity studies with TerrSysMP-CO_2

This chapter presents several sensitivity studies which are performed by modifying the clear sky simulations CS2605, CS2407 and CS1808 as well as the cloud covered run CL0309. The aim is to investigate the response of canopy fluxes on increasing atmospheric CO_2 contents (Section 6.1) and the influence of anthropogenic emissions in densely populated regions (Section 6.2). Moreover, the effect of dynamic CO_2 on canopy fluxes and atmospheric conditions is studied by comparing the fully prognostic CO_2 runs with simulations using the constant background CO_2 concentration (Section 6.3). Furthermore, different temperature and moisture reduction functions of heterotrophic respiration are tested (Section 6.4) and the effects of different plant physiological parameters for crops on canopy fluxes is shown (Section 6.5).

6.1. Response of canopy fluxes on increasing atmospheric CO_2 concentrations

Due to the direct response of stomatal opening on the atmospheric CO_2 concentration (Eq. 2.17) the global increase of atmospheric CO_2 concentrations yields modified transpiration and photosynthesis rates. In order to investigate these effects, three idealized TerrSysMP-CO_2 simulations of the clear sky case study of 12 July 2012 have been performed by neglecting prognostic CO_2 variations (see Eqs. 2.18, left-hand side). This is done to avoid complex feedbacks caused by the atmospheric CO_2 coupling. The results of the simulation with the CLM default CO_2 content of 355 ppmv (i. e. global mean of 1991) are compared with a simulation with 405 ppmv (global mean of $\approx$ 2018) whereas the third run has been initialized with 388 ppmv (mean at midsummer 2012). In the following, these three model simulations are referred to as CS2407-355, CS2407-405 and CS2407ref, respectively.

Fig. 6.1 depicts the percentage differences of canopy fluxes caused by an increase of the atmospheric CO_2 content of about 14% between CS2407-355 and CS2407-405 at a clear sky day in summer at 10 UTC. This increase causes an increase of photosynthesis of 9–11% (i. e. 1.0–1.5 μmol(CO_2)$m^{-2}s^{-1}$) for crops and grassland PFTs (Fig. 6.1a). However, in forests the same CO_2 increase causes only 5–9% (i. e. 1.5–2.5 μmol(CO_2)$m^{-2}s^{-1}$) higher photosynthesis rates with the weakest simulated response for broadleaf forests. The increase of photosynthesis leads to a distinctly stronger atmospheric CO_2 sink at daytime showing 15–18% higher (i. e. more negative) NEE rates of crops and grassland (Fig. 6.1b). In needleleaf and broadleaf forests, this effect is slightly weaker with 10–15% and 7.5–12%, respectively. Canopy transpiration shows quite different reactions. The CO_2 increase yields only slightly reduced transpiration rates of crops (2–3%) whereas the influence in forests is stronger with 4–6% and 6–7% (7.5–15 W m^{-2}) lower transpiration rates for needleleaf and broadleaf trees, respectively (Fig. 6.1c). As a direct consequence of the lower canopy transpiration, the sensible heat fluxes are 1–7% higher in CS2407-405 than in CS2407-355 with the strongest increase ($\approx$ 7%) in broadleaf forests east of the Rhine (Fig. 6.1d). On this particular day, the changes of sensible heat fluxes in crop regions are negligible. In the afternoon, the higher atmospheric CO_2 content in CS2407-405

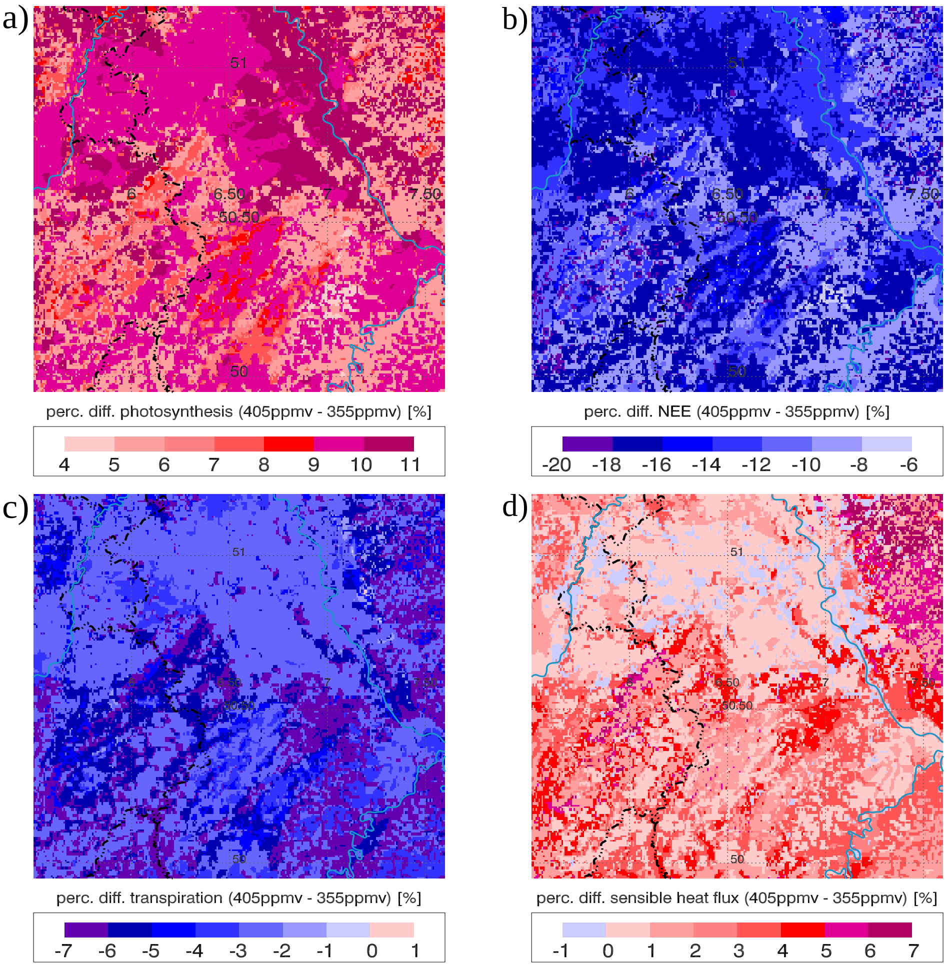

Figure 6.1.: Percentage difference of canopy fluxes between CS2407-405 and CS2407-355 at 10 UTC: a) photosynthesis, b) NEE, c) transpiration, d) sensible heat flux.

has a similar influence on NEE and a slightly weaker (stronger) percentage decrease (increase) of transpiration (photosynthesis) (not shown). The highest increase of the sensible heat flux ($\approx$5–7%) is then simulated for broadleaf forests in the western Eifel region whereas crops and needleleaf forests still show low sensitivity ($<$2.5%) on a CO$_2$ increase of 14% (50 ppmv).

The different responses of crops/grassland and forests on a higher atmospheric CO$_2$ content in CS2407-405 can be explained with different behaviors of the corresponding stomatal resistances. Fig. 6.2 depicts the sunlit and shaded stomatal resistances (r_{st}^{sun} and r_{st}^{sha}) of CS2407ref (388 ppmv) in the late morning. For broadleaf forests a r_{st}^{sha} of 550–700 s m^{-1} is simulated (except along Mosel and Rhine: $<$550 s m^{-1}) as well as 750–1100 s m^{-1} for needleleaf forests (Fig. 6.2a). Thus, especially the stomata of needleleaf trees are only partly open but also for broadleaf trees the environmental conditions are not optimal (optimum $r_{st} \approx 150\,\mathrm{s\,m^{-1}}$). In the Eifel the atmospheric humidity is only moderate (T_{dew} of 9–11 °C), i. e. the ratio $e_s/e_i^* < 1$ in Eq. 2.17 and moderate soil moisture restricts a further increase of A^{sha} (i. e. $\beta_t < 1$ in Eq. 2.26). The additional CO$_2$ in CS2407-455 (i. e. higher c_s) allows a stronger closing of shaded stomata by holding A^{sha} constant. Fig. 6.2b shows a difference of r_{st}^{sha} of 50–110 s m^{-1} between CS2407-355 and CS2407-405 ($\approx$ 10%) with the highest values for needleleaf trees. This re-

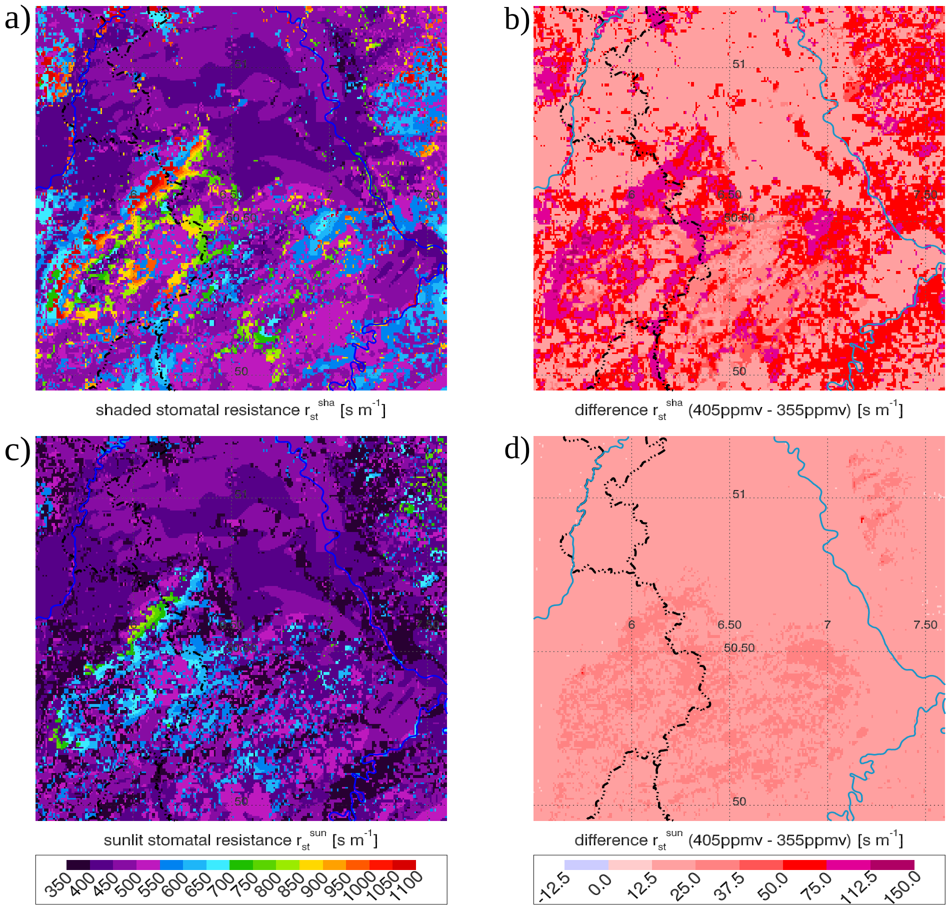

Figure 6.2.: a) Shaded and c) sunlit stomatal resistance (r_{st}^{sha}, r_{st}^{sun}) [s m^{-1}] of CS2407ref and difference of b) r_{st}^{sha} and d) r_{st}^{sun} [s m^{-1}] between CS2407-405 and CS2407-355 (all 10 UTC).

sponse explains the lower transpiration rates in forests. The sunlit stomatal resistance (r_{st}^{sun}) of needleleaf trees ranges from 550–700 s m^{-1} in the central Eifel region to 700–900 s m^{-1} at the Hohes Venn and in parts of the Bergisches Land (Fig. 6.2c). In contrast, r_{st}^{sun} is very low for broadleaf trees with values of 350–400 s m^{-1} in the Mosel valley and in flat terrain and slightly higher values in the Eifel, i. e. broadleaves, which receive direct solar radiation, still have almost optimum conditions. Different from r_{st}^{sha} the higher atmospheric CO_2 content has little influence on r_{st}^{sun} with only 15–30 s m^{-1} higher r_{st}^{sun} in CS2407-405, independent on PFTs, and with the stronger difference in the Eifel region where less atmospheric humidity is simulated than in the flat terrain (Fig. 6.2d). Thus, for sunlit leaves the higher c_s in Eq. 2.17 yields higher A^{sun} by holding r_{st}^{sun} almost constant which explains the higher photosynthesis rates of forest PFTs in CS2407-405.

For crops the conditions and responses on higher atmospheric CO_2 concentrations are quite different than for forests. Both r_{st}^{sun} and r_{st}^{sha} show rather low values of 400–500 s m^{-1}. Only in the Eifel r_{st}^{sun} is slightly higher with up to 550 s m^{-1} caused by low atmospheric humidity. In the crop dominated regions (e. g. Jülicher Börde, Rhine valley) good environmental conditions occur with enough atmospheric humidity (T_{dew} of 11–15 °C). Hence, r_{st}^{sha} and r_{st}^{sun} show only a slight response on the additional CO_2 in CS2407-405 with 15–25 s m^{-1} higher resistances. This is the reason for only slightly reduced transpiration rates of crops whereas the photosynthesis productivity is considerably enhanced. In terms of Eq. 2.17, r_{st} is almost constant, $e_s/e_i^* \approx 1$ and higher c_s directly increases A.

One may conclude that, in general, under equal environmental conditions higher atmospheric CO_2 concentrations yield reduced canopy transpiration and increased photosynthesis rates. On days with "good" environmental conditions (e. g. high atmospheric humidity, wet soil, high temperatures) causing low stomatal resistances, photosynthesis can be considerably enhanced (i. e. more negative NEE) whereas transpiration is only slightly reduced. In situations with detrimental environmental conditions (e. g. low atmospheric humidity, dry soil, very high temperatures), and thus only moderate stomatal opening, an atmospheric CO_2 increase is favorable for plants. It allows stronger stomatal closure resulting in decreased transpiration rates to counteract plant wilting and desiccation. These effects also indicate that day-to-day differences in the daytime CO_2 concentration (see e. g. Chap. 7) as well as considerably increased CO_2 contents in the early morning influence the stomatal control of CO_2 uptake and transpiration and, therefore, prognostic atmospheric CO_2 contents leads to more consistent results.

6.2. Influence of anthropogenic emissions on the atmospheric CO_2 distribution

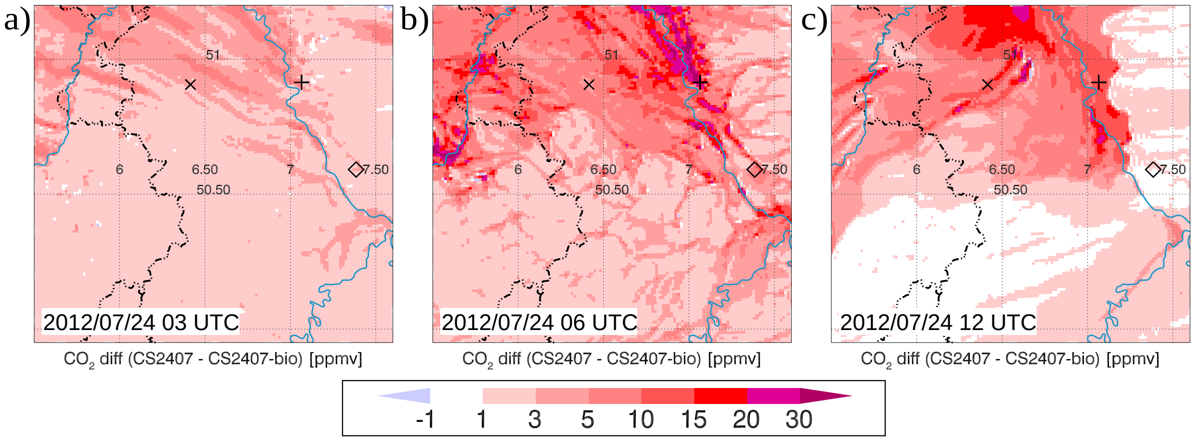

Figure 6.3.: Difference of the CO_2 concentration [ppmv] in the lowermost COSMO level (≈ 10 m) between CS2407 and CS2407-bio at a) 03 UTC, b) 06 UTC and c) 12 UTC. The locations shown in Fig. 6.4 are Jülich (×), Wied valley (◊) and Köln-Gremberghoven (+).

In this section, anthropogenic effects on the simulated CO_2 distribution are analyzed. For this, in addition to CS2407 a second simulation (CS2407-bio) has been performed considering only biogenic CO_2 fluxes in the NRW domain as well as in the ICs and LBCs to eliminate anthropogenic effects, e. g., from cities in the NRW domain or from the nearby Ruhr area. In and around Cologne and Dusseldorf the initial CO_2 content of CS2407 (2012/07/23 18 UTC) is about 10–25 ppmv higher than in CS2407-bio, in the surrounding flat terrain the difference is 3–10 ppmv and in the Eifel the concentrations are similar (not shown). During nighttime this difference remains at this level and the urban effects diminish (Fig. 6.3a). Hence, the CO_2 increase during nighttime is mainly caused by leaf and soil respiration. With the rapidly enhanced road traffic in the morning the difference between CS2407 and CS2407-bio becomes much stronger (Fig. 6.3b). Especially in the flat terrain and in the valleys east of the Rhine (morning rush-hour and stable stratification in the valleys) in CS2407 the CO_2 concentrations are 5–15 ppmv higher than in CS2407-bio. The metropolitan areas Bonn-Cologne-Dusseldorf and Liège stand out with 15–30 ppmv (locally 50 ppmv) higher CO_2 contents. In the following hours, downstream of these big cities the near surface CO_2 concentration remains elevated (3–10 ppmv) and the northwesterly wind advects the higher CO_2 concentrations in the northern part of the Eifel (Fig. 6.3c). In the well-mixed CBL the very strong emissions of power plants are mixed to the surface. The sharp gradient east of the Rhine is the result of a strong wind convergence (NW along the Rhine, E in the Bergisches Land) at this time.

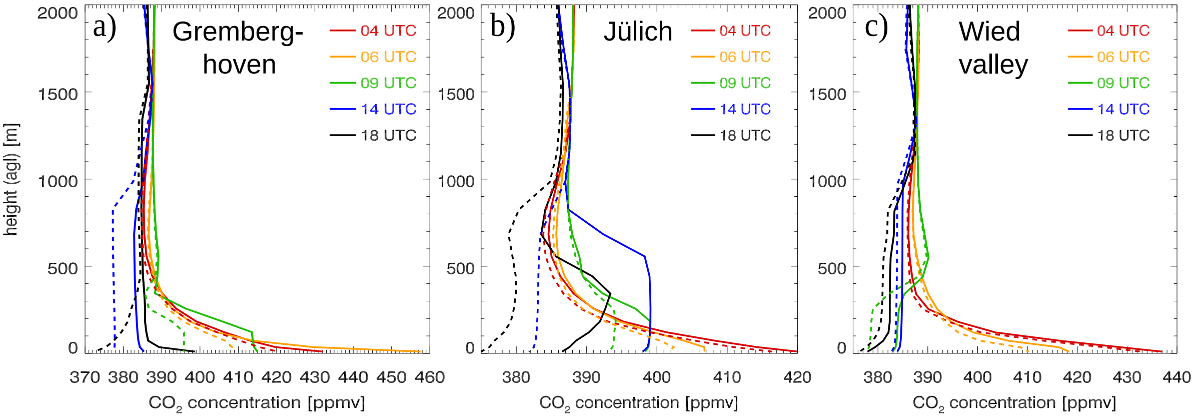

Figure 6.4.: Vertical CO_2 profiles [ppmv] at different times of the day for CS2407 (solid lines) and CS2407-bio (dashed lines): a) Köln-Gremberghoven, b) near Jülich, c) Wied valley.

Fig. 6.4 depicts vertical CO_2 profiles of CS2407 and CS2407-bio at different times of the day. The grid cell at K-Gremberghoven (a) and its neighboring grid cells are characterized by very intense anthropogenic sources (e. g. freight depot, industry, much frequented motorway junctions of A3, A4, A59 and A559). The other locations represent typical rural profiles (southeast of Jülich (b), flat terrain) or in the narrow Wied valley (c). Again, it can be seen that at night the strong near surface increase (≈ 50 ppmv in the Wied valley) is mainly caused by biogenic CO_2 sources (4 UTC). In contrast, at 6 UTC especially at K-Gremberghoven the simulated CO_2 concentration of 458 ppmv is caused by humans (409 ppmv in CS2407-bio). Apart from big cities, anthropogenic effects cause only slightly increased CO_2 contents (Fig. 6.4b, c). At 9 UTC, the development of a well-mixed CBL has begun and the CO_2 concentrations in K-Gremberghoven are still noticeable elevated. Whereas there and around Jülich a surplus of CO_2 occurs in the PBL, in the Wied valley the high photosynthesis rates of broadleaf forests lead to a net CO_2 sink, i. e. lower concentrations than in the free troposphere. At 14 UTC, at K-Gremberghoven and especially the Jülich profile show considerably higher CO_2 contents in CS2407 (≈ 399 ppmv) than in CS2407-bio (≈ 383 ppmv) as a result of advection of high concentrations from the metropolitan region Cologne-Dusseldorf and from the power plants Neurath and Niederaußem to the analyzed location. Without anthropogenic emissions a CO_2 loss is simulated at all profiles (5–8 ppmv lower CO_2 contents in the PBL than in the free troposphere). A further reason of the relatively strong anthropogenic effect in this simulation is a rather shallow PBL (cf. PBL height in Fig. 4.11) with a PBL top of about 600 m at Jülich, 850 m in the Rhine valley and 1000 m in the Wied valley. The PBL height is a key variable for the influence of CO_2 fluxes on the atmospheric CO_2 content (Sarrat *et al.*, 2007b). In the evening, the beginning near surface stabilization and anthropogenic sources can be seen at K-Gremberghoven. In the Wied valley, in the afternoon/evening the effect of human produced CO_2 is weak.

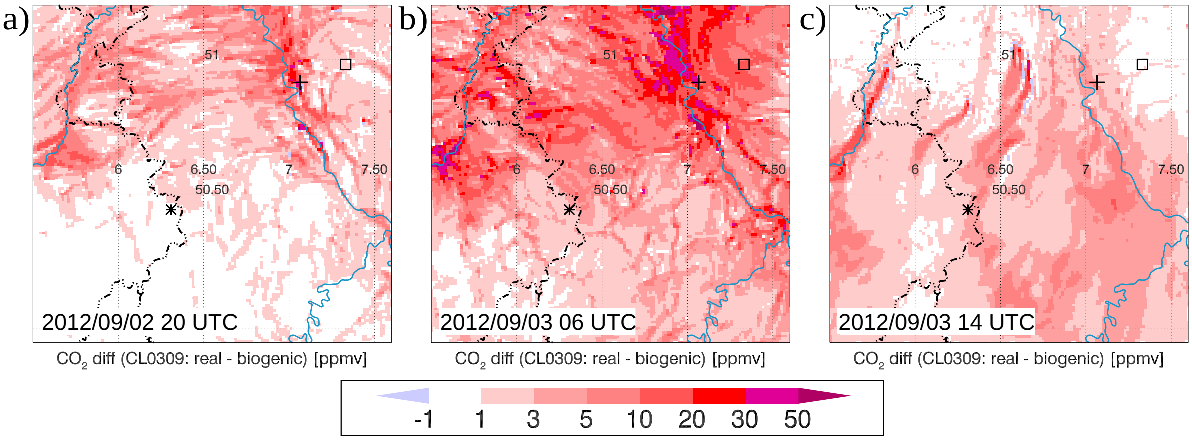

Figure 6.5.: Difference in the CO_2 tracer concentrations of "real" and "biogenic" [ppmv] (lowermost COSMO level) on a) 2012/09/02 20 UTC, b) 2012/09/03 06 UTC and c) 14 UTC. The locations shown in Fig. 6.7 are K-Gremberghoven (+), Agger valley (□), Central Eifel (✱).

In a second experiment, with CL0309 the effect of fossil fuel emissions produced solely from local CO_2 emitters in the NRW domain is analyzed. For this, in the *same* model simulation, additionally to the standard CO_2 tracer ("real", coupled with CLM), a second (passive) CO_2 tracer is included into COSMO. This tracer ("biogenic") receives only local tendencies of biogenic CO_2 fluxes, i. e. anthropogenic effects are excluded. In contrast to above described sensitivity study the differences in the CO_2 distributions are only affected by *local* anthropogenic sources during the simulation whereas the CO_2 ICs and LBCs are the *same*. Fig. 6.5a shows that at 20 UTC (i. e. 2 h after initialization), human produced CO_2 leads to a widespread increase of 1–5 ppmv in the flat terrain and, locally, to an increase of 10–30 ppmv near urban and industrial regions. In the sparsely populated Eifel the difference between "real" and "biogenic" is negligible. At night, the general patterns are similar but the differences in the metropolitan areas decrease (not shown) because compared to biogenic sources in most regions anthropogenic emissions are small ($< 0.5\,\mu\mathrm{mol(CO_2)m^{-2}s^{-1}}$), see Fig. 6.6a. The major sources result from industry and power plants which mainly emit above the nocturnal PBL.

With the beginning road traffic in the morning, the difference between "real" and "biogenic" increases rapidly (Fig. 6.5b) to widespread differences of 5–20 ppmv in flat terrain and in valleys. In and around big cities (Bonn, Cologne, Dusseldorf, Aachen, Liège) the near surface CO_2 concentrations differ by 20–50 ppmv. This clearly indicates the strong anthropogenic influence in the NRW domain. At 6 UTC, except for the southwestern part of the domain, anthropogenic emissions exceed $1\,\mu\mathrm{mol(CO_2)m^{-2}s^{-1}}$ in rural areas, 3–10 $\mu\mathrm{mol(CO_2)m^{-2}s^{-1}}$ in grid cells including high frequent roads and 10–20 $\mu\mathrm{mol(CO_2)m^{-2}s^{-1}}$ in urban areas (locally $> 100\,\mu\mathrm{mol(CO_2)m^{-2}s^{-1}}$ in industrial zones). Thus, in urban areas fossil fuel emissions are the major CO_2 source but also in rural areas these emissions cannot be neglected. As expected, in the afternoon the differences between "real" and "biogenic" are weaker due to vertical mixing in the PBL and the advection of 1–5 ppmv (locally 10 ppmv) higher CO_2 contents towards the

Eifel can be seen. The negligible differences in the northern part result from the inflow of identical LBCs for both CO_2 tracers. An additional simulation similar to CS2407-bio show 3–10 ppmv lower CO_2 contents in the ICs in most regions and 15–50 ppmv lower values near the cities along the Rhine. During the simulation stronger differences occur in urban areas in the morning and downstream of inflowing LBCs (≈ 5–10 ppmv, not shown).

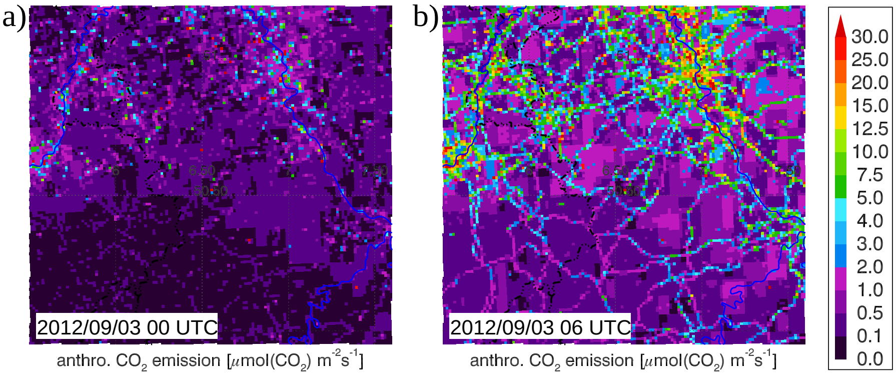

Figure 6.6.: Anthropogenic CO_2 emissions [μmol(CO_2)$m^{-2}s^{-1}$] on 2012/09/03 a) 00 UTC, b) 06 UTC.

The time series shown in Fig. 6.7a indicate that in the Agger valley the strong increase of near surface CO_2 in the first half of the night is caused by biogenic sources and advection of high initial CO_2 contents from the Rhine valley whereas in the morning a slightly stronger influence of local anthropogenic CO_2 (≈ 15 ppmv) can be seen. The almost identical CO_2 content in the afternoon results from equal LBCs. Similar to CS2605 (Fig. 4.12a) at Eifel mountain ridges the diurnal amplitude is low and the slightly higher CO_2 contents of "real" (< 5 ppmv) are caused by advective transport. The time series at K-Gremberghoven show a different behavior with a very prominent peak at 19 UTC for "real" followed by 20–40 ppmv higher concentrations than for the "biogenic" CO_2 tracer at night and in the morning. Whereas "biogenic" decreases after 5:30 UTC due to photosynthesis, the "real" CO_2 tracer remains elevated until 9 UTC when the CBL arises. Fig. 6.7b further manifests the strong local CO_2 source at K-Gremberghoven because the strong difference between "real" and "biogenic" is restricted to the lowest 50 m whereas in 73 m both CO_2 contents differ by only 5–10 ppmv. After 6 UTC, this model level is integrated in the CBL then approaching the CO_2 content in 10 m. After 11 UTC, the CBL exceeds 500 m and both tracers have similar CO_2 contents in all levels.

The relevance of fossil fuel emissions in populated areas has been pointed out, e. g., in Pérez-Landa *et al.* (2007) and Ter Maat *et al.* (2010). Both studies, however, used a rather coarse dataset ($1^\circ \times 1^\circ$) and a simplified disaggregation method by distributing the emissions to urban grid cells only. Moreover, only mobile and non-mobile sources have been distinguished, the latter without diurnal variations. Other studies used a dataset with 10 km resolution (Ahmadov *et al.*, 2007; Tolk *et al.*, 2009; Sarrat *et al.*, 2009) or chose regions where biogenic fluxes are dominant (e. g. Ahmadov *et al.*, 2007; Sarrat *et al.*, 2007b). In contrast, in this study anthropogenic effects in densely populated areas are analyzed using high-resolution (1 km) CO_2 emissions (see Section 2.6). The distinction of six CO_2 producing SNAPs, characterized by different emission time factors (Table 2.1) allows explicit analyses of the effect of different CO_2 sources. Moreover, both the influence of human produced CO_2 in industrial zones and in rural areas with small villages and road networks can be analyzed (Fig. 6.6). The results indicate strongly enhanced CO_2 concentrations near metropolitan areas.

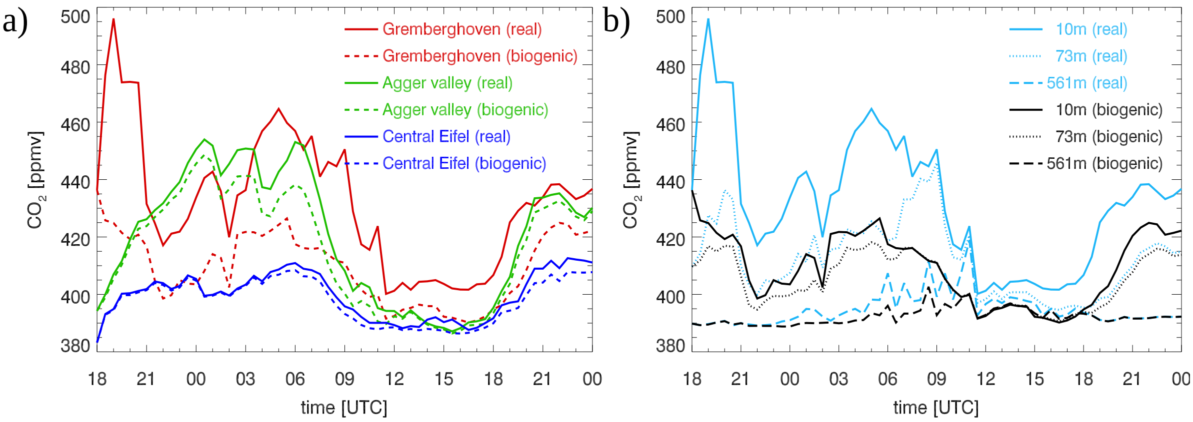

Figure 6.7.: a) Time series of the CO_2 concentration [ppmv] of CL0309 (solid lines: "real", dashed lines: "biogenic") in the lowermost COSMO level, b) time series of the CO_2 concentration [ppmv] at Köln-Gremberghoven in different heights (light blue: "real", black: "biogenic").

6.3. Influence of dynamic CO_2 on canopy fluxes and atmospheric conditions

In this section, the effects of dynamic CO_2 (i. e. prognostic CO_2 or "real" CO_2 contents) are analyzed by comparing both canopy fluxes and atmospheric variables with the ones calculated with additional simulations ("reference") keeping the background CO_2 mixing ratio constant.

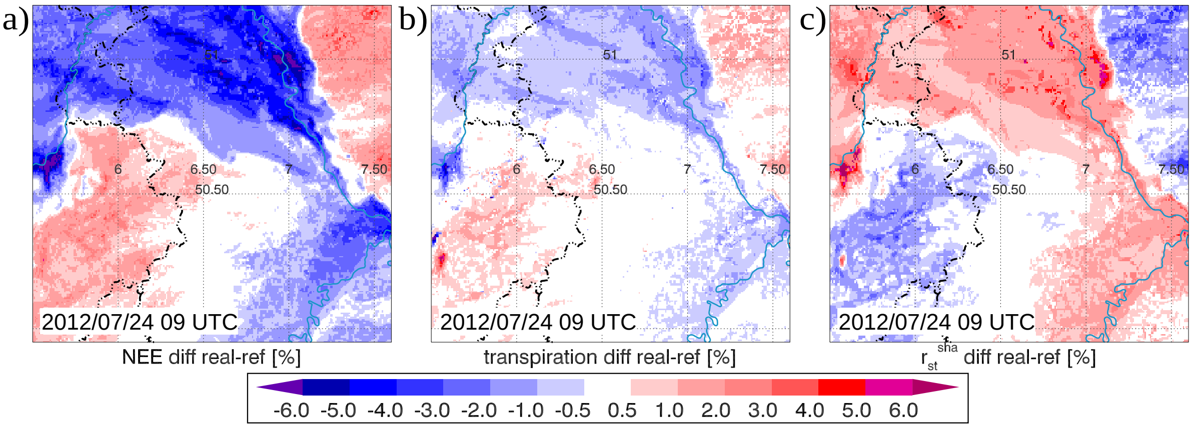

Figure 6.8.: Percentage difference of CS2407 and CS2407ref (9 UTC): a) NEE, b) transpiration, c) r_{st}^{sha}.

In the morning of 24 July 2012 the CO_2 contents in the flat terrain are higher than the background CO_2 of 388 ppmv (see Fig. 4.8c). This causes a more efficient CO_2 uptake by the canopy (i. e. higher photosynthesis rates) than with the background CO_2 (CS2407-ref). In these regions, NEE is increased by 1–5%, i. e. more negative ($\approx$ 0.1–0.5 μmol(CO_2)$m^{-2}s^{-1}$), downstream of cities 7% ($\approx$ 0.7 μmol(CO_2)$m^{-2}s^{-1}$), whereas in the Bergisches Land and in the Belgian Eifel NEE is lower due to low CO_2 concentrations (Fig. 6.8a). Transpiration shows the opposite effect, i. e. lower rates in the flat terrain and higher rates in regions with low CO_2 contents (Fig. 6.8b). The percentage deviations are lower (in most regions 0.5–2% or 0.5–3 W m^{-2}) than for NEE and have no significant effect on the humidity in the PBL. The influence of spatio-temporal CO_2 variations on NEE and transpiration can be explained with the response of the stomatal resistance (r_{st}^{sha}, r_{st}^{sun}) being more open (closed) in regions with lower (higher) CO_2 contents than in CS2407 with a slightly higher percentage difference than for transpiration (Fig. 6.8c).

Earlier in the morning the absolute differences of canopy fluxes are low because the fluxes itself are low. In the afternoon the percentage difference of NEE and transpiration between CS2407 and CS2407ref are low as well (not shown) because the rather homogeneous CO_2 distribution is close to the background CO_2 content (see Fig. 4.8d). In situations with strong moisture stress of plants (low soil moisture and/or low T_{dew}) the influence of spatio-temporal CO_2 variability on transpiration is probably slightly higher because of the stronger sensitivity of r_{st} (see Section 6.1) as well as in weather situations with low PBL heights (i. e. stronger deviation of CO_2 mixing ratios from background CO_2). Nonetheless, in most clear sky situations the effect of dynamic CO_2 on the atmospheric humidity and on canopy fluxes is rather low. The control of transpiration and photosynthesis (i. e. r_{st}) by the atmospheric humidity itself and its heterogeneity is clearly dominant compared to the effects of dynamic CO_2.

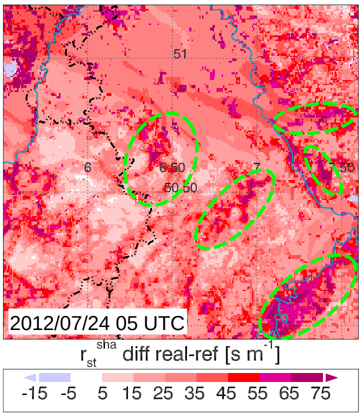

Figure 6.9.: Difference of r_{st}^{sha} [$\mathrm{s\,m^{-1}}$] at 5 UTC, CS2407–CS2407ref.

However, an interesting effect of the strong CO_2 accumulation in narrow valleys can be seen in the early morning when the plants open their stomata for photosynthesis (see Fig. 6.9). In the entire model domain, but especially in the valleys of Eifel, east of the Rhine and along the Mosel, r_{st}^{sha} (and r_{st}^{sun}) of CS2407 is considerably higher than in CS2407ref, i. e. the high CO_2 contents in the morning cause a later opening of the stomata.

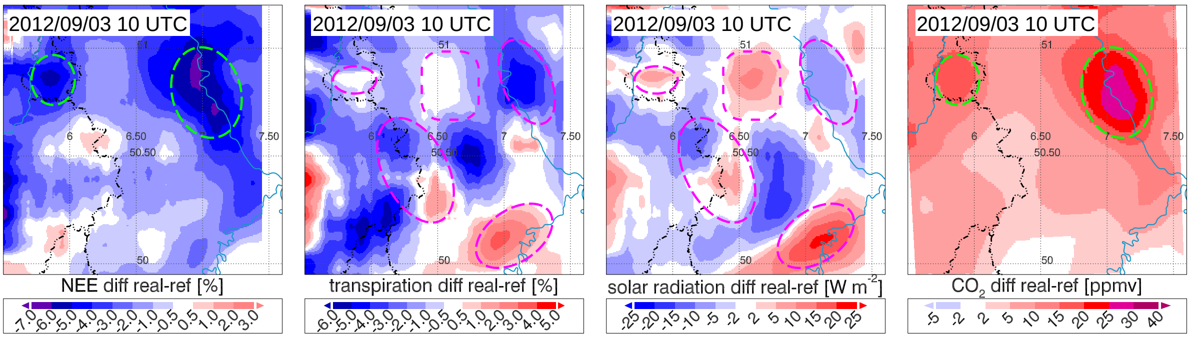

Figure 6.10.: Difference of CL0309 and CL0309ref at 10 UTC: NEE and transpiration [%], incident solar radiation [$\mathrm{W\,m^{-2}}$] and CO_2 mixing ratio [ppmv] (lowermost COSMO level). The CLM variables are spatially averaged over 40 CLM grid cells, CO_2 over 20 COSMO grid cells.

The same numerical experiment has been performed for 3 September 2012 (CL0309) which is characterized by partial cloudiness. The fields depicted in Fig. 6.10 are horizontally averaged to partially filter out the effects of randomly distributed cloud formations. Even the averaged solar radiation indicates significant changes in the distribution of clouds. However, neither in the morning nor in the afternoon with dynamic CO_2 a trend towards more/less cloudiness can be identified. Different from CS2407, in this case study especially in the morning the increased

CO_2 concentrations cause widespread higher CO_2 uptake rates of about 2–4% in rural and 5–7% in densely populated regions. A strong correlation can be seen between high CO_2 mixing ratios and more negative NEE (green areas in Fig. 6.10). In contrast, transpiratiation is only weakly correlated to the atmospheric CO_2 contents. Instead, a stronger correlation occurs between modified transpiration and solar radiation (pink regions). In regions with decreased solar radiation CS0309ref simulates decreased transpiration whereas in regions with increased solar radiation transpiration is either increased as well or shows no deviations if in addition the CO_2 contents are significantly higher. On average, between 6 and 12 UTC transpiration is slightly reduced in CS0309ref (domain mean -1.1%) due to higher r_{st} and photosynthesis is increased (0.8%) due to the higher CO_2 content. In the afternoon, with CO_2 contents being closer to the background CO_2 mixing ratios, all correlations are less evident. However, the differences in the formation of convective clouds between CL0309 and CL0309ref increase leading to mesoscale deviations of transpiration by ±5–7%, locally $\lesssim 10\%$ (not shown).

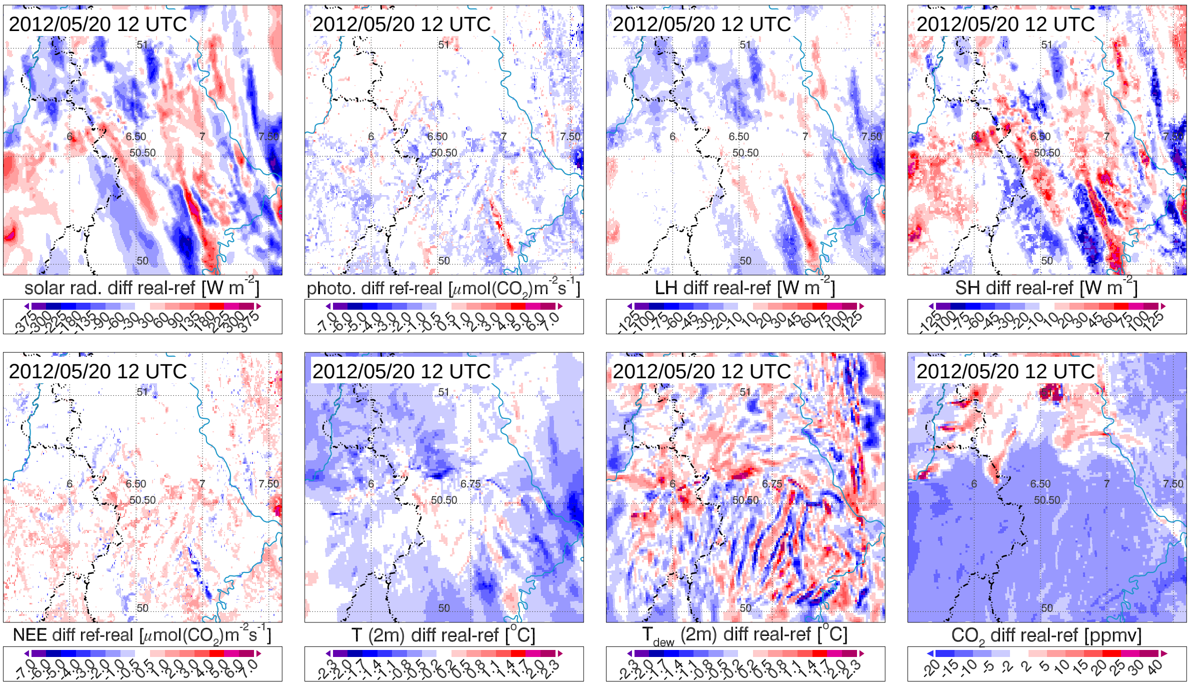

Figure 6.11.: Difference of CP2005 and CP2005ref at 12 UTC (20 May): incident solar radiation [W m^{-2}], photosynthesis [μmol(CO_2)m^{-2}s^{-1}], LH flux [W m^{-2}], SH flux [W m^{-2}], NEE [μmol(CO_2)m^{-2}s^{-1}], 2m-temperature [°C], T_{dew} in 2 m [°C], CO_2 mixing ratio [ppmv].

Fig. 6.11 depicts the difference of several atmospheric variables and canopy fluxes (without averaging of the fields) on 20 May 2012 at 12 UTC. At this time, convective cloudiness occurs in the NRW domain. In most regions, the dynamic CO_2 of CP2005 is 2–10 ppmv lower than the background CO_2 (CP2005ref). Slightly higher CO_2 contents are simulated in the northern part and distinctly higher CO_2 contents near power plants. Although in CP2005 the deviation of CO_2 contents from the background CO_2 is weak, the formation of clouds is significantly influenced as shown in the simulated incident solar radiation. The locations where convective clouds develop are different in CP2005 and CP2005ref. However, similar to CL0309 both in the morning (-0.65%) and in the afternoon (-0.01%) a significant trend to more/less clouds is not apparent. Due to the lower CO_2 contents in CP2005 the CO_2 uptake by photosynthesis of plants is on average lower than in CP2005ref and some correlation can be seen between photosynthesis (and NEE) and solar radiation. Latent and sensible heat fluxes are mostly influenced by different cloud patterns as indicated by a rather close correlation (instead of an anticorrelation) of both energy fluxes. On average, the simulated temperature in 2 m of CP2005 is slightly colder than in CP2005ref. Different from the 2m-temperature the dew point temperatures in 2 m show rather randomly distributed deviations up to ± 2.5 °C, especially in mountainous regions. At the subsequent day, the corresponding differences at noon and in the afternoon are quite similar to the ones depicted in Fig. 6.11 (not shown).

Finally, Fig. 6.12 depicts the different precipitation patterns of CP2005 (red) and CP2005ref (blue). In CP2005ref the very intense convective cell in eastern Belgium (18–20 UTC) is not simulated. Instead, in the afternoon some showers develop in the central Eifel region and at 17 UTC an intense convective cell is simulated in Belgium further to the west. Significant differences can also be seen for convective cells in the Bergisches Land in the afternoons of 20 and 21 May. This indicates that dynamic CO_2 has also an influence on convective initiation in weather situations with weak synoptic forcing. However, no clear relationship can be found between the locations of convection and the spatial distributions of CO_2 concentrations, humidity and temperature (not shown). Thus, in this case only randomly occurring secondary effects (e. g. cloud distribution, randomly wind fluctuations) and not the CO_2 distribution itself cause these differences.

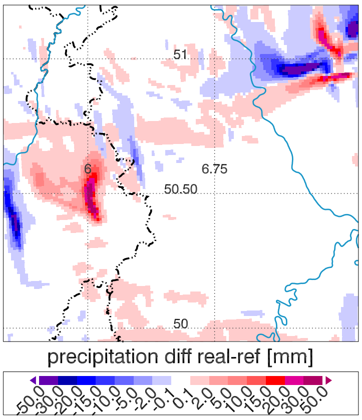

Figure 6.12.: Difference of 48h-precipitation [mm], CP2005–CP2005ref.

In conclusion, these sensitivity studies show that especially in the morning, when the CO_2 concentrations in rural/urban regions are significantly lower/higher than the background CO_2 content, the canopy exchange of CO_2 and H_2O is affected. However, in clear sky cases both the amount and the spatial distribution of humidity in the PBL is the dominant controlling factor of NEE and transpiration against the spatio-temporal atmospheric CO_2 variability. Thus, the prognostic treatment of atmospheric CO_2 mixing ratios has no significant effect on the evolution of the PBL. In the case of clouds and precipitation developing in the numerical simulation, the locations of convective cloud formations are significantly influenced showing differences even in mesoscale cloud patterns. However, neither a significant trend to more/less cloudiness is simulated nor the differences can be attributed to the CO_2 distribution or modified canopy fluxes. In fact, randomly secondary effects of dynamic CO_2 cause these modifications.

6.4. Sensitivity of different temperature functions for heterotrophic respiration

The temperature dependency of microbial activity in the soil (Section 2.4.5) is still in the focus of current research both for numerical models and for experimental approaches (e. g. Graf *et al.*, 2008). The response of different temperature functions $f(T_{soil})$ on heterotrophic respiration and finally on the atmospheric CO_2 variability is analyzed for the CS2605 (moderate temperatures) and CS1808 (hot at daytime, warm nights). In several model runs, $f(T_{soil})$ has been changed (e. g. Q_{10}=1.5, Q_{10}=2.0, RothC function) equally for all PFTs and soil types.

Fig. 6.13 depicts exemplarily the different heterotrophic respiration rates of the simula-

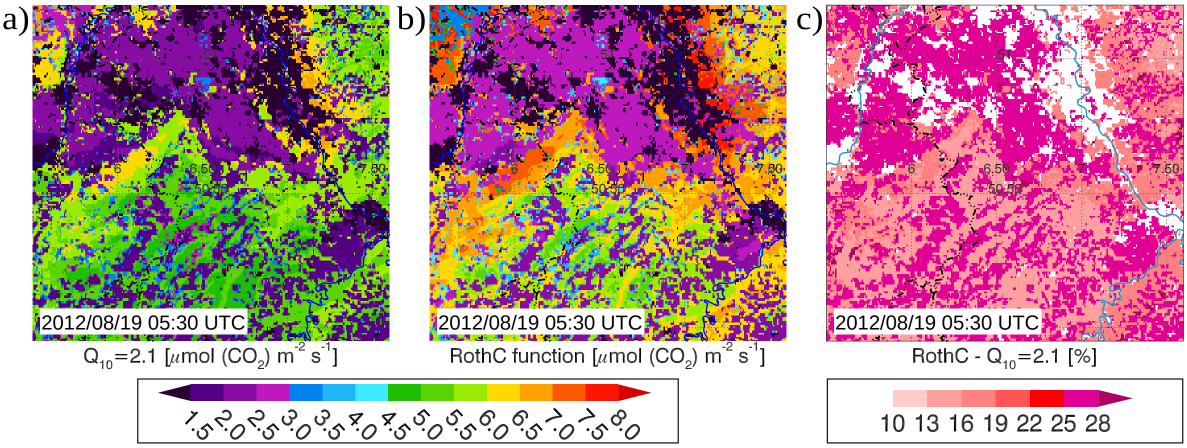

Figure 6.13.: Heterotrophic respiration [μmol(CO$_2$)m^{-2}s^{-1}] of a) CS1808 and b) CS1808-RothC on 2012/08/19 05:30 UTC and c) the percentage difference between these simulations.

tions with Q_{10}=2.1 (CS1808) and with the RothC temperature function (CS1808-RothC) in the morning of 19 August 2012. In the arable flat terrain in the north, with Q_{10}=2.1 respiration rates of 1.9–2.4 μmol(CO$_2$)m^{-2}s^{-1} are simulated whereas with the RothC function (Eq. 2.33) 2.4–3.0 μmol(CO$_2$)m^{-2}s^{-1} are obtained. Thus, heterotrophic respiration in CS1808-RothC is 26–28% stronger than in CS1808 (Fig. 6.13c). In forests, in CS1808 (CS1808-RothC) respiration rates of 4.7–5.5 μmol(CO$_2$)m^{-2}s^{-1} (5.3–6.2 μmol(CO$_2$)m^{-2}s^{-1}) are simulated in the Eifel ($T_{\min}$ = 16–20 °C, 2 m above ground) and 6.0–6.8 μmol(CO$_2$)m^{-2}s^{-1} (7.0–7.9 μmol(CO$_2$)m^{-2}s^{-1}) in the Rhine valley and along the Hohes Venn ($T_{\min}$ = 20–25 °C). This corresponds to a difference of 13–18% between the two simulations. The stronger heterotrophic respiration in the afternoon shows a similar percentage difference (12–15%) in forests but a smaller difference of 19–24% for crops, the smallest difference occurring in the flat terrain at temperatures higher than 30 °C. On 26 May 2012, a comparison of the respiration rates between CS2605 (Q_{10}=2.0) and CS2505-RothC leads to comparable percentage differences for forests and for crops during nighttime (not shown). However, in the afternoon for crops the percentage difference between Q_{10}=2.0 and the RothC function further increases (see also Fig. 6.14b) to about 35% instead of a decreasing difference as on 19 August 2012.

In order to understand the differences between the Q_{10} and the RothC function, at three selected grid points soil respiration is analyzed in combination with $f(T_{soil})$ in different soil depths (Fig. 6.14). "Kölner Bucht" represents a typical agricultural field (PFT=15) on 26 May 2012. In the uppermost soil layer (0.0–1.75 cm) the RothC function shows a high diurnal variation ranging from 1.4 (3–5 UTC) at T_{soil}=12 °C to 3.6 (13–14 UTC) at T_{soil}=24 °C. Moreover, at any time the curve is above the Q_{10}-functions. The exponential behavior of Q_{10}=2.0 shows a smaller amplitude than the RothC function and only a value of 2.8 in the afternoon. Q_{10}=1.5 strongly underestimates the temperature dependency of soil respiration. Whereas in the morning the difference between the temperature functions is weak (1.1–1.4), in the afternoon the difference is very strong (1.8–3.6). Note, that the difference between Q_{10}=2.0 and the RothC function is maximal for T_{soil}=24 °C (cf. Fig. 2.10a). In soil layer 3 (4.5–9.05 cm) the diurnal amplitudes are smaller caused by higher soil temperatures in the morning and colder temperatures in the late afternoon. Again the RothC function is above the Q_{10} functions. In layer 6 (28.9–49.3 cm) T_{soil} is almost constant at (≈16 °C) but still the RothC function is

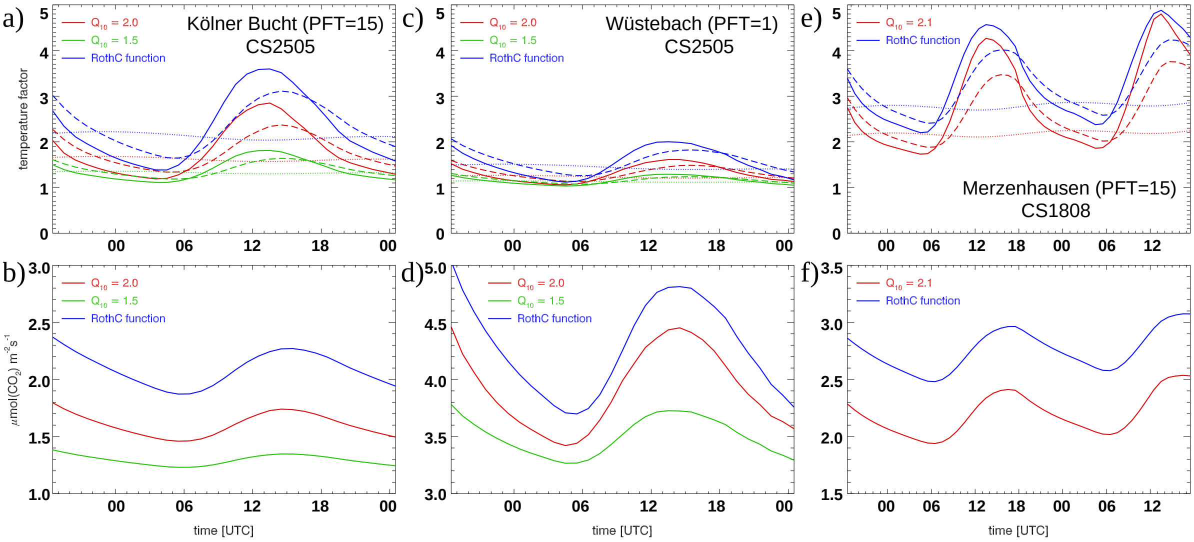

Figure 6.14.: Course of $f(T_{soil})$ (a, c, e) and heterotrophic respiration [μmol(CO$_2$)m^{-2}s^{-1}] (b, d, f) simulated with CS2605 (Kölner Bucht, Wüstebach) and CS1808 (Merzenhausen). Solid lines in (a, c, e) represent CLM soil layer 1, dashed lines soil layer 3 and dotted lines soil layer 6.

higher (2.1) than the Q_{10}-functions (1.7 and 1.35). Thus, CS2605-RothC calculates the highest respiration rates and a stronger diurnal variation than CS2605 caused by the higher diurnal variation of heterotrophic respiration in the topsoil. Due to the maximum difference between Q_{10}=2.0 and the RothC function at 24 °C, in the afternoon the percentage difference between the two simulations is stronger than in the morning.

In the needleleaf forest near Wüstebach (Fig. 6.14c, d) the simulated amplitudes of all temperature functions are considerably smaller than those of the agricultural field in the Kölner Bucht. The reasons for this are lower air temperatures in the central Eifel and, even more important, lower T_{soil} of forest soils in the afternoon compared to agricultural soils (see Section 4.1.5). The RothC curves are above the Q_{10} curves with a smaller difference in the subsoil than in the Kölner Bucht caused by lower T_{soil} of about 12.5 °C. In the morning, in the topsoil the temperature functions are similar because the soil temperature is near the RothC reference temperature (i. e. $f(T_{soil}) \approx 1$). The higher diurnal variation of heterotrophic respiration is mainly a result of the high temperature sensitivity of respiration in the O horizon and the higher fraction of respiration in the topsoil (see Section 4.1.5).

Finally, the simulated $f(T_{soil})$ and respiration rates at the agricultural field near Merzenhausen (Fig. 6.14e, f) show the conditions at high afternoon temperatures (> 30 °C) and warm nights of 18 and 19 August 2012. Contrary to the behavior at moderate afternoon temperatures (Fig. 6.14a, b), in this case study, with Q_{10}=2.1 in layer 1 similar respiration rates are simulated as for the RothC function (especially on 19 August)[1]. At soil temperatures near 30 °C both functions have similar values because the slope of the RothC function is dampened at high T_{soil} (Figs. 6.14e, 2.10a). Thus, on this day the diurnal variation for crops in CS1808 is higher than in CS1808-RothC. Moreover, at any time the respiration rates in the upper topsoil are 1.5–2.0-fold higher than in CS2605 yielding a higher fraction of heterotrophic respiration coming from the upper soil layers. In soil layer 3 the amplitudes of both temperature functions

---

[1] except for very high temperatures Q_{10}=2.1 is comparable to Q_{10}=2.0 (see Fig. 2.10a)

are similar with higher values for the RothC function (also in layer 6). Thus, heterotrophic respiration in CS1808-RothC is still stronger than in CS1808 but with a smaller percentage difference for crops in the afternoon.

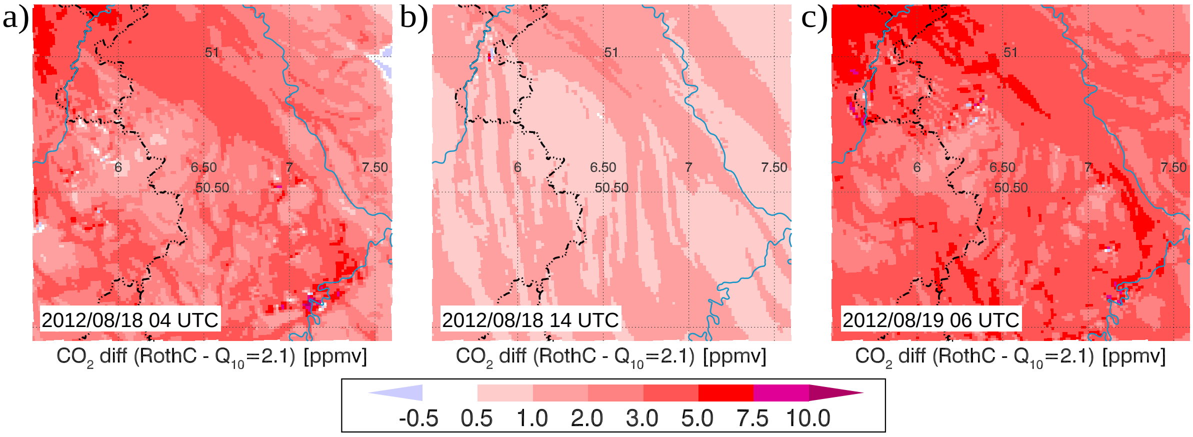

Figure 6.15.: Difference of simulated CO_2 content [ppmv] between CS1808-RothC and CS1808 (lowermost level) on a) 2012/08/18 04 UTC, b) 14 UTC and on c) 2012/08/19 06 UTC.

One may conclude that RothC using its original temperature function causes higher respiration rates for all PFTs and almost the complete temperature range of the summer season in Central Europe ($\approx$5–35 °C). The changed NEE also influences the atmospheric CO_2 concentrations. Fig. 6.15 compares the near surface CO_2 distribution of CS1808-RothC with CS1808. During nighttime and in the early morning of 18 August 2012 CS1808-RothC simulates 3–5 ppmv higher CO_2 contents in flat terrain and in valleys and smaller differences in mountainous regions. Along the Mosel even local differences of 8–12 ppmv occur as a result of a calm and very stable stratified atmosphere, there. As usual, in the afternoon (Fig. 6.15b) the difference is rather small (0.5–2.0 ppmv in most regions) due to vertical turbulent mixing whereas in the following night (Fig. 6.15c) the difference between the two runs is even higher than in the night before with widespread higher concentrations of 3–6 ppmv in CS1808-RothC. Even in the colder night of CS2605 differences of several ppmv are simulated mainly resulting from still high temperatures in the first half of the night (not shown).

6.5. Different plant physiological parameters for crops

The verification of simulated fluxes (NEE, LH, SH) with EC fluxes (Chap. 5) has indicated that CLM unsatisfactorily represents field observations of crops (PFT=15) made during the corresponding growing and mature stages. Sulis *et al.* (2015) developed new plant physiological parameters for winter wheat and sugar beet based on multi-year field measurements, carried out around Jülich, and a comprehensive literature study. They found a significantly better agreement between observed and simulated monthly averaged diurnal cycles of SH and LH as well as "drastic" improvements of NEE as compared with simulations using the plant physiological parameters of CLM3.5 (in the following referred to as 'clmcrop'). The better photosynthesis rates mainly result from improved parameters controlling RuBisCO enzyme kinematics, i. e. CN_L, F_{LNR}, SLA_0 (see Sulis *et al.*, 2015, Table 1). For winter wheat, e. g., a lower leaf C:N ratio (CN_L) of 14.0 ('clmcrop': 25.0) and a lower SLA_0 of 0.028 (0.050) leads to a higher area-based leaf nitrogen content (N_a, see Eq. 2.24) which in turn enhances $V_{c,\max}$ (see Eq. 2.22). The triplication of F_{LNR} to 0.3 (0.1) has the same effect and, thus, photosynthesis rates increase. The notably higher leaf N contents are probably related to extensive fertilization at the considered crop fields which is not accounted for in the model parameterization (Sulis *et al.*, 2015). Moreover, a lower slope parameter $m = 7$ (9) causes a higher photosynthesis rate with the same r_{st} (see Eq. 2.17). To analyze the effect of these modifications within the NRW domain for single days, the clear sky case studies have been repeated by using the winter wheat parameters (referred to as CS2605-wheat, CS2407-wheat) instead of the 'clmcrop' parameters.

6.5.1. Modified canopy fluxes and atmospheric CO$_2$ mixing ratios

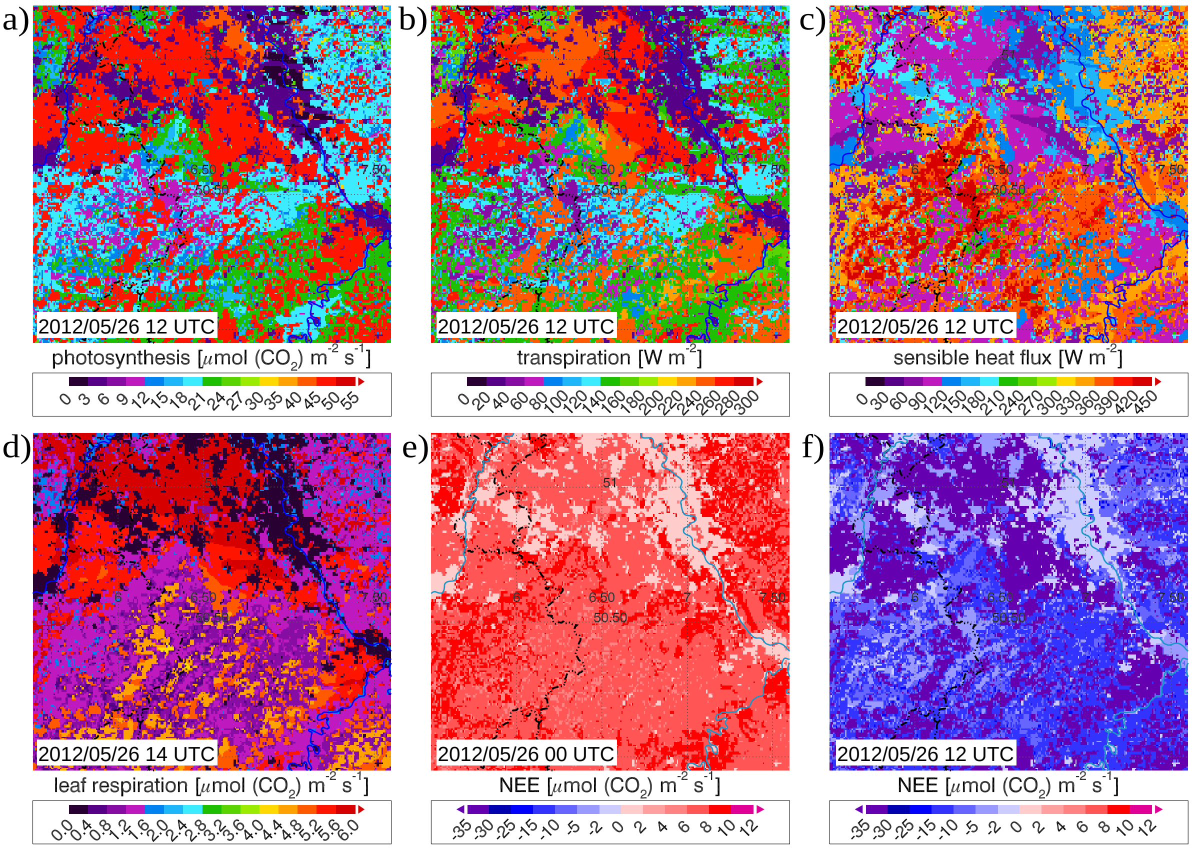

Figure 6.16.: Simulated canopy fluxes of CS2605-wheat: a) photosynthesis, b) transpiration, c) SH flux at 12 UTC, d) leaf respiration at 14 UTC and NEE at e) 00 UTC and f) 12 UTC. Photosynthesis, leaf respiration, NEE: [μmol(CO$_2$)m^{-2}s^{-1}], transpiration, SH flux: [W m^{-2}].

In contrast to CS2605 (Section 4.1.2, Fig. 4.4), in CS2605-wheat the highest photosynthesis and transpiration rates are simulated for large crop areas in the flat terrain (Figs. 6.16a, b). At 12 UTC, photosynthesis of winter wheat is about 2.5–3-fold and transpiration about 2.25–2.5-fold higher than in CS2605 (i. e. 'clmcrop'). For CS2407-wheat a similar trend can be seen with 2.5-fold and twofold higher photosynthesis and transpiration rates than in CS2407, however stronger photosynthesis and transpiration of forests and slightly lower rates of winter wheat than in CS2605-wheat allow less spatial heterogeneity on that day (not shown). A direct consequence of higher transpiration rates (i. e. higher LH fluxes) are lower sensible heat fluxes in agricultural regions than those of 'clmcrop' and those of other PFTs, both in CS2605-wheat and CS2407-wheat (Fig. 6.16c). However, the deviation is smaller than for transpiration caused by a higher absorption of solar radiation using the winter wheat parameters. Leaf respiration (Fig. 6.16d) of winter wheat is many times higher than with the 'clmcrop' parameters and in the order of soil respiration in the afternoon. At night, NEE is comparable (slightly lower) to NEE of forests in CS2605-wheat (CS2407-wheat) and it is the major CO$_2$ sink at daytime (Figs. 6.16e, f). In general, the fluxes of CS2605-wheat seem to be more realistic than those of CS2605. However, CS2407-wheat overestimates the fluxes of crops because the LAI is still 1.6 in July but a large fraction of agricultural fields are cultivated with cereal crops which are already fully ripe or even harvested (see Section 6.5.2).

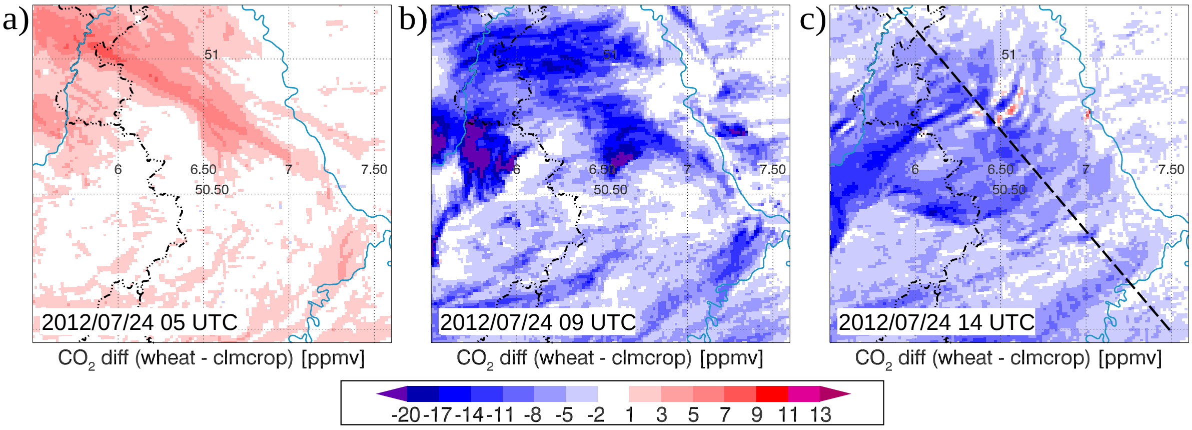

Figure 6.17.: Difference of the simulated CO$_2$ mixing ratio [ppmv] (lowermost COSMO level) between CS2407-wheat and CS2407 at a) 05 UTC, b) 09 UTC and c) 14 UTC.

The influence of modified canopy fluxes on CO$_2$, temperature and humidity in the PBL is described for CS2407-wheat[2]. Fig. 6.17 compares the near surface CO$_2$ contents of CS2407-wheat with CS2407. Higher leaf respiration rates of winter wheat than in CS2407 at night cause a stronger CO$_2$ accumulation showing 2–8 ppmv higher CO$_2$ concentrations in the flat terrain but negligible differences in mountainous regions which are mainly covered with forests and grassland (Fig. 6.17a). In CS2605-wheat, the difference is even stronger (5–15 ppmv) because additionally to leaf respiration also autotrophic respiration is increased. Between 5 and 9 UTC, intensified photosynthesis leads to a much faster reduction of CO$_2$ mixing ratios. Due to low wind speeds, especially above large agricultural areas (e. g. Jülicher Börde, northern part of BE, southwest of Koblenz, district Heinsberg) widespread lower CO$_2$ contents than in CS2407 are simulated ($\approx$ 10–20 ppmv, locally $<$ 20 ppmv) whereas in the other regions the differences are less evident (Fig. 6.17b). Thus, with the new plant physiological parameters a significantly stronger horizontal heterogeneity develops in the PBL with CO$_2$ contents ranging from 360 ppmv in northern Belgium and in the Siebengebirge to 390 ppmv in the eastern Eifel region and 420 ppmv in the Kölner Bucht (Fig. 6.19a). In the following hours, the CO$_2$ distribution in the CBL smooths and the lower CO$_2$ contents are advected towards the northern Eifel region (Fig. 6.17c). CS2605-wheat shows a similar behavior (not shown).

---

[2] To compare with Section 4.1.3, CS2407-wheat is analyzed, although the canopy fluxes of winter wheat may be too strong. However, the sensitivity of the PBL on different plant physiological parameters can be studied.

A vertical cross section (Fig. 6.18a) exhibits strong horizontal gradients in the well-mixed CBL in the afternoon with the lowest CO_2 mixing ratios above and downstream of crop dominated areas (50.55–50.75 °N) but also rather low CO_2 contents in the rural Eifel. As described in Section 4.1.3, the about 20 ppmv higher values in the northern part result from fossil fuel emissions and from the inflow of high CO_2 contents at the northern lateral boundaries. Compared to CS2407, in the entire CBL the CO_2 contents of CS2407-wheat are lower (Fig. 6.18b) with the highest deviations (≈ 10 ppmv) above crops between Euskirchen and Düren (50.7–50.85 °N).

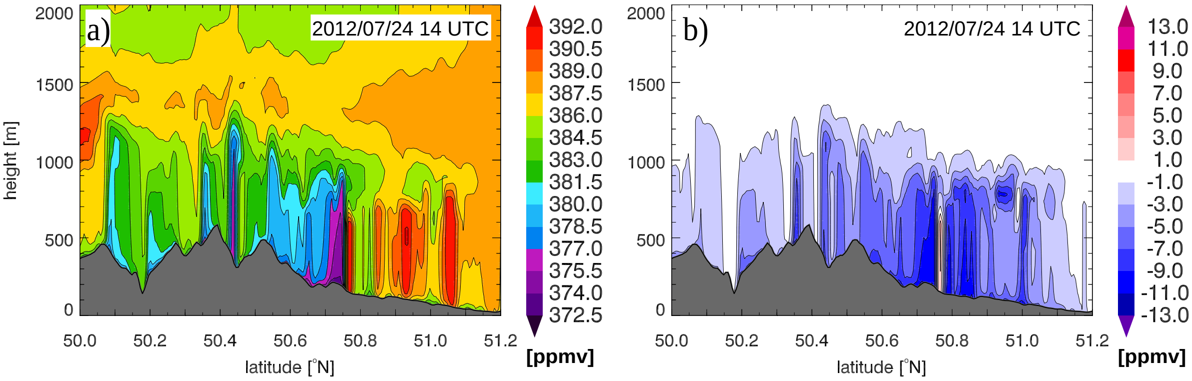

Figure 6.18.: Vertical cross sections (dashed line in Fig. 6.17c) of a) CO_2 mixing ratio [ppmv] of CS2407-wheat and b) difference to CS2407 [ppmv], both at 14 UTC.

Additionally, the distinctly higher transpiration rates of winter wheat cause higher humidity in the CBL. Fig. 6.19b indicates on average 1.0–1.25 °C (locally > 2°C) higher 2 m dew point temperatures at 14 UTC. In contrast, the 2 m temperature of CS2407-wheat is on average 0.5–0.7 °C lower than in CS2407 due to stronger evaporative cooling (Fig. 6.19c).

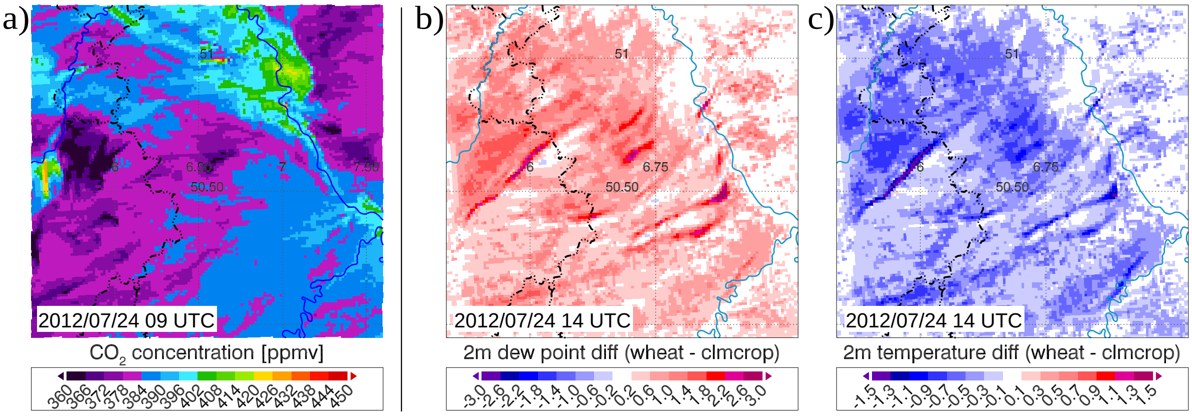

Figure 6.19.: a) Simulated CO_2 mixing ratio [ppmv] of CS2407-wheat in the lowermost COSMO level at 09 UTC; difference of b) 2 m dew point temperature [°C] and c) 2 m temperature [°C] between CS2407-wheat and CS2407 at 14 UTC.

Fig. 6.20a compares the diurnal course of CO_2 of CS2605-wheat with CS2605 in an agricultural area. In 10 m height the diurnal variation is about 20 ppmv higher than in CS2605. Moreover, about 8 ppmv lower CO_2 mixing ratios are simulated at daytime as well as a much faster decrease in the morning. The distinctly lower CO_2 concentrations in 10 m than in 122 m reveal a strong CO_2 sink of winter wheat. This feature is not simulated in CS2605 where the CO_2 fluxes are much weaker. In 122 m, at night the CO_2 mixing ratios of CS2605-wheat and CS2605 are similarly showing that the stronger respiration only influences the lower decameters of the atmosphere whereas stronger differences can be seen after including this height into the CBL at daytime. Finally, as Fig. 4.12b, Fig. 6.20b compares the simulated diurnal CO_2 cycle with measured mixing ratios in 102.5 m height near Jülich. The CO_2 cycle of CS2605-wheat matches the measured CO_2 concentrations quite well. Especially the fast decrease in the morning and the daytime CO_2 mixing ratios are in much better agreement in CS2605-wheat than in CS2605 but also the nocturnal CO_2 concentrations are more realistic.

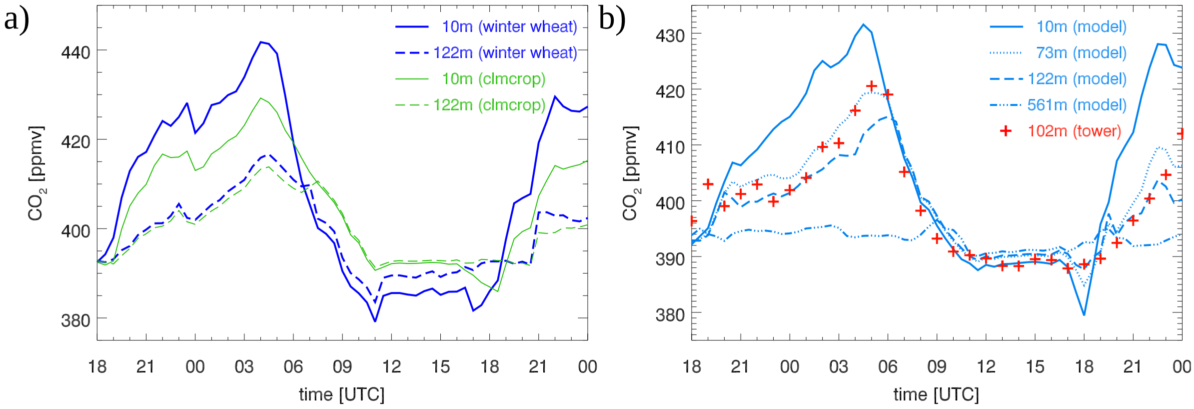

Figure 6.20.: a) Comparison of simulated CO_2 time series [ppmv] of CS2605-wheat (blue) and CS2605 (green) above a crop area near Zülpich, b) same as Fig. 4.12b, but for CS2506-wheat.

6.5.2. Verification with EC measurements

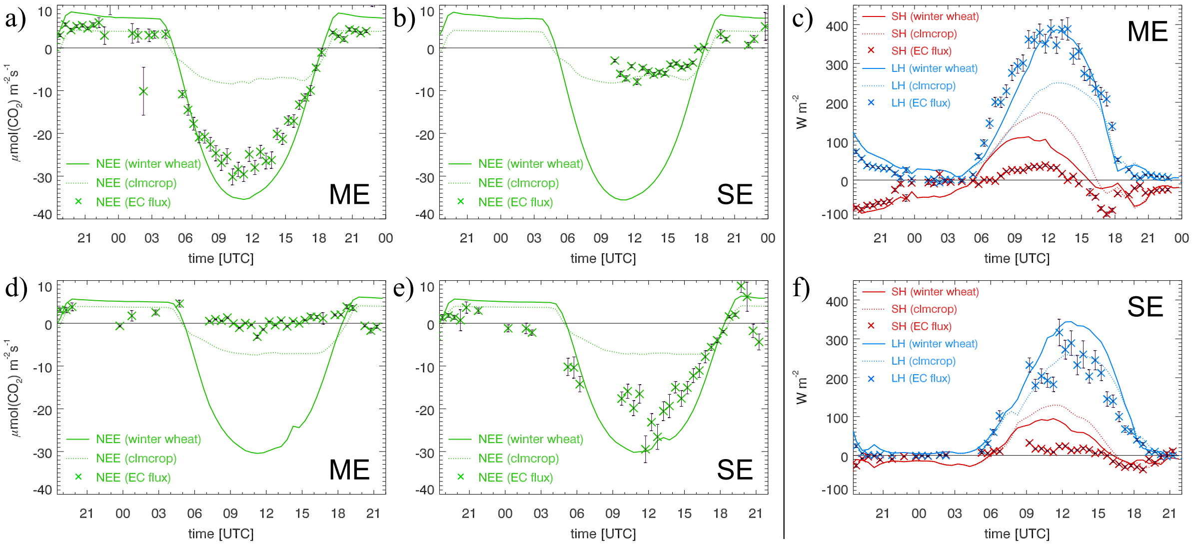

Figure 6.21.: Comparison of EC fluxes (crosses) of NEE [μmol(CO_2)$m^{-2}s^{-1}$], LH and SH [W m^{-2}] at Merzenhausen (ME) and Selhausen (SE) with simulated fluxes using winter wheat (solid lines) and 'clmcrop' parameters (dotted lines) on 2012/05/26 (a–c) and 2012/07/24 (d–f).

The simulated canopy fluxes of crops of CS2605-wheat and CS2407-wheat are compared with EC measurements in Merzenhausen and Selhausen. At Merzenhausen (winter wheat), NEE is simulated clearly better using the plant physiological parameters of winter wheat (solid lines) than with the 'clmcrop' parameters (dotted lines, Fig. 6.21a). Whereas for CS2605 NEE is strongly underestimated at daytime, for CS2605-wheat only a slight *over*estimation can be seen. Different from CS2605 no daytime saturation (i. e. capacity utilization limitation) occurs because of the higher $V_{c,\max}$ values. The monthly averaged diurnal cycle of NEE for a winter wheat field in May 2013, however, shows slightly *under*estimated NEE (Sulis *et al.*, 2015, Fig. 6). NEE chamber measurements at a winter wheat field near Selhausen on 25 May 2012 (cf. Fig. 5.2) confirm the better agreement of NEE using the winter wheat parameters instead of 'clmcrop'. At night, soil respiration seems to be slightly overestimated in CS2605-wheat but the high uncertainty of measured fluxes in stable stratified nights has to be considered.

Consistent with NEE, the partitioning of absorbed solar radiation in latent and sensible heat fluxes is clearly improved in CS2605-wheat (Fig. 6.21c). The LH flux is simulated well but the SH flux is still overestimated by TerrSysMP-CO_2. The NEE at Selhausen (potatoes) cannot be represented with the applied LAI because the potato plants are in a very early growing stage (plant height: 13 cm) and produce little photosynthesis (Fig. 6.21b).

The 'clmcrop' parameters would lead to a better agreement but for the wrong reasons. In contrast to these results, in CS2407-wheat, the simulation of NEE for the winter wheat field in Merzenhausen fails because at this time the cereals are fully ripe (i. e. "Gelbreife") and, therefore, photosynthesis is negligible. Consistently, LH fluxes are strongly overestimated. This may cause too low CO_2 mixing ratios and a too moist and cold PBL above large cereal crop areas. However, NEE at the potato field in Selhausen is simulated rather well, even using the winter wheat parameters (Fig. 6.21e). The LH flux shows no clear improvement compared with 'clmcrop' (Fig. 6.21f), the SH flux is slightly improved but it is still overestimated which seems to be either an artifact of TerrSysMP-CO_2 or of the measurements.

The comparison with EC stations clearly indicates a better representation of the plant physiological behavior of cereal crops using the new winter wheat parameters of Sulis *et al.* (2015). The diurnal cycles of NEE, LH and SH fluxes are improved in the growing and mature stage of cereal crops, i. e. in spring and early summer, compared to the 'clmcrop' parameters. However, the characterization of agriculture (PFT=15) by means of monthly LAI values averaged over *all* arable land and only *one* plant physiological parameter set – as currently done in TerrSysMP(-CO_2) – is not appropriate in the NRW domain in which the agricultural cultivation very diverse. Instead, several agricultural PFTs (e. g. cereal crops, maize, vegetables) having their own plant physiological parameters and seasonal LAI cycles (i. e. different sowing, growing, mature and harvest times, see Table A.2 in the appendix) would be preferable. However, consistent datasets for the NRW domain or for the larger nesting domains are rare. One option is the MODIS Land Cover Type 5 (PFT classification) dataset which is also the basis of the current land cover map of the NRW domain (Shrestha *et al.*, 2014). This PFT classification distinguishes between cereal (e. g. wheat, barley, rye, oats) and broadleaf crops (e. g. sugar beet, cabbage, potatoes, oilseed radish and other vegetables) and could be used for the winter wheat and sugar beet parameters in combination with separated seasonal LAIs for these plant species.

Because these model modifications are beyond the scope of this study, it is proceeded using one crop "PFT" with the default seasonal LAI cycle (Shrestha *et al.*, 2014) but with the winter wheat parameters of Sulis *et al.* (2015) for all "crop" grid points. In consideration that in the MODIS dataset about 75–80% of all arable areas in the NRW domain are allocated to cereal crops, this assumption is reasonable, at least before progressed senescence and harvest of cereal crops in mid/late summer. However, after harvest of cereal crops in late summer as well as above a large broadleaf crop area between Aachen and Liège in early summer the simulated NEE and the LH flux may be overestimated due to the inappropriate LAI. This may lead to a low (wet) bias of the simulated CO$_2$ mixing ratio (humidity) in the PBL.

6.5.3. Improvement of the CO$_2$ budget

date	**2012/05/26**	**2012/07/24**
photosynthesis	−11.729 (−7.088)	−11.053 (−7.315)
leaf respiration	*1.543 (0.530)*	*1.536 (0.555)*
soil respiration	*5.737 (4.996)*	*4.987 (5.134)*
total respiration	7.280 (5.526)	6.524 (5.690)
anthro. emissions	1.878 [Sat]	1.796 [Tue]
budget	**−2.570** (+0.316)	**−2.735** (+0.170)

Table 6.1.: CO$_2$ budget [μmol(CO$_2$)m^{-2}s^{-1}] of CS2605-wheat and CS2407-wheat (− sink, + source). The values of CS2605 and CS2407 ('clmcrop' parameters) are in parentheses.

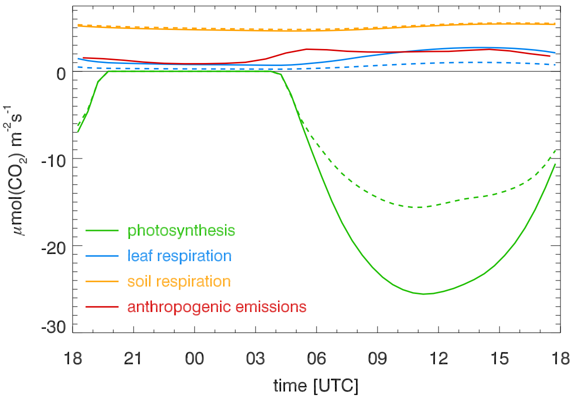

Figure 6.22.: CO$_2$ fluxes of CS2407-wheat (solid lines) and CS2407 (dashed lines) averaged over the NRW domain [μmol(CO$_2$)m^{-2}s^{-1}].

With the change of the plant physiological parameters of PFT=15 (37% of the NRW domain) from the 'clmcrop' to the winter wheat parameters, the CO$_2$ budget of the *entire* domain changes significantly (Table 6.1). The averaged photosynthesis rates in CS2605-wheat and CS2407-wheat are considerably higher ($\approx 11\,\mu$mol(CO$_2$)m^{-2}s^{-1}) than the ones of CS2605 and CS2407 ($\approx 7\,\mu$mol(CO$_2$)m^{-2}s^{-1}). The averaged maximum CO$_2$ uptake in CS2407-wheat reaches about 26 μmol(CO$_2$)m^{-2}s^{-1} (11:30 UTC) whereas the maximum CO$_2$ uptake in CS2407 ($\approx 15.5\,\mu$mol(CO$_2$)m^{-2}s^{-1}) is simulated slightly earlier (10:45 UTC) (Fig. 6.22). Although only the parameters of crops have been changed, the spatially averaged leaf respiration increases about three-fold and is then in the order of anthropogenic emissions. Soil respiration also changes slightly due to modified autotrophic respiration. Even by including the relatively intense anthropogenic emissions (≈ 20% of the total CO$_2$ source) a significant net CO$_2$ loss is simulated for these clear sky days. This seems to be more realistically than the CO$_2$ gain in the corresponding simulations with the 'clmcrop' parameters because it is better in accordance with the measured decrease of 20–25 ppmv in the averaged CO$_2$ concentrations at the Jülich tower during spring and summer (Fig. 7.2). Moreover, both the natural CO$_2$ sink of vegetated canopies as well as the averaged net CO$_2$ sink over the entire NRW domain are conform with the maps of "CarbonTracker Europe" (2014) showing monthly net CO$_2$ fluxes of the same order of magnitude over Central Europe. One may conclude that the change of the plant physiological parameters of the PFT=15 to the winter wheat parameters of Sulis *et al.* (2015) yields an improved CO$_2$ budget for the NRW domain, at least before progressed senescence and harvest of cereal crops (i. e. about end of July).

7. Dependence of vertical CO_2 distribution on atmospheric stratification

In this chapter, the CO_2 variability is investigated in a period of eight consecutive days with different weather conditions. The main focus is on the relationship of vertical CO_2, temperature and wind profiles. The simulations are compared with observations of CO_2 mixing ratios and meteorological state variables in several heights at a tall tower near Jülich. In order to estimate the effect of advective transport of CO_2 concentrations the land use and phenology stages are studied and the simulated CO_2 fluxes are compared with fluxes of several EC stations.

7.1. Characterization of the meteorological tower near Jülich

The results of TerrSysMP-CO_2 simulations are compared with observations made on a 124 m tall meteorological tower near Jülich (50.91 °N, 6.41 °E, 91 m a.s.l., see Fig. 3.1), operated by the Forschungszentrum Jülich GmbH (Jülich tower, Fig. 7.1). The tower is located north of the research center at the eastern side of an about 90 m × 40 m wide clearing surrounded by a small and about 25 m tall broadleaf forest. Most of the surrounding area is flat (Jülicher Börde) and is characterized by arable land use (see Section 7.2). However, 3 km to the northeast the up to 302 m high spoil heap Sophienhöhe influences the local wind system. Two opencast mines (Inden, Hambach) are located in the nearby area of the tower and about 10 km southwest of the tower the coal-fired power plant Weisweiler is an intense CO_2 source. Additional anthropogenic CO_2 emissions come from Jülich, located about 2 km to the northwest, the research center and a sugar factory in the southeast of Jülich.

height	**observations**
12.5 m	temperature, relative humidity, wind speed, $\mathbf{CO_2}$ (LI-840A)
20.0 m	temperature, relative humidity, wind speed, [$\mathbf{CO_2}$ (out of order in summer 2014)]
32.5 m	temperature, relative humidity, wind speed and direction, radiation, $\mathbf{CO_2}$ (LI-840A)
52.5 m	temperature, relative humidity, wind speed and direction, $\mathbf{CO_2}$ (LI-840A)
82.5 m	temperature, relative humidity, wind speed
102.5 m	temperature, relative humidity, wind speed, $\mathbf{CO_2}$ (FGGA)
120.0 m	temperature, relative humidity, wind speed and direction, radiation

Table 7.1.: Important observations on the Jülich tower used for this study.

The Jülich tower has seven platforms (12.5 m, 20.0 m, 32.5 m, 52.5 m, 82.5 m, 102.5 m, 120.0 m) with cantilever arms (Fig. 7.1) being equipped with meteorological instruments and instruments for scientific purposes. In order to investigate the diurnal variation and vertical distribution of CO_2 (and H_2O) mixing ratios in the PBL, three LI-840A gas analyzers[1] have been installed on the tower in 12.5 m, 32.5 m and 52.5 m height. Additionally, at the 102.5 m platform

---

[1] LI-840A CO_2/H_2O Gas Analyzer (LI-COR Biosciences, Lincoln, USA)

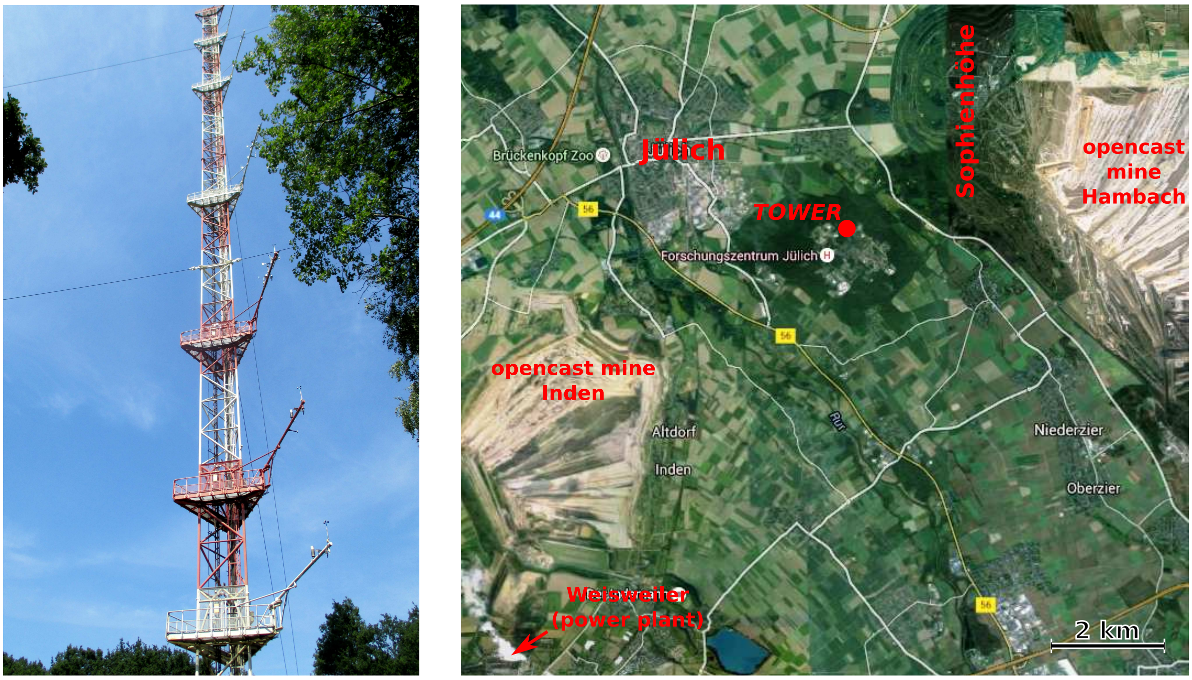

Figure 7.1.: Meteorological tower of the Forschungszentrum Jülich GmbH (left) and the geographical location (right), *source of map*: `https://maps.google.de` (*requested on 2015/10/23*) .

the FGGA[2] provides CO_2 mixing ratios. This height is already appropriate to precisely estimate CO_2 contents in the well-mixed PBL at daytime (Haszpra *et al.*, 2015). CO_2 mixing ratios are also observed in 20 m height, but in summer 2014 the analyzer was out of order and is not further specified, here. The LI-840A gas analyzers measure CO_2 in 1-min intervals but the values are averaged piecewise over 10 min to be consistent with the meteorological observations and the CO_2 measurements in 102.5 m. Table 7.1 summarizes the most important observations.

Fig. 7.2 depicts the CO_2 mixing ratios in 12.5 m height from April 2014 to August 2015. The growing season can be clearly seen on the considerably higher daily amplitudes than in the winter months. In the summer season, photosynthesis causes a strong CO_2 uptake at daytime whereas during nighttime pronounced soil respiration leads to a strong CO_2 increase near the surface, especially when a stable stratified nocturnal PBL forms (Section 7.3.5). In the winter months, the biogenic CO_2 fluxes are low due to negligible leaf mass and cold soil and atmospheric temperatures. The moving average over 5 days (blue curve) shows the dependency of mean CO_2 contents on different large-scale weather situations. Moreover, the moving average over 30 days (green curve) gives a rough approximation of the seasonal variation of about 20–25 ppmv with the highest values in the beginning of the growing season and the lowest values in August/September. This pronounced seasonal amplitude is the result of the special location of the tower, far away from coasts and in a region with high anthropogenic emissions in the near and wider surroundings. Most tall towers measuring background CO_2 mixing ratios are located on mountain tops, e. g. at Ochsenkopf (Pillai *et al.*, 2011), or far away from intense biogenic or anthropogenic sources, e. g. Mauna Loa (Hawaii) (Keeling *et al.*, 1996), therefore

---

[2] Fast Greenhouse Gas Analyzer CO_2 CH_4 H_2O (Los Gatos Research, Mountain View, USA), data downloaded from: `https://amica.icg.kfa-juelich.de/TowerObservations`

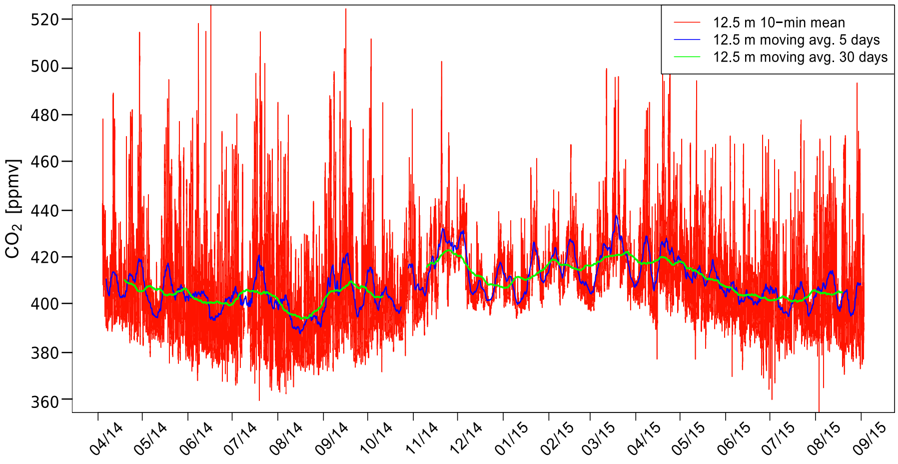

Figure 7.2.: CO_2 mixing ratios [ppmv] on the Jülich tower in 12.5 m height (red curve). The moving averages over 5 and 30 days are depicted as blue and green lines, respectively.

showing lower seasonal variations. In 102.5 m, the seasonal variation is similar but the daily amplitudes are considerably smaller than in 12.5 m (not shown).

7.2. Phenology and arable land use in 2014

The findings of this chapter will show that advective transport of CO_2 concentrations strongly controls the simulated CO_2 patterns in the PBL. Thus, for an interpretation of observed CO_2 contents on the Jülich tower, the biogenic CO_2 fluxes in the near and wider surroundings have to be considered which depend on different plant species and their phenological stage. The predominant land use in the Jülicher Börde is arable land (see Fig. 3.2a) with diverse cultivated plants. Fig. 7.3 depicts the arable land use of the district Düren and its adjacent districts in 2014[3]. More than half of all agricultural areas are cultivated with cereal crops (e. g. wheat, barley, rye). Hence, with having only *one* PFT in TerrSysMP-CO_2 representing the entire arable land, the use of the plant physiological parameters of winter wheat is most appropriate. Further common cultivated plants are sugar beet (18%) and other broadleaf crops (potatoes: 6%, vegetables: 3%). Rapeseed (7%) and maize (9%) are important atmospheric CO_2 sinks in the early and later growing season, respectively. The local occurrence of cultivated plants also depends on climatic conditions (i. e. orographic height) and soil quality.

Different from 2012 and caused by a sequence of unusually high temperatures in February, March and April, in 2014 an exceptional anomaly of the timing of phenological stages was observed with a 3–4 weeks earlier beginning of the growing season. Below-average temperatures in May and ordinary temperatures in June led to a slight normalization, however, the timing of the phenological stages are still about 1–2 weeks earlier than the average. This fact has to be considered for the comparison of observed and simulated canopy fluxes using a 10-year mean for the seasonal course of LAIs in TerrSysMP-CO_2 (Shrestha *et al.*, 2014).

To estimate the representativity of simulated canopy fluxes in 3–10 June 2014 (Section 7.3), Table 7.2 lists the observed timings of the phenological stages at several locations around Jülich as well as the average timings in NRW. Rapeseed (not included in Table 7.2) is already fully

---

[3] a list and pie charts of arable land use separated in each district can be found in the appendix

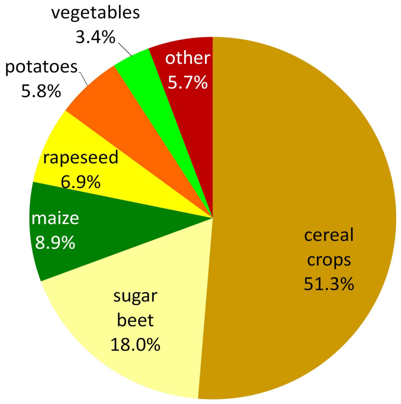

land use	area [ha]	percentage
cereal crops	76986.7	51.3%
sugar beet	27081.7	18.0%
maize	13351.1	8.9%
rapeseed	10393.0	6.9%
potatoes	8715.1	5.8%
vegetables	5038.0	3.4%
other	8547.0	5.7%
total	150112.5	100.0%

Figure 7.3.: Arable land use [ha, %] of the districts Rhein-Erft-Kreis, Heinsberg, Düren, Euskirchen and Städte Region Aachen in 2014 (Landwirtschaftskammer Nordrhein-Westfalen, 2015).

winter wheat				**maize**			
Ährenschieben: ∅ NRW 05/18 (−13 days)				**Auflaufen: ∅ NRW 05/02 (−8 days)**			
Aachen-Orsbach	05/16	Eschweiler	05/18	Aachen-Orsbach	05/02	Hambach	05/04
Hambach	05/06	Euskirchen	05/21	Eschweiler	05/01	Euskirchen	05/06
Gelbreife: ∅ NRW 07/10 (−9 days)				**Fahnenschieben: ∅ NRW 07/15 (+1 days)**			
Aachen-Orsbach	07/05	Eschweiler	07/16	Aachen-Orsbach	07/18	Hambach	07/10
Hambach	06/27	Euskirchen	07/13	Eschweiler	07/19	Euskirchen	07/18
winter rye				**potatoes**			
Blühende: ∅ NRW 06/06 (−3 days)				**Bestand geschlossen: ∅ NRW 05/25 (−7 days)**			
Hambach	06/06	Hennef	06/09	Eschweiler	05/31	Hambach	05/06
Gelbreife: ∅ NRW 07/07 (−6 days)				Euskirchen	05/28	Hennef	05/23
Hambach	07/01	Euskirchen	07/19	Bonn-Rodderberg	05/06		
Hennef	06/27						
winter barley				**beets**			
Gelbreife: ∅ NRW 06/17 (−9 days)				**Bestand geschlossen: ∅ NRW 05/30 (−11 days)**			
Aachen-Orsbach	06/12	Hambach	06/07	Aachen-Orsbach	05/29	Hambach	05/23
Euskirchen	06/12	Hennef	06/09	Eschweiler	05/29	Euskirchen	05/30
Bonn-Rodderberg	06/07			Hennef	05/23	Bonn-Rodderberg	05/20

Table 7.2.: Timing of phenology stages of agricultural cultivated plants in NRW in 2014 (Deutscher Wetterdienst, 2015), extract from Table A.3. Deviations from the longtime average are in parentheses. Detailed descriptions of the phenology stages can be found in Table A.2.

matured and, thus, photosynthesis is very low. The "Ährenschieben" (begin of formation of ears) of winter wheat and winter rye, the most common cereal crops in NRW, was 3 (rye) to 5 (wheat) weeks ago and winter rye (wheat) reached the end of anthesis ("Blühende") in (some weeks before) the simulated period. The "Gelbreife" (change of grain color from green to yellow) was observed about 3–4 weeks after the simulated week. Hence, the photosynthesis rates of these crops already fall below their maximum (during anthesis) but were still moderate to high. Winter barley has an earlier growing season and especially in the flat terrain around Jülich (e. g. Hambach) and along Rhine and Sieg (e. g. Bonn-Rodderberg, Hennef) the "Gelbreife" was observed during the simulated period. Thus, CO_2 assimilation rapidly decreases at this time (see Section 7.3.3). Maize was between "Auflaufen" (begin of sprout) and "Fahnenschieben" (begin of formation of panicles). Hence, moderate photosynthesis can be assumed. Potatoes and beets were rapidly growing and reached the phenology stage "Bestand geschlossen" (50% of plants touch plants of the adjacent sowing row) on average some days before the simulated week. However, the growing stage strongly depends on the sowing time and plant type. With the rapidly increasing leaf mass NEE strongly increases.

In summary, in the simulated week the potential photosynthesis rates of cereal crops decreased and were already lower than the optimum. The potential CO_2 assimilation of maize and broadleaf crops were moderate and increased. In contrast, TerrSysMP-CO_2 assumes the highest LAI, i. e. maximal photosynthesis rates, for June because normally cereal crops are during anthesis at this time. This may lead to overestimated NEE rates of PFT "crops" in the flat terrain (Section 7.3.3). In mountainous regions, the observed growing stages are 2–3 weeks later than in the flat terrain. Here, the simulated fluxes are probably simulated realistically.

7.3. Simulation of 3–10 June 2014

7.3.1. Model nesting strategy

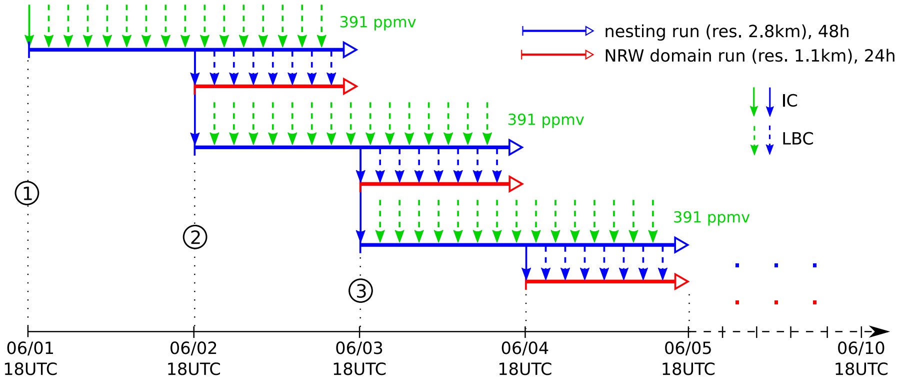

Figure 7.4.: Model nesting strategy of the TerrSysMP-CO_2 simulation, see text for further explanations.

In order to study the reasons for very different diurnal variations and vertical gradients of CO_2 concentrations at the Jülich tower between 3 and 10 June 2014 (Sections 7.3.4–7.3.5) this period has been simulated with TerrSysMP-CO_2. Because nudging of atmospheric state variables and CO_2 or other data assimilation methods have been avoided to ensure a free model prediction, this period has to be split into several short-time simulations. For that, the following model nesting strategy has been applied (Fig. 7.4). An initial nesting run is started on 1 June 2014, 18 UTC (①). This simulation is initialized with a homogeneous background CO_2 content of 391 ppmv and runs 48 h using the background CO_2 content as hourly lateral boundary conditions (LBC). After 24 h (2 June, 18 UTC, ②), both the simulated CO_2 distribution and meteorological fields of this run are used to initialize the first 24 h simulation for the NRW domain which additionally receives hourly CO_2 and meteorological LBCs from the nesting simulation. At the same time, a second nesting simulation is started using the CO_2 distribution of the first nesting simulation (and COSMO analyses for meteorological fields) as initial conditions (IC) and then runs again 48 h with 391 ppmv as hourly LBC. On 3 June, 18 UTC (③), the second 24 h simulation for the NRW domain is started as well as the third 48 h nesting simulation, both using the CO_2 distribution of the second nesting run as IC. This procedure is repeated every 24 h. The initialization of the nesting runs with the CO_2 distribution from the previous nesting run allows to test the CO_2 budget better than with artificially forcing the simulation to the background CO_2 content in every nesting simulation.

7.3.2. Meteorological situation

On 3 June 2014, Central Europe was in front of an upper level trough west of Great Britain in a region with weak pressure gradients. In the NRW domain it was partly cloudy (cumulus) overlayed with cirrus clouds in the afternoon. Some showers developed and the wind was weak. On 4 June, a short-wave trough formed in the southern part of the upper level trough and moved to the English Channel inducing a low pressure system over England. Ahead of its cold front, in the morning a band of light stratiform rain passed the NRW domain. In the afternoon along a convergence line the rain was more convective. The temperatures were low and the wind continuously increased to a moderate breeze. The passage of the cold front in the late evening was accompanied with intense showers and a moderate to strong southwesterly wind. The wind continued on 5 June before it weakened in the afternoon. To the rear of the cold front, the temperatures were cold at night (4–9 °C) and stayed rather cool at daytime with also low dew point temperatures. The sky was partly cloudy on 5 June. In the following days (6–8 June), in front of a long-wave trough over the Atlantic a southerly flow advected very warm air masses towards Central Europe with distinctly increasing specific humidity on 7 June. The temperature increased from about 20 °C (5 June) to 27–32 °C (7/8 June). The 6 June was a ideal clear sky day and on 7 June cirrus fields reduced solar radiation slightly. Fair weather conditions occurred on 8 June, however with some clouds in the northwestern model domain resulting from nocturnal thunderstorms in BeNeLux. On 9 June, at noon in the potentially unstable air mass a supercell storm developed and in the evening a very severe squall line passed NRW with damaging wind gusts. Unfortunately, both convective systems are not captured by the model. Instead, in the second half of the night thunderstorms are simulated in BeNeLux. On 10 June, NRW remained in the warm and moist air mass and fair weather conditions occurred with only some light showers/thunderstorms in the evening.

In general, the different weather situations are captured well by the model. The wind speeds and directions as well as the atmospheric humidity is simulated fairly well. Moreover, cloudiness and the temperature increase agree with observations. However, the temperature amplitudes near the surface are underestimated by TerrSysMP-CO_2 tending to too warm temperatures at night and too low temperatures in the afternoon.

In Fig. 7.5 the simulated temperature, radiation, wind and humidity are compared with observations on the Jülich tower. Both in the model and in the observation the moderate temperatures on 3–5 June, the high temperatures on 7–10 June and the intense warm advection on 6 June are apparent. Especially on 5 and 7 June the simulated 2 m temperature is in good agreement with the observations whereas on 8 June the daytime temperature is too low caused by a simulated advection of cooler air masses from cloudy regions in BeNeLux. Moreover, in several nights (3/4/6/7 June) the simulated 2 m temperature is too warm whereas the maximum temperatures are underestimated (6/8/9 June) although the weather station is in a forest clearing. In contrast, in 120 m a.g.l. the simulated temperature amplitudes are very similar to the observations (deviations $< 1\,°C$), except on 8 June (not shown). The temperature drop and the colder temperatures in the evening of 9 June resulted from the squall line.

On most days, the radiation budget is simulated fairly well, especially on the the clear sky day (6 June) as well as on 8 June and even the cloudiness on 4 June is predicted well. Only on 5 June, the cumulus clouds induced by the low pressure system over the Netherlands are underestimated by TerrSysMP-CO_2 and on 10 June the radiation is slightly higher than in reality. The low peak in the observed radiation on 9 June is caused by the supercell storm.

The atmospheric flow 120 m a.g.l. is in good accordance with the tower observations. The

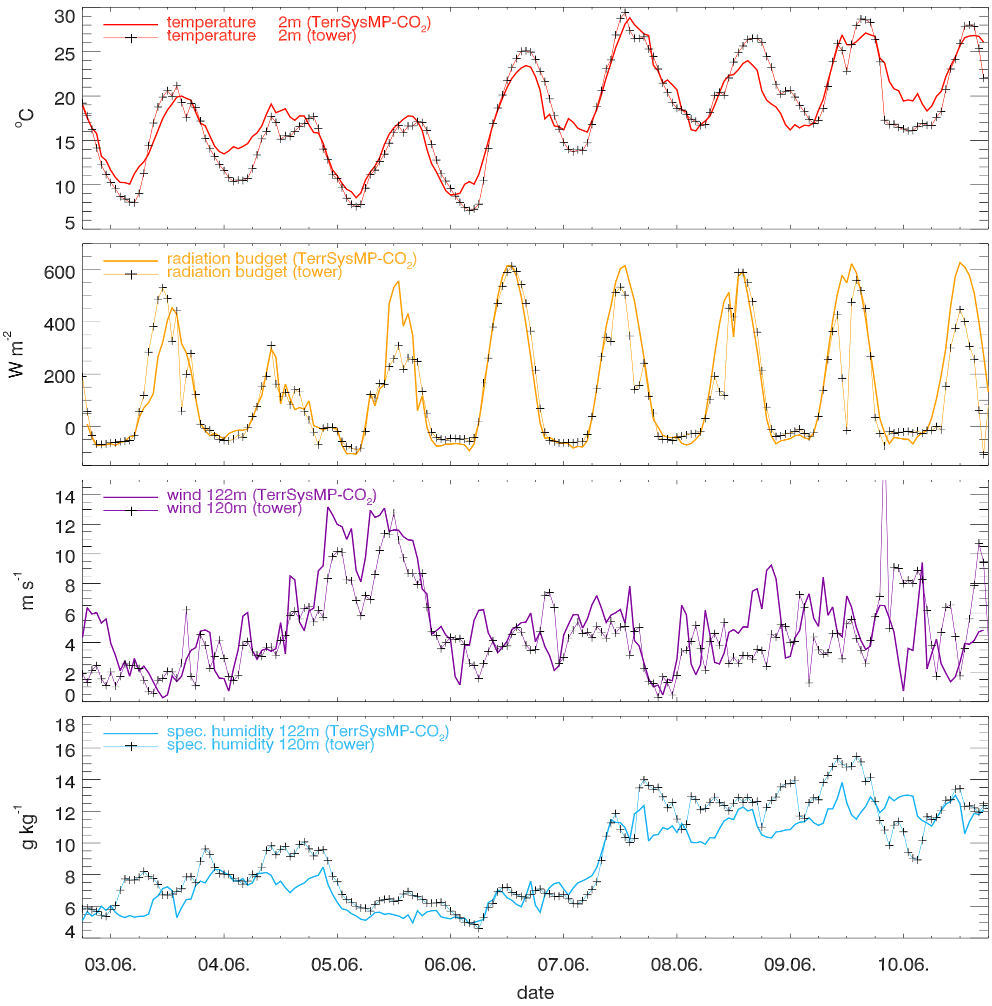

Figure 7.5.: Comparison of simulated (thick solid lines) and observed (crosses) temperature in 2 m [°C], total radiation budget [$\mathrm{W\,m^{-2}}$] as well as wind speed [$\mathrm{m\,s^{-1}}$] and specific humidity [$\mathrm{g\,kg^{-1}}$] at the 120 m platform of the Jülich tower (122 m in TerrSysMP-CO_2).

simulated low wind speeds on 3 June, the increasing winds on 4 June and the high wind speeds on 5 June are very similar to the measured wind at the uppermost platform. The low to moderate winds between 6 and 9 June are well represented and even short time effects (e. g. almost calm conditions in the evening of 7 June) are captured by the model. The only significant deviations from the measured wind are the missing wind peak of the squall line and the higher wind speeds afterwards. The 10 m wind of TerrSysMP-CO_2 cannot be compared with the observations because of the location of the tower (small forest clearing) and it agrees better with the wind at the 32.5 m platform, i. e. 8–10 m above the forest height (not shown).

The general behavior of the simulated and observed specific humidity 120 m a.g.l. is similar with rather low values between 3 and 6 June, especially after the cold front on 5 and 6 June (4.5–7.5 $\mathrm{g\,kg^{-1}}$), and rather high values between 7 and 10 June. From the evening of 7 June to the afternoon of 9 June the simulated specific humidity (10–14 $\mathrm{g\,kg^{-1}}$) is slightly below the observed values (11–15.5 $\mathrm{g\,kg^{-1}}$), possibly one of the reasons for the missing convective activity on 9 June in the simulation. The deviations due to the squall line are apparent.

7.3.3. Comparison of simulated NEE with EC stations

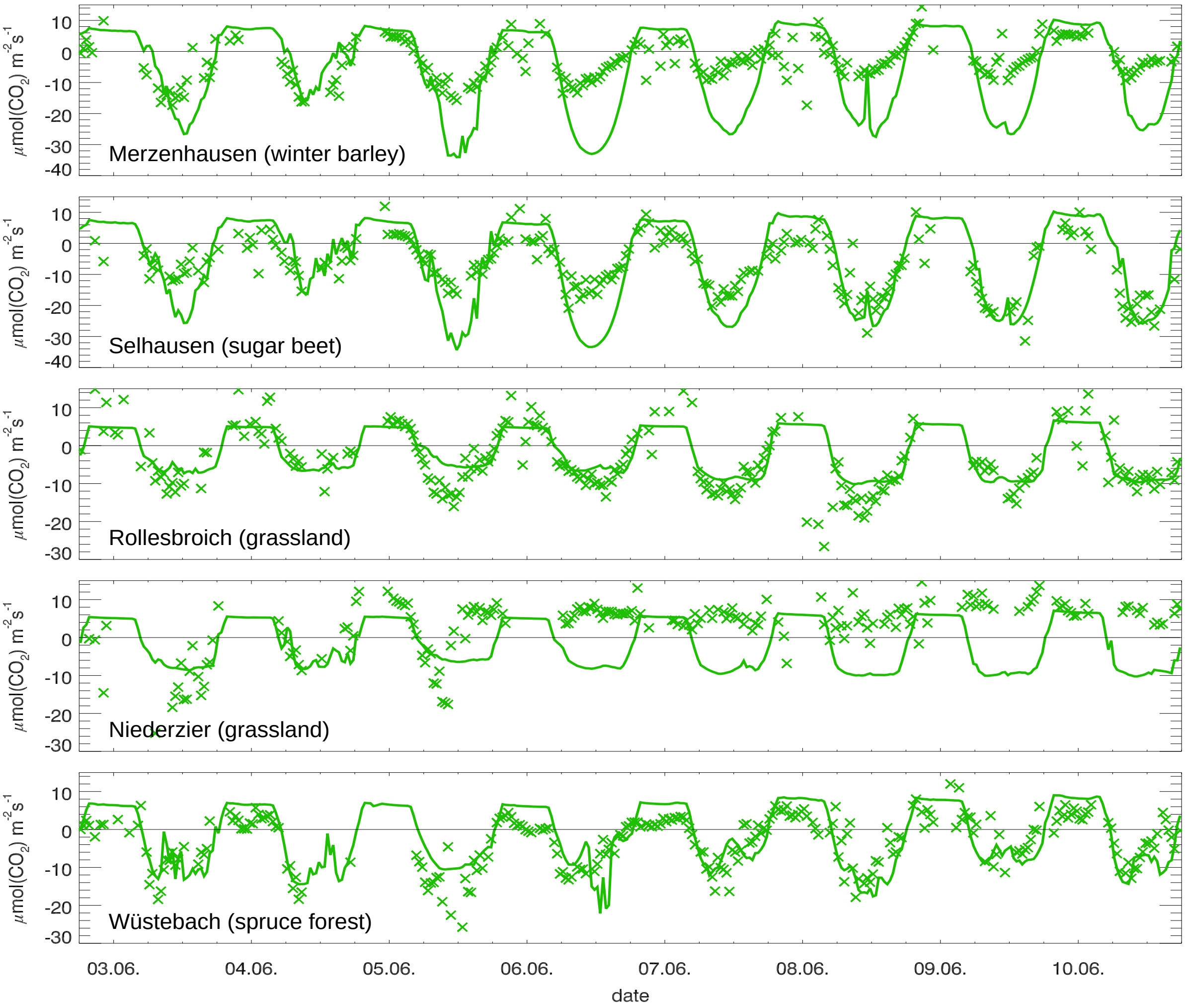

Figure 7.6.: Comparison of simulated (solid lines) and observed (crosses) NEE in Merzenhausen, Selhausen, Rollesbroich, Niederzier and Wüstebach.

In this section, the NEE of different plant species is compared with simulated NEE of different PFTs. In 2014, the Merzenhausen field was cultivated with winter barley. On average, TerrSysMP-CO_2 simulates higher photosynthesis rates than in the observations, i. e. at daytime the simulated NEE is more negative than the EC fluxes. A closer look shows that at daytime the observed NEE is higher on 3–5 June and decreases to the end of the period. Considering the findings of Section 7.2, at this time winter barley was in the transition to the "Gelbreife" stage and the very warm temperatures and fair weather conditions in the second half of this period enhanced this process. This explains the strong overestimation[4] of NEE on 6–10 June. On 3 June, the simulated NEE agrees better with the EC fluxes and in the morning TerrSysMP-CO_2 even underestimates NEE due to stronger radiative attenuation than in reality (see Fig. 7.5). The CO_2 flux on the cloud covered 4 June is well represented and the overestimation of simu-

---

[4] as in Section 5.1, under-/overestimation of NEE refers to the absolute values of NEE

lated NEE on 5 June is partly a result of underestimated cloudiness. An analysis of nighttime respiration is difficult because of the few reliable measurements, nonetheless the simulated respiration rates are in the range of the observations. A comparison of simulated NEE using the winter wheat parameters with a winter wheat (or winter rye) field being less senescent than winter barley would probably lead to a much better agreement but, unfortunately, EC fluxes at a winter wheat field are not available in 2014.

The Selhausen field was tilled with sugar beet. Although the plant physiological parameters of winter wheat are used, NEE agrees better than at the winter barley field. The observed daytime NEE increases from 3 to 10 June due to rapidly growing plants. Between 27 May and 11 June, the vegetation height increased from 20 cm to 35 cm. On 8–10 June (high temperatures and specific humidity) the simulated fluxes coincide well with the EC fluxes. On 7 June and especially on 6 June, at noon/afternoon the simulated NEE is more negative than at the sugar beet field. On both days, at noon and in the afternoon the measured specific humidity was low compared to the subsequent days (Fig. 7.7). Moreover, TerrSysMP-CO_2 overestimates the specific humidity in the afternoon of 7 June. Thus, for sugar beet plants moisture limitation of photosynthesis is stronger than in the simulation, partly caused by the overestimated specific humidity (7 June). Probably, additionally the wilting of sugar beet is more sensitive to low atmospheric humidity and low soil moisture than estimated with the winter wheat (i. e. cereal crops) parameters in TerrSysMP-CO_2. On the cloudy day (4 June), NEE is simulated well.

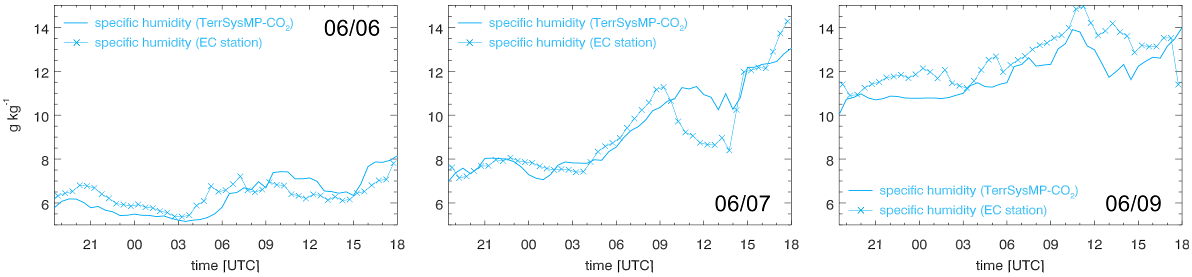

Figure 7.7.: Simulated (thick line) and measured (thin line, crosses) specific humidity [g kg^{-1}] at the Selhausen field (sugar beet) on 2014/06/06, 06/07 and 06/09.

The simulated daytime NEE is in satisfactory accordance with the observed CO_2 fluxes at the meadow near Rollesbroich having a measured grass height of about 25 cm. On most days the measured CO_2 uptake is in the range of the simulated NEE or slightly stronger. On 5 June, in the morning and at noon the observed NEE is more negative than in the simulations. Satellite images indicate cloudless conditions in this time window in the central Eifel region whereas in the TerrSysMP-CO_2 results cumulus clouds partially influence photosynthesis. Nighttime respiration cannot be analyzed due to a lack of reliable fluxes. At the pasture near Niederzier, on 3 and in the morning of 5 June the simulated NEE underestimates the observed CO_2 uptake slightly stronger than in Rollesbroich whereas on 4 June the CO_2 fluxes are realistically simulated. The stronger deviations are caused by a very tall grass of 117 cm at this site. In the afternoon of 5 June, the grass was cut and, thus, photosynthesis cannot be analyzed any more. Instead, in the subsequent days respiration can be estimated. Compared with the simulated nighttime NEE, on 5–7 June the observed CO_2 flux at daytime is in the range of or slightly higher than in the simulation. With consideration of higher temperatures at daytime and additionally fresh grass litter, soil respiration of grasslands seems to be well represented by TerrSysMP-CO_2. The slightly more positive fluxes on 9 June are possible caused by intense respiration of fresh grass litter at temperatures of about 30 °C.

Finally, the simulated NEE of needleleaf trees is compared with the CO_2 flux at the spruce forest near Wüstebach. As in the case studies in 2012, on most days the simulated CO_2 fluxes agree fairly well with the observations. This holds in particular for 3 June as well as for 7–10 June. Hence, the plant physiological parameters seem to be appropriate for a typical needleleaf forest in Central Europe. Only on 5 June the measured CO_2 fluxes tend to be more negative than in the simulation, however the high wind speeds on this day lead to highly fluctuating EC fluxes which are possibly erroneous. The simulated NEE peaks in the afternoon of 6 June cannot be seen in the observations, possibly due to deviating atmospheric humidity.

To conclude, NEE of needleleaf forests and grasslands are quite well simulated. For arable land the evaluation is more difficult. With only one PFT representing the entire arable land, the *simulated* NEE at each "crop" grid point is comparable. However, in reality the NEE of arable land is very heterogeneous depending on the physiological behavior of different plant species and on their different phenological stages. In the simulated period, the observed NEE at the barley field is considerably lower than in the simulations due to progressed senescence. For other cereal crops (e. g. wheat, rye) the results probably would be more realistic. Especially on the first days, NEE at the sugar beet field is slightly overestimated due to the early growing stage. Interestingly, in the second half of the simulation, NEE of sugar beet is realistically simulated although the plant physiological parameters of winter wheat are used. With using an average LAI for the *entire* arable land, in the simulated period the spatially averaged NEE seems to be slightly overestimated partially caused by the time shift of phenological stages. Considering the high fraction of arable land in the flat terrain, this leads to lower CO_2 contents over large arable areas than in reality (see next section). Similarly, Sarrat *et al.* (2009) recognized too high simulated CO_2 uptake rates in areas characterized by winter crops when a non-negligible fraction of the land is covered with maize having a later growing season. With the consideration of a maize fraction in their simulations the CO_2 budget could be improved. The results can be transferred to the LH fluxes. However, a comparison of specific humidity with the observations in Selhausen and Merzenhausen gives no clear indication of overestimated humidity in arable regions (not shown). An additional restriction is a possible overestimation of the fraction of cultivated arable land because with a grid resolution of 500 m for CLM small fallow fields or meadows between large arable fields are ignored and are allocated to the PFT "crop".

7.3.4. Diurnal variation of CO_2 in TerrSysMP-CO_2 and at the Jülich tower

Depending on the weather conditions and atmospheric stratifications the diurnal variation of CO_2 contents is very different from day to day and in different atmospheric heights. Fig. 7.8 depicts the simulated and measured CO_2 variability at the Jülich tower for 3–10 June 2014.

The CO_2 concentrations on the Jülich tower show high diurnal variations on 3, 4 and 6–8 June. In contrast, on 5, 9 and 10 June the CO_2 amplitudes between maximal CO_2 mixing ratios at night and minimum CO_2 mixing ratios at daytime were lower (Fig. 7.8a). On days with high diurnal variations, the highest CO_2 concentrations were observed within the forest canopy (i. e. 12.5 m) whereas in greater heights the nocturnal CO_2 increase is weaker. A closer look indicates that on these days the CO_2 increase in different heights differs from day to day. In the night to 7 June, the different CO_2 increases in different heights are apparent. On 3 June the CO_2 increase in 32.5 m and 52.5 m is rather pronounced whereas in the nights to 4 and 6 June the CO_2 concentrations in 32.5 m and 52.5 m are rather low in the first half of the night but strongly increase after midnight (32.5 m) or in the early morning (52.5 m). On 5, 9 and 10

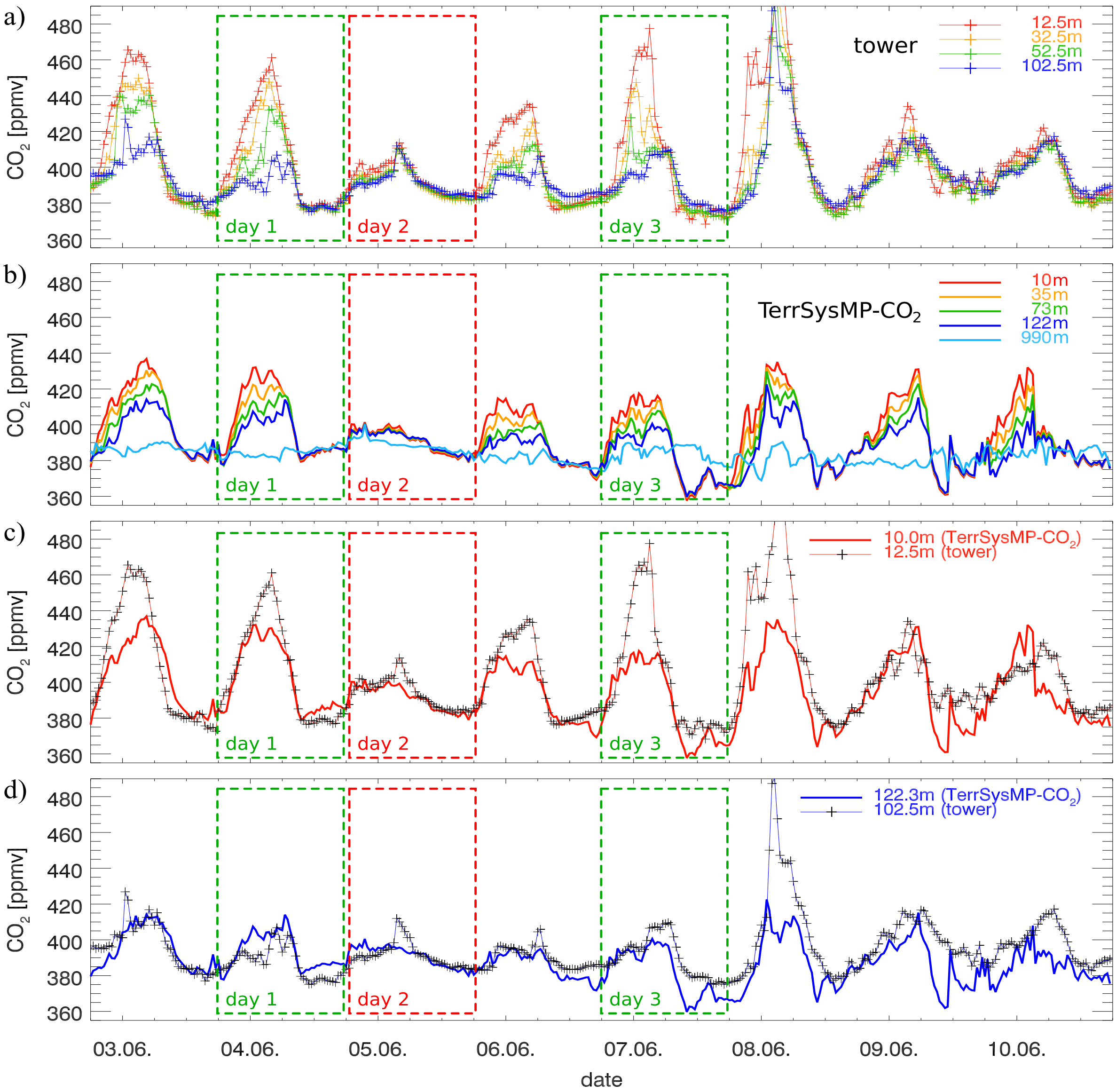

Figure 7.8.: Diurnal variation of CO_2 [ppmv] in the PBL at the Jülich tower: a) observations in several heights, b) TerrSysMP-CO_2 simulation, c) comparison of TerrSysMP-CO_2 and Jülich tower in 10.0 m (12.5 m) and d) in 122.3 m (102.5 m). Days 1–3 are analyzed in Section 7.3.5.

June the CO_2 contents in all atmospheric heights are similar throughout the entire day with slightly stronger fluctuations in 12.5 m on 9 June. In the well-mixed convective boundary layer (CBL) at daytime, the concentrations in every height are very similar[5].

In the night to 8 June, the behavior of CO_2 differs from the other days with a very strong increase in every height up to 490 ppmv in 102.5 m and 515 ppmv in 12.5 m. Fig. 7.9a indicates

---

[5] Systematic shifts of a few ppmv in the observations, which can appear in the calibration procedure due to the measurement inaccuracy, are eliminated by subtracting the mean deviations from the CO_2 mixing ratios of the reference height in 52.5 m at CBL conditions during the entire calibration period (≈ 4 weeks). This rough correction can be made because the main interest is not on the accurate CO_2 content but on the daily CO_2 amplitudes in different heights being 1–2 orders of magnitude greater than the measurement inaccuracy.

that this strong peak at first occurred in 102.5 m (1:30–3:00 UTC) and was mixed *down* to the other heights in the subsequent 60 min. This can only be explained by advection of high CO_2 concentrations towards the Jülich tower. About 1.5 h before that peak (0 UTC) the measured wind in 120 m turned from WNW to SSW (200–210°) and two hours later back to WNW (not shown). Considering the measured wind speed of 2.0–3.5 $m\,s^{-1}$ (i. e. 7.7–12.6 $km\,h^{-1}$, Fig. 7.5) this peak probably originated from the Weisweiler power plant (distance: 9.7 km, 215°). This temporary wind turn is not simulated and, thus, the exceptionally behavior of CO_2 does not occur in the simulations. Hence, this night is not analyzed in this study.

The simulated CO_2 contents in the lowermost 4 COSMO levels (10 m, 35 m, 73 m, 122 m) and in 990 m are shown in Fig. 7.8b. Similar to the observations, for 5 June the lowest daily amplitude and almost the same mixing ratios in all levels are simulated. This can be explained with rather high wind speeds on this day leading to permanent turbulent mixing within the PBL. On 5, 9 and 10 June the simulated and observed daily amplitudes are similar whereas on 3, 4, 7 and 8 June the simulated CO_2 amplitudes are lower than the observed ones, especially in the lowermost level. The reasons for this are analyzed in detail in the next section. TerrSysMP-CO_2 captures the general behavior of decreasing CO_2 amplitudes with height, however the vertical gradients of the simulated CO_2 mixing ratios significantly differ from the observations. A significant difference between the observations and the simulation can be seen in the first half of the night to 10 June. Due to the missing squall line in TerrSysMP-CO_2, the simulated atmosphere is more stable leading to a strong vertical CO_2 gradient whereas in the observations the atmosphere is turbulent causing vertically rather homogeneous CO_2 contents. In the second half of the night, gust fronts of simulated thunderstorms in the NRW domain also destabilisize the simulated atmosphere. Finally, in about 1 km height the CO_2 contents in the simulated period show some variability but no diurnal variations.

In Fig. 7.8c the simulated and observed CO_2 concentrations in 10 and 12.5 m, respectively, are compared. At the Jülich tower this height can be considered to be within the forest canopy. The underestimation of the daily amplitudes on 3, 4 and 6–8 June by $\approx 1/3$ is apparent. The simulated nocturnal CO_2 mixing ratios are too low. In contrast, the CO_2 contents in the night to 5 June, on 5 June and in the nights to 9 and 10 June are simulated fairly well. On 3–6 June, the simulated CO_2 mixing ratios at daytime (i. e. CBL) agree well with the observations.

Especially on 7 and 9 June, for several hours the simulated CO_2 contents deviate 10 ppmv (7 June) to 20 ppmv (9 June) from the observed CO_2 concentrations. On 7 June, in that period low CO_2 mixing ratios originating over large arable areas are advected by a gentle to moderate southeasterly wind. As described in Section 7.3.3, the net CO_2 uptake of arable land use is overestimated in the simulations, thus causing low concentrations there and downstream of this region. In an additional sensitivity simulation using the default plant physiological parameters of CLM (i. e. lower NEE, cf. Section 6.5) these negative deviations do not occur (Fig. 7.9b), however in the afternoon the simulated CO_2 contents are slightly too high. During the night, the difference of both simulations is less because in the stable stratified nocturnal PBL the locally respired CO_2 is more important than advection of CO_2 from the surrounding regions. On 9 June, the negative deviations can also partly be explained by advection of CO_2 mixing ratios coming from the same region (Fig. 7.9c) but different synoptic conditions (Section 7.3.2) additionally contribute to these deviations, at least in the afternoon. This indicates that horizontal advection strongly determines the CO_2 contents measured on a tower. Tolk *et al.* (2009) also found that high CO_2 uptake rates of *crops* have a significant effect on CO_2 mixing ratios measured on the Cabauw tower which is located at a *grassland* site.

Compared with the conditions in 10 m, the deviations between the nocturnal CO_2 contents

35 m and 73 m a.g.l. and the corresponding CO_2 contents measured at the Jülich tower are less pronounced (not shown). Similarly, in Sarrat *et al.* (2009) the simulated CO_2 contents agree better with measurements in 60 m a.g.l. than near the surface. Finally, in the entire period the measured CO_2 mixing ratios 102.5 m a.g.l. are rather similar to the simulations in 122 m height (Fig. 7.8d). Except for the night to 8 June, the measured daily amplitudes are considerably lower than near the surface and are in accordance with the simulations. The lower simulated CO_2 concentrations on 7 and 9 June at daytime can even be seen in that height, i. e. the entire CBL is influenced by the overestimated NEE of large arable areas.

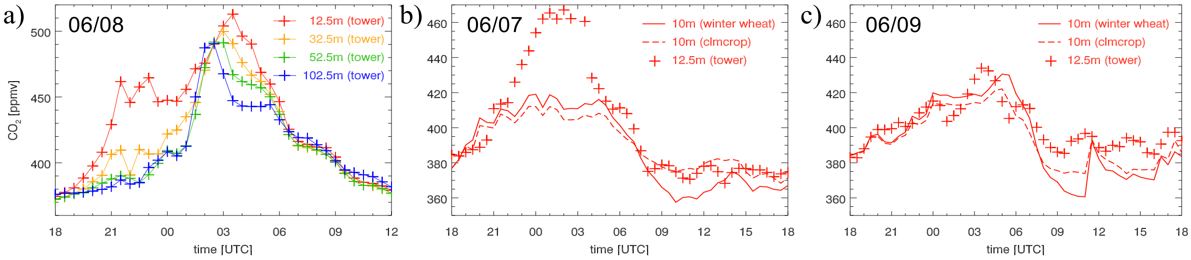

Figure 7.9.: a) CO_2 mixing ratios [ppmv], measured on the Jülich tower on 2014/06/08, b) comparison of measured (crosses) with simulated CO_2 mixing ratios [ppmv] using the winter wheat (solid line) and 'clmcrop' parameters (dashed line) on 2014/06/07 and c) on 06/09.

7.3.5. Relationship of atmospheric stability and vertical CO_2 profiles

In order to understand why on some days the daily amplitudes of CO_2 mixing ratios are simulated well, but on some days not, the vertical profiles of temperature and CO_2 mixing ratios are analyzed for three days. On days 1 and 3, the simulated increase of CO_2 concentrations near the surface is underestimated (green boxes in Fig. 7.8) whereas on day 2 the simulated amplitudes of CO_2 mixing ratios are well represented (red boxes).

In the night to 4 June (day 1), until 1 UTC the CO_2 increase in 10 m height is predicted well (Fig. 7.10a). Afterwards, at the Jülich tower a further CO_2 accumulation up to 461 ppmv is observed whereas in the simulation the CO_2 contents remain between 425 and 435 ppmv. In higher elevations (53/73 m and 103/122 m) the simulated CO_2 mixing ratios are higher than in the observations until 1:30 and 3:30 UTC, respectively, and afterwards the measured CO_2 concentrations exceed (53/73 m) or approach (103/122 m) those of TerrSysMP-CO_2. With the evolution of a CBL in the morning (6–8 UTC) the simulated and observed CO_2 mixing ratios are in good agreement, but are slightly overestimated in the afternoon.

The vertical temperature and CO_2 profiles at different times are depicted in Fig. 7.10b and c, respectively. At 20 UTC, the simulated temperature profile indicates a well-mixed PBL above 200 m and an isothermic stratification (17 °C) between 10 and 73 m. The temperatures at the Jülich tower are ≈ 2 °C colder, but the profile is almost isothermic as well. Thus, the simulated and observed CO_2 mixing ratios and vertical gradients are in good agreement. The decrease of CO_2 with height indicates that NEE is already positive at this time.

In the simulation, the isothermic stratification below 122 m persists at 22 and 0 UTC, but the observations show a different behavior. Between 20 and 22 UTC, the air within the canopy (2–20 m) cools down to 13.0–13.5 °C whereas above the forest (32.5–120.0 m) the isothermic stratification (14.5–15 °C) continues. As a direct consequence, the CO_2 concentration decreases slightly stronger with height than in the simulations. Until 0 UTC, at the tower a temperature

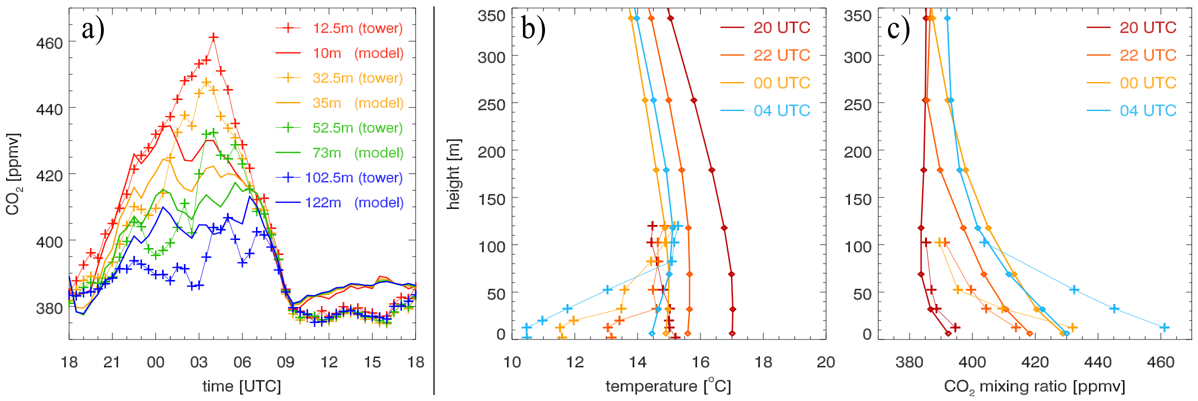

Figure 7.10.: 2014/06/04 (day 1): a) simulated (solid lines) and observed (lines with crosses) CO_2 mixing ratios [ppmv] in different heights; simulated (solid lines) and observed (lines with crosses) vertical profiles of b) temperature [°C] and c) CO_2 mixing ratios [ppmv] on the Jülich tower at different times of the day.

inversion develops with 15.2 °C in 120 m and 11.5 °C in 10 m height. The stronger cooling within the forest canopy is apparent leading to the strongest temperature increase between 20.0 and 32.5 m. The inversion inhibits vertical turbulence causing an intensification of the vertical CO_2 gradient. This leads to similar CO_2 contents near the surface and lower CO_2 contents in higher elevations compared with the simulation. The decoupling of forest air masses characterized by low temperatures within the canopy (2–20 m), a pronounced inversion between 20 and 32.5 m and a moderate inversion above 32.5 m is a common feature at the Jülich tower and is observed in all cloud- and windless nights (3, 4, 6–8 June). This can be explained with the special location of the tower in a small clearing surrounded by a forest because "both the net radiative flux divergence and the heat storage change in the canopy elements are quite different in a forested volume relative to an unforested volume" (Froelich *et al.*, 2011, p. 958).

In the following hours, the temperature inversion intensifies leading to strong vertical CO_2 gradients at the Jülich tower. At 4 UTC, the simulated temperature profile shows a weak inversion below 73 m and, thus, the vertical CO_2 gradients are slightly stronger than at 22 and 0 UTC. At the tower, a strong inversion of 4.5 °C between 10 and 82.5 m and a weak inversion in higher elevations are observed indicating an about 80 m deep stable nocturnal boundary layer. Hence, a strong CO_2 decrease is measured with 461 ppmv in 12.5 m and 404 ppmv in 102.5 m. In the morning, the transition from a stable nocturnal PBL to a convective PBL is simulated about 1 h earlier than at the Jülich tower and leads to a vertically homogeneous CO_2 distribution both in the simulation and in the observations (see Fig. 7.10a).

The conditions in the subsequent night (day 2) are quite different. Between 21 and 23 UTC, a cold front passes Jülich with enhanced wind speeds and an efficient turbulent mixing of free tropospheric CO_2 contents to the surface. Therefore, a significant nocturnal CO_2 increase is not observed (and simulated) and the CO_2 contents are similar in each of the considered levels (Fig. 7.11a). Only the 10 m observations show a few ppmv higher CO_2 contents than on the other measurement heights. Similar to 8 June, the spontaneous CO_2 increase of 10–15 ppmv at the Jülich tower at 3 UTC is correlated with a wind turning to 210–230° suggesting an influence of the Weisweiler power plant. However, the simulations – which also consider CO_2 emissions of power plants – simulate only slightly higher CO_2 contents downstream of these strong CO_2 sources (not shown). At daytime, the simulated and observed CO_2 mixing ratios continuously

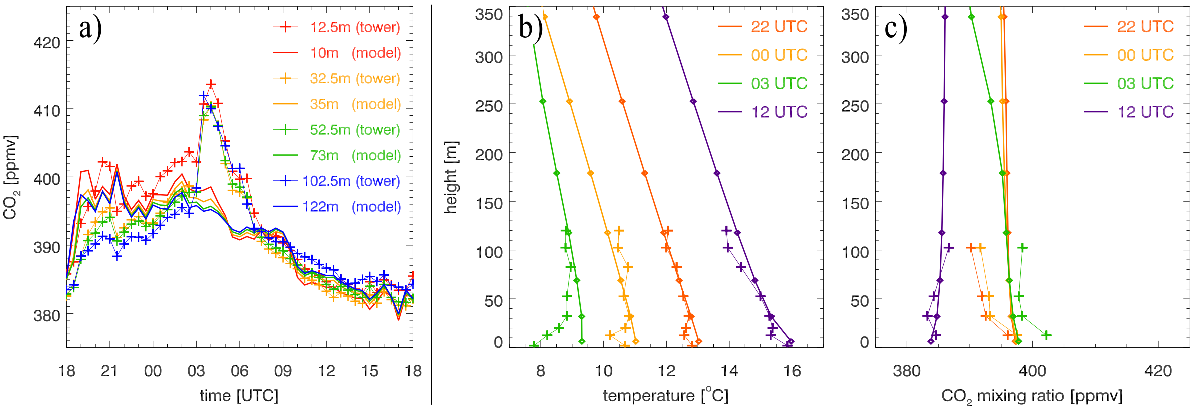

Figure 7.11.: As Fig. 7.10 but for 2014/06/05 (day 2).

decrease and are in very good agreement.

The vertical temperature and CO$_2$ profiles (Fig. 7.11b, c) indicate CBL conditions at 22 UTC. Both in the simulation and at the Jülich tower the atmosphere is dry-adiabatically stratified. Therefore, a vertically homogeneous CO$_2$ distribution is simulated in the well-mixed PBL. Similarly, in the observations the CO$_2$ content is vertically rather constant in the lower atmosphere but 4 ppmv higher mixing ratios occur in 12.5 m height. Two hours later (0 UTC), still a dry-adiabatic vertical temperature gradient is simulated and the temperature profile agrees well with the measured one. Both the simulated and observed CO$_2$ mixing ratios and the low vertical gradients are very similar than at 22 UTC. At 3 UTC, the simulated temperature decrease with height is no longer dry-adiabatically but turbulence is still strong enough for vertical mixing of CO$_2$ partly resulting from a strong wind shear. At the Jülich tower, the atmospheric stratification above the forest top is a bit more stable than in the simulations and within the forest canopy a weak inversion is observed. However, a strong increase of the measured wind with height (12.5 m: 0.7 m s^{-1}, 120.0 m: 8.2 m s^{-1}), i. e. a strong wind shear, allows efficient turbulent mixing. The reason of the observed CO$_2$ increase, ≈ 5–7 ppmv in each height between 0 and 3 UTC, is unclear and does not occur in the simulation. At noon (12 UTC), the atmosphere is again dry-adiabatically stratified and the measured and simulated CO$_2$ mixing ratios represent typically profiles for CBL conditions, i. e. weak vertical gradients. In general, for this day both the CO$_2$ mixing ratios and the vertical gradients are well simulated. A dry-adiabatic stratification and/or a strong vertical wind shear cause efficient vertical mixing during night and at daytime resulting in rather homogeneous CO$_2$ profiles.

The night to 7 June (day 3) is a case with an exceptionally sharp near-surface temperature inversion. Until 1 UTC, the CO$_2$ content in 12.5 m height strongly increases up to 465 ppmv and the maximum (478 ppmv) is reached at 3 UTC (Fig. 7.12a). This intense CO$_2$ accumulation is not simulated, i. e. during the whole night the simulated CO$_2$ mixing ratios remain below 420 ppmv. In 32.5 m height, until 0 UTC the CO$_2$ concentration increases up to 447 ppmv. However, in the second half of the night, a decrease to 414 ppmv (2 UTC) is measured, i. e. the CO$_2$ mixing ratios are considerably lower than in 12.5 m height. Except for the strong increase between 22:30 and 0:30 UTC and for a second peak at 3 UTC the simulated CO$_2$ mixing ratios better agree with the observations than in the lowermost level. Different from the lower levels, 52.5 m and 102.5 m a.g.l. the nocturnal CO$_2$ increase is weak. In 52.5 m height, the CO$_2$ mixing ratios remain below 415 ppmv, except for one single peak at 23:30 UTC. In 102.5 m height, until

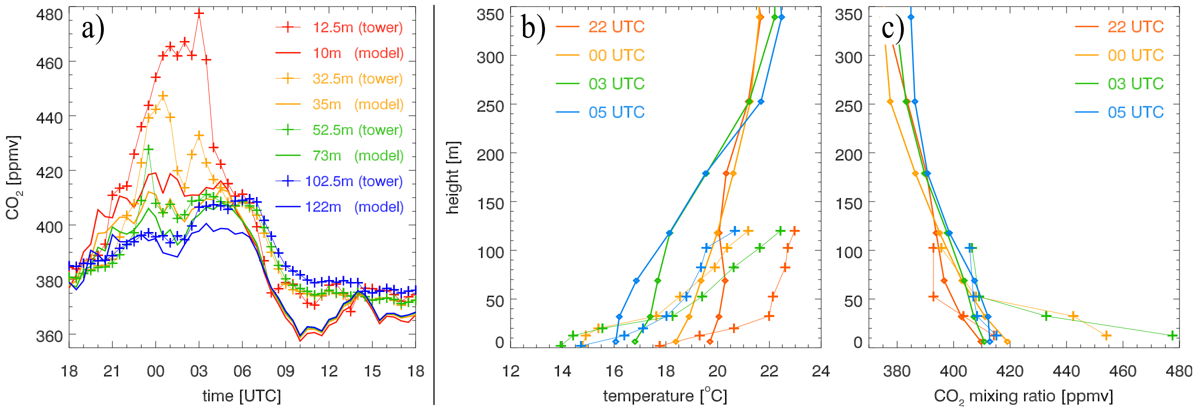

Figure 7.12.: As Fig. 7.10 but for 2014/06/07 (day 3).

2 UTC the CO_2 contents are even below 400 ppmv and increase to 407–410 ppmv between 3 and 7 UTC. In these heights, the CO_2 mixing ratios are simulated fairly well. At daytime, the CO_2 contents are underestimated which has already been discussed in the previous section.

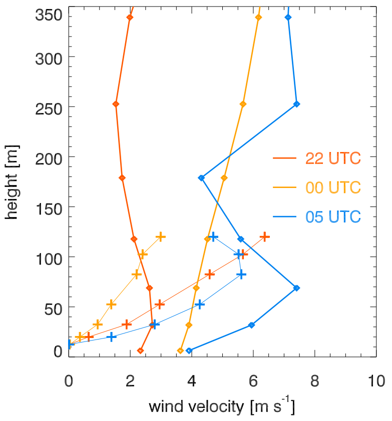

Figure 7.13.: Observed (thin lines, crosses) and simulated (thick lines) wind profiles of day 3.

A consideration of the vertical temperature and CO_2 profiles (Fig. 7.12b, c) help to understand the contrasting behavior of the lower and higher elevations. At 22 UTC, between 2.0 and 32.5 m a strong inversion is observed (4.2 °C temperature increase in 30 m) whereas TerrSysMP-CO_2 simulates only a slight inversion of 0.6 °C below the lowermost 73 m. Above 32.5 m the observed temperature inversion is weaker. Therefore, between 12.5 m and 52.5 m the observed vertical CO_2 gradient is stronger than in the simulation and negligible between 52.5 m and 102.5 m. However, comparing the strong difference of the atmospheric stratification the deviation of the simulated vertical CO_2 gradient is less than expected. The reason for this is a rather pronounced vertical wind shear in the observations (Fig. 7.13) enhancing vertical mixing at this time. This vertical wind increase is not simulated. Until 0 UTC, the observed temperature inversion extends to higher elevations (6.4 °C between 2 and 120 m) and is most pronounced around the forest top (20.0–32.5 m). The observed wind shear weakens. Hence, due to the inhibited vertical turbulence an intense near surface CO_2 accumulation is possible as well as a strong vertical gradient between 32.5 and 52.5 m height. Different from the observations, TerrSysMP-CO_2 simulates a relatively uniform vertical temperature increase of 2.8 °C below 250 m. Thus, both the vertical gradients and the near surface accumulation of CO_2 mixing ratios are significantly underestimated.

Between 0 and 3 UTC the observed inversion further strengthens reaching a quite extreme increase of 8.5 °C between 2 and 120 m height. This explains the pronounced near surface CO_2 accumulation (478 ppmv) as well as the distinctly lower concentrations in 32.5 m (433 ppmv) and 52.5 m height (409 ppmv). Again, the simulated temperature inversion as well as the vertical CO_2 gradients are strongly underestimated. It shows that the deviating CO_2 mixing rations between the simulation and the observations are the result of a deficient representation of atmospheric stability leading to a too strong vertical turbulent transport. This is a common problem of turbulence schemes used in NWP models simulating a too deep nocturnal PBL resulting in too weak CO_2 accumulation near the surface (see also Tolk *et al.*, 2009). Finally, at 5 UTC the observed temperature inversion begins to weaken, especially in higher elevations, and the wind has a pronounced maximum at 82.5 m. The enhanced vertical wind shear allows a stronger turbulent mixing and, thus, the simulated and observed CO_2 profiles are better in accordance than in the previous hours. Different from the observations, at this time the simulated temperature inversion between 35 and 250 m is strongest and similar to the observations which explains the better match of CO_2 mixing ratios.

In the night to 9 June, the simulated and observed atmospheric stratification is comparable and characterized by almost isothermic temperature profiles until 0 UTC and a week but deep inversion later on (not shown). This results in similar vertical CO_2 gradients in the simulation and in the observations, again showing that the deviation of the near surface CO_2 concentrations combined with underestimated vertical gradients in days 1 and 3 are mainly the result of an incorrect representation of the atmospheric stratification.

For the comparison of simulated CO_2 profiles and meteorological variables with observations made on the Jülich tower, the environment of the tower has to be considered. The 25 m tall forest surrounding the clearing, where the tower is located, clearly influences the microclimate. In clear sky nights forests affect radiative cooling because the rates of cooling of leaves and branches of trees differ from the rate of cooling of air. This influences the heat transfer between canopy elements and the air (Froelich *et al.*, 2011). At the Jülich tower, the modified shape of temperature profiles in cloudless nights is apparent (Fig. 7.14). Different from typical nocturnal temperature inversions with the strongest vertical temperature gradient near the surface, at the tower the strongest gradients are measured regularly between 20.0–32.5 m height (see e. g. the night of 2/3 June at 21/23 UTC, Fig. 7.14). Below, the temperature inversion is lower caused by the heat storage of the canopy elements. The pronounced inversion near the canopy top inhibits a vertical exchange of air from the canopy layer to the air above the forest. This causes an enhanced accumulation of respired CO_2 within the canopy. In the second half of the night, the vertical extent of inversions increase (1 UTC) but the strongest gradient further occurs at the forest top. In almost every cloudless morning, 52.5 m a.g.l. significantly higher temperatures are registered than above/below that height (9 UTC) caused by the still shallow PBL and intense heating above the forest due to the low albedo of forests. In the afternoon (14 UTC), the dry-adiabatic temperature profile is modified by the tall vegetation typically showing a weak temperature inversion between 32.5 and 52.5 m and often a superadiabatic temperature gradient between 52.5 and 82.5 m height.

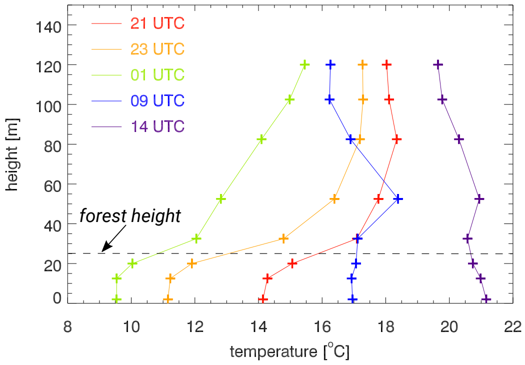

Figure 7.14.: Temperature profiles measured on the Jülich tower on 2014/06/02–03 at different times of the day.

Additionally, the wind is significantly influenced by the forest, although the tower is not located directly in the forest. Within the forest canopy the measured wind speeds are distinctly lower than above shallow canopies. Hence, the air motion below the forest top cannot be compared with the simulated 10 m wind. Typically, an exponential increase with height occurs within the forest (e. g. Brunet *et al.*, 1994; Finnigan, 2000) and a logarithmic wind profile is observed above an inflection point near the forest top. This wind shape cannot be clearly seen in the considered period, but an analysis of the mean wind in the summer season of 2014 indicates such a wind profile at the Jülich tower (Kern, 2015). This significantly influences the turbulent behavior. Both the modified temperature and wind profiles strongly affect the CO_2 mixing ratios within the forest canopy. However, TerrSysMP-CO_2 does not account for processes induced by tall vegetation which partially explains the analyzed deviations. Moreover, at night tall towers capture only the local CO_2 distribution (Haszpra, 1999). Hence, in a future study the behavior of TerrSysMP-CO_2 should be compared with CO_2 measurements made in more homogeneous regions, e. g., at the Cabauw tower in the Netherlands.

7.3.6. CO_2 budget in the NRW domain

date	**06/03**	**06/04**	**06/05**	**06/06**	**06/07**	**06/08**	**06/09**	**06/10**	**total**
weather	*PC*	*SR*	*PC*	*CS*	*CC*	*PC*	*PC*	*LS*	
photo.	−10.14	−8.272	−10.51	−11.66	−11.96	−11.85	−11.74	−11.47	**−10.95**
leaf resp.	*1.437*	*1.370*	*1.176*	*1.503*	*2.178*	*2.223*	*2.463*	*2.611*	***1.870***
soil resp.	*5.445*	*5.527*	*5.462*	*5.544*	*5.890*	*6.173*	*6.329*	*6.578*	***5.863***
total r.	6.882	6.897	6.638	7.047	8.018	8.445	8.792	9.188	**7.738**
anthro.	1.997	2.011	2.024	2.046	1.640	1.525	1.883	1.997	**1.890**
budget	−1.264	+0.636	−1.850	−2.567	−2.303	−1.876	−1.064	−0.286	**−1.322**

Table 7.3.: CO_2 budget of the simulated week [μmol(CO_2)$m^{-2}s^{-1}$]. The abbreviations for weather are: *PC* - partly cloudy, *SR* - strat. rain, *CS* - clear sky, *CC* - cirrus clouds, *LS* - light showers.

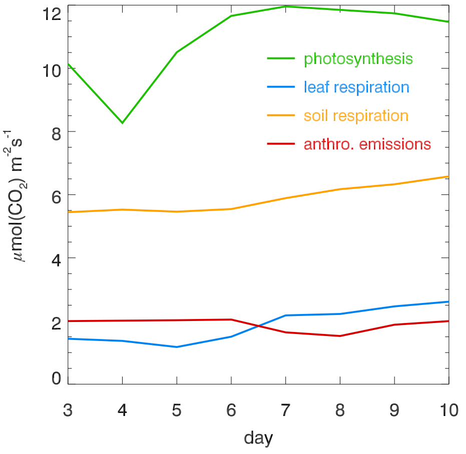

Figure 7.15.: Absolute val. of daily CO_2 fluxes [μmol(CO_2)$m^{-2}s^{-1}$].

Finally, the CO_2 budget in the simulation period has been calculated. On clear sky days and days with partly cloudiness or cirrus cloudiness the photosynthesis rates only slightly enhance with increasing temperature and humidity from 10.1–10.5 μmol(CO_2)$m^{-2}s^{-1}$ (3–5 June) to 11.5–12.0 μmol(CO_2)$m^{-2}s^{-1}$ (6–10 June) (see Table 7.3, Fig. 7.15). Thus, photosynthesis is mainly controlled by solar radiation and only secondarily by temperature. In contrast, total soil respiration increases ≈ 20% with increasing soil temperature from 5.4 to 6.6 μmol(CO_2)$m^{-2}s^{-1}$. An even stronger relative increase (≈ 75%) is simulated for leaf respiration (Fig. 7.15) due to the Q_{10} dependency of $V_{c,\max}$ (see Eq. 2.26). Hence, the net loss of atmospheric CO_2 of the first five days of this period is higher than in the last three days (see e. g. 10 June). Only on 4 June (cloudy and rainy) a net CO_2 gain is simulated (Table 7.3). In Fig. 7.15 the lower anthropogenic emissions at the weekend (7/8 June) are evident. In summary, in this period an average CO_2 loss of −1.32 μmol(CO_2)$m^{-2}s^{-1}$ per day is simulated which is realistically for warm and sunny weather in summer. Anthropogenic emissions represent 19.6% of the total CO_2 source. However, the anomaly of the observed phenology in 2014 (see Section 7.2) is not considered in the LAI of this simulation. Thus, the overestimated CO_2 assimilation rates of agricultural fields (cf. Section 7.3.3) probably lead to a slightly too strong CO_2 loss in this period.

8. Summary and concluding remarks

8.1. Summary and conclusion

This study investigated mesoscale patterns and diurnal variations of atmospheric CO_2 mixing ratios as well as the processes which control this variability by means of high-resolution numerical simulations. The model system TerrSysMP (Shrestha *et al.*, 2014) has been extended by a fully prognostic treatment of atmospheric CO_2 mixing ratios forming the new model version TerrSysMP-CO_2. This model includes a two-way coupling of CO_2 (atmosphere ↔ biosphere): the actual CO_2 distribution is used to calculate the biogenic CO_2 fluxes with the biospheric model CLM and, in turn, these fluxes influence the atmospheric CO_2 distribution in the NWP model COSMO. Thus, photosynthesis and transpiration is represented more realistically in CLM. Additionally to the spatio-temporal varying atmospheric humidity, the water and CO_2 exchange between the canopy and the atmosphere is influenced by the response of the opening of leaf stomata to prognostically varying atmospheric CO_2 mixing ratios.

CLM has been extended by parameterizations of soil respiration. Heterotrophic respiration is calculated with the carbon turnover model RothC (Coleman and Jenkinson, 2008) by using characteristic TOC depth profiles for each PFT based on measurements in NRW. To avoid a long model spin-up the initial C-pools of RothC are determined with pedotransfer functions. The parameterization explicitly considers the effect of soil temperature and soil moisture on the CO_2 production in the soil. For the estimation of belowground autotrophic respiration a simple parameterization has been developed using averaged rates of past photosynthesis and leaf respiration. The latter is calculated by means of the maximum rate of carboxylation.

Additionally to the biogenic CO_2 fluxes anthropogenic CO_2 emissions have been included as CO_2 sources which contribute to the atmospheric CO_2 budget in populated regions. The most recent high-resolution gridded dataset of European anthropogenic CO_2 emissions is used, issued by the TNO. This emission inventory is based on yearly official national reports of emitted air pollutants and the CO_2 emissions are separated into several SNAPs describing the origin of the emissions (e. g. power generation, industry, road traffic). The data has been downscaled to a 1 km resolution by the RIU and with emission time factors hourly CO_2 fluxes can be determined from the annual emissions of this emission inventory.

High-resolution model simulations (grid sizes: 0.5 km for CLM, 1.1 km for COSMO) have been performed using TerrSysMP-CO_2 for a region in western Germany and parts of BeNeLux (NRW domain). The domain includes the low mountain range Eifel as well as the densely populated Rhine valley with the metropolises Cologne, Dusseldorf and Bonn. Two of the main objectives of these simulations were both the influence of orographically induced mesoscale circulations by complex terrain and the effect of fossil fuel emissions on the spatio-temporal patterns of atmospheric CO_2 mixing ratios in a region including densely populated areas. Initial conditions and lateral boundary conditions of meteorological variables and CO_2 have been provided by nesting simulations of TerrSysMP-CO_2 (grid size: 2.8 km) over different sub-continental domains depending on the dominant wind direction.

At first, the spatio-temporal variability of NEE, photosynthesis and transpiration was investigated. The fluxes are strongly PFT dependent showing higher rates for broadleaf forests than for needleleaf forests and grassland. Photosynthesis and transpiration of arable land (crops) are low. In situations with low humidity in the PBL both photosynthesis and transpiration are considerably lower than for moister conditions. This is the result of increasing stomatal resistances with decreasing humidity in combination with high temperatures and high irradiation. Needleleaf trees are most sensitive to low atmospheric humidity. Additionally, the spatial distribution of atmospheric CO_2 influences the stomatal resistance leading to slightly lower/higher transpiration/photosynthesis rates in regions with high near surface CO_2 concentrations as compared to model simulations using a constant CO_2 mixing ratio. However, in most situations the effect of modified canopy transpiration on the humidity and temperature distribution in the PBL is negligible except from deviations caused by random variations of convective cloud formation and precipitation. Atmospheric humidity and its spatial variability is clearly the more dominant atmospheric forcing variable for canopy fluxes.

On clear sky days, the simulations indicate a pronounced diurnal variation of CO_2 in the PBL. The highest concentrations occur in the early morning being the result of near surface CO_2 accumulation due to soil respiration. With the onset of photosynthesis strongly decreasing atmospheric CO_2 contents are simulated followed by turbulent vertical transport within the PBL at daytime. In situations with weak synoptic forcing, in mountainous regions distinct horizontal CO_2 gradients arise between narrow valleys and mountain ridges during night and in the morning. These are the result of mesoscale flows and turbulence patterns induced by complex terrain. Above mountain ridges TKE is produced by wind shear leading to an efficient vertical transport of respired CO_2 whereas in valleys TKE is consumed allowing a strong near surface CO_2 accumulation. Valley breezes further intensify the horizontal CO_2 gradients. Hence, in regions with complex terrain, the spatial CO_2 distribution is strongly controlled by the mesoscale atmospheric flow but *not* by the spatial distribution of different dominant land use classes characterizing the landscape, at least during night. Moreover, fossil fuel burning, mainly by urban traffic, industry and power plants, is an important source of atmospheric CO_2 in the NRW domain. Especially in the morning rush-hour, significant higher CO_2 contents are simulated in and downstream of densely populated regions. About 20% of the total CO_2 source in the NRW domain results from anthropogenic emissions, produced mainly in the metropolises along the Rhine and the Maas and by the big power plants.

Additionally, the effect of clouds on canopy fluxes and atmospheric CO_2 mixing ratios was analyzed. The response of the canopy to radiative attenuation by clouds can be very diverse. Thick stratiform or convective clouds (radiation $< 100\,\mathrm{W\,m^{-2}}$) cause (partly) closure of the stomata of plants because photosynthesis is not effective and leaf water can be saved. With higher solar radiation (100–$300\,\mathrm{W\,m^{-2}}$) both photosynthesis and transpiration is limited but the stomatal resistance is only slightly increased. The light limitation of photosynthesis is partially compensated by low transpiration rates, i. e. leaves can leave their stomata open. High irradiation in combination with low humidity and high temperatures also reduces photosynthesis due to moisture stress of plants whereas slightly reduced radiation caused by thin clouds yield the highest simulated photosynthesis rates. In the morning, clouds can suppress or delay both the onset of CO_2 uptake by photosynthesis as well as the formation of a convective PBL, both resulting in particularly high near surface CO_2 contents.

Precipitation can have contrasting effects on CO_2 production in the soil. Heavy (convective) precipitation can cause strong local decreases of soil respiration due to soil moisture close to 100% saturation in the subsoil, where the greatest fraction of CO_2 production occurs. This reduces heterotrophic and autotrophic respiration significantly persisting several hours after the rain event. On the other hand, especially after a long dry period, stratiform rain can enhance soil respiration. If the soil is detrimentally dry prior to the rain the additional water infiltrating into the topsoil improves the soil water conditions there so that CO_2 production is less moisture limited. Moreover, the decomposition of aboveground litter and in the O horizon is strengthened by rain. Due to the humid climate and predominant loamy soils (i. e. high water holding capacity) in the NRW domain, moisture reduction is only significant after long dry periods in summer or after long intense rain periods. Soil temperature is the major control of soil respiration. Nevertheless, the explicit consideration of soil moisture changes in TerrSysMP-CO_2 leads to a more consistent representation of soil respiration than in most other biosphere-atmosphere models which neglect moisture dependencies of soil respiration.

The performance of TerrSysMP-CO_2 was verified with EC measurements of CO_2 and energy fluxes (LH/SH). The NEE as well as the LH and SH fluxes of needleleaf forest are in good agreement with observed fluxes above a spruce forest in the Eifel. In contrast, both for cereal (e. g. wheat, barley) and for broadleaf crops (e. g. sugar beet, vegetables) in their growing and mature stage the NEE and LH fluxes are strongly underestimated using the default plant physiological parameters of crops in CLM. These parameters constrain NEE at low values due to a much too low capacity utilization limitation of photosynthesis. Obviously, the parameters are inappropriate for intensively fertilized arable fields in NRW reaching up to three-fold higher NEE. A similar trend can be seen for grassland but the deviations are less evident. With a change to the winter wheat parameters of Sulis *et al.* (2015) both NEE and the partitioning of LH and SH fluxes are significantly improved. An additional restriction of TerrSysMP-CO_2 is the use of only *one* PFT for all cultivated plants. The high heterogeneity of NEE and LH/SH fluxes resulting from the diversity of agricultural cultivations in this regions cannot be simulated for plants having different growing seasons and plant physiological parameters. This leads to erroneous CO_2 and energy fluxes and atmospheric CO_2 mixing ratios at and downstream of large arable areas. The verification of soil respiration indicates a good agreement with observations but the sensitivity on soil temperature is underestimated. This mainly results from the negligence of diurnal variations of autotrophic respiration. However, the deviations are much smaller compared to the uncertainty of photosynthesis rates at daytime.

Finally, the simulated vertical CO_2 distribution in the atmosphere was compared with measurements on a 124 m tall tower. Both in the observations and in the simulation the daily amplitudes and the vertical CO_2 gradients depend on the weather situation. On days with strong synoptic forcing (i. e. fronts, rain, high wind speeds) the diurnal variation of CO_2 is low and the vertical CO_2 profiles show well-mixed conditions. TerrSysMP-CO_2 well predicts the vertical temperature and CO_2 profiles as well as the temporal variations throughout the day. In contrast, in clear sky and windless nights a strong CO_2 accumulation was observed within the forest canopy. At higher elevations the nocturnal CO_2 increase is distinctly lower. The different nocturnal CO_2 increase in different heights is also simulated by TerrSysMP-CO_2, but the vertical gradients of CO_2 mixing ratios are in some nights strongly underestimated. The nocturnal temperature inversions at the tower are much stronger than in the simulation where the nocturnal PBL is deeper with a weaker temperature inversion. Thus, vertical mixing is stronger inhibited than in the simulation explaining the pronounced observed near surface accumulation of CO_2. However, these deviations are to some extent the result of the forest surrounding the tower location. The measured temperature and wind profiles clearly indicate effects of tall vegetation showing a decoupling of the air within the canopy from the air above. Such effects cannot be simulated by TerrSysMP-CO_2 and partially explain the large differences.

This study presented new insights into the atmospheric and biospheric controls of observed mesoscale heterogeneity of the CO_2 in the PBL in a region including complex terrain and urban areas. The interrelation of CO_2 patterns, orography and heterogeneous land use could be explored by TerrSysMP-CO_2. This information is of particular interest to upscale local flux measurements to the mesoscale, the only spatial scale which is insufficiently known, yet.

8.2. Outlook

The recent version of TerrSysMP-CO_2 is already a valuable tool for analyses of mesoscale processes in the atmosphere as well as of heterogeneous biogenic fluxes. Further model development can be directed towards additional agricultural PFTs (e. g. cereal crops, sugar beet, maize) with different plant physiological parameters and growing seasons. This would improve simulated canopy fluxes as well as the CO_2, humidity and temperature distribution within the PBL, in particular in regions where diverse cultivated plants are the dominant land cover. Moreover, a more detailed map of the horizontal distribution of different soil types as well as a separation into topsoil and subsoil having different soil properties and clay contents would lead to more consistent calculations of heterotrophic respiration and soil hydrology.

In additional sensitivity studies different turbulence schemes being already included in the atmospheric model (COSMO) of TerrSysMP-CO_2 can be used to study which parameterization is most appropriate for the simulation of stable nocturnal PBLs. However, the weakness of turbulence schemes in current NWP models for the simulation of stable atmospheric conditions is well known. Furthermore, the model performance can be tested for different regions. Simulated CO_2 contents can be compared, e. g., with observations made on the Cabauw tower which is located at a grassland site in flat terrain, i. e. in a more homogeneous landscape.

The tower observations have clearly indicated the influence of forests on the near surface CO_2 accumulation as well as on the momentum flow and on vertical temperature profiles. With a refinement of the vertical grid spacing in the lower levels of TerrSysMP-CO_2 the surface layer canopy representation in the current model can be extended to a multi-layer canopy approach. This parameterization then explicitly resolves the effect of pressure and viscous drag forces on the atmospheric flow induced by tall vegetation as well as modifications in TKE production/dissipation. The canopy fluxes are vertically resolved and the effects of radiative attenuation by tall vegetation can be considered in the atmospheric component. It is expected that with these model extensions the thermo-hydrodynamic effects induced by land surface heterogeneities are represented more realistically leading to significantly improved simulations of the vertical and horizontal distribution of CO_2 patterns and atmospheric variables. Thus, measured CO_2 profiles of a tall tower can be better compared to simulated mixing ratios.

The representative nature of measured CO_2 becomes even more questionable in tracer transport modes with a rather coarse grid resolution as used in inversion studies (van der Molen and Dolman, 2007). The high-resolution model TerrSysMP-CO_2 is valuable for the quantification of this representation error. Except for regions with flat terrain away from coasts and homogeneous land cover this high model resolution is necessary to capture mesoscale circulations and the resulting CO_2 distributions. Thus, TerrSysMP-CO_2 provides important information that can be used to adapt continental atmospheric CO_2 measurements before including these into regional scale numerical inversion models. This enables a more accurate determination of regional and mesoscale biogenic CO_2 flux patterns by means of inverse modeling which in the end are essential for precise simulations of the future CO_2 increase and global warming by regional and global climate models.

A. Supplementary figures and tables

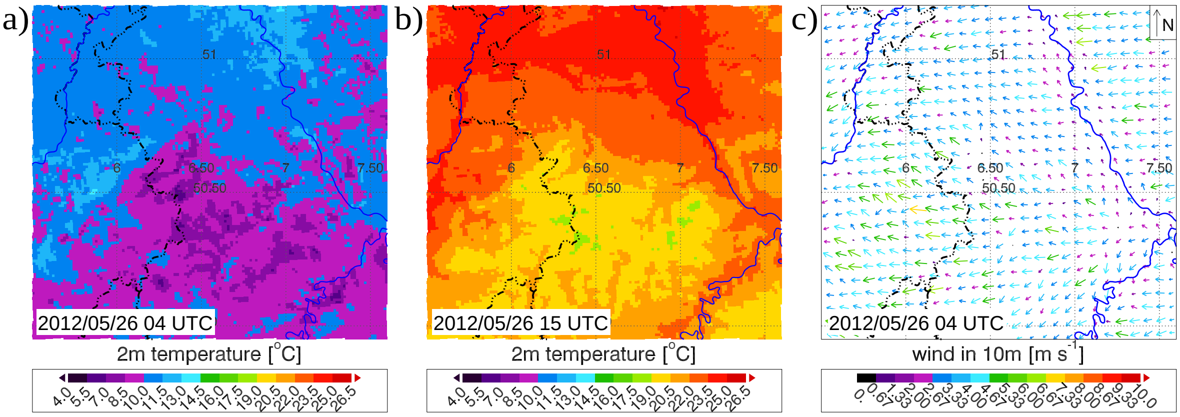

Figure A.1.: Meteorological situation on 2012/05/26.

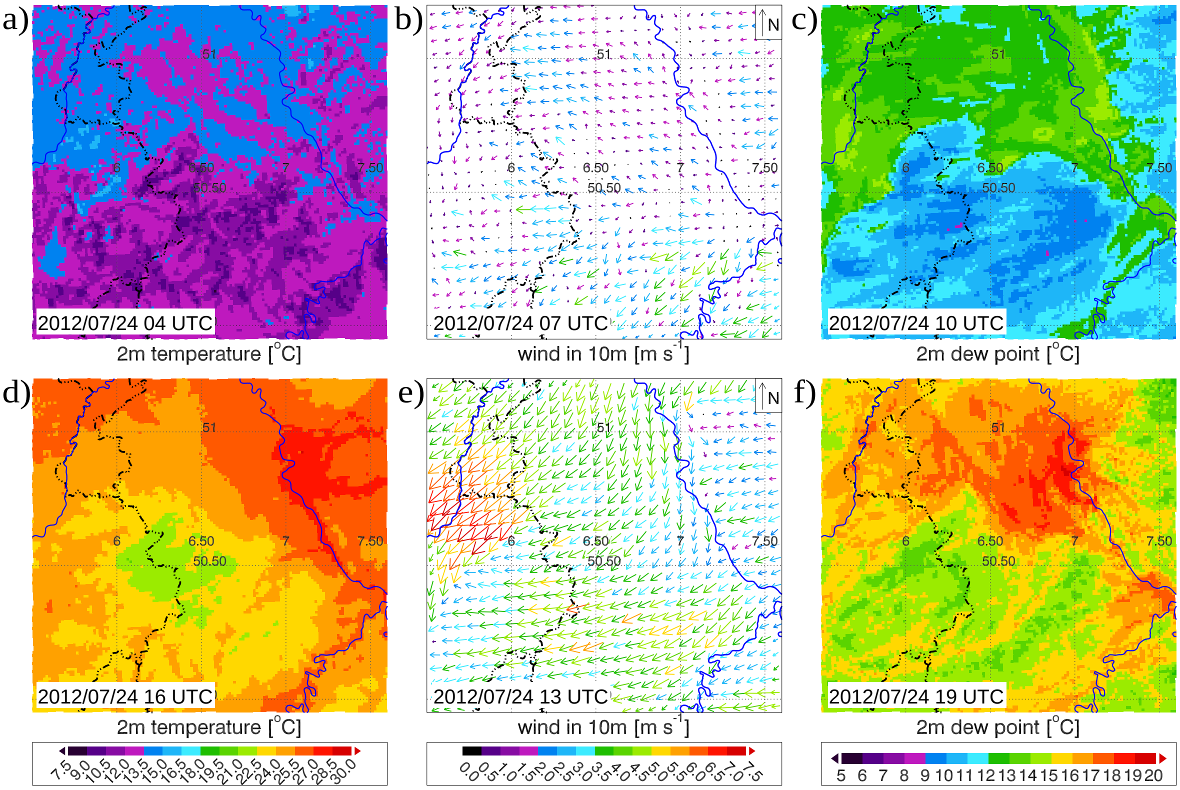

Figure A.2.: Meteorological situation on 2012/07/24.

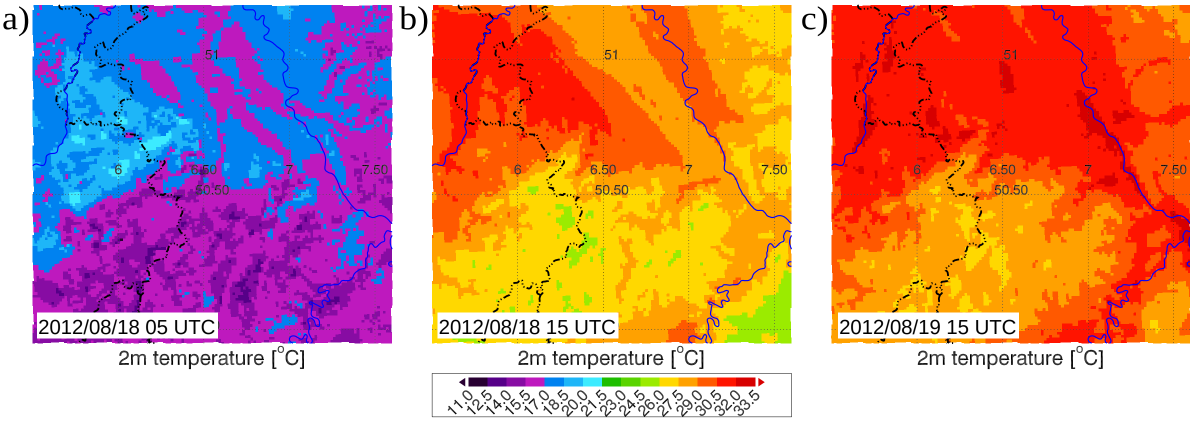

Figure A.3.: Meteorological situation on 2012/08/18–19 (1).

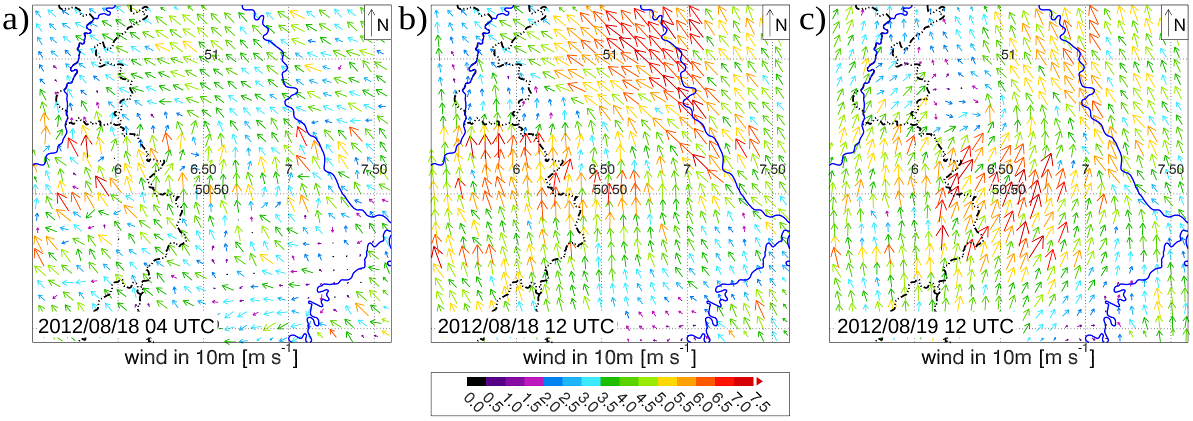

Figure A.4.: Meteorological situation on 2012/08/18–19 (2).

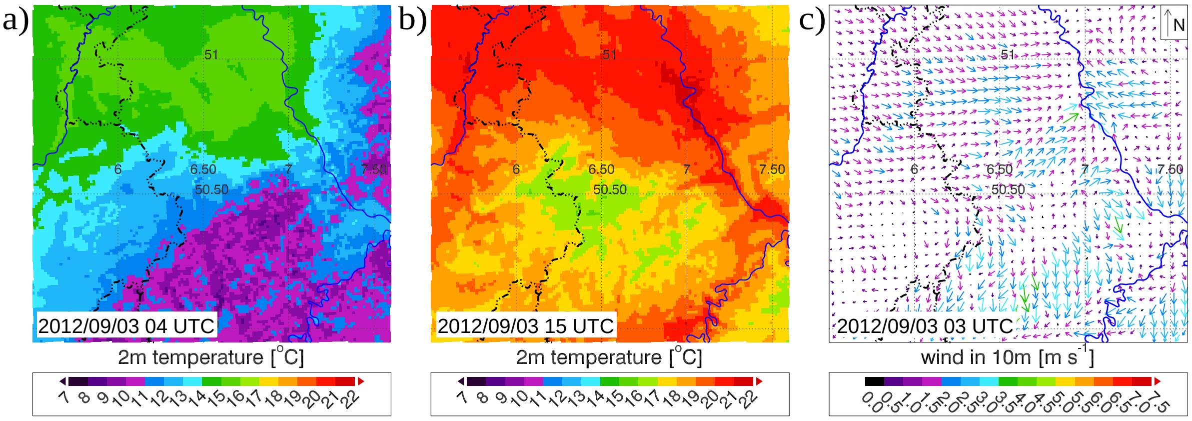

Figure A.5.: Meteorological situation on 2012/09/03.

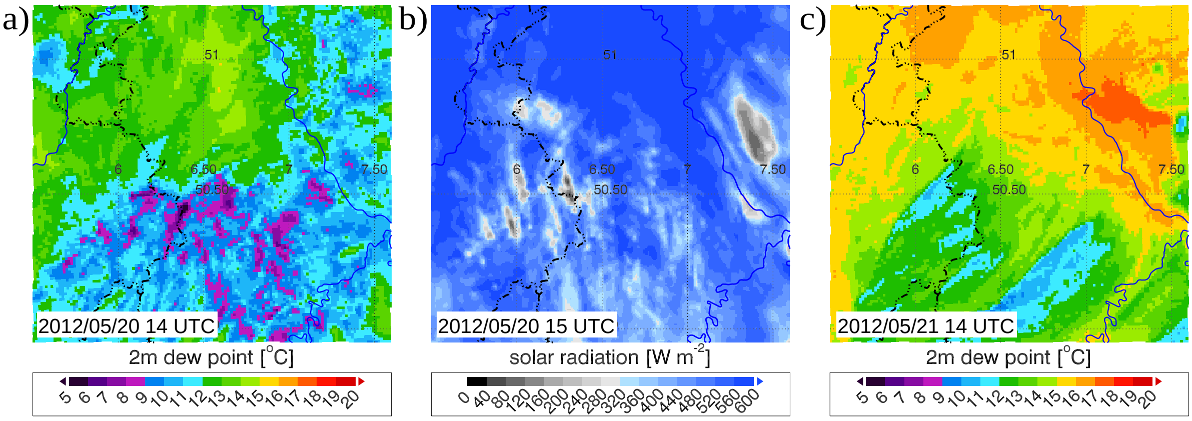

Figure A.6.: Meteorological situation on 2012/05/20–21.

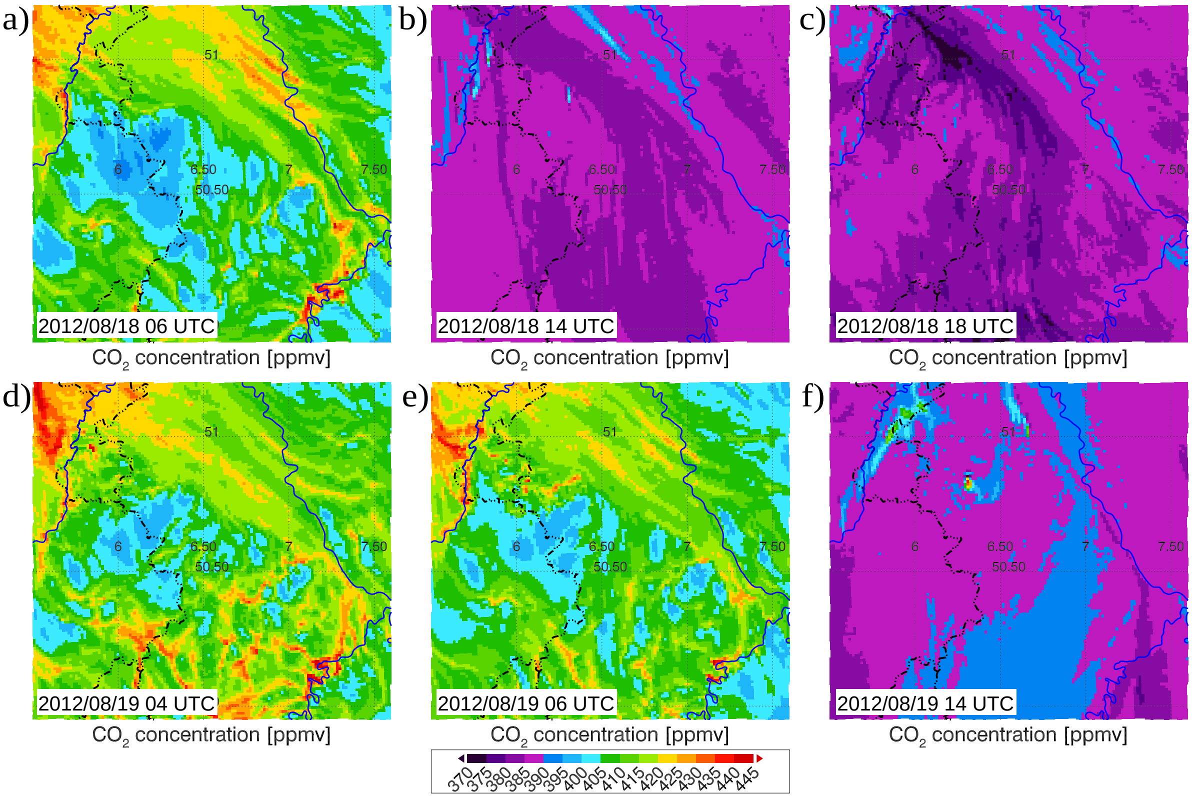

Figure A.7.: CO$_2$ concentration [ppmv] on 2012/08/18–19 in the lowermost COSMO level ($\approx 10\,\text{m}$).

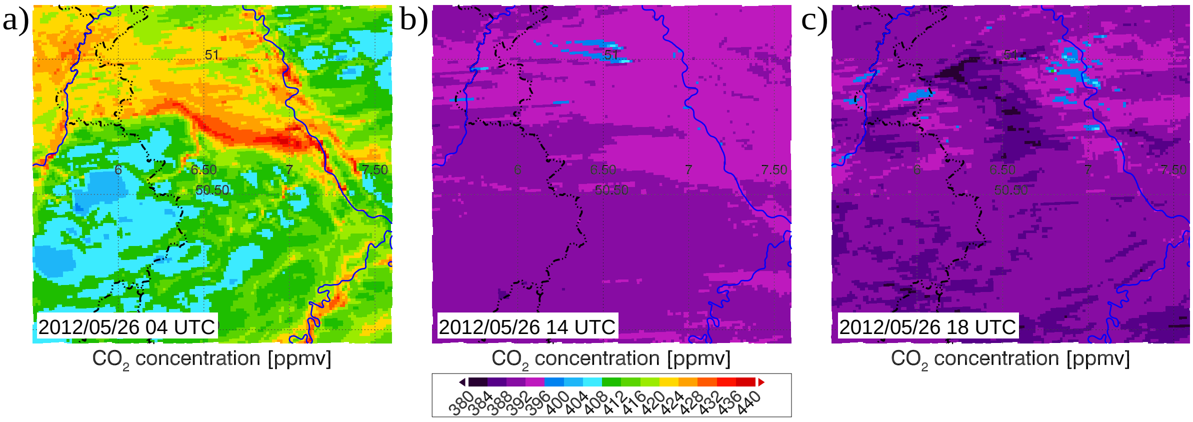

Figure A.8.: CO$_2$ concentration [ppmv] on 2012/05/26 in the lowermost COSMO level ($\approx$ 10 m).

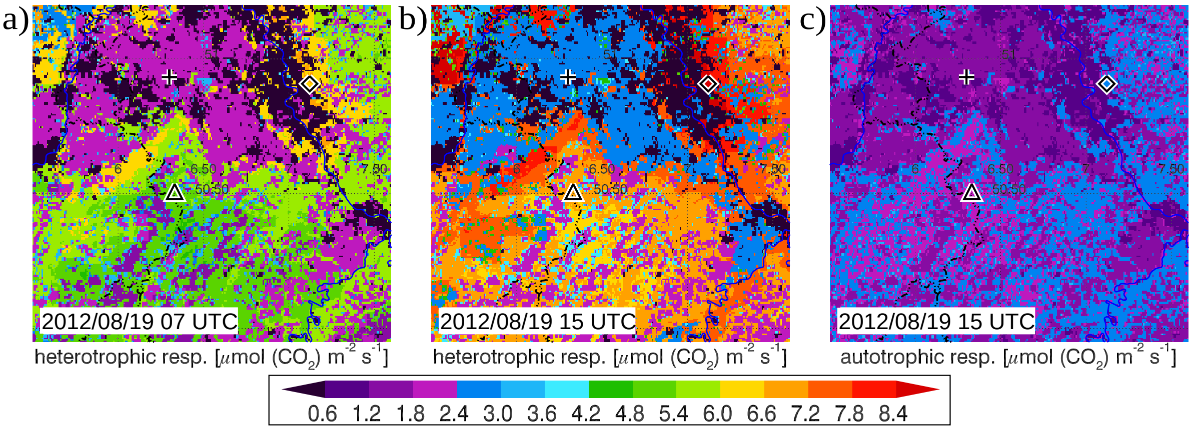

Figure A.9.: Simulated heterotrophic respiration [μmol(CO$_2$)m^{-2}s^{-1}] on 2012/08/19 at a) 07 UTC and b) 15 UTC and c) autotrophic respiration at 15 UTC.

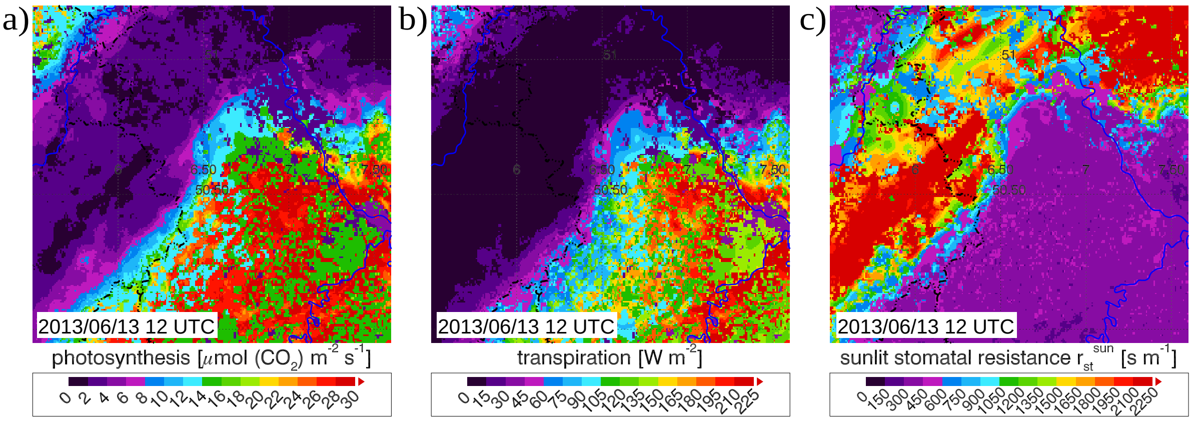

Figure A.10.: Simulated a) photosynthesis [μmol(CO$_2$)m^{-2}s^{-1}], b) transpiration [W m^{-2}] and c) sunlit stomatal resistance [s m^{-1}] on 2013/06/13 12 UTC.

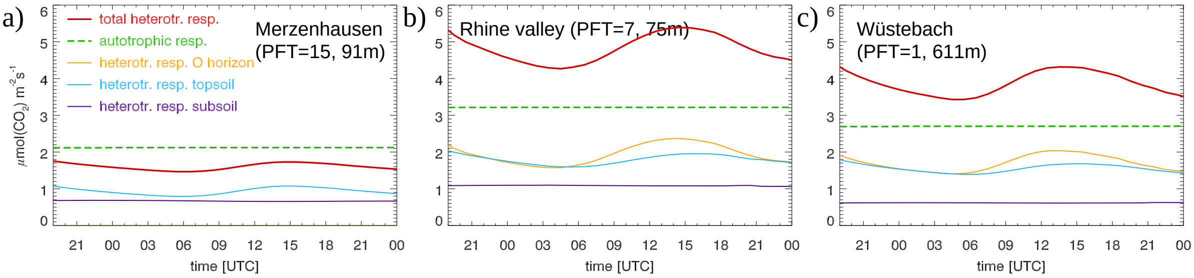

Figure A.11.: Diurnal variation of heterotrophic respiration [μmol(CO$_2$)m^{-2}s^{-1}] (solid lines), its components (O horizon, topsoil, subsoil) and autotrophic respiration [μmol(CO$_2$)m^{-2}s^{-1}] (dashed line) of CS2605 at a) Merzenhausen, b) Rhine valley and c) Wüstebach.

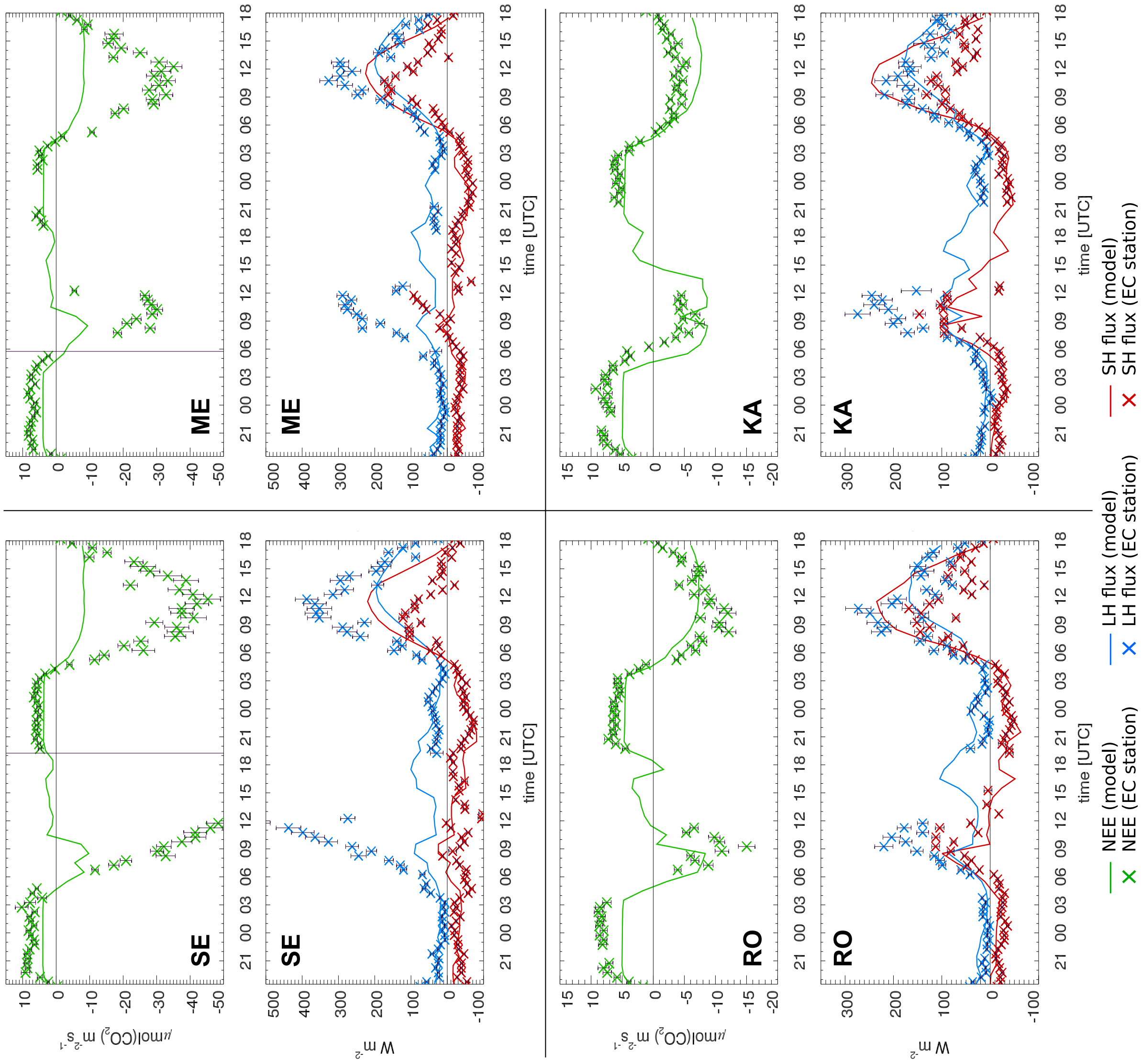

Figure A.12.: EC measurements of NEE, LH and SH on 2013/06/13–14 at Selhausen, Merzenhausen, Rollesbroich and Kall-Sistig.

district	**Rhein-Erft-Kreis**		**Heinsberg**		**Düren**		**Euskirchen**		**St. Reg. Aachen**		**total**	
land use	area [ha]	percent	area [ha]	percent	area [ha]	percent	area [ha]	percent	area [ha]	percent	area [ha]	percent
cereal crops	18037.5	52.7%	14057.7	42.7%	23265.9	51.4%	16306.2	59.9%	5319.4	50.3%	**76986.7**	**51.3%**
sugar beet	7318.8	21.4%	5798.9	17.6%	8966.0	19.8%	3015.4	11.1%	1982.7	18.8%	**27081.7**	**18.0%**
maize	1188.0	3.5%	5502.6	16.7%	3357.4	7.4%	1967.7	7.2%	1335.4	12.6%	**13351.1**	**8.9%**
rapseed	2332.8	6.8%	1632.3	5.0%	3183.2	7.0%	2882.2	10.6%	362.6	3.4%	**10393.0**	**6.9%**
potatoes	2038.1	6.0%	2467.1	7.5%	3188.2	7.1%	383.6	1.4%	638.2	6.0%	**8715.1**	**5.8%**
vegetables	1653.4	4.8%	943.8	2.9%	1363.9	3.0%	901.6	3.3%	175.4	1.7%	**5038.0**	**3.4%**
other	1659.0	4.8%	2489.3	7.6%	1890.6	4.2%	1752.9	6.4%	755.3	7.1%	**8547.0**	**5.7%**
total	**34227.4**	**100.0%**	**32891.7**	**100.0%**	**45215.1**	**100.0%**	**27209.5**	**100.0%**	**10568.9**	**100.0%**	**150112.5**	**100.0%**

Table A.1.: Arable land use of the districts Rhein-Erft-Kreis, Heinsberg, Düren, Euskirchen and Städte Region Aachen in 2014 (Landwirtschaftskammer Nordrhein-Westfalen, 2015).

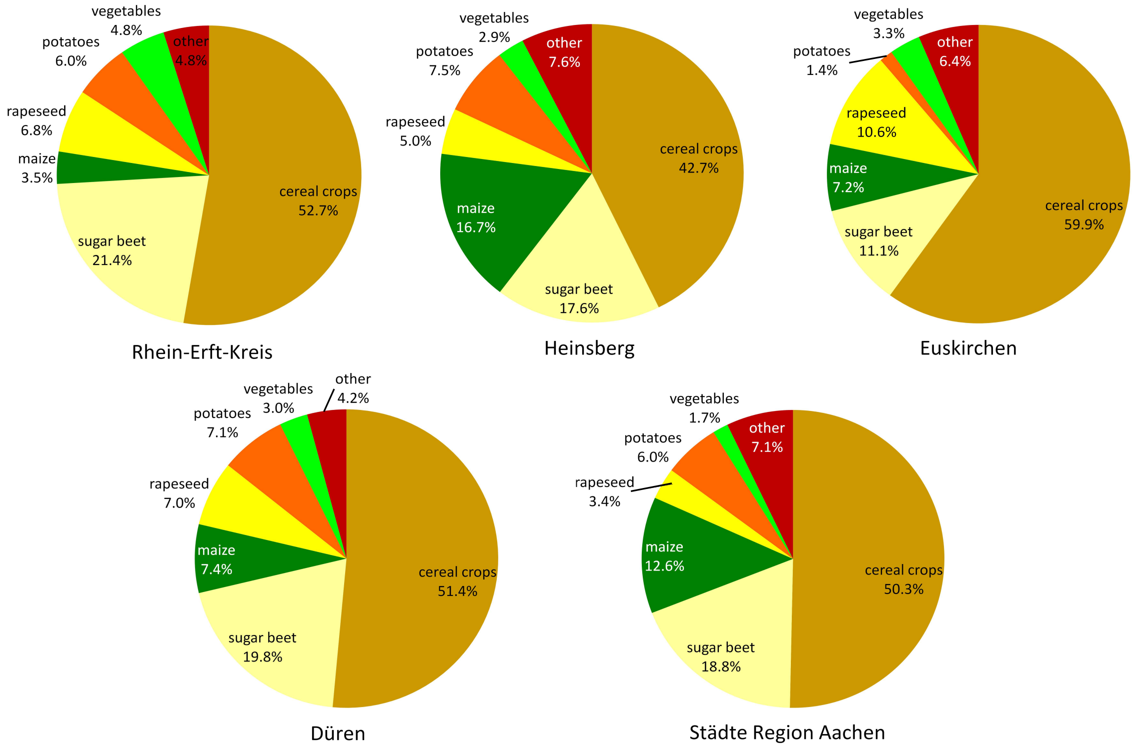

Figure A.13.: Arable land use [%] of the districts Rhein-Erft-Kreis, Heinsberg, Düren, Euskirchen and Städte Region Aachen in 2014 (Landwirtschaftskammer Nordrhein-Westfalen, 2015).

plant type	***phenology stage***	***average phenology date***	
		NRW	**RLP**
winter wheat	Ährenschieben	05/27 (−4 days)	05/27 (−4 days)
	Gelbreife	07/19 (±0 days)	07/16 (−2 days)
winter rye	Ährenschieben	05/09 (−4 days)	05/09 (−5 days)
	Blühbeginn	05/26 (−4 days)	05/25 (−3 days)
	Blühende	06/07 (−2 days)	06/05 (−4 days)
	Gelbreife	07/19 (+2 days)	07/09 (−3 days)
winter barley	Ährenschieben	05/10 (−4 days)	05/13 (−2 days)
	Gelbreife	06/25 (−1 days)	06/26 (−3 days)
winter rapeseed	Blühbeginn	04/17 (−7 days)	04/16 (−10 days)
	Blühende	05/20 (−1 days)	05/22 (−2 days)
	Ernte	07/30 (+5 days)	07/28 (+4 days)
maize	Auflaufen	05/10 (±0 days)	05/14 (−2 days)
	Fahnenschieben	07/17 (+3 days)	07/20 (+1 days)
	Blühbeginn	07/27 (+4 days)	07/27 (±0 days)
	Milchreife	08/21 (+3 days)	08/22 (+1 days)
	Ernte (Silage)	09/22 (−1 days)	09/30 (+4 days)
potatoes	Auflaufen	05/08 (±0 days)	05/14 (+3 days)
	Bestand geschlossen	06/01 (±0 days)	06/12 (+4 days)
beets	Auflaufen	04/28 (−2 days)	04/22 (−8 days)
	Bestand geschlossen	06/04 (−6 days)	06/13 (−2 days)

Table A.2.: Timing of phenology stages of agricultural cultivated plants in NRW and RLP in 2012 (Deutscher Wetterdienst, 2015). Deviations from the longtime average are in parentheses. **Definition of phenology stages:** *Schossen*: begin of formation of stalks (first stalk node above surface); *Ährenschieben*: begin of formation of ears; *Blühbeginn*: 5% of the flowers are open (begin of anthesis); *Blühende*: end of anthesis; *Gelbreife*: change of grain color from green to yellow in 50% of the ears; *Ernte*: harvest; *Auflaufen*: begin of sprout (plants 1 cm above surface); *Fahnenschieben*: begin of formation of panicles; *Milchreife*: achievement of final size of kernels (maize); *Knospenbildung*: begin of formation of buds (rapeseed); *Bestand geschlossen*: 50% of plants touch plants of the adjacent sowing row.

North Rhine-Westphalia				***Rhineland-Palatinate***			
winter wheat							
Schossen: ∅ NRW 04/04 (−21 days)				**Schossen: ∅ RLP 04/11 (−15 days)**			
Aachen-Orsbach	03/31	Eschweiler	04/10	Prüm	04/12	Nürburg-Barweiler	04/09
Hambach	03/24	Hennef	04/20	Welling	04/06		
Ährenschieben: ∅ NRW 05/18 (−13 days)				**Ährenschieben: ∅ RLP 05/19 (−12 days)**			
Aachen-Orsbach	05/16	Eschweiler	05/18	Prüm	05/21	Nürburg-Barweiler	05/28
Hambach	05/06	Euskirchen	05/21	Ahrbrück	05/24	Welling	05/20
Hennef	05/17	Bonn-Rodderberg	05/18				
Gelbreife: ∅ NRW 07/10 (−9 days)				**Gelbreife: ∅ RLP 07/06 (−12 days)**			
Aachen-Orsbach	07/05	Eschweiler	07/16	Prüm	07/24	Nürburg-Barweiler	07/28
Hambach	06/27	Euskirchen	07/13	Welling	05/24		
Hennef	06/27	Bonn-Rodderberg	06/27				
Ernte: ∅ NRW 07/29 (−6 days)				**Ernte: ∅ RLP 07/26 (−8 days)**			
Aachen-Orsbach	07/22	Eschweiler	07/20	Prüm	08/21	Nürburg-Barweiler	08/04
Hambach	07/16	Euskirchen	07/27	Welling	07/19		
Hennef	07/30	Bonn-Rodderberg	07/19				
winter rye							
Schossen: ∅ NRW 03/31 (−15 days)				**Schossen: ∅ RLP 04/04 (−12 days)**			
Hambach	03/16	Euskirchen	04/01	Prüm	04/02	Welling	04/01
Hennef	03/23						
Ährenschieben: ∅ NRW 04/30 (−13 days)				**Ährenschieben: ∅ RLP 05/03 (−11 days)**			
Hambach	04/21	Eschweiler	04/27	Prüm	05/13	Welling	04/30
Hennef	04/30						
Blühbeginn: ∅ NRW 05/20 (−10 days)				**Blühbeginn: ∅ RLP 05/18 (−10 days)**			
Hambach	05/03	Hennef	05/17	Prüm	05/20	Welling	05/20
Blühende: ∅ NRW 06/06 (−3 days)				**Blühende: ∅ RLP 06/02 (−7 days)**			
Hambach	06/06	Hennef	06/09	Prüm	06/17	Welling	06/07

Gelbreife: ∅ NRW 07/07 (−6 days)				**Gelbreife: ∅ RLP 07/04 (−7 days)**			
Hambach	07/01	Euskirchen	07/19	Prüm	07/24	Welling	07/03
Hennef	06/27						
winter barley							
Schossen: ∅ NRW 03/29 (−18 days)				**Schossen: ∅ RLP 04/04 (−15 days)**			
Aachen-Orsbach	03/24	Hambach	03/18	Prüm	04/02	Welling	03/28
Eschweiler	03/23	Euskirchen	04/01				
Hennef	03/29						
Ährenschieben: ∅ NRW 04/28 (−16 days)				**Ährenschieben: ∅ RLP 05/01 (−14 days)**			
Aachen-Orsbach	04/26	Hambach	04/23	Prüm	05/05	Welling	04/26
Eschweiler	04/24	Euskirchen	04/22				
Hennef	04/25	Bonn-Rodderberg	04/30				
Gelbreife: ∅ NRW 06/17 (−9 days)				**Gelbreife: ∅ RLP 06/16 (−13 days)**			
Aachen-Orsbach	06/12	Hambach	06/07	Prüm	06/30	Welling	06/10
(Eschweiler)	06/23	Euskirchen	06/12				
Hennef	06/09	Bonn-Rodderberg	06/07				
winter rapeseed							
Knospenbildung: ∅ NRW 03/14 (−26 days)				**Knospenbildung: ∅ RLP 03/17 (−25 days)**			
Aachen-Orsbach	03/02	Hambach	03/10	Prüm	03/24	Welling	03/17
Eschweiler	03/14	Euskirchen	03/21			Nürburg-Barweiler	03/19
Blühbeginn: ∅ NRW 04/01 (−23 days)				**Blühbeginn: ∅ RLP 04/05 (−21 days)**			
Aachen-Orsbach	03/21	Hambach	03/23	Prüm	04/16	Welling	03/31
Eschweiler	03/29	Euskirchen	03/24			Nürburg-Barweiler	04/15
Blühende: ∅ NRW 05/08 (−13 days)				**Blühende: ∅ RLP 05/09 (−15 days)**			
Aachen-Orsbach	05/09	Hambach	05/05	Prüm	05/21	Welling	05/08
Eschweiler	05/02	Euskirchen	05/06			Nürburg-Barweiler	05/24
Ernte: ∅ NRW 07/20 (−5 days)				**Ernte: ∅ RLP 07/18 (−6 days)**			
Aachen-Orsbach	07/18	Hambach	07/17	Prüm	07/23	Welling	07/16
Eschweiler	07/18	Euskirchen	07/17			Nürburg-Barweiler	07/27
maize							
Auflaufen: ∅ NRW 05/02 (−8 days)				**Auflaufen: ∅ RLP 05/15 (−1 days)**			
Aachen-Orsbach	05/02	Hambach	05/04	Prüm	06/01	Nürburg-Barweiler	06/02
Eschweiler	05/01	Euskirchen	05/06				
Fahnenschieben: ∅ NRW 07/15 (+1 days)				**Fahnenschieben: ∅ RLP 07/18 (±0 days)**			
Aachen-Orsbach	07/18	Hambach	07/10	Prüm	07/23	Nürburg-Barweiler	07/30
Eschweiler	07/19	Euskirchen	07/18				
Blühbeginn: ∅ NRW 07/23 (±0 days)				**Blühbeginn: ∅ RLP 07/26 (−1 days)**			
Aachen-Orsbach	07/21	Hambach	07/16	Prüm	07/30	Nürburg-Barweiler	08/05
Eschweiler	07/23	Euskirchen	07/28				
Milchreife: ∅ NRW 08/16 (−1 days)				**Michreife: ∅ RLP 08/19 (−2 days)**			
Aachen-Orsbach	08/18	Hambach	08/05	Prüm	09/01	Nürburg-Barweiler	09/12
(Eschweiler)	08/24	Euskirchen	08/10				
Ernte (Silage): ∅ NRW 09/27 (+4 days)				**Ernte (Silage): ∅ RLP 10/03 (+7 days)**			
Aachen-Orsbach	10/12	Hambach	10/01	Prüm	10/14	Nürburg-Barweiler	10/29
Eschweiler	09/29						
potatoes							
Auflaufen: ∅ NRW 05/02 (−6 days)				**Auflaufen: ∅ RLP 05/02 (−9 days)**			
Eschweiler	05/04	Hambach	04/09	Prüm	05/01	Nürburg-Barweiler	06/15
Euskirchen	05/06	Hennef	04/25	Welling	04/28		
Bonn-Rodderberg	04/21						
Bestand geschlossen: ∅ NRW 05/25 (−7 days)				**Bestand geschlossen: ∅ RLP 06/06 (−2 days)**			
Eschweiler	05/31	Hambach	05/06	Prüm	06/12	Nürburg-Barweiler	07/25
Euskirchen	05/28	Hennef	05/23	Welling	05/23		
Bonn-Rodderberg	05/06						
beets							
Auflaufen: ∅ NRW 04/16 (−14 days)				**Auflaufen: ∅ RLP 04/16 (−14 days)**			
Aachen-Orsbach	04/05	Hambach	04/05	Prüm	04/23	Welling	04/15
Eschweiler	04/12	Euskirchen	04/17				
Hennef	04/26						
Bestand geschlossen: ∅ NRW 05/30 (−11 days)				**Bestand geschlossen: ∅ RLP 06/04 (−11 days)**			
Aachen-Orsbach	05/29	Hambach	05/23	Prüm	06/16	Welling	05/31
Eschweiler	05/29	Euskirchen	05/30				
Hennef	05/23	Bonn-Rodderberg	05/20				

Table A.3.: As Table A.2 but for 2014 and with additional locations in the NRW domain (DWD, 2015).

List of symbols and abbreviations

Symbols

A/A^{can}	leaf/canopy (gross) photosynthesis rate	$[\mu\mathrm{mol\,m^{-2}s^{-1}}]$
$A^{sun/sha}$	sunlit/shaded canopy (gross) photosynthesis rate	$[\mu\mathrm{mol\,m^{-2}s^{-1}}]$
$a_{dir/dif}$	direct/diffuse albedo	
a_{R25}	specific activity of RuBisCO (CO$_2$ fixation per mass of RuBisCO and time)	$[\mu\mathrm{mol\,g^{-1}s^{-1}}]$
$a(N)$	nitrogen availability factor	
b	fraction CO$_2$/(BIO+HUM)	
c_a	CO$_2$ partial pressure of ambient air of the leaf (or of the canopy)	[Pa]
c_{atm}	CO$_2$ partial pressure at atmospheric forcing height	[Pa]
c_h	volumetric heat capacity	
c_i	intercellular CO$_2$ partial pressure of the leaf	[Pa]
C_i	carbon pool i with i=DPM,RPM,BIO,HUM	$[\mathrm{t\,ha^{-1}}]$
$C_{i,new}$	carbon pool i after decomposition	$[\mathrm{t\,ha^{-1}}]$
c_p/c_v	specific heat at constant pressure/volume	$[\mathrm{J\,kg^{-1}K^{-1}}]$
c_r	plant retainment factor of decomposition	
c_s	CO$_2$ partial pressure at leaf surface	[Pa]
$clay$	clay content	[%]
CN_L	leaf C:N ratio	$[\mathrm{kg\,kg^{-1}}]$
D_d	direct throughfall of canopy water	$[\mathrm{kg\,m^{-2}s^{-1}}]$
D_r	canopy drip	$[\mathrm{kg\,m^{-2}s^{-1}}]$
DL	day length	[s]
e_a	water vapor pressure af ambient air of the leaf (or of the canopy)	[Pa]
e_{atm}	water vapor pressure at atmospheric forcing height	[Pa]
e_g	ground water vapor pressure	[Pa]
E_g	evaporation of the ground	$[\mathrm{W\,m^{-2}}]$
e_{es}	effective surface water vapor pressure	[Pa]
e_i^*	saturated water vapor pressure inside the leaf	[Pa]
e_s	water vapor pressure at leaf surface	[Pa]
$E_{\mathrm{SNAP}i}$	anthropogenic emission of SNAP i	$[\mathrm{kg\,m^{-2}s^{-1}}]$
e_v	vegetation (canopy) water vapor pressure	[Pa]
E_v	evapotranspiration of vegetation	$[\mathrm{kg\,m^{-2}s^{-1}}]$
E_w	evaporation from wet canopy	$[\mathrm{kg\,m^{-2}s^{-1}}]$
$f_{e,root}$	effective root fraction	
F_g	heat flow at the ground	$[\mathrm{W\,m^{-2}}]$
$\widehat{f_h}_{auto}$	moisture reduction factor of autotrophic respiration	
$\mathbf{F^{l/f}}$	turbulent flux of liquid/frozen water	$[\mathrm{kg\,m^{-2}s^{-1}}]$
F_{LNR}	fraction of leaf nitrogen in RuBisCO	$[\mathrm{kg\,kg^{-1}}]$
F_{NR}	mass ratio of total RuBisCO molecular mass to N in RuBisCO	$[\mathrm{kg\,kg^{-1}}]$
f_{root}	root fraction	
$f_{sun/sha}$	sunlit/shaded leaf fraction of a canopy	
$\mathbf{F^v}$	turbulent flux of water vapor	$[\mathrm{kg\,m^{-2}s^{-1}}]$
F_z	subsurface heat flow at depth z	$[\mathrm{W\,m^{-2}}]$
$\mathbf{g}$	acceleration of gravity	$[\mathrm{m\,s^{-2}}]$
g_{can}	canopy conductance	$[\mathrm{m\,s^{-1}}]$
g_{st}	leaf stomatal conductance	$[\mathrm{m\,s^{-1}}]$
$g_{st,\min}$	minimum stomatal conductance	$[\mathrm{m\,s^{-1}}]$
h	soil pressure head	[m]

h_1	air entry pressure (saturation suction)	[m]
h_2	pressure head of optimal soil respiration	[m]
h_3	pressure head when soil respiration ceases	[m]
$\mathbf{H}$	heat flux vector	[W m^{-2}]
$H_{g/v}$	sensible heat flux of ground/vegetation	[W m^{-2}]
h_{soil}	soil depth	[m]
$I^{l/f}$	phase transition rate of liquid/frozen water	[kg m^{-3}s^{-1}]
k	hydraulic conductivity	[m s^{-1}]
K	direct beam light extinction coefficient	
K_c	Michaelis-Menten constant for CO_2	[Pa]
K_o	Michaelis-Menten constant for O_2	[Pa]
L	leaf area index (m^2 (one-sided) leaf area per m^2 ground area)	[m^2 m^{-2}]
$L^{sun/sha}$	sunlit/shaded leaf area index	[m^2 m^{-2}]
$\downarrow L$	incident longwave radiation	[W m^{-2}]
$\uparrow L$	emitted longwave radiation	[W m^{-2}]
$L_{g/v}$	net longwave radiation absorbed by the ground/vegetation	[W m^{-2}]
$l_{V/S}$	latent heat of vaporization/sublimation	[m^{2}s^{-2}]
m	empirical scaling factor of r_{st}	
M_{CO_2}	molar mass of CO_2	[kg mol^{-1}]
M_{ma}	molar mass of moist air	[kg mol^{-1}]
N_a	area-based leaf nitrogen concentration	[kg m^{-2}]
n_v	linear slope coefficient of vertically increasing SLA	
o_i	intercellular O_2 partial pressure	[Pa]
p	atmospheric pressure	[Pa]
p_{atm}	pressure at atmospheric forcing height	[Pa]
P	total precipitation	[kg m^{-2}s^{-1}]
$\mathbf{P^{l/f}}$	diffusion flux of liquid/frozen water	[kg m^{-2}s^{-1}]
p_{surf}	(COSMO) atmospheric pressure at the surface	[Pa]
PAR	absorbed photosynthetically active radiation	[W m^{-2}]
$PAR^{sun/sha}$	sunlit/shaded PAR	[W m^{-2}]
q_{CO_2}	(mass) specific CO_2 mixing ratio	[kg kg^{-1}]
q_g	ground water flow	[kg m^{-2}s^{-1}]
$q^{l/f}$	(mass) specific content of liquid/frozen water	[kg kg^{-1}]
q^v	(mass) specific content of water vapor	[kg kg^{-1}]
q^v_{surf}	(COSMO) specific content of water vapor at the surface	[kg kg^{-1}]
q_z	soil water flow at depth z	[kg m^{-2}s^{-1}]
$\mathbf{R}$	radiative net flux	[W m^{-2}]
r_a	aerodynamic resistance	[s m^{-1}]
$r_{a,can}$	aerodynamic resistance within the canopy	[s m^{-1}]
R_a	(total) autotrophic respiration ($R_{leaf} + R_{auto}$)	[μmol m^{-2}s^{-1}]
R_{auto}	belowground autotrophic respiration (root, rhizosphere, mycorrhiza)	[μmol m^{-2}s^{-1}]
r_b	leaf boundary layer resistance	[s m^{-1}]
$r_b^{sun/sha}$	canopy sunlit/shaded (big leaf) boundary layer resistance	[s m^{-1}]
r_{can}	canopy resistance	[s m^{-1}]
$r_{can}^{sun/sha}$	sunlit/shaded canopy resistance	[s m^{-1}]
r_{es}	surface resistance	[s m^{-1}]
R_L	gas constant of dry air	[m^{2}s^{-2}K^{-1}]
R_{leaf}	leaf respiration rate	[μmol m^{-2}s^{-1}]
R_{leaf}^{can}	canopy scale leaf respiration rate	[μmol m^{-2}s^{-1}]
R_h	heterotrophic respiration	[μmol m^{-2}s^{-1}]
R_{plant}	total plant respiration	[μmol m^{-2}s^{-1}]
R_{root}	root respiration	[μmol m^{-2}s^{-1}]
r_{st}	leaf stomatal resistance	[s m^{-1}]
$r_{st}^{sun/sha}$	canopy sunlit/shaded (big leaf) stomatal resistance	[s m^{-1}]
R_{surf}	surface runoff	[kg m^{-2}s^{-1}]
S	total shortwave (solar) radiation	[W m^{-2}]
$\downarrow S_{dir/dif}$	incident direct beam/diffuse shortwave (solar) radiation	[W m^{-2}]

$S_{g/v}$	solar radiation absorbed by the ground/vegetation	[W m^{-2}]
S_0	total shortwave (solar) radiation at the top of the canopy	[W m^{-2}]
SLA	specific leaf area (leaf area per leaf mass)	[m^2 g^{-1}]
SLA_0	specific leaf area at the top of the canopy	[m^2 g^{-1}]
$SLA^{sun/sha}$	sunlit/shaded specific leaf area	[m^2 g^{-1}]
T	temperature	[K, °C]
$\mathbb{T}$	general stress tensor	[kg m^{-1}s^{-2}]
T_{atm}	temperature at atmospheric forcing height	[K]
T_{dew}	dew point temperature	[°C]
T_{es}	effective surface temperature	[K]
T_l	leaf temperature	[K]
T_{ref}	reference temperature of RothC	[°C]
T_{soil}	soil temperature	[°C]
T_{surf}	(COSMO) surface temperature	[K]
T_v	vegetation (canopy) temperature	[K]
T_g	ground temperature	[K]
$T_{\min\,/\,\max}$	minimum/maximum 2 m air temperature of the day	[°C]
T_{virt}	virtual temperature	[K]
TP/TP^{can}	leaf/canopy transpiration	[W m^{-2}, kg m^{-2}s^{-1}]
u/v	zonal/meridional wind speed	[m s^{-1}]
$\mathbf{v}$	relative velocity	[m s^{-1}]
$V_{c,\max}$	maximum rate of carboxylation	[μmol m^{-2}s^{-1}]
$V_{c,\max\,25}$	maximum rate of carboxylation at 25 °C	[μmol m^{-2}s^{-1}]
$V_{c,\max}^{sun/sha}$	sunlit/shaded maximum rate of carboxylation	[μmol m^{-2}s^{-1}]
w_c	RuBisCO limitation rate of photosynthesis	[μmol m^{-2}s^{-1}]
w_{dew}	liquid canopy water (i. e. dew)	[kg m^{-2}]
w_e	capacity utilization limitation rate of photosynthesis	[μmol m^{-2}s^{-1}]
w_j	light limitation rate of photosynthesis	[μmol m^{-2}s^{-1}]
x_L	overlying leaf area index	[m^2 m^{-2}]
α	quantum efficiency (molecular mass CO_2 per molecular mass of photons)	[μmol mol^{-1}]
β_{tran}	beta transpiration factor	
Γ_*	CO_2 compensation point	[Pa]
λ	thermal conductivity	[W m^{-1}K^{-1}]
λ_{C_i}	optimum decomposition rate of carbon pool i	[(year)$^{-1}$]
λ_{litter}	optimum decomposition rate of litter	[(year)$^{-1}$]
λ_O	optimum decomposition rate of O horizon	[(year)$^{-1}$]
θ	total volumetric water content	[m^3 m^{-3}]
θ_{liq}	volumetric content of liquid water	[m^3 m^{-3}]
ρ	air density	[kg m^{-3}]
ρ_B	bulk density of the soil	[kg m^{-3}]
$\tau_{x/y}$	zonal/meridional momentum flux	[kg m^{-1}s^{-2}]
$\boldsymbol{\Omega}$	angular velocity of the earth	[m s^{-1}]

Abbreviations

a.g.l.	above ground level	[m]
a.s.l.	above sea level	[m]
BATS	Biosphere-Atmosphere Transfer Scheme	
BE	Belgium	
Bft	Beaufort	
BIO	microbial biomass	[t ha^{-1}]
CBL	convective boundary layer	
CLM	Community Land Model (former: Common Land Model)	
CN-Model	Carbon-Nitrogen Model of CLM3.5	
COSMO	Consortium for Small-scale Modeling	
CO_2	carbon dioxide	

DGVM	dynamic global vegetation model	
DPM	decomposable plant material	[t ha^{-1}]
DWD	German Meteorological Service (Deutscher Wetterdienst)	
EC	eddy covariance	
GPP	gross primary production	[μmol m^{-2}s^{-1}]
HLUG	Hessisches Landesamt für Umwelt und Geologie	
HUM	humified organic material	[t ha^{-1}]
HYMACS	Hybrid Mass Flux Convection Scheme	
IC	initial condition	
IOM	inert organic matter	[t ha^{-1}]
LAI	(one-sided) leaf area index	
LANUV	Landesamt für Natur Umwelt und Verbraucherschutz NRW	
LBC	lateral boundary condition	
LH	(canopy) latent heat flux	[W m^{-2}]
N	nitrogen	
NEE	net ecosystem exchange	[μmol m^{-2}s^{-1}]
NEP	net ecosystem production	[μmol m^{-2}s^{-1}]
NL	the Netherlands	
NPP	net primary production	[μmol m^{-2}s^{-1}]
NRW	North Rhine-Westphalia	
NWP	numerical weather prediction	
PBL	planetary boundary layer	
PFT	plant functional type	
ppmv	parts per million by volume	
RIU	Rheinisches Institut für Umweltforschung an der Universität zu Köln	
RLP	Rhineland-Palatinate	
RothC	Rothamsted carbon turnover model	
RPM	resistant plant material	[t ha^{-1}]
RuBisCO	Ribulose-1,5-biphosphate carboxylase/-oxygenase	
RuBP	Ribulose-1,5-biphosphate	
SAI	stem area index	
SH	(canopy) sensible heat flux	[W m^{-2}]
SNAP	Source Nomenclature for Air Pollution	
SOM	soil organic matter	[t ha^{-1}]
TerrSysMP	Terrestrial Systems Modeling Platform	
TKE	turbulent kinetic energy	[m^{2}s^{-2}]
TNO	Netherlands Organisation for Applied Scientific Research	
TOC	total organic carbon	[t ha^{-1}]

Bibliography

Ahmadov R, Gerbig C, Kretschmer R, Koerner S, Neininger B, Dolman AJ, Sarrat C. 2007. Mesoscale covariance of transport and CO_2 fluxes: Evidence from observations and simulations using the WRF-VPRM coupled atmosphere-biosphere model. *Journal of Geophysical Research: Atmospheres (1984–2012)* **112**(D22).

Arrhenius S. 1898. Über die Reaktionsgeschwindigkeit bei der Inversion von Rohrzucker durch Säuren. *Zeitschrift für Physik Chemique* **4**: 226–248.

Bahn M, Rodeghiero M, Anderson-Dunn M, Dore S, Gimeno C, Drösler M, Williams M, Ammann C, Berninger F, Flechard C, Jones S, Balzarolo M, Kumar S, Newesely C, Priwitzer T, Raschi A, Siegwolf R, Susiluoto S, Tenhunen J, Wohlfahrt G, Cernusca A. 2008. Soil respiration in European grasslands in relation to climate and assimilate supply. *Ecosystems* **11**(8): 1352–1367.

Bahn M, Schmitt M, Siegwolf R, Richter A, Brüggemann N. 2009. Does photosynthesis affect grassland soil-respired CO_2 and its carbon isotope composition on a diurnal timescale? *New Phytologist* **182**(2): 451–460.

Baldauf M, Seifert A, Förstner J, Majewski D, Raschendorfer M, Reinhardt T. 2011. Operational convective-scale numerical weather prediction with the COSMO model: Description and sensitivities. *Monthly Weather Review* **139**(12): 3887–3905.

Ball JT. 1988. An analysis of stomatal conductance. PhD thesis, Stanford University, Stanford.

Bauer J, Weihermüller L, Huisman JA, Herbst M, Graf A, Sequaris JM, Vereecken H. 2012. Inverse determination of heterotrophic soil respiration response to temperature and water content under field conditions. *Biogeochemistry* **108**: 119–134.

Boesch H, Baker D, Connor B, Crisp D, Miller C. 2011. Global characterization of CO_2 column retrievals from shortwave-infrared satellite observations of the Orbiting Carbon Observatory-2 mission. *Remote Sensing* **3**(2): 270–304.

Bonan GB. 1996. Land surface model (LSM version 1.0) for ecological, hydrological, and atmospheric studies: Technical description and users guide. National Center for Atmospheric Research (NCAR), Boulder, CO (United States). Climate and Global Dynamics Division.

Bonan GB. 2008. *Ecological climatology: concepts and applications.* Cambridge University Press.

Borchard N, Schirrmann M, von Hebel C, Schmidt M, Baatz R, Firbank L, Vereecken H, Herbst M. 2015. Spatio-temporal drivers of soil and ecosystem carbon fluxes at field scale in an upland grassland in Germany. *Agriculture, ecosystems & environment* **211**: 84–93.

Borken W, Davidson EA, Savage K, Gaudinski J, Trumbore SE. 2003. Drying and wetting effects on carbon dioxide release from organic horizons. *Soil Science Society of America Journal* **67**(6): 1888–1896.

Bott A. 1989. A positive definite advection scheme obtained by nonlinear renormalization of the advective fluxes. *Monthly Weather Review* **117**(5): 1006–1016.

Brunet Y, Finnigan JJ, Raupach MR. 1994. A wind tunnel study of air flow in waving wheat: single-point velocity statistics. *Boundary-Layer Meteorology* **70**(1-2): 95–132.

"CarbonTracker Europe". 2014. Global monthly 1° x 1° resolution CO_2 flux data (2001–2011). URL `ftp://ftp.wur.nl/carbontracker/data/fluxes/data_flux1x1_monthly`. Heruntergeladen am 08.04.2014, Wageningen University.

Clapp RB, Hornberger GM. 1978. Empirical equations for some soil hydraulic properties. *Water Resources Research* **14**(4): 601–604.

Coleman K, Jenkinson DS. 2008. RothC-26.3. A model for the turnover of carbon in soil. URL `http://www.rothamsted.ac.uk/aen/carbon/mod26_3_win.pdf`. IACR-Rothamsted, Harpenden. Abgerufen am 24.03.2013.

Collatz GJ, Ball JT, Grivet C, Berry JA. 1991. Physiological and environmental regulation of stomatal conductance, photosynthesis and transpiration: A model that includes a laminar boundary layer. *Agricultural and Forest Meteorology* **54**(2): 107–136.

Cosby BJ, Hornberger GM, Clapp RB, Ginn TR. 1984. A statistical exploration of the relationships of soil moisture characteristics to the physical properties of soils. *Water Resources Research* **20**(6): 682–690.

Dai Y, Dickinson RE, Wang YP. 2004. A two-big-leaf model for canopy temperature, photosynthesis, and stomatal conductance. *Journal of Climate* **17**(12): 2281–2299.

Dai Y, Zeng Q. 1997. A land surface model (IAP94) for climate studies part I: Formulation and validation in off-line experiments. *Advances in Atmospheric Sciences* **14**(4): 433–460.

Dai Y, Zeng X, Dickinson RE, Baker I, Bonan GB, Bosilovich MG, Denning AS, Dirmeyer PA, Houser PR, Niu G, Oleson KW, Schlosser CA, Yang ZL. 2003. The Common Land Model. *Bulletin of the American Meteorological Society* **84**(8): 1013–1023.

Davidson EA, Janssens IA. 2006. Temperature sensitivity of soil carbon decomposition and feedbacks to climate change. *Nature* **440**: 165–173.

Deutscher Wetterdienst. 2015. Eintrittsdaten phänologischer Phasen für landwirtschaftliche Kulturpflanzen (Sofortmelder) für die Jahre 2012 und 2014. Grundversorgung des Deutschen

Wetterdienstes (DWD) (Katalog Spezialdienstleistungen), DWD, Offenbach.

Dickinson RE, Kennedy PJ, Henderson-Sellers A. 1993. Biosphere-Atmosphere Transfer Scheme (BATS) version 1e as coupled to the NCAR Community Climate Model. Technical report, National Center for Atmospheric Research (NCAR), Boulder, CO (United States). Climate and Global Dynamics Division.

Dolman A, Noilhan J, Durand P, Sarrat C, Brut A, Piguet B, Butet A, Jarosz N, Brunet Y, Loustau D, Lamaud E, Tolk L, Ronda R, Miglietta F, Gioli B, Magliulo V, Esposito M, Gerbig C, Korner S, Glademard O, Ramonet M, Ciasis P, Neininger B, Hutjes R, Elbers J, Macatangay R, Schrems O, Perez-Landa G, Sanz M, Scholz Y, Facon G, Ceschia E, Beziat P. 2006. The CarboEurope regional experiment strategy. *Bulletin of the American Meteorological Society* **87**(10): 1367–1379.

Doms G, Baldauf M. 2015. A description of the nonhydrostatic regional COSMO model. part I: Dynamics and numerics. URL `http://www.cosmo-model.org/content/model/documentation/core/cosmoDyncsNumcs.pdf`. Technical report, Deutscher Wetterdienst, Offenbach, Germany.

Doms G, Förstner J, Heise E, Herzog HJ, Mironov D, Raschendorfer M, Reinhardt T, Ritter B, Schrodin R, J-P S, Vogel G. 2011. A description of the nonhydrostatic regional COSMO model. part II: Physical parameterization. URL `http://www.cosmo-model.org/content/model/documentation/core/cosmoPhysParamtr.pdf`. Technical Report, Deutscher Wetterdienst, Offenbach, Germany.

Ekblad A, Högberg P. 2001. Natural abundance of ^{13}C in CO_2 respired from forest soils reveals speed of link between tree photosynthesis and root respiration. *Oecologia* **127**(3): 305–308.

Farquhar GD, von Caemmerer Sv, Berry JA. 1980. A biochemical model of photosynthetic CO_2 assimilation in leaves of C_3 species. *Planta* **149**(1): 78–90.

Finnigan J. 2000. Turbulence in plant canopies. *Annual Review of Fluid Mechanics* **32**(1): 519–571.

Franko U, Oelschlägel B, Schenk S. 1995. Modellierung von Bodenprozessen in Agrarlandschaften zur Untersuchung der Auswirkungen möglicher Klimaveränderungen. UFZ-Bericht 3/1995, UFZ-Umweltforschungszentrum Leipzig-Halle GmbH, Leipzig.

Freedman JM, Fitzjarrald DR, Moore KE, Sakai RK. 2001. Boundary layer clouds and vegetation-atmosphere feedbacks. *Journal of Climate* **14**(2): 180–197.

Froelich NJ, Grimmond CSB, Schmid HP. 2011. Nocturnal cooling below a forest canopy: Model and evaluation. *Agricultural and forest meteorology* **151**(7): 957–968.

Geels C, Gloor M, Ciais P, Bousquet P, Peylin P, Vermeulen AT, Dargaville R, Aalto T, Brandt J, Christensen JH, Frohn LM, Haszpra L, Karstens U, Rödenbeck C, Ramonet M, Carboni G, Santaguida G. 2007. Comparing atmospheric transport models for future regional inversions over Europe – part 1: Mapping the atmospheric CO_2 signals. *Atmospheric Chemistry and Physics* **7**(13): 3461–3479.

Gerbig C, Dolman AJ, Heimann M. 2009. On observational and modelling strategies targeted at regional carbon exchange over continents. *Biogeosciences* **6**(10): 1949–1959.

Graf A, Prolingheuer N, Schickling A, Schmidt M, Schneider K, Schüttemeyer D, Herbst M, Huisman JA, Weihermüller L, Scharnagl B, Steenpass C, Harms R, Vereecken H. 2011. Temporal downscaling of soil carbon dioxide efflux measurements based on time-stable spatial patterns. *Vadose Zone Journal* **10**(1): 239–251.

Graf A, Weihermüller L, Huisman JA, Herbst M, Bauer J, Vereecken H. 2008. Measurement depth effects on the apparent temperature sensitivity of soil respiration in field studies. *Biogeosciences* **5**(4): 1175–1188.

Hanson PJ, Edwards NT, Garten CT, Andrews JA. 2000. Separating root and soil microbial contributions to soil respiration: A review of methods and observations. *Biogeochemistry* **48**(1): 115–146.

Haszpra L. 1999. On the representativeness of carbon dioxide measurements. *Journal of Geophysical Research: Atmospheres (1984–2012)* **104**(D21): 26 953–26 960.

Haszpra L, Barcza Z, Haszpra T, Pátkai ZS, Davis KJ. 2015. How well do tall-tower measurements characterize the CO_2 mole fraction distribution in the planetary boundary layer? *Atmospheric Measurement Techniques* **8**(4): 1657–1671.

Herbst M, Hellebrand HJ, Bauer J, Huisman JA, Šimůnek J, Weihermüller L, Graf A, Vanderborght J, Vereecken H. 2008. Multiyear heterotrophic soil respiration: Evaluation of a coupled CO_2 transport and carbon turnover model. *Ecological modelling* **214**(2): 271–283.

Högberg P, Read DJ. 2006. Towards a more plant physiological perspective on soil ecology. *Trends in Ecology & Evolution* **21**(10): 548–554.

Jarvis PG. 1976. The interpretation of the variations in leaf water potential and stomatal conductance found in canopies in the field. *Philosophical Transactions of the Royal Society of London B: Biological Sciences* **273**(927): 593–610.

Jenkinson DS. 1990. The turnover of organic carbon and nitrogen in soil. *Philosophical Transactions of the Royal Society B: Biological Sciences* **329**(1255): 361–368.

Keeling CD, Chin JFS, Whorf TP. 1996. Increased activity of northern vegetation inferred from atmospheric CO_2 measurements. *Nature* **382**: 11.

Kern M. 2015. Analyse von lokaler Turbulenz in der untersten Atmosphäre anhand von CO_2. Master's thesis, Meteorologisches Institut, Universität Bonn. 110 S.

Kuell V, Bott A. 2008. A hybrid convection scheme for use in non-hydrostatic numerical weather prediction models. *Meteorologische Zeitschrift* **17**(6): 775–783.

Kuell V, Bott A. 2011. Simulation of non-local effects of convection with the hybrid mass flux convection scheme HYMACS. *Meteorologische Zeitschrift* **20**(2): 227–241.

Kuenen JJP, Visschedijk AJH, Jozwicka M, Denier van der Gon H. 2014. TNO-MACC_II emission inventory; a multi-year (2003–2009) consistent high-resolution European emission inventory for air quality modelling. *Atmospheric Chemistry and Physics* **14**(20): 10 963–10 976.

Kupisch M, Stadler A, Langensiepen M, Ewert F. 2015. Analysis of spatio-temporal patterns of CO_2 and H_2O fluxes in relation to crop growth under field conditions. *Field Crops Research* **176**: 108–118.

Landesamt für Natur, Umwelt und Verbraucherschutz Nordrhein-Westfalen (LANUV). 2012. Fachinformationssystem Stoffliche Bodenbelastung. URL `http://www.lanuv.nrw.de/boden/boschu-lua/fisstobo.html`. LANUV © Land NRW, Recklinghausen.

Landwirtschaftskammer Nordrhein-Westfalen. 2015. Landwirtschaftliche Nutzungsdaten für die Landkreise Heinsberg, Düren, Städte Region Aachen und Rhein-Erft-Kreis (Flächenprinzip). Bonn.

Langensiepen M, Kupisch M, van Wijk MT, Ewert F. 2012. Analyzing transient closed chamber effects on canopy gas exchange for optimizing flux calculation timing. *Agricultural and forest meteorology* **164**: 61–70.

Lauvaux T, Uliasz M, Sarrat C, Chevallier F, Bousquet P, Lac C, Davis KJ, Ciais P, Denning AS, Rayner PJ. 2008. Mesoscale inversion: First results from the CERES campaign with synthetic data. *Atmospheric Chemistry and Physics* **8**(13): 3459–3471.

Lin YL, Farley RD, Orville HD. 1983. Bulk parameterization of the snow field in a cloud model. *Journal of Climate and Applied Meteorology* **22**(6): 1065–1092.

Lloyd J, Francey RJ, Mollicone D, Raupach MR, Sogachev A, Arneth A, Byers JN, Kelliher FM, Rebmann C, Valentini R, Wong SC, Bauer G, Schulze ED. 2001. Vertical profiles, boundary layer budgets, and regional flux estimates for CO_2 and its $^{13}C/^{12}C$ ratio and for water vapor above a forest/bog mosaic in central Siberia. *Global Biogeochemical Cycles* **15**(2): 267–284.

Lloyd J, Taylor JA. 1994. On the temperature dependence of soil respiration. *Functional ecology* **8**: 315–323.

Mauder M, Cuntz M, Drüe C, Graf A, Rebmann C, Schmid HP, Schmidt M, Steinbrecher R. 2013. A strategy for quality and uncertainty assessment of long-term eddy-covariance measurements. *Agricultural and Forest Meteorology* **169**: 122–135.

McGuire AD, Sitch S, Clein JS, Dargaville R, Esser G, Foley J, Heimann M, Joos F, Kaplan J, Kicklighter DW, Meier RA, Melillo JM, Moore III B, Prentice I, Ramankutty N, Reichenau T, Schloss A, Tian H, Williams LJ, Wittenberg U. 2001. Carbon balance of the terrestrial biosphere in the twentieth century: Analyses of CO_2, climate and land use effects with four process-based ecosystem models. *Global Biogeochemical Cycles* **15**(1): 183–206.

McInnes G. 1996. EMEP/CORINAIR atmospheric emission inventory guidebook - first edition. European Environment Agency (EEA).

Mellor GL, Yamada T. 1982. Development of a turbulence closure model for geophysical fluid problems. *Reviews of geophysics and space physics* **20**(4): 851–875.

Moyano FE, Kutsch WL, Rebmann C. 2008. Soil respiration fluxes in relation to photosynthetic activity in broad-leaf and needle-leaf forest stands. *Agricultural and Forest Meteorology* **148**(1): 135–143.

Nelson DW, Sommers LE. 1996. Total carbon, organic carbon, and organic matter. *Methods of soil analysis* **3**(3): 961–1010.

Nicholls ME, Denning AS, Prihodko L, Vidale PL, Baker I, Davis K, Bakwin P. 2004. A multiple-scale simulation of variations in atmospheric carbon dioxide using a coupled biosphere-atmospheric model. *Journal of Geophysical Research: Atmospheres (1984–2012)* **109**(D18).

Niu GY, Yang ZL, Dickinson RE, Gulden LE. 2005. A simple TOPMODEL-based runoff parameterization (SIMTOP) for use in global climate models. *Journal of Geophysical Research: Atmospheres (1984–2012)* **110**(D21).

Oleson KW, Lawrence DM, Bonan GB, Flanner MG, Kluzek E, Lawrence PJ, Levis S, Swenson SC, Thornton PE. 2010. Technical description of version 4.0 of the Community Land Model (CLM).

Pérez-Landa G, Ciais P, Gangoiti G, Palau JL, Carrara A, Gioli B, Miglietta F, Schumacher M, Millán MM, Sanz MJ. 2007. Mesoscale circulations over complex terrain in the Valencia coastal region, Spain – part 2: Modeling CO_2 transport using idealized surface fluxes. *Atmospheric Chemistry and Physics* **7**(7): 1851–1868.

Peters W, Krol MC, Van Der Werf GR, Houweling S, Jones CD, Hughes J, Schaefer K, Masarie KA, Jacobson AR, Miller JB, Cho CH, Ramonet M, Schmidt M, Ciattaglia L, Apadula F, Helta D, Meinhardt F, di Sarra AG, Piacentino S, Sferlazzo D, Aalto T, Hatakka J, Strom J, Haszpra L, Meijer HAJ, van der Laan S, Neubert REM, Jordan A, Rodo X, Morgui JA, Vermeulen AT, Popa E, Rozanski K, Zimnoch M, Manning AC, Leuenberger M, Uglietti C, Dolman AJ, Ciais P, Heimann M, Tans PP. 2010. Seven years of recent European net terrestrial carbon dioxide exchange constrained by atmospheric observations. *Global Change Biology* **16**(4): 1317–1337.

Pillai D, Gerbig C, Ahmadov R, Rödenbeck C, Kretschmer R, Koch T, Thompson R, Neininger B, Lavrié JV. 2011. High-resolution simulations of atmospheric CO_2 over complex terrain

– representing the Ochsenkopf mountain tall tower. *Atmospheric Chemistry and Physics* **11**(15): 7445–7464.

Pouliot G, Pierce T, van der Gon HD, Schaap M, Moran M, Nopmongcol U. 2012. Comparing emission inventories and model-ready emission datasets between Europe and North America for the AQMEII project. *Atmospheric Environment* **53**: 4–14.

Prentice IC, Farquhar GD, Fasham MJR, Goulden ML, Heimann M, Jaramillo VJ, Kheshgi HS, LeQuéré C, Scholes RJ, Wallace DWR. 2001. *The carbon cycle and atmospheric carbon dioxide*. Cambridge University Press.

Qu W, Bogena HR, Huisman JA, Schmidt M, Weuthen A, Schilling B, Vereecken H. 2015. The integrated water balance and soil data set of the Rollesbroich hydrological observatory. *Earth System Science Data (ESSD)* Submitted.

Raschendorfer M. 2011. The new turbulence parameterization of LM. *Cosmo Newsletter* **1**: 89–97.

Reinhardt T, Seifert A. 2006. A three-category ice scheme for LMK. *Cosmo Newsletter* **6**: 115–120.

Ritter B, Geleyn JF. 1992. A comprehensive radiation scheme for numerical weather prediction models with potential applications in climate simulations. *Monthly Weather Review* **120**(2): 303–325.

Rödenbeck C, Gerbig C, Trusilova K, Heimann M. 2009. A two-step scheme for high-resolution regional atmospheric trace gas inversions based on independent models. *Atmospheric Chemistry and Physics* **9**(14): 5331–5342.

Ronda RJ, De Bruin HAR, Holtslag AAM. 2001. Representation of the canopy conductance in modeling the surface energy budget for low vegetation. *Journal of Applied Meteorology* **40**(8): 1431–1444.

Ryan MG. 1991. Effects of climate change on plant respiration. *Ecological Applications* **1**(2): 157–167.

Ryan MG, Law BE. 2005. Interpreting, measuring, and modeling soil respiration. *Biogeochemistry* **73**(1): 3–27.

Sarrat C, Noilhan J, Dolman AJ, Gerbig C, Ahmadov R, Tolk LF, Meesters AGCA, Hutjes RWA, Ter Maat HW, Pérez-Landa G, Donier S. 2007b. Atmospheric CO_2 modeling at the regional scale: An intercomparison of 5 meso-scale atmospheric models. *Biogeosciences* **4**(6): 1115–1126.

Sarrat C, Noilhan J, Lacarrere P, Ceschia E, Ciais P, Dolman A, Elbers JA, Gerbig C, Gioli B, Lauvaux T, Miglietta F, Neininger B, Ramonet M, Vellinga O, Bonnefond JM. 2009. Mesoscale modelling of the CO_2 interactions between the surface and the atmosphere applied to the april 2007 CERES field experiment. *Biogeosciences* **6**: 633–646.

Sarrat C, Noilhan J, Lacarrere P, Donier S, Lac C, Calvet JC, Dolman AJ, Gerbig C, Neininger B, Ciais P, Paris JD, Boumard F, Ramonet M, Butet A. 2007a. Atmospheric CO_2 modeling at the regional scale: Application to the CarboEurope Regional Experiment. *Journal of Geophysical Research: Atmospheres (1984–2012)* **112**(D12).

Schaap M, Roemer M, Sauter F, Boersen G, Timmermans R, Builtjes PJH, Vermeulen AT. 2005. LOTOS-EUROS: Documentation. TNO report, 2005/297.

Schneider W, Bott A. 2014. On the time-splitting errors of one-dimensional advection schemes in numerical weather prediction models; a comparative study. *Quarterly Journal of the Royal Meteorological Society* **140**(684): 2321–2329.

Schomburg A, Venema V, Lindau R, Ament F, Simmer C. 2010. A downscaling scheme for atmospheric variables to drive soil–vegetation–atmosphere transfer models. *Tellus B* **62**(4): 242–258.

Shrestha P, Sulis M, Masbou M, Kollet S, Simmer C. 2014. A scale-consistent terrestrial systems modeling platform based on COSMO, CLM, and ParFlow. *Monthly Weather Review* **142**(9): 3466–3483.

Šimůnek J, Suarez DL. 1993. Modeling of carbon dioxide transport and production in soil: 1. model development. *Water Resources Research* **29**(2): 487–497.

Smallman TL, Moncrieff JB, Williams M. 2013. WRFv3. 2-SPAv2: Development and validation of a coupled ecosystem–atmosphere model, scaling from surface fluxes of CO_2 and energy to atmospheric profiles. *Geoscientific Model Development* **6**(4): 1079–1093.

Stadler A, Rudolph S, Kupisch M, Langensiepen M, van der Kruk J, Ewert F. 2015. Quantifying the effects of soil variability on crop growth using apparent soil electrical conductivity measurements. *European Journal of Agronomy* **64**: 8–20.

Steffens W. 2007. Bodenkarte zur Standorterkundung, Verfahren: Rollesbroich (Landwirtschaft), 1:2.500. Geologischer Dienst Nordrhein-Westfalen, Krefeld.

Stewart JB. 1988. Modelling surface conductance of pine forest. *Agricultural and Forest meteorology* **43**(1): 19–35.

Suarez DL, Šimůnek J. 1993. Modeling of carbon dioxide transport and production in soil: 2. parameter selection, sensitivity analysis, and comparison of model predictions to field data. *Water Resources Research* **29**(2): 499–513.

Sulis M, Langensiepen M, Shrestha P, Schickling A, Simmer C, Kollet SJ. 2015. Evaluating the influence of plant-specific physiological parameterizations on the partitioning of land surface energy fluxes. *Journal of Hydrometeorology* **16**(2): 517–533.

Takahashi T, Sutherland SC, Sweeney C, Poisson A, Metzl N, Tilbrook B, Bates N, Wanninkhof R, Feely RA, Sabine C, Olafsson J, Nojiri Y. 2002. Global sea–air CO_2 flux based on climatological surface ocean pCO_2, and seasonal biological and temperature effects. *Deep Sea Research Part II: Topical Studies in Oceanography* **49**(9): 1601–1622.

Tang J, Baldocchi DD, Xu L. 2005. Tree photosynthesis modulates soil respiration on a diurnal time scale. *Global Change Biology* **11**(8): 1298–1304.

Ter Maat HW, Hutjes RWA, Miglietta F, Gioli B, Bosveld FC, Vermeulen AT, Fritsch H. 2010. Simulating carbon exchange using a regional atmospheric model coupled to an advanced land-surface model. *Biogeosciences* **7**(8): 2397–2417.

Thornton PE, Law BE, Gholz HL, Clark KL, Falge E, Ellsworth DS, Goldstein AH, Monson RK, Hollinger D, Falk M, Chenj J, Sparks JP. 2002. Modeling and measuring the effects of disturbance history and climate on carbon and water budgets in evergreen needleleaf forests. *Agricultural and forest meteorology* **113**(1): 185–222.

Thornton PE, Rosenbloom NA. 2005. Ecosystem model spin-up: estimating steady state conditions in a coupled terrestrial carbon and nitrogen cycle model. *Ecological Modelling* **189**(1): 25–48.

Thornton PE, Zimmermann NE. 2007. An improved canopy integration scheme for a land surface model with prognostic canopy structure. *Journal of Climate* **20**(15): 3902–3923.

Tiedtke M. 1989. A comprehensive mass flux scheme for cumulus parameterization in large-scale models. *Monthly Weather Review* **117**(8): 1779–1800.

Tolk LF, Peters W, Meesters AG, Groenendijk M, Vermeulen AT, Steeneveld GJ, Dolman AJ. 2009. Modelling regional scale surface fluxes, meteorology and CO_2 mixing ratios for the Cabauw tower in the Netherlands. *Biogeosciences* **6**(10): 2265–2280.

Uebel M, Bott A. 2015. Mesoscale air transport at a midlatitude squall line in Europe – a numerical analysis. *Quarterly Journal of the Royal Meteorological Society* , in press.

Umweltbundesamt. 2015. Emissionen von direkten und indirekten Treibhausgasen und von Schwefeldioxid. URL `http://www.umweltbundesamt.de/daten/klimawandel/treibhausgas-emissionen-in-deutschland`. Abgerufen am 08.06.2015, Umweltbundesamt, Dessau-Roßlau.

Valcke S. 2013. The OASIS3 coupler: a European climate modelling community software. *Geoscientific Model Development* **6**(2): 373–388.

van der Molen MK, Dolman AJ. 2007. Regional carbon fluxes and the effect of topography on the variability of atmospheric CO_2. *Journal of Geophysical Research: Atmospheres (1984–2012)* **112**(D1).

van Genuchten MT. 1980. A closed form equation for predicting the hydraulic conductivity of unsaturated soils. *Soil Science Society of America Journal* **44**(5): 892–898.

van't Hoff MJH. 1884. Etudes de dynamique chimique. *Recueil des Travaux Chimiques des Pays-Bas* **3**(10): 333–336.

Visschedijk A, Zandveld P, Denier van der Gon H. 2007. A high resolution gridded European emission database for the EU integrated project GEMS. TNO report, 2007-A-R0233/B.

Wang YP, Leuning R. 1998. A two-leaf model for canopy conductance, photosynthesis and partitioning of available energy. I. model description and comparison with a multi-layered model. *Agricultural and Forest Meteorology* **91**(1): 89–111.

Wegener O. 2008. Untersuchung des Einflusses des Klimawandels auf die CO_2-Freisetzung aus Böden ausgewählter hessischer Dauerbeobachtungsflächen – Abschlussbericht. URL `http://klimawandel.hlug.de/fileadmin/dokumente/klima/inklim_plus/berichte/boden.pdf`. Auftraggeber: Hessisches Landesamt für Umwelt und Geologie (HLUG), Auftragnehmer: AGROFOR Consulting, Dipl.-Ing. agr. Oliver Wegener, Wettenberg.

Weihermüller L, Graf A, Herbst M, Vereecken H. 2013. Simple pedotransfer functions to initialize reactive carbon pools of the RothC model. *European Journal of Soil Science* **64**(5): 567–575.

White MA, Thornton PE, Running SW, Nemani RR. 2000. Parameterization and sensitivity analysis of the BIOME-BGC terrestrial ecosystem model: net primary production controls. *Earth interactions* **4**(3): 1–85.

Zeng X, Decker M. 2009. Improving the numerical solution of soil moisture-based richards equation for land models with a deep or shallow water table. *Journal of Hydrometeorology* **10**(1): 308–319.

Zhang D, Hui D, Yiqi L, Zhou G. 2008. Rates of litter decomposition in terrestrial ecosystems: global patterns and controlling factors. *Plant Ecology* **1**(2): 85–93.

BONNER METEOROLOGISCHE ABHANDLUNGEN

Herausgegeben vom Meteorologischen Institut der Universität Bonn durch Prof. Dr. H. FLOHN (Hefte 1-25), Prof. Dr. M. HANTEL (Hefte 26-35), Prof. Dr. H.-D. SCHILLING (Hefte 36-39), Prof. Dr. H. KRAUS (Hefte 40-49), ab Heft 50 durch Prof. Dr. A. HENSE.

Heft 1-49: siehe `http://www.meteo.uni-bonn.de/bibliothek/bma`

Heft 50: ***Petra Friederichs***: Interannuelle und dekadische Variabilität der atmosphärischen Zirkulation in gekoppelten und SST-getriebenen GCM-Experimenten. 2000, 133 S. + VIII. € 25

Heft 51: ***Heiko Paeth***: Anthropogene Klimaänderungen auf der Nordhemisphäre und die Rolle der Nordatlantik-Oszillation. 2000, 168 S.+ XVIII. € 28

Heft 52: ***Hildegard Steinhorst***: Statistisch-dynamische Verbundsanalyse von zeitlich und räumlich hoch aufgelösten Niederschlagsmustern: eine Untersuchung am Beispiel der Gebiete von Köln und Bonn. 2000, 146 S. + XIV. € 25

Heft 53: ***Thomas Klein***: Katabatic winds over Greenland and Antartica and their interaction with mesoscale and synoptic-scale weather systems: three-dimensional numerical models. 2000, 146 S. + XIV. € 25

Heft 54: ***Clemens Drüe***: Experimentelle Untersuchung arktischer Grenzschichtfronten an der Meereisgrenze in der Davis-Straße. 2001, 165 S. + VIII. € 28

Heft 55: ***Gisela Seuffert***: Two approaches to improve the simulation of near surface processes in numerical weather prediction models. 2001, 128 S. + VI. € 25

Heft 56: ***Jochen Stuck***: Die simulierte axiale atmosphärische Drehimpulsbilanz des ECHAM3-T21 GCM. 2002, 202 S. + VII. € 30

Heft 57: ***Günther Haase***: A physical initialization algorithm for non-hydrostatic weather prediction models using radar derived rain rates. 2002, 106S. + IV. € 25

Heft 58: ***Judith Berner***: Detection and Stochastic Modeling of Nonlinear Signatures in the Geopotential Height Field of an Atmospheric General Circulation Model. 2003, 157 S. + VIII. € 28

Heft 59: ***Bernd Maurer***: Messungen in der atmosphärischen Grenzschicht und Validation eines mesoskaligen Atmosphärenmodells über heterogenen Landoberflächen. 2003, 182 S. + IX. € 30

Heft 60: ***Christoph Gebhardt***: Variational reconstruction of Quaternary temperature fields using mixture models as botanical – climatological transfer functions. 2003, 204 S. + VIII. € 30

Heft 61: ***Heiko Paeth***: The climate of tropical and northern Africa – A statistical-dynamical analysis of the key factors in climate variability and the role of human activity in future climate change. 2005, 316 S. + XVI. € 15

Heft 62: ***Christian Schölzel***: Palaeoenvironmental transfer functions in a Bayesian framework with application to Holocene climate variability in the Near East. 2006, 104 S. + VI. € 15

Heft 63: ***Susanne Bachner***: Daily precipitation characteristics simulated by a regional climate model, including their sensitivity to model physics, 2008, 161 S. € 15

Heft 64: ***Michael Weniger***: Stochastic parameterization: a rigorous approach to stochastic three-dimensional primitive equations, 2014, 148 S. + XV. open access[1]

Heft 65: ***Andreas Röpnack***: Bayesian model verification: predictability of convective conditions based on EPS forecasts and observations, 2014, 152 S. + VI. open access[1]

Heft 66: ***Thorsten Simon***: Statistical and Dynamical Downscaling of Numerical Climate Simulations: Enhancement and Evaluation for East Asia, 2014, 48 S. + VII. + Anhänge open access[1]

Heft 67: ***Elham Rahmani***: The Effect of Climate Change on Wheat in Iran, 2014, [erschienen] 2015, 96 S. + XIII. open access[1]

Heft 68: ***Pablo A. Saavedra Garfias***: Retrieval of Cloud and Rainwater from Ground-Based Passive Microwave Observations with the Multi-frequency Dual-polarized Radiometer ADMIRARI, 2014, [erschienen] 2015, 168 S. + XIII. open access[1]

Heft 69: ***Christoph Bollmeyer***: A high-resolution regional reanalysis for Europe and Germany - Creation and Verification with a special focus on the moisture budget, 2015, 103 S. + IX. open access[1]

Heft 70: ***A S M Mostaquimur Rahman***: Influence of subsurface hydrodynamics on the lower atmosphere at the catchment scale, 2015, 98 S. + XVI. open access[1]

Heft 71: ***Sabrina Wahl***: Uncertainty in mesoscale numerical weather prediction: probabilistic forecasting of precipitation, 2015, 108 S. open access[1]

Heft 72: ***Markus Übel***: Simulation of mesoscale patterns and diurnal variations of atmospheric CO_2 mixing ratios with the model system TerrSysMP-CO_2, 2015, [erschienen] 2016, II, 158 S. open access[1]

---

[1] Available at `http://hss.ulb.uni-bonn.de/fakultaet/math-nat/`

Meteorologisches Institut
Mathematisch Naturwissenschaftliche Fakultät
Universität Bonn